



Universitat
de les Illes Balears

DOCTORAL THESIS
2018

**ACTIVE SHEAR STRENGTHENING OF
REINFORCED CONCRETE BEAMS USING
Ni-Ti-Nb SHAPE MEMORY ALLOYS**

Joan M. Rius Gibert



Universitat
de les Illes Balears

DOCTORAL THESIS
2018

Doctoral Programme of Physics

**ACTIVE SHEAR STRENGTHENING OF
REINFORCED CONCRETE BEAMS USING
Ni-Ti-Nb SHAPE MEMORY ALLOYS**

Joan M. Rius Gibert

Thesis Supervisor: Antoni Cladera Bohigas

Thesis Supervisor: Carlos Ribas González

Thesis tutor: Eduard Cesari Aliberch

Doctor by the Universitat de les Illes Balears

ABSTRACT

Shear strengthening of existing structures is often required as shear failures in reinforced concrete (RC) members are associated with brittle collapses, it being essential to avoid this kind of failure. This thesis presents comprehensive research on the feasibility of using Shape Memory Alloys (SMA) to actively strengthen shear critical beams. Specifically, an SMA (Ni-Ti-Nb) with wide hysteretic behavior in terms of the range of transformation temperatures for martensite and austenite phases has been applied for active external shear strengthening of RC beams using the special property of Shape Memory Effect (SME). SME refers to the phenomenon whereby SMAs can return to a predefined shape upon heating (activation). When the deformation of a prestrained SMA is constrained upon heating, it is not possible for the SMA to recover its previous shape and, therefore, it develops recovery stresses. These recovery stresses may be used for prestressing concrete members.

It should be highlighted that most of the frequently used shear strengthening technologies, e.g. strengthening with fiber reinforced polymers (FRP), are passive technologies: it is necessary for the strengthened structure to increase its deformation and reach an elevated level of damage before the strengthening material can start contributing. Alternatively, a previous unloading process of the structure to recover deformations may be needed before strengthening with passive technologies. The technology proposed in this doctoral thesis uses SME to actively confine and prestress the strengthened concrete member. In this way, the strengthening material immediately begins working upon installation and activation.

A complete thermo-mechanical characterization of the Ni-Ti-Nb wires used has been carried out to assess adequacy for the shear strengthening of RC beams in the ambient temperatures range for civil engineering structures. This experimental campaign for characterization of SMA included a set of tensile tests at different temperatures and another set of recovery stress tests. It has been concluded that the Ni-Ti-Nb wires show promising performance.

An experimental shear strengthening campaign comprising the performance of tests to failure on 20 small-scale concrete beams with activated external shear reinforcement was carried out. Pseudo-spirals of 3 mm diameter Ni-Ti-Nb wires, or wires with a U-shape configuration, were placed around the RC beams in order to confine them and close shear

cracks (if any) at activation. The experiment results show a successful increase in shear strength and the deflection measured at failure of the retrofitted beams.

The effect of the geometrical imperfections of the reinforcement has also been studied and possible pre-stressing losses due to these imperfections have been evaluated by means of a new experimental campaign. The result is that Ni-Ti-Nb wires show promising performance despite possible imperfections upon installation in small-scale elements.

Finally, two different shear models —the Compression Chord Capacity Model (CCCM) and shear provisions in Eurocode 2— have been used to predict the shear strength of the tested specimens. The experiment results and predictions showed good correlation, especially for the CCCM, which also showed good correlation in terms of the observed crack patterns.

Based on the previously summarized research work, we can conclude that the proposed technology for active shear strengthening of RC beams works properly.

RESUMEN

El refuerzo a cortante de estructuras en servicio es requerido a menudo debido a que las roturas por cortante en elementos de hormigón armado (HA) están asociadas a roturas frágiles y, así, es esencial evitar este tipo de fallo. Esta tesis presenta una investigación exhaustiva sobre la viabilidad del uso de Aleaciones con Memoria de Forma (AMF) para reforzar activamente vigas críticas a cortante. Específicamente, se ha aplicado una AMF (Ni-Ti-Nb) con un amplio comportamiento histerético en términos del rango de temperaturas de transformación para las fases de martensita y austenita para el refuerzo externo activo a cortante de vigas de HA usando la propiedad especial del Efecto Memoria de Forma (EMF). El EMF se refiere al fenómeno por el cual las AMF pueden volver a una forma predefinida al calentarse (activación). Cuando al calentar una AMF predeformada su deformación se ve restringida, ésta no puede recuperar su forma previa y, por tanto, desarrolla tensiones de recuperación. Estas tensiones de recuperación pueden usarse para pretensar elementos de hormigón.

Debe destacarse que la mayoría de las más frecuentes tecnologías de refuerzo a cortante, por ejemplo, el refuerzo con polímeros reforzados con fibra (PRF), son tecnologías pasivas: es necesario que la estructura reforzada aumente su deformación y alcance un nivel elevado de daño antes de que el material de refuerzo pueda empezar a contribuir. Alternativamente, puede ser necesario un proceso de descarga previo de la estructura para recuperar deformaciones antes de su refuerzo con tecnologías pasivas. La tecnología propuesta en esta tesis doctoral utiliza el EMF para restringir y pretensar activamente un elemento de hormigón. De esta forma, el material de refuerzo empieza a trabajar inmediatamente después de su instalación y activación.

Se ha llevado a cabo una caracterización termo-mecánica completa de los alambres de Ni-Ti-Nb usados para evaluar su adecuación para el refuerzo a cortante de vigas de HA en el rango de temperaturas habituales para estructuras de ingeniería civil. Esta campaña experimental para la caracterización de la AMF ha incluido un conjunto de ensayos de tracción a diferentes temperaturas y otro conjunto de ensayos de tensiones de recuperación. Se ha concluido que los alambres de Ni-Ti-Nb muestran un rendimiento prometedor.

Se ha realizado una campaña experimental de refuerzo a cortante de vigas que ha consistido en realizar ensayos a rotura de 20 vigas de hormigón a pequeña escala con refuerzo a cortante externo activado. Se han colocado pseudo-espирales de alambres de Ni-Ti-Nb de 3 mm de diámetro, alrededor de vigas de HA para confinarlas y cerrar las grietas de cortante (si existen) durante la activación. También se ha usado una configuración de refuerzo con alambres en forma de U. Los resultados experimentales muestran un significativo incremento de la resistencia a cortante y de la deflexión medida en rotura de las vigas reforzadas.

También se ha estudiado el efecto de las imperfecciones geométricas del refuerzo y se han evaluado las posibles pérdidas previas de tensiones debidas a estas imperfecciones mediante una nueva campaña experimental. Se ha concluido que los alambres de Ni-Ti-Nb muestran un rendimiento prometedor a pesar de las posibles imperfecciones durante la instalación en elementos a pequeña escala.

Finalmente, se han aplicado dos modelos de cortante diferentes: el Modelo de capacidad del cordón comprimido (CCCM) y las especificaciones de cortante del Eurocódigo 2, para predecir la resistencia a cortante de las vigas ensayadas. Se ha logrado un buen ajuste entre los resultados experimentales y las predicciones, especialmente para el CCCM, que también ha mostrado una buena correlación en términos de los patrones de grietas observados.

De los trabajos de investigación previamente revisados, se puede concluir que la tecnología propuesta para el refuerzo activo a cortante de vigas de HA funciona adecuadamente.

RESUM

El reforç a tallant d'estructures en servei és requerit sovint pel fet que els trencaments a tallant en elements de formigó armat (FA) estan associats a trencaments fràgils i, així, és essencial evitar aquest tipus de fallada. Aquesta tesi presenta una investigació exhaustiva sobre la viabilitat de l'ús d'Aliatges amb Memòria de Forma (AMF) per reforçar activament bigues crítiques a tallant. Específicament, s'ha aplicat una AMF (Ni-Ti-Nb) amb un ampli comportament histerètic en termes del rang de temperatures de transformació per a les fases de martensita i austenita per al reforç extern actiu a tallant de bigues de FA usant la propietat especial de l'Efecte de Memòria de Forma (EMF). L'EMF es refereix al fenomen pel qual les AMF poden tornar a una forma prèvia en ser escalfada (activació). Quan a l'escalfar una AMF predeformada la seva deformació es veu restringida, no pot recuperar la seva forma prèvia i, per tant, desenvolupa tensions de recuperació. Aquestes tensions de recuperació poden usar-se per pretensar elements de formigó.

Cal destacar que la majoria de les més freqüents tecnologies de reforç a tallant, per exemple, el reforç amb polímers reforçats amb fibra (PRF), són tecnologies passives: cal que l'estructura reforçada augmenti la seva deformació i arribar un nivell elevat de dany abans que el material de reforç pugui començar a contribuir. Alternativament, pot ser necessari un procés de descàrrega previ de l'estructura per recuperar deformacions abans del seu reforç amb tecnologies passives. La tecnologia proposada en aquesta tesi doctoral utilitza l'EMF per a restringir i pretensar activament un element de formigó. D'aquesta manera, el material de reforç comença a treballar immediatament després de la seva instal·lació i activació.

S'ha dut a terme una caracterització termo-mecànica completa dels filferros de Ni-Ti-Nb usats per avaluar la seva adequació per al reforç a tallant de bigues de FA en el rang de temperatures habituals per a estructures d'enginyeria civil. Aquesta campanya experimental per a la caracterització de l'AMF ha inclòs un conjunt d'assajos de tracció a diferents temperatures i un altre conjunt d'assajos de tensions de recuperació. S'ha conclòs que els filferros de Ni-Ti-Nb mostren un rendiment prometedori.

S'ha realitzat una campanya experimental de reforç a tallant de bigues que ha consistit en realitzar assaigs a trencament de 20 bigues de formigó a petita escala amb reforç a tallant extern activat. S'han col·locat pseudo-espitals de filferros de Ni-Ti-Nb de 3 mm de diàmetre,

al voltant de bigues de FA per confinar-les i tancar les esquerdes de tallant (si existeixen) durant l'activació. També s'ha fet servir una configuració de reforç amb filferros en forma de U. Els resultats experimentals mostren un significatiu increment de la resistència a tallant i de la deflexió mesurada en trencament de les bigues reforçades.

També s'ha estudiat l'efecte de les imperfeccions geomètriques del reforç i s'han avaluat les possibles pèrdues prèvies de tensions degudes a aquestes imperfeccions mitjançant una nova campanya experimental. S'ha conclòs que els filferros de Ni-Ti-Nb mostren un rendiment prometedor malgrat les possibles imperfeccions durant la instal·lació en elements a petita escala.

Finalment, s'han aplicat dos models de tallant diferents: el Model de capacitat del cordó comprimit (CCCM) i les especificacions de tallant de l'Eurocodi 2, per predir la resistència a tallant de les bigues assajades. S'ha aconseguit un bon ajust entre els resultats experimentals i les prediccions, especialment per al CCCM, que també ha mostrat una bona correlació en termes dels patrons d'esquerdes observats.

Dels treballs d'investigació prèviament revisats, es pot concloure que la tecnologia proposada per al reforç actiu a tallant de bigues de FA funciona adequadament.

AGRAÏMENTS

En primer lloc voldria agrair als dos directors d'aquesta tesi doctoral el seu suport i confiança en mi per dur-la a terme: el Dr. Antoni Cladera Bohigas i el Dr. Carlos Ribas González. Ha estat una experiència enriquidora treballar amb ells, tant a nivell tècnic com humà. He de destacar el bon tracte que he rebut durant les diferents fases de treball i la seva disponibilitat i implicació per clarificar els dubtes que s'han anat presentant. En particular, he d'agrar a n'Antoni haver-me proposat participar en els diversos projectes d'investigació, el primer allà a finals de 2013, i que hagin pogut culminar en aquesta tesi. A en Carlos li he d'agrar la confiança incondicional en l'obtenció de resultats en el transcurs de les investigacions. La resta del grup d'investigació Enginyeria de la construcció i les Estructures (ConStruct) tenen també el meu reconeixement. En especial, en Benito Mas, pel seu suport i dedicació exhaustius durant la preparació i realització de les campanyes experimentals de les bigues. També al Dr. Luis Montoya i al Dr. Joaquín Ruiz agraeixo el seu suport en la fase final de laboratori. A ells vaig “donar el testimoni” per les posteriors campanyes experimentals. També voldria agrair al tutor d'aquesta tesi, el Dr. Eduard Cesari Aliberch, el compliment diligent de la seva tasca de tutorització.

Vull fer també extensiu l'agraïment a tot el personal de la UIB que d'una manera o altra ha intervingut, col·laborat i/o donat suport en les diferents tasques de laboratori realitzades. En particular, a en Toni Dols del laboratori de materials i assaigs de l'Escola Politècnica Superior, al Dr. Joan Cifre del laboratori científic-tècnic i al Dr. Joan Torrens del laboratori de ciència de materials del Departament de Física.

També vull mencionar i agrair a altres empreses i entitats que han col·laborat en diferents tasques: Refer pel subministrament del Ni-Ti-Nb, el material més important del treball, el que té “memòria”; Pastor, pel subministrament del formigó així com per disposar de les seves instal·lacions i el seu suport en el formigonat de les bigues; i Labartec per la realització dels assajos de l'acer.

Además, y en relación a otras entidades con las que he tenido relación durante la tesis, quiero agradecer a la Universidad de Coruña (UdC), por haberme acogido durante mi corta estancia en Coruña donde estuve perfectamente atendido. En especial, a Fernando Varela y compañía.

D'altra banda, voldria fer un salt en el temps cap a finals del anys 90 i tornar al Departament d'Enginyeria del Terreny de la UPC. Perquè he de dir que el període vital del meu doctorat es va iniciar en aquella època a la UPC a Barcelona. Allà vaig aconseguir la suficiència investigadora l'any 1998 que m'ha permès al cap dels anys continuar el Doctorat aquí a la UIB. Vull, doncs, expressar també el meu agraïment personal a la gent del departament d'Enginyeria del Terreny de la UPC, pel període que hi vaig passar de docència i investigació. En especial, al que va ser el meu professor de geotècnia a Camins i tutor Dr. Alberto Ledesma, i també al Dr. Eduardo Alonso, director del departament en aquella època i al Dr. Josep Antoni Gili, el meu tutor de tesina d'especialitat, al grup de geòlegs encapçalat pel Dr. Jordi Corominas i al Dr. José Moya, company de treballs de camp. Agraïment extensiu també a la resta de tècnics i personal del departament i del laboratori de Geotècnia.

Abans d'acabar aquests agraïments, vull expressar moltíssima gratitud als meus pares. Si puc escriure això, i amb els anys això es veu molt clar, és gràcies a ells. També a la meva família nombrosa: a na Beni per acompanyar-me i a en Joan, en Jaume i na Júlia per seguir-nos.

Aquesta tesi doctoral ha estat desenvolupada en el marc de dos projectes. El projecte "*BIA2015-64672-C4-3-R: Desarrollo de técnicas de refuerzo de estructuras de hormigón con materiales avanzados y sus modelos mecánicos de comportamiento para la extensión de su vida útil*", cofinançat per la Agència Estatal d'Investigació i els Fons Europeus de Desenvolupament Regional (FEDER), que forma part d'un projecte coordinat entre la Universitat Politècnica de Catalunya, la Universitat Politècnica de València, la Universidad de Coruña i la Universitat de les Illes Balears. I el projecte "*BIA2012-31432: Materiales inteligentes en hormigón estructural. Aplicación de aleaciones con memoria de forma como refuerzo a cortante en elementos lineales*", cofinançats per MINECO y EDRF.



CONTENTS

ABSTRACT.....	I
RESUMEN.....	III
RESUM.....	V
AGRAÏMENTS.....	VII
CONTENTS.....	IX
List of figures.....	XIII
List of tables.....	XIX
1. INTRODUCTION.....	1
1.1 RESEARCH MOTIVATION	1
1.2 RESEARCH SCOPE AND SIGNIFICANCE	3
1.3 OUTLINE AND CONTENTS OF THE THESIS.....	3
2. STATE OF THE ART.....	5
2.1 SHEAR STRENGTH OF REINFORCED CONCRETE BEAMS	5
2.1.1 SHEAR TRANSFER MECHANISMS.....	5
2.1.2 CONSIDERED SHEAR MODELS	8
2.1.3 SHEAR STRENGTHENING OF RC BEAMS	16
2.2 SHAPE MEMORY ALLOYS IN STRUCTURAL ENGINEERING	22
2.2.1 INTRODUCTION TO SMAs	22
2.2.2 FUNDAMENTALS OF SMAs.....	25
2.3 KEY PROPERTIES OF SMAs FOR STRUCTURAL ENGINEERING	30
2.3.1 THE SHAPE MEMORY EFFECT	30
2.3.2 THE PSEUDO-ELASTICITY	32
2.3.3 THE DAMPING EFFECT	33
2.4 REVIEW OF SOME SMAs FOR STRUCTURAL ENGINEERING APPLICATIONS.....	34

2.4.1	INTRODUCTION TO DIFFERENT SMAs.....	34
2.4.2	BINARY Ni-Ti ALLOYS	36
2.4.3	Ni-Ti-Nb ALLOYS IN STRUCTURAL ENGINEERING.....	46
2.5	ACTIVE STRENGTHENING OF REINFORCED CONCRETE BEAMS USING SHAPE MEMORY ALLOYS.....	49
2.5.1	PRESTRESSING THROUGH SMA WIRES.....	49
2.5.2	ACTIVE CONFINEMENT.....	54
2.5.3	PERFORMANCE OF RECOVERY STRESSES	58
2.5.4	ACTIVE STRENGTHENING OF RC BEAMS USING Ni-Ti-Nb.....	60
3.	RESEARCH OBJECTIVES.....	63
3.1.	SHORT SUMMARY OF THE STATE OF THE ART	63
3.2.	SPECIFIC OBJECTIVES	64
3.3.	METHODOLOGY	64
4.	CHARACTERIZATION OF THE Ni-Ti-Nb WIRES	67
4.1	OBJECTIVES AND BRIEF SUMMARY OF THE TESTS	67
4.2	MATERIAL COMPOSITION	68
4.3	TRANSFORMATION TEMPERATURES.....	69
4.4	THERMO-MECHANICAL CHARACTERIZATION.....	72
4.4.1	TEST EQUIPMENT AND INSTRUMENTATION.....	72
4.4.2	PLANNING OF THE TESTS	73
4.4.3	TEST PROCEDURE.....	76
4.4.4	SUMMARY OF THE TEST RESULTS.....	78
4.4.5	RECOVERY STRESS-TEMPERATURE PHASE DIAGRAM	80
4.4.6	OTHER DETAILED RESULTS.....	85
4.5	CONCLUSIONS ON Ni-Ti-Nb CHARACTERIZATION.....	96
5.	EXPERIMENTAL CAMPAIGN ON ACTIVE SHEAR STRENGTHENING OF RC BEAMS USING Ni-Ti-Nb WIRES	99
5.1	OBJECTIVE OF THE EXPERIMENTAL CAMPAIGN.....	99
5.2	DESIGN OF THE TEST SPECIMENS.....	100
5.3	FABRICATION OF THE TEST SPECIMENS. CONCRETE AND STEEL PROPERTIES	106

5.4	STRENGTHENING OF THE BEAM SPECIMENS	111
5.5	INSTRUMENTATION AND TESTING PROCEDURE.....	114
5.6	RESULTS OF EXPERIMENTAL TESTS AND DISCUSSION.....	117
5.6.1	OBSERVED BEHAVIOR AND SHEAR STRENGTH.....	117
5.6.2	MEASURED STRAINS	128
5.7	COMPARATIVE ANALYSIS OF THE BEAM TESTS	138
5.8	CONCLUSIONS OF THE BEAM EXPERIMENTAL CAMPAIGN.....	139
6.	EXPERIMENTAL STUDY OF THE Ni-Ti-Nb RECOVERY STRESSES UNDER NON- IDEALIZED CONDITIONS	141
6.1	PLANING OF THE TESTS AND TEST PROCEDURE.....	141
6.2	TEST RESULTS.....	144
6.3	RECOVERY STRESS OF THE STRENGTHENING WIRES.....	149
6.4	CONCLUSIONS OF THE Ni-Ti-Nb RECOVERY STRESSES UNDER NON- IDEALIZED CONDITIONS	153
7.	COMPARISON OF THE RC BEAM TESTS RESULTS WITH THE PREDICTIONS BY TWO DIFFERENT SHEAR STRENGTH MODELS	155
7.1	STRESSES IN STRENGTHENING WIRES DERIVED FROM THE EXPERIMENTAL CAMPAIGNS	156
7.2	PREDICTIONS CONSIDERING THE EXPERIMENTALLY OBTAINED STRESSES IN THE STRENGTHENING Ni-Ti-Nb WIRES	158
7.2.1	PREDICTIONS BY THE COMPRESSION CHORD CAPACITY MODEL (CCCM)	158
7.2.2	PREDICTIONS BY THE SHEAR DESIGN EQUATIONS IN EUROCODE 2 (EC2)	166
7.2.3	COMPARISON BETWEEN THE TEST RESULTS AND THE PREDICTIONS OF CCCM AND EC2	170
7.3	DESIGN SHEAR STRENGTH OF STRENGTHENED BEAMS	172
7.4	CONCLUSIONS OF APPLICATION OF SHEAR MODELS	175
8.	CONCLUSIONS AND FUTURE WORK.....	177
	REFERENCES.....	187
	APPENDIX. EXPERIMENTAL CAMPAIGN OF STRENGTHENED RC BEAMS AND MODEL CALCULATIONS	205



List of figures

Figure 2.1. Shear transfer mechanisms (STM) in a RC beam with rectangular cross section: a) beam actions, b) cantilever action, c) aggregate interlock, d) dowel action, e) residual tensile strength of concrete and f) arching action. From (Ribas González & Fernández Ruiz 2017).....	6
Figure 2.2. a) Picture of a strengthened beam showing the development of the first and the second branches of critical crack, and b) schematic internal forces for STM in a RC beam with stirrups (Marí et al. 2015)	8
Figure 2.3. Truss model and notation for shear reinforced members (CEN 2002).....	10
Figure 2.4. Passive shear strengthening methods for RC beam: a) extra stirrups and concrete, b) steel fiber concrete, c) epoxy bonded steel plates and d) FRPs. From (Ferreira 2013)	18
Figure 2.5. Schematic pictures of flexural strengthening methods: a) externally bonded FRP laminate, b) NSM FRP strips, and c) NSM FRP bars. From (El-Hacha & Soudki 2013).....	19
Figure 2.6. Steel tendons active shear strengthening methods for RC beam: a) external and b) internal. From (Ferreira 2013).....	21
Figure 2.7. Beam retrofitting in shear using steel ribbons: a) arranged along full depth of the beam, and b) arranged along part of the cross-section depth of the beam. From (Colajanni et al. 2017)	22
Figure 2.8. Different atomic behaviors of: a) stress-induced martensitic transformation by distortion in Ni-Ti alloys and b) plastic deformation by slip. From (Maruyama & Kubo 2011).....	26
Figure 2.9. Schematic definition of forward and reverse martensitic transformation temperatures related to Martensite fraction. From (Cladera, Weber, et al. 2014).....	27
Figure 2.10: Schematic phase diagrams for Ni-Ti alloy, showing: a) detwinning of Ni-Ti with applied stress; b) the unloading and subsequent heating to austenite under no deformation constraint for Ni-Ti, and c) pseudo-elastic loading path for Ni-Ti and ordinary plastic deformation. From (Cladera, Weber, et al. 2014).....	28
Figure 2.11: Typical stress-strain-temperature diagram for Ni-Ti alloys. From (Cladera, Weber, et al. 2014).....	28
Figure 2.12. Diagram of the shape memory effect (white arrows) and the two-way shape memory effect (grey arrows). From (Santamarta et al. 2005).....	31
Figure 2.13. Stress-strain diagrams and dissipated energy: (a) martensitic damping ($T < A_s$); (b) damping in austenite (super elasticity) From (Cladera, Oller, et al. 2014).....	34
Figure 2.14. Schematic stress-strain curves of shape memory alloys (left) and associated transformation temperature profiles at zero stress (right) in terms of the martensitic phase fraction (f): a), b) Actuator-like change of strain and stiffness against a constant force; c), d) shape memory effect in the cases of free recovery and constrained recovery; e), f) pseudo-elasticity; and g), h) martensitic damping. From (Janke et al. 2005).....	36
Figure 2.15. Pseudo-elastic stress-strain behavior of the Ni-Ti alloy 0.5 mm diameter wire used as fiber reinforcement of a beam. From (Shajil et al. 2012).....	42
Figure 2.16. Cyclic stress-strain behavior of the Ni-Ti alloy. From (Abdulridha et al. 2013)	44
Figure 2.17. Stress-strain behavior of the Ni-Ti alloy tested by (Mas et al. 2016a).....	45
Figure 2.18. Comparison between brittle and ductile shear failures. (Mas et al. 2016a).....	45
Figure 2.19. Schematic stress-strain diagrams of prestraining and generation of recovery stresses during the activation of the reverse transformation in a constrained SMA: a) Narrow hysteresis alloy, i.e., Ni-Ti; b) Wide hysteresis alloy, i.e., Ni-Ti-Nb. From (Cladera, Weber, et al. 2014)	47

Figure 2.20. Schematic thermomechanical paths during the activation and cooling of a constrained SMA: a) narrow hysteresis alloy, i.e., Ni–Ti; b) wide hysteresis alloy, i.e., Ni–Ti–Nb. From (Cladera, Weber, et al. 2014)	47
Figure 2.21. a) Schematic drawing of the bonding test set-up and b) Cross-section of the tested Ni-Ti wire. From (Mas et al. 2017)	51
Figure 2.22. Some analyzed possibilities of external reinforcement from (Soroushian et al. 2001): a) longitudinal corrective force and b) local post-tensioning for enhancement of shear resistance	51
Figure 2.23. Section and detail of NSM SMA bar for prestressing technique. From (Rojob & El-hacha 2017)	53
Figure 2.24. Schematic drawings of a confined concrete column uniaxial compressive test: a) Concrete element confined with SMA spirals, b) Cross-section before heating, c) Cross-section after heating, and d) Uniaxial compressive test stress–strain path comparison between confined and unconfined test. From (Cladera, Oller, et al. 2014), adapted from (Shin & Andrawes 2010)	55
Figure 2.25. Stress-strain relationship for test specimens without confinement, confined with SMAs, GFRP, or SMA-GFRP hybrid fabrics (Cladera, Oller, et al. 2014).....	55
Figure 2.26. a) Example of application of SMA spirals for active confinement of bridge piers (Dommer & Andrawes 2012) and b) general view and cross section of lab specimen of RC columns retrofit by SMA wire jackets (Choi, Choi, et al. 2012).....	56
Figure 2.27. Comparison of Stress-strain relationship for proposed plasticity model and experimental results (Chen & Andrawes 2017b).	57
Figure 2.28. Scheme of active confinement of non-circular prisms in (Chen et al. 2014).....	58
Figure 2.29. Schematic graphs of stress recovery developing under: a) initial gap and b) elastic constraint condition. From (Lee et al. 2015).....	59
Figure 4.1. 300 mm long Ni-Ti-Nb samples ready to be tested	68
Figure 4.2. Test equipment at UIB laboratories employed for the SMA physical characterization: a) EDX equipment at SCT lab, b) resistance test equipment at the Material Science lab of the Dept. of Physics of the UIB, and c) DSC test equipment at SCT lab.....	69
Figure 4.3. Schematic graph of phase transformation in SMAs according to temperature with a wide hysteretic behavior. Adapted from (Cladera, Weber, et al. 2014)	69
Figure 4.4. Differential Scanning Calorimetry (DSC) result of Ni-Ti-Nb test carried out.....	71
Figure 4.5. Temperature dependence of resistance for a Ni-Ti-Nb sample. Data are normalized to the value of resistance at 390 °K: a) first cycle, and b) second cycle.....	71
Figure 4.6. Martensite fraction-temperature graph of the two cycles of the tested Ni-Ti-Nb alloy samples from resistance tests.....	72
Figure 4.7. Experimental set-up for tensile tests: a) Load frame and b) inside view of thermal chamber	72
Figure 4.8 a) thermocouples along a sample and b) HBM data acquisition system for the thermocouples	73
Figure 4.9. A Ni-Ti-Nb sample between clamps (150 mm tested sample and 75 mm within each clamp) ready to be tested	76
Figure 4.10. Recovery stress tests at different temperatures (stress-temperature curve)	80
Figure 4.11. Recovery stress tests: a) Stress-time curve and b) temperature-time curve	81

Figure 4.12. Recovery stress test #3 (5 points temperature logging uniformly distributed on the sample: temp1 upper part of the sample to temp5 lower part of it)	82
Figure 4.13. Monotonic tensile tests for austenite samples at different test temperatures	83
Figure 4.14. Adjusted diagram for phase transformation M_s and M_f	84
Figure 4.15. Calculated phase transformation diagram for Ni-Ti-Nb and recovery stress tests.	84
Figure 4.16. a) Monotonic tensile tests of Ni-Ti-Nb wires in martensite phase. b) Schematic graph of determination of elastic modulus (E) and yield strength ($f_{y,0.002}$) for test #4 at RT (strain depicted up to 10 %).	86
Figure 4.17. Cyclic tensile tests of Ni-Ti-Nb wires in martensite phase	87
Figure 4.18. Monotonic tensile tests at different temperatures carried out immediately after recovery stresses generation: a) stress-strain graph and b) Stress-time graph. Note stress drop during cooling down to 0 °C on sample #14.....	88
Figure 4.19. Stress-time graph of monotonic tensile tests at different temperatures carried out immediately after recovery stresses generation and calculated phase transformation diagram for Ni-Ti-Nb	89
Figure 4.20. Cyclic tensile tests after recovery stresses generation	91
Figure 4.21. Stress-time graph of cyclic tensile tests with previous heat treatment tests. Note stress drop during cooling down to 0 °C on sample #15 and stress increment during heating to 40 °C on sample #13.....	91
Figure 4.22. Monotonic tensile test of the austenite sample #16 and one-cycle tensile test of the austenite sample #17 obtained by heating a martensite sample (strain free).	92
Figure 4.23. Cyclic tensile test of the austenite sample #18 obtained by heating a martensite sample (strain free).	93
Figure 4.24. Monotonic tensile tests for austenite samples at different test temperatures	94
Figure 4.25. One cycle tensile tests for austenite samples at different test temperatures	94
Figure 4.26. Cyclic tensile tests for austenite samples at different test temperatures	95
Figure 5.1. a) Main RC beam geometry characteristics, b) schematic drawing of central point load configuration, c) geometry and dimensions for reference beams (without external strengthening), and d) geometry and dimensions for specimens with external strengthening (SMA wires).....	101
Figure 5.2. Beams 1 to 5 geometries and strain-gauge locations of the beam specimens for phase 1.....	104
Figure 5.3. Beams 6 to 10 geometries and strain-gauge locations of the beam specimens for phase 2.....	105
Figure 5.4. a) Instrumented longitudinal reinforcement of a beam before casting, b) fresh concrete, c) the first concrete batch, and d) concrete beams ready to be tested	106
Figure 5.5 a) Standard cubes and, b) cylinders in the test frame	107
Figure 5.6. Stress-strain curves for $\phi 16$ mm bars used as longitudinal reinforcement	109
Figure 5.7 a) Front view, and b) rear view of a beam specimen, c) detail of the anchoring using U-Bolt saddle clamps, and d) activation process with heat gun	111
Figure 5.8. a) Strengthened beam with U-shape stirrups, b) detail of grooves in a beam, and c) spiral confining only the concrete compression chord of a beam.....	112

Figure 5.9. Comparison of wire reinforcement in beam: before activation on left hand side wire and after activation on right hand side	113
Figure 5.10. Test set-up with instrumentation devices: a) front view and b) back view.	115
Figure 5.11. Load cell during a test with photography twin cameras and video equipment recording	116
Figure 5.12. Monitoring devices: a) Linear position transducers located in a beam, b) strain gauge for longitudinal reinforcement, and c) strain gauge installed on Ni-Ti-Nb wire	116
Figure 5.13. a) Hydraulic actuator carrying out a test and b) data acquisition system.	117
Figure 5.14. Shear force-deflection for reference beams (1.1 and 1.2), strengthened beams with pitch equal to 100 mm (2.1 and 2.2), beams with the spiral un-activated (3.1a and 3.2a), and strengthened beams with pitch equal to 75 mm (5.1 and 5.2)	120
Figure 5.15. Beam 3.1a after peak load. Note that even after peak load, the wires already show some gap (vertical links)	120
Figure 5.16. Shear force-deflection for reference beams (1.1 and 1.2), strengthened beams (2.1 and 2.2) and strengthened beams after pre-cracking (4.1 and 4.2). All strengthened beams with pitch equal to 100 mm .	122
Figure 5.17. Shear force-deflection for reference beams with the spiral un-activated (3.1a and 3.2a) and the same beams with the spiral activated after the first collapse (3.1b and 3.2b)	122
Figure 5.18. Shear force-deflection for reference beams (6.1 and 6.2), strengthened beams with grooved wires (7.1 and 7.2), beams with U-shape stirrups (8.1 and 8.2), and beams with spirals confining only the concrete compression chord (9.1 and 9.2)	123
Figure 5.19. Shear force-deflection for reference beams (6.1 and 6.2), strengthened beams with U-shape stirrups with pitch equal to 100 mm (8.1 and 8.2), and with pitch equal to 75 mm (10.1 and 10.2)	124
Fig. 5.20 a) – j) Photographs of first phase beam specimens just after their maximum load was achieved and their crack patterns, with the numbering of the vertical links crossing the critical crack (except for beam 5.2 failed in bending)	125
Fig. 5.20 k) – t). Photographs of second phase beam specimens just after their maximum load was achieved and their crack patterns, with the numbering of the vertical links crossing the critical crack	126
Figure 5.21a. Strains measured in the longitudinal reinforcement of beams 1.1, 1.2, 2.1 and 2.2. A schematic drawing of the locations of the gauges is depicted on graph of beam 1.1	129
Figure 5.21b. Strains measured in the longitudinal reinforcement of beams: 3.1a, 3.1b, 3.2a, 3.2b, 4.1, 4.2, 5.1 and 5.2	130
Figure 5.22. Strains measured in the longitudinal reinforcement of beams of the second phase	131
Figure 5.23. Strains measured in the spiral vertical links in beams 2.1, 2.2, 3.1a, 3.1b, 3.2a, 3.2b, 4.1, 4.2, 5.1, and 5.2. Schematic drawings of the locations of the gauges are depicted on graphs of beams 2.1 and 2.2	133
Figure 5.24. Strains measured in the vertical links of the spirals in beams 7.1, 7.2, 8.1, 8.2, 9.1, 9.2, 10.1 and 10.2	134
Figure 5.25. Beam 4.2 with shear strengthening ready to be activated after the application of a pre-load (highlighted fissures) with specially protected strain gauges	135
Figure 6.1. a) Heating with a heat gun during activation of a sample, and b) installed sample between clamps with initial curvature	142
Figure 6.2. Recovery stress tests (stress-time). Pre-load of 8 MPa	144

Figure 6.3. Recovery stress tests (stress-time). Pre-load of 40 MPa 145

Figure 6.4. Initial imperfection (curvature) of SMA wires: a) before activation at tensile test, after activation at tensile test, c) before activation on a beam, d) after activation on a beam, and e) schematic drawing of the length before (l_f) and after activation (l_o)..... 147

Figure 6.5. Recovery stress tests with initial imperfection 147

Figure 6.6 Recovery stress-initial imperfection relationship for different tests carried out and adjusted curve for modeling purposes 148

Figure 6.7. Two wires with U-bolt union sample between clamps ready to be tested..... 149

Figure 6.8. Monotonic tensile test on U-bolt anchorage sample 149

Figure 6.9. Schematic picture of beam cross-section and the wire installation 150

Figure 6.10. Beams 2.1, 2.2, 3.1a, 3.2a, 4.1, 4.2, 5.1, and 5.2 during spiral installation (initial imperfection before activation)..... 150

Figure 6.11. Beams 7.1, 7.2, 8.1, 8.2, 9.1, and 10.1 during wire installation (initial imperfection before activation)..... 151

Figure 7.1. a) Schematic stress-strain path of Ni-Ti-Nb wires installed in the tested strengthened RC beams, and b) stress-strain graph of observed recovery stresses in tested wires 158

Figure 7.2. First branch of the critical crack and stirrup contribution. From (Marí et al. 2015)..... 160

Figure 7.3. Main geometric parameters for reference beam 1.1 163

Figure 7.4. Main geometric parameters for strengthened beam 2.1 166



List of tables

Table 2.1. Summary of dimensionless shear contributing components and factors considered in the Multi Action Model for members cracked in bending. From (Cladera, Marí, et al. 2016)	13
Table 2.2. Summary of basic CCCM formulation particularized for reinforced concrete beams with rectangular cross-sections. From (Cladera, Marí, et al. 2016).....	16
Table 2.3. Some alloys exhibiting shape memory effect (SME), pseudo-elasticity (PE) and damping effect(DE). Adapted from (Janke et al. 2005) and (Cladera, Weber, et al. 2014)	35
Table 4.1. List of main characteristics of planned tests of Ni-Ti-Nb wires	75
Table 4.2. Summary of average thermo-mechanical properties of the Ni-Ti-Nb wires at RT.....	78
Table 4.3. Summary of the Ni-Ti-Nb characterization test results	79
Table 4.4. Tests data for phase transformation regions of NI-Ti-Nb wires (stress-temperature)	84
Table 4.5. Properties of Ni-Ti-Nb wires in monotonic tensile tests	86
Table 4.6. Properties of Ni-Ti-Nb wires in cyclic tensile tests in martensite phase	87
Table 4.7. Final recovery stresses values on the samples in the previous recovery stress test	89
Table 4.8. Properties of Ni-Ti-Nb wires in monotonic tensile tests after recovery stresses generation	89
Table 4.9. Properties of Ni-Ti-Nb wires in cyclic tensile tests after recovery stresses generation	90
Table 4.10. Recovery strains on the samples with the previous treatment	92
Table 4.11. Properties of austenite samples (stress free) in monotonic and cyclic tensile tests	92
Table 4.12. Mechanical properties of austenite samples in monotonic and cyclic tensile tests.....	95
Table 5.1. Characteristics of the tested beam specimens.....	102
Table 5.2. Results of compressive and splitting strength tests performed	110
Table 5.3. Summary of beam test results.....	118
Table 5.4. Strains ($\mu\epsilon$) at beam failure measured in the gauges of the vertical links of the beams. In bold gauges in links of spans that failed in shear	132
Table 5.5. Strains ($\mu\epsilon$) measured in strain gauges attached to vertical links crossed by the first branch of the critical crack	137
Table 5.6. Summary of average test results of the whole experimental campaign	138
Table 6.1. List of planned tests under non-idealized conditions.....	143
Table 6.2. Recovery stresses of the samples with the heat gun activation treatment	145
Table 6.3. Measured recovery stresses on the samples with initial imperfection (curvature)	148
Table 6.4. Measured imperfection (i_0) and obtained recovery stresses (σ_R) for tested beams.....	152

Table 7.1. Recovery stresses and final developed stresses in the strengthening wires at beam failure for tested beams	157
Table 7.2. Predictions by the CCCM: a) for phase 1 beams, and b) for phase 2 beams	161
Table 7.3. Predictions by the EC 2: a) for phase 1 beams and b) for phase 2 beams	167
Table 7.4. Summary of average comparison values of the whole experimental program and predicted shear strengths	171
Table 7.5. CCCM predictions of designed beams and comparison with average test values	174

1. INTRODUCTION

1.1 RESEARCH MOTIVATION

Strengthening of reinforced concrete (RC) members in structural engineering is a methodology to address deficiencies from several causes, e.g. design mistakes, changes in the use of a structure, repairing damaged structures or new code requirements, among many others. These deficiencies could lead to shear failures of RC members (a type of failure associated with brittle collapses) which could cause sudden material and human losses. It is therefore clearly necessary that this type of failure be avoided and, for this reason, shear strengthening of existing structures is sometimes required.

Strengthening technologies for critical shear beams may be classified into two categories: passive strengthening and active strengthening methods. In both cases, the strengthening increases structure safety (by means of increasing strength), but when using passive strengthening methods, e.g. common strengthening with fiber reinforced polymers (FRP), it is necessary for the strengthened structure to increase its deformation and level of damage before engaging the strengthening material. Alternatively, before undertaking strengthening, the structure should be partially, or totally, unloaded. This way the strengthening material could contribute as soon as the structure is reloaded. When using active strengthening methods, the structure is prestressed, or actively confined when the strengthening material

is correctly installed. However, active strengthening methods generally require hydraulic jacks and anchorages, so it is often necessary to maintain a large work area to accommodate these auxiliary elements. These drawbacks may be overcome using a material that does not require prestressing elements to be activated. One of these is shape memory alloys (SMAs) that only require a simple action such as raising the temperature to be activated.

SMAs are materials that have the ability to achieve high deformations and to recover such deformations after unloading or upon heating. These properties of pseudo-elasticity and shape memory effect are useful for structural engineering. The shape memory effect is the property by which the material, after being subjected to a process of loading and unloading with apparently “permanent” deformations, can return to its previous form by raising its temperature to a certain level. This effect is the result of the reversible phase transformation that SMAs undergo, known as martensitic transformation, involving austenite and martensite solid phases of SMAs and it can be produced by changes in temperature or by the action of stresses for the envisaged application. Alloys with this shape memory effect include Ni-Ti binary alloys.

One of the drawbacks of these materials is that the phase transformations take place at typical service temperatures in civil engineering structures and this makes them inappropriate for proper performance. Nevertheless, there are SMAs, such as Ni-Ti-Nb, that may be stable in this range of temperatures. Its development as a strengthening material would be valuable and its application in civil engineering and building structures be useful.

This Ph.D. thesis has been developed with the framework of the following projects: “BIA2015-64672-C4-3-R: Development of strengthening techniques with advanced materials for concrete structures and their mechanical behavior models to extend their lifetime”, co-funded by the *Agencia Estatal de Investigación* (Spanish Government Research Agency) and the European Regional Development Fund (ERDF), and “BIA2012-31432: Smart materials in structural concrete. Application of Shape Memory Alloys as shear reinforcement in lineal members” co-funded by the *Ministerio de Economía y Competitividad* (Ministry of Finance and Competitiveness – MINECO) and ERDF.

1.2 RESEARCH SCOPE AND SIGNIFICANCE

The main objective of this Ph.D. thesis is to develop a new technology for shear strengthening of RC members by means of shape memory alloys. Specifically, rectangular RC beams have been strengthened using pseudo-rectangular spirals of Ni-Ti-Nb wires. The proposed technology uses the shape memory effect to actively confine or prestress the strengthened concrete member, meaning the strengthening material immediately begins to actively work upon installation and activation. The experimental results show a promising performance of the proposed technology, successfully increasing the shear strength and deflections of the retrofitted beams measured at failure.

The research significance of the work developed in the thesis is it being the first reported practical application of an SMA for shear strengthening of RC members using Ni-Ti-Nb wires. No hydraulic jack has been used to develop the prestraining forces. The specific characteristics of this alloy make it stable at service temperatures of civil engineering. The development of a shear strengthening technology with this SMA will be the main contribution of this research.

1.3 OUTLINE AND CONTENTS OF THE THESIS

This document is organized in eight chapters. After this first introductory chapter, the second looks at a state-of-the-art analysis from two different perspectives: shear strength of RC members and shape memory alloys applied to structural engineering. The third chapter presents the specific objectives of the thesis in each phase of the planned work and in each knowledge field.

Chapter four presents the experimental campaign for the thermo-mechanical characterization of the SMA used (Ni-Ti-Nb wires of 3 mm diameter). Different mechanical and thermal properties were tested in a load frame with a thermal chamber: tensile tests in austenite and martensite, recovery stress tests, material composition determination and tests to determine phase transformation temperatures were carried out. The laboratory tests were carried out in different loading conditions (monotonic, cyclic) and at different temperatures to verify the material behavior in the typical temperature range of structural engineering.

The results of the tests are set out and analyzed. The conclusions of the thermo-mechanical properties of the SMA are stated.

Chapter five presents the experimental campaign for active shear strengthening of small-scale RC beams using the previously characterized Ni-Ti-Nb wires. This experimental campaign had different stages: the design and casting of the beams; the design and fabrication of different shear strengthening elements from the Ni-Ti-Nb wires; the instrumentation of the beams and SMA elements to acquire data from tests, and the performance of the tests in a load frame in two different phases. The experimental results of these tests are also presented, and the acquired data analyzed. The conclusions of this work are also presented.

Chapter six includes another experimental campaign planned and performed to study the behavior of the Ni-Ti-Nb wires under actual non-idealized conditions of the wires after installation around the RC beams. Additional recovery stress tests were carried out with activation similar to on-site conditions (heat gun) instead of inside a thermal chamber. Moreover, further tests were carried out to study the effect of initial imperfections of the placement of the wires around the RC beams (non-perfectly straight wires) in the generation of recovery stresses. The results of the tests are set out and analyzed. The conclusions of the thermo-mechanical properties of the SMA under actual non-idealized conditions are stated.

Chapter seven compares the strengthened RC beams experiment results to the predictions from two different shear models: The Compression Chord Capacity Model (CCCM) and the shear equations included in Eurocode 2 (a widely used model in Europe). The specific behavior of SMAs (developing recovery stresses when restrained during the activation process) is taken into account in the models as a stress in the transverse reinforcement or yield strength in the design of the beams. The agreement and differences between the predictions and experiment results are analyzed. The conclusions regarding to the validation of those two existing shear design models are presented.

Chapter eight presents the overall conclusions of the work performed in the thesis and some future research lines are indicated.

References of all cited works and an appendix of the test results for the beam experimental campaign and main model calculations are included in the final sections.

2. STATE OF THE ART

2.1 SHEAR STRENGTH OF REINFORCED CONCRETE BEAMS

As previously exposed in chapter 1, shear failures in reinforced concrete (RC) members are associated with brittle collapses, which may cause sudden material and human losses. It is obviously necessary to avoid this type of failure. For this reason, shear strengthening of existing structures is sometimes necessary. Strengthening is often needed to address deficiencies of various causes, e.g. design mistakes, changes in the use of a structure, or new code requirements, among other causes.

2.1.1 SHEAR TRANSFER MECHANISMS

The ASCE-ACI Committee 445 published in 1998 a report with several approaches to shear design of structural concrete (ASCE-ACI Committee 445 1998). The report included a list of the main shear transfer mechanisms (STM), as an update of that of 1973 (ASCE-ACI Committee 426 1973). Hence, STM are normally classified into beam STM (figure 2.1a, where the internal lever arm remain constant) and the arching action (figure 2.1f, where the lever arm varies) (Ribas González & Fernández Ruiz 2017).

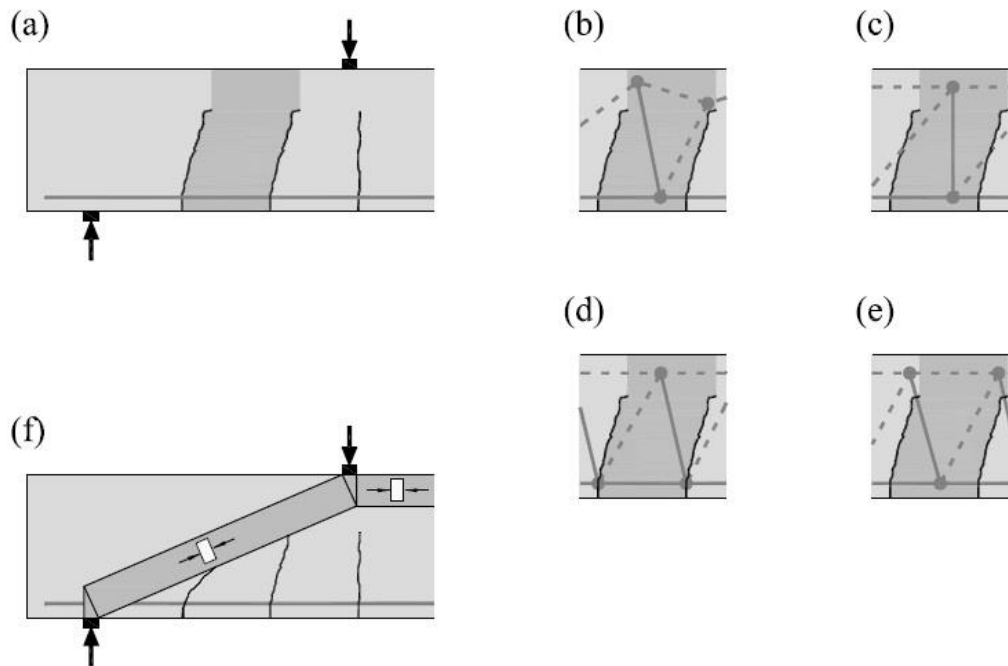


Figure 2.1. Shear transfer mechanisms (STM) in a RC beam with rectangular cross section: a) beam actions, b) cantilever action, c) aggregate interlock, d) dowel action, e) residual tensile strength of concrete and f) arching action. From (Ribas González & Fernández Ruiz 2017)

The STM are normally named:

- Compression chord or cantilever action (figure 2.1b): the shear resisted by the uncracked concrete chord.
- Aggregate interlock (figure 2.1c): the friction forces developed along the crack length, which are contrary to the relative displacement of both crack surfaces.
- Dowel action (figure 2.1d): the shear strength provided by the longitudinal reinforcement.
- Residual tensile stresses of concrete (figure 2.1e): crossing the inclined cracks, which act as a tie of a truss jointly with the compression chord, the tensile reinforcement and the concrete struts.

Additionally, the shear strength provided by the transverse reinforcement, if it exists. Therefore, it is commonly accepted that the shear strength in a RC beam is provided by several STM, whose relative contribution changes as the load increases (Reineck 1991), (Marí et al. 2015), (Cladera, Marí, et al. 2016), (Ribas González & Fernández Ruiz 2017), (Bairán et al. 2018).

At the ultimate load state, shear and bending are resisted by the contribution of the concrete and the contribution of longitudinal and transverse reinforcements. The concrete contribution is the shear resisted in the un-cracked compression chord (V_c), the shear transferred across web cracks: the tensile stresses transferred along the cracks and the aggregate interlock depending both on its width (V_w), and the dowel action in the longitudinal reinforcement (V_l). The transverse reinforcement contribution is produced by the reinforcement crossing the diagonal critical shear crack (V_s). The importance of the different contributing actions is considered to be variable as cracks open and propagate. A beam showing a developed critical crack with the first and the second branches is depicted in figure 2.2a, and a schematic drawing showing the STM for a rectangular section of a RC beam with stirrups is depicted in figure 2.2b.

Therefore, it can be considered that the shear strength, V_u in Eq. (2.1), is the sum of the different contribution of concrete and the transverse reinforcement:

$$V_u = (V_c + V_w + V_l) + V_s \quad (2.1)$$

To reach this conclusion and others, a lot of research has been conducted during last century on the shear strength of concrete members (Regan 1993). The understanding of STM has been a topic of major concern in structural engineering and many shear strength models, analytical and numerical ones, have been developed to explain them (Nielsen et al. 1978), (Vecchio & Collins 1986), (Petrangeli et al. 1999), (Bentz 2000), (Bairan & Mari 2006), (Navarro Gregori et al. 2007), (Saritas & Filippou 2009), (Ferreira et al. 2013), (Reineck 1991), (Zararis & Papadakis 2001), (Zararis 2006), (Choi & Park 2007), (Wolf & Frosch 2007), (Collins et al. 2008), (Muttoni & Fernandez-Ruiz 2008), (Colajanni et al. 2012), (Marí et al. 2015).

The different models have focused on one or more different mechanisms, depending on the relative importance assigned to them by the authors. In general, failure occurs when the shear critical crack propagates to the load application point, as predicted by different shear mechanical models.

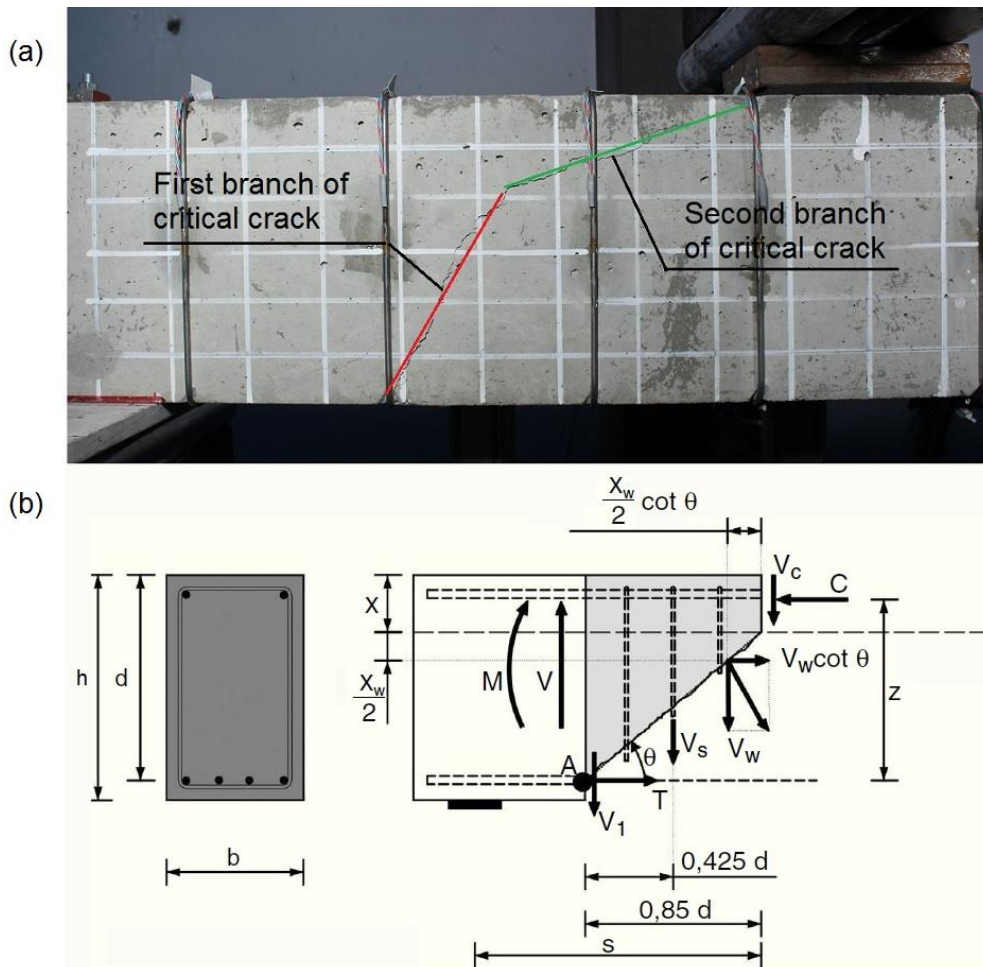


Figure 2.2. a) Picture of a strengthened beam showing the development of the first and the second branches of critical crack, and b) schematic internal forces for STM in a RC beam with stirrups (Marí et al. 2015)

2.1.2 CONSIDERED SHEAR MODELS

Many current models that consider shear strength of RC members have been developed from specific experiments carried out considering the above mentioned key aspects of shear mechanisms like compression field approaches or truss approaches. Most of them are complex to apply and inconvenient for engineering practice and design. Further, their applicability might be limited to the range of experiments used to derive them (Marí et al. 2015).

Two different shear models are presented and summarized in the next paragraphs. They will be used in Chapter 7 to compare their predictions to the experimental results. The given equations in next subsections are derived for reinforced rectangular cross-section members.

- **EUROCODE 2 MODEL (EC-2)**

Two different models are considered for the shear resistance of members with and without shear reinforcement. An empirical equation is considered for members without stirrups based in (Zsutty 1968). For members with stirrups, the EC-2 proposes the use of a variable angle truss model without concrete contribution (Walraven et al. 2008).

For RC members without shear reinforcement the shear strength is given by Eq. (2.2):

$$V_{Rd,c} = \left[\frac{0.18}{\gamma_c} k (100 \rho_l f_{ck})^{1/3} \right] bd \quad (2.2)$$

with a minimum given by Eq. (2.3):

$$V_{Rd,min} = [0.035 k^{3/2} (f_{ck})^{1/2}] bd \quad (2.3)$$

where,

f_{ck} is characteristic concrete compressive strength in MPa and $f_{ck} \leq 90$ MPa,

γ_c partial safety factor for concrete,

$k = 1 + \sqrt{\frac{200}{d}} \leq 2.0$, is the size factor, where d is expressed in mm,

$\rho_l = \frac{A_{sl}}{bd} \leq 0.02$, is longitudinal tension reinforcement ratio,

A_{sl} is the area of the anchored tensile reinforcement,

b is the width of the cross-section in mm, and

d is the effective depth of a cross section, in mm.

For members with shear reinforcement, the shear strength is based on a truss model (figure 2.3). Limiting values for the angle of the inclined struts in the web are given. Furthermore, the EC2 formulation distinguishes in the equations the inclination of shear reinforcement between vertical or inclined shear reinforcement, being the vertical stirrups a particular case of the later.

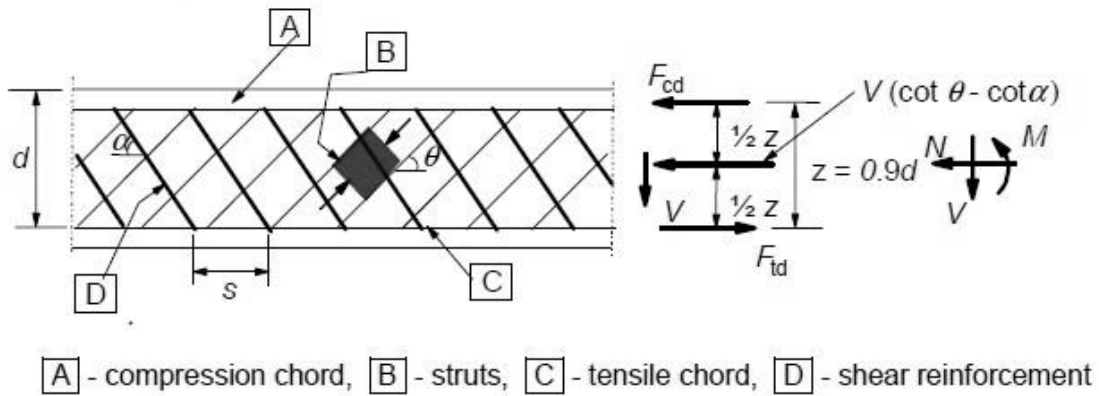


Figure 2.3. Truss model and notation for shear reinforced members (CEN 2002)

The shear resistance for members with vertical shear reinforcement is given by the lesser of Eqs. (2.4) or (2.5):

$$V_{Rd,s} = \frac{A_{sw}}{s} z f_{ywd} \cot \theta \quad (2.4)$$

$$V_{Rd,max} = b z v f_{cd} / (\cot \theta + \tan \theta) \quad (2.5)$$

where,

A_{sw} is the cross-sectional area of the shear reinforcement,

s is the spacing of the stirrups,

z is the inner lever arm, for a member with constant depth, corresponding to the maximum bending moment in the element under consideration. In the shear analysis, the approximate value $z = 0,9d$ may normally be used

f_{ywd} is the yield strength of the shear reinforcement,

θ is the inclination of concrete struts, the angle between the concrete compression struts and the main tension chord,

v is the effectiveness factor, it may be taken to be 0.6 for $f_{ck} \leq 60$ MPa, and $0.9 - f_{ck}/200 > 0.5$ for high strength concrete beams, and

f_{cd} is the design value of the concrete compression strength in the direction of the longitudinal member axis.

The recommended limiting values for $\cot \theta$ are given by the expression (2.6):

$$1 \leq \cot\theta \leq 2.5 \quad (2.6)$$

For members with inclined shear reinforcement, the shear resistance is the smaller value of Eqs. (2.7) and (2.8):

$$V_{Rd,s} = \frac{A_{sw}}{s} z f_{ywd} (\cot\theta + \cot\alpha) \sin\alpha \quad (2.7)$$

$$V_{Rd,max} = b z v f_{cd} (\cot\theta + \cot\alpha) / (1 + \cot^2\theta) \quad (2.8)$$

where,

α is the inclination angle, the angle between the shear reinforcement and the main tension chord (figure 2.3).

Note that if $\alpha = 90^\circ$ equations 2.7 and 2.8 become identical to Eqs. 2.4 and 2.5, respectively.

- THE COMPRESSION CHORD CAPACITY MODEL (CCCM)

Recent models have been developed to improve the design of RC members, specifically in shear, as the Multi-Action Shear Model (MASM) (Marí et al. 2015) and the Compression Chord Capacity Model (CCCM) (Cladera, Marí, et al. 2016) that was recently presented as a design-oriented model for the shear strength of reinforced concrete (RC) and prestressed concrete (PC) beams.

The CCCM is a simplification of the MASM. The MASM, based on classic mechanics, proposes explicit equations for the different STM: shear transferred through the un-cracked concrete in the compression chord, by through residual tensile stresses in the cracked concrete web, by through the dowel effect of the longitudinal reinforcement, and shear transferred through the shear reinforcement, if it exists. The use of explicit equations for each shear resisting action may result in an approach too complex for daily engineering practice. For this reason, a transparent simplification was undertaken, under the premise that the shear transferred by the compression chord is the main resisting action in the considered failure state, deriving the CCCM.

In the MASM, it is considered that the shear strength (V_u) is the sum of the shear resisted by the concrete and by the transverse reinforcement (V_s), and it must be lower than the shear force that produce failure in the concrete struts. The concrete contribution is explicitly

separated into the shear resisted in the un-cracked compression chord (V_c), shear transferred across web cracks (V_w) and the dowel action in the longitudinal reinforcement (V_l). The importance of the different contributing actions is considered to be variable as cracks open and propagate, but the MASM just consider an ultimate limit state situation for simplicity. Eq. (2.9) shows shear strength of RC beams:

$$V_u = (V_c + V_w + V_l) + V_s = f_{ctm}bd(v_c + v_w + v_l + v_s) \quad (2.9)$$

The shear force that produces failure in the concrete struts is given by Eq. (2.10):

$$V_{Rd,max} = b z v f_{ctm} \frac{\cot \theta}{1 + \cot^2 \theta} \quad (2.10)$$

where,

v_c (lower case variable) is the dimensionless value of un-cracked compression chord concrete contribution,

v_w (lower case variable) is the dimensionless value of shear transferred across the web critical crack,

v_l (lower case variable) is the dimensionless value of dowel action in the longitudinal reinforcement,

v_s (lower case variable) is the dimensionless value of transversal reinforcement contribution and,

f_{ctm} is the mean value of the concrete tensile strength.

The rest of the variables have been defined in the previous section of the Eurocode 2 model. The different shear contributions considered in the Multi-Action Shear Model are given in Eqs. 2.11 to 2.17 in table 2.1 for the particular case of members without axial loads (non-prestressed members or without tensile or compression loads) and with rectangular cross-section. The general equations may be found in (Marí et al. 2015), (Cladera et al. 2015) and (Marí et al. 2016).

Table 2.1. Summary of dimensionless shear contributing components and factors considered in the Multi Action Model for members cracked in bending. From (Cladera, Marí, et al. 2016)

Equations	Expressions
Compression chord	$v_c = \zeta \left[(0.88 + 0.7v_s) \frac{x}{d} + 0.02 \right]$ (2.11)
Cracked concrete web	$v_w = 167 \frac{f_{ctm}}{E_{cm}} \left(1 + \frac{2G_f E_{cm}}{f_{ctm}^2 d} \right)$ (2.12)
Longitudinal reinforcement	$if v_s > 0 \rightarrow v_l = 0.23 \frac{\alpha_e \rho_l}{1-x/d}$ (2.13a)
	$if v_s = 0 \rightarrow v_l = 0$ (2.13b)
Transversal reinforcement	$v_s = (d - x) \cot \theta \frac{A_{sw} f_{yw}}{s f_{ctm} b d} \approx \frac{0.85 d A_{sw} f_{yw}}{s f_{ctm} b d}$ (2.14)
Factors	Expressions
Size and slenderness effect	$\zeta = 1.2 - 0.2a \geq 0.65$ (a in meters) (2.15a)
	$\zeta = \frac{2}{\sqrt{1 + \frac{d_0}{200}}} \left(\frac{d}{a} \right)^{0.2} \geq 0.45$ ($d_0 = d \nless 100$ mm) (2.15b)
Relative neutral axis depth	$\frac{x}{d} = \alpha_e \rho_l \left(-1 + \sqrt{1 + \frac{2}{\alpha_e \rho_l}} \right) \approx 0.75 (\alpha_e \rho_l)^{1/3}$ (2.16)
Critical crack inclination	$\cot \theta = \frac{0.85d}{d-x} \leq 2.5$ (2.17)

where,

ζ is the size and slenderness effect,

x is the neutral axis depth (x/d is the relative neutral axis depth),

G_f is the concrete fracture energy, given by $G_f = 0.028 f_{cm}^{0.18} d_{max}^{0.32}$

E_{cm} is the secant modulus of elasticity of concrete, $E_{cm} = 22000 (f_{cm}/10)^{0.3} \nless 39$ GPa

f_{cm} is the mean value of the cylinder concrete compressive strength,

E_s is the modulus of elasticity of longitudinal reinforcement,

α_e is modular ratio (E_s / E_{cm}),

- ρ_l is longitudinal tension reinforcement ratio (A_{slong} / bd)
- A_{slong} is area of the steel longitudinal reinforcement in tension,
- f_{yw} is yield strength of the transverse shear reinforcement, and
- a is shear span.

The size and slenderness effect may be considered with two different equations: Eq. 2.15a is based on Zararis 2001 model (Cladera, Marí, et al. 2016) and Eq. 2.15b is based on Bažant and neural network analysis (Cladera et al. 2017).

The use of explicit equations for each shear resisting action may result in an approach too complex for daily engineering practice. For this reason, a transparent simplification was carried out, under the premise that the shear transferred by the compression chord is the main resisting action in the considered failure state.

The shear strength of a RC beam with rectangular cross-section is considered as the sum of the concrete contribution (V_{cu}) and the shear reinforcement contribution (V_{su}) that includes the concrete contribution increase due to confinement, and is given by Eq. (2.18):

$$V_{Rd} = V_{cu} + V_{su} \leq V_{Rd,max} \quad (2.18)$$

where strut crushing is given by Eq. (2.19):

$$V_{Rd,max} = b z v f_{cd} (\cot \theta + \cot \alpha) / (1 + \cot^2 \theta) \quad (2.19)$$

where α , already defined in the previous section of Eurocode 2 model, is shown in figure 2.3.

The concrete contribution is given by Eq. (2.20):

$$V_{cu} = 0.3 \zeta \frac{x}{d} f_{cd}^{2/3} bd \leq V_{cu,min} = 0.25 \left(\zeta K_c + \frac{20}{d_0} \right) f_{cd}^{2/3} bd \quad (2.20)$$

where $K_c = \frac{x}{d} \geq 0.2$.

The contribution caused by the shear reinforcement, including the increase on the concrete contribution due to the confinement produced by the stirrups, is given by Eq. (2.21):

$$V_{su} = \frac{A_{sw}}{s} f_{ywd} (d - x) \sin \alpha (\cot \theta + \cot \alpha) (1 + \Delta_{Vcu}) \quad (2.21)$$

The CCCM was not initially derived specifically as a model taking into account externally added strengthening reinforcement. However, it may be used without any problem as it takes into account the confinement produced by the shear reinforcement. In fact, it explicitly accounts for the portion of the shear resisted thanks to the concrete confinement within the stirrups in the compression chord, through the term given by Eq. (2.22) that is used in Eq. (2.21):

$$\Delta_{Vcu} = \zeta \frac{x}{d} \quad (2.22)$$

A summary of the main expressions and factors governing the shear strength is presented in table 2.2 for the particular case of RC beams with rectangular cross section. See Reference (Cladera, Marí, et al. 2016) for a detailed description of each expression and all factors.

The complete derivation of these equations can be found in (Marí et al. 2015), (Cladera et al. 2015), (Cladera, Marí, et al. 2016), and (Marí et al. 2016). The model was first developed for reinforced beams with fiber reinforced polymers (FRP) reinforcing bars (Marí et al. 2014) and (Oller et al. 2015). Extensions of the model were developed for non-slender beams, steel fiber reinforced concrete, fatigue, external shear strengthening using innovative materials (Cladera et al. 2017).

In chapter 7, the EC2 and CCCM shear models will be applied for the specific tested beams of the experimental campaign of this research.

Table 2.2. Summary of basic CCCM formulation particularized for reinforced concrete beams with rectangular cross-sections. From (Cladera, Marí, et al. 2016)

Equations	Expressions
Shear strength	$V_{Rd} = V_{cu} + V_{su} \leq V_{Rd,max}$ (2.18)
Strut crushing	$V_{Rd,max} = b z v f_{cd} \frac{\cot\theta + \cot\alpha}{1 + \cot^2\theta}$ (2.19)
Concrete contribution	$V_{cu} = 0.3\zeta \frac{x}{d} f_{cd}^{2/3} b d \nless V_{cu,min} = 0.25 \left(\zeta K_c + \frac{20}{d_0} \right) f_{cd}^{2/3} b d$ (2.20)
Shear reinforcement and concrete contribution increase due to confinement	$V_{su} = \frac{A_{sw}}{s} f_{ywd} (d - x) \sin\alpha (\cot\theta + \cot\alpha) (1 + \Delta_{Vcu})$ (2.21)
Factors	Expressions
Size and slenderness effect	$\zeta = \frac{2}{\sqrt{1 + \frac{d_0}{200}}} \left(\frac{d}{a} \right)^{0.2} \geq 0.45 \quad (d_0 = d \nless 100 \text{ mm})$ (2.15b)
Relative neutral axis depth	$\frac{x}{d} = \alpha_e \rho_l \left(-1 + \sqrt{1 + \frac{2}{\alpha_e \rho_l}} \right) \approx 0.75 (\alpha_e \rho_l)^{1/3}$ (2.16)
Non-dimensional confinement factor	$\Delta_{Vcu} = \zeta \frac{x}{d}$ (2.22)
Crack inclination	$\cot\theta = \frac{0.85d}{d-x} \leq 2.5$ (2.17)

2.1.3 SHEAR STRENGTHENING OF RC BEAMS

Repairing of damaged RC structures or strengthening of existing ones due to new requirements has become a critical issue in recent times. There exist many different techniques to repair or strengthen reinforced concrete structures, e.g. reparation with steel plates, reinforced jacketing by means of concrete (RC jackets), mortars, metallic fabric jackets, FRP composite jackets (externally bonded FRP strips and sheets, near surface mounted (NSM) FRP rods) are among the most used methods.

Strengthening methods to improve the performance of structures have been extensively studied, for example in seismic assessment and retrofit of RC buildings (FIB - bulletin 24 2003). In case of strengthening systems with FRP, (Bakis et al. 2002) reviewed the

applications of FRP composites in construction and (FIB - bulletin 35 2006), specifically reviewed the retrofitting of concrete structures using FRP for seismic applications. There are several civil structural applications, among them: (Van Den Einde et al. 2003), (Hollaway 2010), (Kotynia et al. 2014), (Derkowski 2015) and (Deng et al. 2017). In the case of shear strengthening, less studies have been done and few models exist. (Colotti et al. 2005) studied analytical model for RC beams reinforced in shear. (Adhikary & Mutsuyoshi 2006) reviewed different techniques for shear strengthening of RC beams. (Ferreira 2013) developed a numerical model for strengthening shear critical frame concrete structures. (Colajanni et al. 2016) presented a new retrofitting method for increasing the shear and flexural capacity for RC beams. Specifically, the method was based on the use of longitudinal steel angles and prestressed stainless-steel ribbons to increase their strength and ductility. Moreover, the steel ribbons were able to confine concrete, improving the deformation capacity of the retrofitted beams.

The strengthening technologies for critical shear beams may be classified into two categories: passive strengthening and active strengthening methods. In both cases, the strengthening increases the safety of the structure and its strength for future applications of load, but when using passive strengthening methods, it is necessary for the strengthened structure to increase its deformation and level of damage before engaging the strengthening material. Alternatively, the structure may be unloaded before conducting the strengthening. This way, the strengthening material can contribute as soon as additional load is applied (or the deformation is increased again). When using active strengthening methods, the structure is pre-stressed or actively confined when the strengthening material is placed. However, active strengthening methods generally require hydraulic jacks and anchorages, so it is often necessary to maintain a large work area to accommodate these auxiliary elements and to carry out sometimes complex procedures, in special when working with active FRP strengthening systems.

- PASSIVE STRENGTHENING METHODS

Among the passive strengthening methods, the supplementation of extra transversal steel and enlarging the concrete beam web (concrete jacketing), schematically depicted in figure 2.4a, is supposed to be the most commonly used passive method. Hence, it is necessary to

make holes (or grooves) in the concrete on the top of the slab, to be able to put around the cross section new extra stirrups, and new concrete is casted or sprayed to the element. For example, (Souza & Appleton 1997) studied the efficiency in increasing the shear capacity of this methodology. Other related passive techniques are the application of steel reinforced shotcrete (figure 2.4b) or epoxy bonded steel plates (figure 2.4c), although these methods have the drawback of loss of bonding because the strengthening material is not anchored to the compressive zone. A popular alternative inside the passive methods is the strengthening with externally bonded FRP, depicted in figure 2.4d, because of some advantages: generally good corrosion behavior, low weight, high tensile strength and adaptability of stiffness to design requirements.

Concerning to shear strengthening, FRP can be externally bonded with the direction of the fibers coincident to that of maximum principal tensile stresses, although it is more common to place them vertically in practice. Nevertheless, some drawbacks can be mentioned: linear elastic failure without plastic deformations, high cost, possible thermal incompatibilities with concrete or brittle delaminating failure modes.

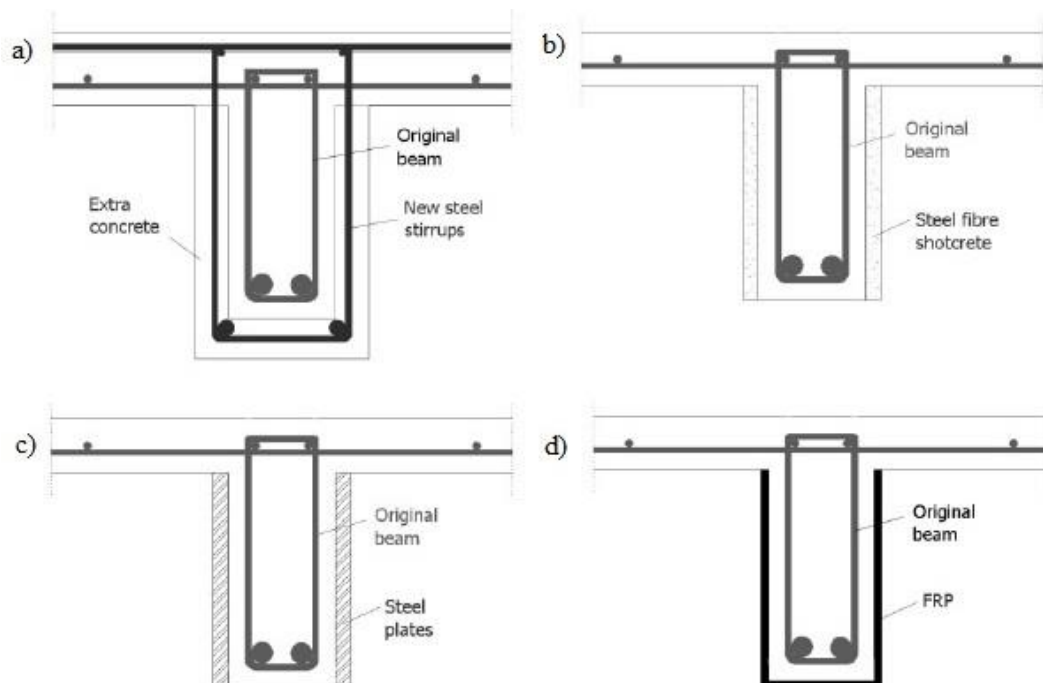


Figure 2.4. Passive shear strengthening methods for RC beam: a) extra stirrups and concrete, b) steel fiber concrete, c) epoxy bonded steel plates and d) FRPs. From (Ferreira 2013)

Different references related to the application of FRP to critical shear beams confirm their applicability in a wide range of cases. Recent examples of good performance are commented below. (Foster et al. 2013) used externally bonded FRP fabric to transfer shear forces across a diagonal crack. (Chalioris et al. 2014) experimentally observed the improvement in performance efficiency of using thin RC layers (using self-compacted concrete) as jacketing respect other methods like FRP jackets. (Baggio et al. 2014) investigated the effectiveness of using different commercially manufactured carbon FRP sheets to increase the shear capacity of RC shear critical beams. (Ruano et al. 2014) retrofitted RC beams with steel fiber reinforced concrete to improve the shear behavior. (Lin et al. 2017) experimentally studied RC members, e.g. precast concrete connections, with reinforcing steel bars across a shear plane strengthened using carbon FRP (CFRP) strips externally bonded to resist shear transfer.

Near mounted surface (NMS) strengthening is one specific method for flexural reinforcement alternative to external bonded methods (figure 2.5), and do not have some of the drawbacks of external bonded methods: occurrence of debonding, and exposure to the external environment. (Yu et al. 2011) experimentally studied RC beams strengthened with external prestressed wire ropes obtaining an improvement of the shear capacity of strengthened beams, an effective limitation of cracks, and a reduction of stirrup strains. (El-Hacha & Soudki 2013) presented a review of NMS of FRP reinforcement and showed advantages of this specific method.

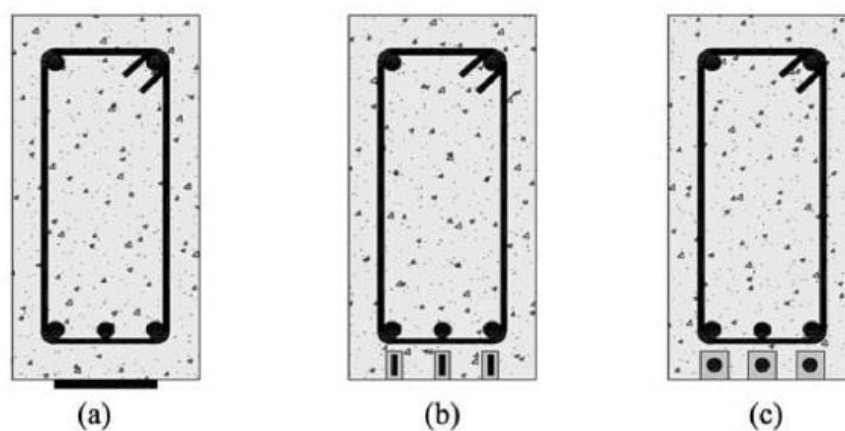


Figure 2.5. Schematic pictures of flexural strengthening methods: a) externally bonded FRP laminate, b) NSM FRP strips, and c) NSM FRP bars. From (El-Hacha & Soudki 2013)

The use of a spiral reinforcement has already shown important benefits as internal reinforcement for shear, using common materials or even shape memory alloys. (Yang et al. 2011) tested T-beams using spiral-type wire rope as shear reinforcement and the results showed highly favorable performance for controlling the diagonal crack width and enhancing the ductility of beams failing in shear. (De Corte & Boel 2013) performed bending tests using spiral shaped stirrups and confirmed that it is a valid alternative and that they could be incorporated in international codes. (Karayannis & Chalioris 2013) concluded that the use of rectangular spiral reinforcement provided enhanced bearing capacity and improved shear performance in rectangular cross-section RC beams. (Azimi et al. 2016) evaluated RC joints subjected to cyclic loading using different spiral patterns: conventional rectangular and twisted opposed rectangular spirals, and the results revealed improved ultimate lateral resistant, energy dissipation capacity, and ductility for the new proposed connection. (Mas et al. 2016a) assessed the possibility of obtaining more ductile shear failures using internal pseudo-elastic (Ni-Ti) SMA rectangular spirals as shear reinforcement in RC beams. They obtained highly deformable concrete members even for beams failing in shear. It was observed that the beams internally reinforced with Ni-Ti spirals were able to sustain a significant load after the full development of the critical shear crack, enhancing other resisting mechanisms at failure, such as the dowel effect, the shear transferred by the shear reinforcement, and the arch effect.

- ACTIVE STRENGTHENING METHODS

Post-tensioning repair techniques are a widely used retrofitting method for enhancing flexural capacity of RC frame structures. In terms of active shear strengthening, the application of active methods like steel tendons or wire ropes as represented in figure 2.6a (external steel tendon), in figure 2.6b (internal steel tendon), and others like external wire ropes, are efficient methods to increase shear resistance of RC cross-sections.

The use of prestressed transversal reinforcement can provide an active confinement to the concrete section and it may allow the development of the flexural capacity of beams. (Ferreira et al. 2016) experimentally studied and numerically modelled vertically prestressed bonded and un-bonded RC beams with good results in terms of shear strength increase.

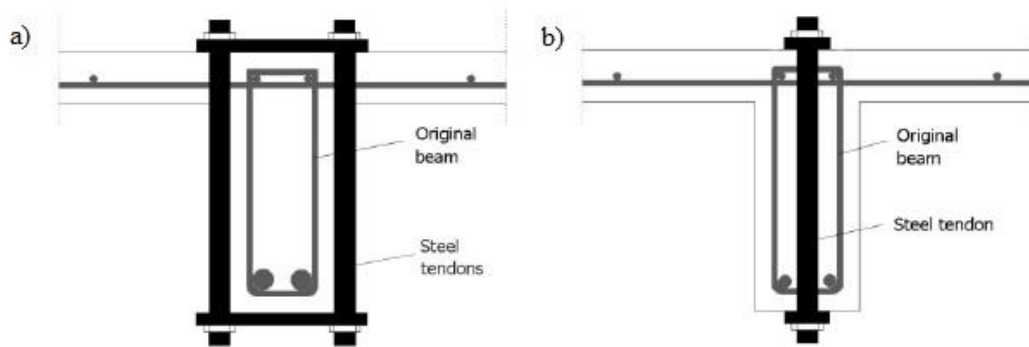


Figure 2.6. Steel tendons active shear strengthening methods for RC beam: a) external and b) internal. From (Ferreira 2013)

External prestressing methods have been widely employed mainly for flexural reinforcement (horizontal or longitudinal direction). Apart from conventional steel tendons as longitudinal prestressing and post-tensioning (Park et al. 2010), other materials have been used to avoid drawbacks of steel being externally mounted, like carbon fiber reinforced polymers (CFRP) tendons, basalt FRP or hybrid FRP (Wang et al. 2014).

(Herbrand & Classen 2015) tested in shear continuous prestressed concrete beams with external steel longitudinal tendons determining a major influence of the concrete for them and an additional axial load due to external prestressing had only a rather small influence on the ultimate shear capacity.

Recently, other methodologies are under investigation, such as (Colajanni et al. 2017), that investigated the efficiency of an alternative retrofitting method for increasing the flexural and/or shear capacity in RC beams, based on the use of pretensioned stainless steel ribbons, concluding an increment of efficiency in shear capacity. The method tested different retrofitting configurations: beams strengthened in shear with three vertical overlapping ribbons arranged along the full depth of the beam (figure 2.7a) and beams strengthened with vertical ribbons along part of the cross-section depth (figure 2.7b), in order to represent an intervention of retrofitting in the presence of the floor slab and the consequent inability to wrap the whole beam. They found an increase of efficiency in shear capacity of the method and of its competitiveness compared to traditional methods, due to its easy installation. It was also stated the need of further research. The recent publication of this work, during the final development of the present investigation, confirm a topic of major concern that is beam retrofitting using simple and easy to install, but effective, methods.

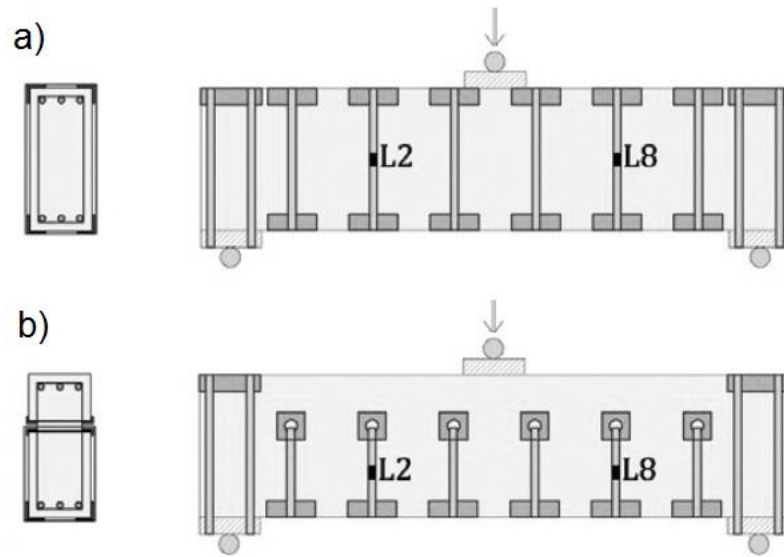


Figure 2.7. Beam retrofitting in shear using steel ribbons: a) arranged along full depth of the beam, and b) arranged along part of the cross-section depth of the beam. From (Colajanni et al. 2017)

2.2 SHAPE MEMORY ALLOYS IN STRUCTURAL ENGINEERING

2.2.1 INTRODUCTION TO SMAs

SMAs are metallic alloys that have the property of returning to a previous shape after undergoing large deformations by means of changes of temperatures or by the action of stresses, among other causes. This kind of memory effect they undergo is related to solid-to-solid phase transformation and it is called the martensitic transformation. During this process, SMAs can recover high inelastic strains (apparently permanent strains). This kind of alloys have been widely studied since they were first discovered in mid twentieth century (Kurdjumov & Khandros 1949).

From a material point of view, SMAs have been widely studied within the martensitic transformation phenomenon studies. Since the discovery of the shape memory effect (SME) in Ni-Ti alloys in 1963, a large amount of research has been conducted. (Buehler et al. 1963) noticed good mechanical properties for Ni-Ti alloys, comparable to other engineering metals, and shape recovery capability. Afterwards, the term Nitinol was adopted in honor of their

discovery at the Naval Ordnance Laboratory (NOL), and triggered research interest into SMAs (Lagoudas 2008).

The basic understanding on the relationship between the microstructure and the corresponding deformation was also established (Miyazaki et al. 1986) and, as a consequence, engineering and other commercial applications have been developed (Jani et al. 2014), including civil engineering structures (Janke et al. 2005) even in structural applications of prestressing (Maji & Negret 1998) or RC bridges (Alam et al. 2008).

Nevertheless, research work is still ongoing even at material level. In recent studies, (Kustov et al. 2012) from Department of Physics of UIB, studied thermal properties of martensitic transformation and indicated that some questions are far from being solved. (Hui Shi 2014) concluded that further research work is needed as some research questions are not considered ended in the case of Ni-Ti-Nb, after a wide study of characteristics and properties, from functional ones to micro/nano-structures, of such alloy.

The special properties of SMAs have been also widely applied in several commercial applications from biomedicine and electronics, to aero-spatial, mechanical, structural engineering, and others. The most interesting ones in the framework of this work are structural engineering applications. The next paragraphs are a summary of the development of such applications.

Related to the pioneer structural engineering applications of SMAs, (Mazzolani & Mandara 2002) illustrated the potential of SMA new materials and technologies in the restoration and preservation of cultural heritage. SMA devices were installed in specific locations of structures for seismic protection of monuments, i. e. vertical steel tie-rods in series with SMA devices were inserted into a bell tower and prestressed to increase its flexural strength. (Watanabe et al. 2002) reported the fabrication of SMA smart composites for architectural and civil engineering applications. Application of SMAs in structural concrete were already under research since the beginning of this century. (Sakai et al. 2003) studied self-restoration of concrete beams using SMA wires, (Ocel et al. 2004) developed steel beam-column connections using SMAs, (Moser 2005) studied prestressing of concrete by SMA short fibers, and (Penar 2005) studied recentering beam-column connections using SMAs.

Reviews of structural engineering applications were also being published in the first years of twenty-first century: (Janke et al. 2005) overviewed applications of SMAs in civil engineering structures indicating limitations and innovative ideas. (Song, Ma, et al. 2006) reported different applications of SMAs in civil structure control: passive, semi-active and active as if is necessary an external power source to apply forces to structures. (Alam et al. 2007) presented alternatives to extend the use of SMAs to enhance performance and safety of civil structures. (Tyber et al. 2007) provided basic material characterization of commercial Ni-Ti SMAs for structural engineering applications. (Alam et al. 2008) overviewed smart RC bridges based on SMAs, (Johnson et al. 2008) reported testing of devices for bridge retrofitting based on Ni-Ti SMAs. (Motavalli et al. 2009) reviewed applications of SMAs for civil engineering structures. (Ozawa et al. 2011) reported SMA applications in construction and housing. (Ozbulut et al. 2011) reviewed seismic response control using SMAs. (Torra et al. 2011) studied mitigation of extreme loads in civil engineering using SMAs. (Cui et al. 2012) researched progress of smart concrete structures reinforced by SMAs. (Debbarma & Saha 2012b) highlighted the useful properties of SMAs towards utilization in concrete structures as reinforcement in concrete flexural members, analyzed the effect of their properties in the structural behavior of RC beams and its application in different standard codes. (Jani et al. 2014) reviewed SMA research summarizing recent advances and showing new applications and opportunities. (Cladera, Oller, et al. 2014) reported pilot experiences in application of shape memory alloys in structural concrete, remarked the advantages and improvements of the behavior of concrete structures when using SMAs and collected the critical unsolved aspects that could be a starting point for the development of future research in this field. (Menna et al. 2015) explained useful and wide applications of SMAs in Structural Engineering.

Some other references of valuable interest are: ‘Engineering Aspects of SMA’ (Duerig et al. 1990), ‘Shape Memory Materials’ (Otsuka & Wayman 1998), ‘Shape Memory Alloys’ (Lagoudas 2008), and ‘Shape-memory Alloys Handbook’ (Lexcellent 2013).

2.2.2 FUNDAMENTALS OF SMAs

The martensitic transformation of SMAs is related to the phenomenology of phase transformation between martensite and austenite solid phases and to their crystallographic structure. The martensitic transformation, or forward transformation, is induced upon cooling the austenite phase (stable at high temperatures) and consists of the formation of martensite phase (stable at low temperatures).

The austenite phase (generally cubic crystal structure) has a different crystal structure than a martensite (tetragonal, orthorhombic or monoclinic). The transformation from one structure to another does not occur by diffusion of atoms, but by lattice distortion. It is known as martensitic transformation and each martensitic crystal obtained with different orientation direction or variant can exist in two different forms: twinned martensite (combination of “self-accommodated” martensitic variants) and detwinned martensite (reoriented) in which a specific variant is dominant.

The martensitic transformation is a diffusionless, solid state displacive transformation in which the atoms move cooperatively and is normally accompanied by shear stresses that deform the structure homogeneously and that give rise to a change in the crystal structure as well as the associated volume (Otsuka & Wayman 1998). Because it is a diffusionless displacive transformation, the new phase is constituted through small coordinated displacements of the atoms, where the displacements of neighboring atoms are smaller than the original interatomic distance. That is, two adjacent atoms will continue to be neighbors after the transformation and will conserve the atomic composition and the order of the initial phase. Although the variation in the relative position of the atoms is very small, the coordinated movement of all the atoms leads to changes in volume and may bring about significant macroscopic deformations. Moreover, the diffusionless property of the martensitic transformation means that this can be obtained almost instantaneously at low temperatures where the diffusive movements of the atoms are negligible.

Figure 2.8a schematically shows the atomic arrangement in a hypothetical lattice after mechanically induced martensitic transformation. The lattice is distorted without reorganization of the atoms (neighbors stay neighbors). This martensitic transformation is sometimes called thermoelastic and is typical for Ni–Ti-alloys, and it usually shows a small

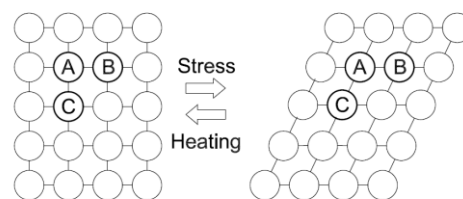
hysteresis. In a plastic deformation, on the other hand, the atoms are rearranged by slip, as shown in figure 2.8b. In this case, the neighbors are changed, but the lattice structure remains intact. This plastic transformation can occur in a general alloy or in an SMA and cannot be reversed by a temperature change because the crystal structure is identical to the original state.

The martensitic transformation can be produced by changes in temperature or by the action of stresses. In the former case, the martensitic transformation takes place within a finite interval of temperatures, during which there is a coexistence of the two phases: austenite and martensite. The martensitic transformation, or forward transformation, is induced upon cooling the austenite phase (high symmetry and stable at high temperatures) and consists of the appearance of the martensite phase (low symmetry and stable at low temperatures).

In the absence of applied stresses, four main different transformation temperatures exist related to martensitic transformation (figure 2.9):

- M_s : temperature at which forward transformation starts (from austenite to martensite) during cooling process.
- M_f : temperature at which forward transformation finishes, continuing the above cooling process.
- A_s : temperature at which reverse transformation starts (from martensite to austenite) during heating process.
- A_f : temperature at which reverse transformation finishes continuing the above heating process.

a) Stress-induced martensite transformation by distortion



b) Plastic deformation by slip

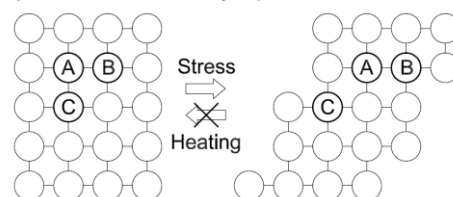


Figure 2.8. Different atomic behaviors of: a) stress-induced martensitic transformation by distortion in Ni-Ti alloys and b) plastic deformation by slip. From (Maruyama & Kubo 2011)

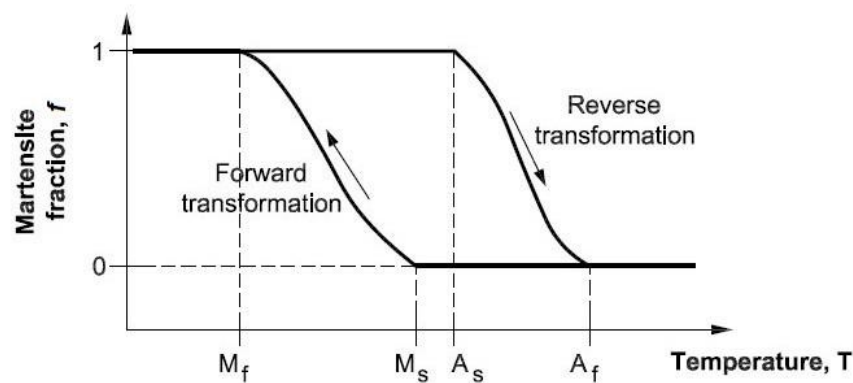


Figure 2.9. Schematic definition of forward and reverse martensitic transformation temperatures related to Martensite fraction. From (Cladera, Weber, et al. 2014)

Given a material at temperature T , if the temperature is appropriate for the material to be in austenite ($T > A_f$), the forward transformation can be induced, by cooling the material. The formation of martensite will start at temperature ‘martensite start’ (M_s) and will finish at temperature ‘martensite finish’ (M_f). Next, if the temperature is appropriate for the material to be in martensite ($T < M_f$), the reverse transformation can be induced, by heating the material. Analogously to the above, the formation of austenite will start at temperature ‘austenite start’ (A_s) and will finish at temperature ‘austenite finish’ (A_f). These transformations show thermal hysteresis, that is, the forward and reverse transformations do not take place at the same temperature ranges (figure 2.9).

When this thermal hysteresis is small, from a few degrees to some tens of degrees, the transformation is thermoelastic, which is of significant importance so that the shape effect and pseudo-elasticity may take place.

Furthermore, the martensitic transformation can be temperature induced, mechanical induced or a combination of both treatments that leads to different variants (Lagoudas 2008). When a SMA in martensite phase is deformed due to external forces, its crystal structure changes to the variant, or variants, which enable(s) it to accommodate the maximum elongation and, as such, allow “permanent” deformations. If subsequently the change of phase from martensite to austenite is brought about (reverse transformation), by raising the temperature, the SMA regains its cubic crystal structure, returning to its original shape if deformations are unconstrained, or generating recovery stresses otherwise.

It is also possible to induce martensitic transformation through the application of an external force on a SMA that is in the austenite phase ($T > A_f$). In this case, the martensitic transformation is the same as the one commented above, with the main difference that, by inducing the transformation through an external force, only variants with an intrinsic change of shape in the direction of the force applied will appear. Total recovery from this deformation, on ceasing to apply the force, takes place through the reverse martensitic transformation.

Accordingly, the stress-strain diagram of a SMA will be different depending on whether the material is in the austenite or martensite phase and is highly dependent on temperature. Figures 2.10 and 2.11 show a schematic behavior of a typical Ni-Ti alloy in phase diagrams (stress–temperature) and stress–strain curves for different thermomechanical paths.

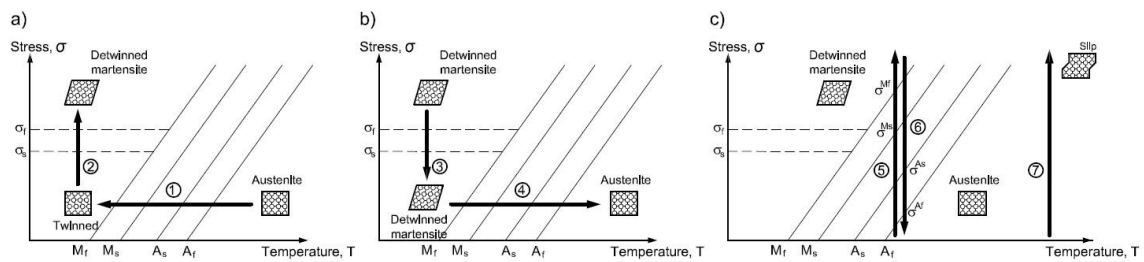


Figure 2.10: Schematic phase diagrams for Ni-Ti alloy, showing: a) detwinning of Ni-Ti with applied stress; b) the unloading and subsequent heating to austenite under no deformation constraint for Ni-Ti, and c) pseudo-elastic loading path for Ni-Ti and ordinary plastic deformation. From (Cladera, Weber, et al. 2014)

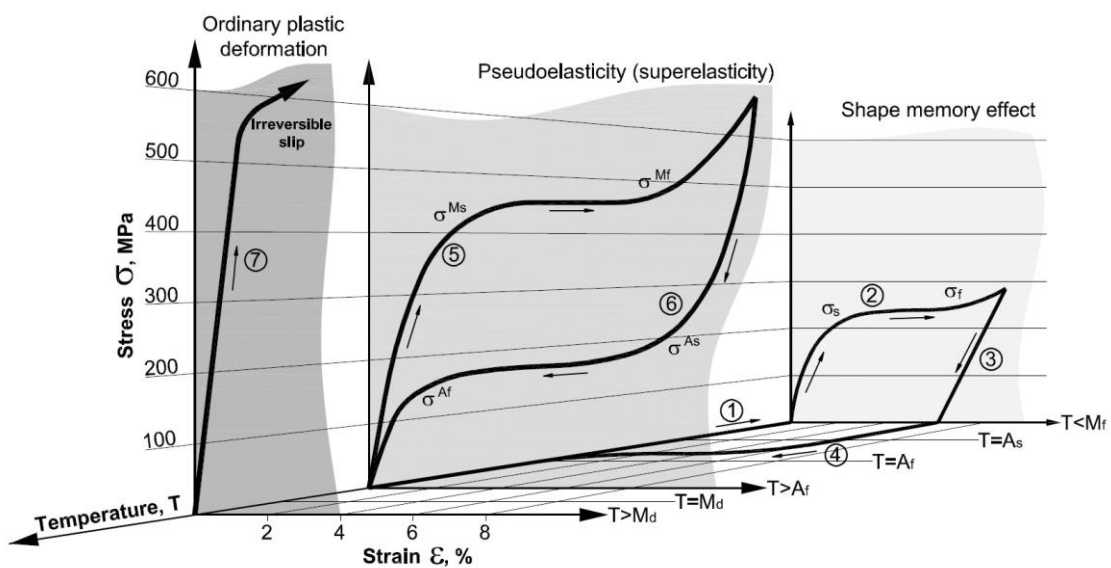


Figure 2.11: Typical stress-strain-temperature diagram for Ni-Ti alloys. From (Cladera, Weber, et al. 2014)

When an SMA with a thermoelastic martensitic transformation is cooled below M_f in the absence of an applied load, the crystal structure changes from austenite to martensite (forward transformation, see figure 2.9). The arrangement of variants occurs such that the average macroscopic shape change is negligible, which results in twinned martensite (path 1 in figures 2.10a and 2.11). If the twinned martensite is deformed due to external forces, its crystal structure changes to the variant, or variants, which enable(s) it to accommodate the maximum elongation and, as such, allow permanent deformations (detwinned martensite), as can be schematically seen in path 2 of figures 2.10a and 2.11. In this step, the applied stress must be sufficiently large (σ_s) to start the detwinning process. The total detwinning of martensite is reached with the detwinning finish stress (σ_f). After unloading (path 3 in figures 2.10b and 2.11), the martensite remains detwinned. After this loading-unloading process remnant strains are obtained, as can be seen in figure 2.11 after path 3. The change in the phase from detwinned martensite to austenite can be brought about by raising the temperature (path 4 in figures 2.10b and 2.11), and the SMA regains its cubic crystal structure, returning to its original shape if the deformations are unconstrained or generating recovery stresses otherwise. As the material recover its previous shape, this behavior is known as shape memory effect.

On the other hand, another different behavior can be observed if under an applied load the crystal structure changes from austenite to martensite and the arrangement of variants occurs such that the average macroscopic shape change results directly in detwinned martensite (path 5 in figures 2.10c and 2.11) if a characteristic value of stress (σ^{Mf}) for each SMA is reached in the diagram. The initial formation of detwinned martensite will have been started at a lower value of stress (σ^{Ms}). Then, the unloading process results directly in austenite (recovering initial deformation) if another characteristic value of stress (σ^{Af}) for each SMA is reached in the diagram (path 6 in figures 2.10c and 2.11). The initial formation of austenite will have been started at a higher value of stress (σ^{As}). This effect is known as pseudo-elasticity.

In figure 2.10, the slopes of the lines, or boundaries, that define the transformation temperatures are known as “stress influence coefficients”. It is typically assumed that each pair of lines for the two transformations shares a characteristic slope (Lee et al. 2013),

although this assumption is not necessarily the case for other kind of SMAs, like Fe-Mn-Si alloys, anyway they may show shape memory effect as well (Cladera, Weber, et al. 2014).

Finally, there is another key temperature ($T = M_d$) above which the pseudo-elasticity is not shown any more and the behavior of the alloy is as other conventional ones, i. e. after reaching the elastic limit in a loading process (path 7 in figures 2.10 and 2.11), plastic strains (irreversible) are obtained.

2.3 KEY PROPERTIES OF SMAs FOR STRUCTURAL ENGINEERING

The thermo-mechanical behavior is a key aspect to some macroscopic observed properties that SMAs exhibit and for different technical developed applications. In terms of structural engineering, three main key properties are related to SMAs: shape memory effect (SME), pseudo-elasticity and damping capacity. As stated before, the SME is an essential property for the featured strengthening technology.

2.3.1 THE SHAPE MEMORY EFFECT

As mentioned above, SME is the material property of returning to a previous shape after undergoing large deformations by means of changes of temperatures and/or by the action of stresses. The SME for the recovery of the macroscopic shape the material had through heating (reverse transformation) does not generally work in the opposite direction, that is, upon re-cooling the material itself does not return spontaneously to the shape it took when it was in martensitic phase. The alloys that enable the original shape to be recovered in the two directions undergo the so-called two-way SME (Jani et al. 2014).

This effect, already depicted in figure 2.11 (paths 2-3-4-1) in terms of stress-strain-temperature, can also be seen in figure 2.12. In figure 2.12a the material is initially found in austenite phase. Upon cooling it without a concomitant force, a self-accommodated martensite is formed, thus conserving the initial macroscopic shape. Once in martensite (figure 2.12b), the application of an external force can significantly deform the material

(figure 2.12c), even after ceasing to apply the force (figure 2.12d). In this situation, simple heating will lead the material to recover its original shape. After a training process, the material could spontaneously recover, with heating or cooling, both its original shape (figure 2.12a) and that of the deformed martensite (figure 2.12d), respectively. In contrast to the one-way memory effect, the two-way shape memory effect is not spontaneous, but rather the alloy must, previously, be subjected to a training process.

For low temperatures ($T < M_f$), when loading a SMA, after an initial elastic branch defined by the elastic modulus of the martensite, there is a inelastic branch. In the event of unloading, deformations would be produced for a null level of stresses, apparently “permanent” deformations if we use the simile with conventional steel, as represented in figure 2.11 paths 1, 2 and 3. However, if in this situation the SMA is heated above the temperature of transformation from martensite to austenite ($T > A_f$) the reverse transformation takes place and the material will return to the origin of the stress-strain diagram as represented in figure 2.11 path 4, thus cancelling out the “permanent” deformations that had come about upon unloading, should these not be impeded. This effect is what is known by the name **shape memory**, as the alloy seems to remember its ancient shape, but this effect is strongly dependent on temperature (Uchida et al. 2011).

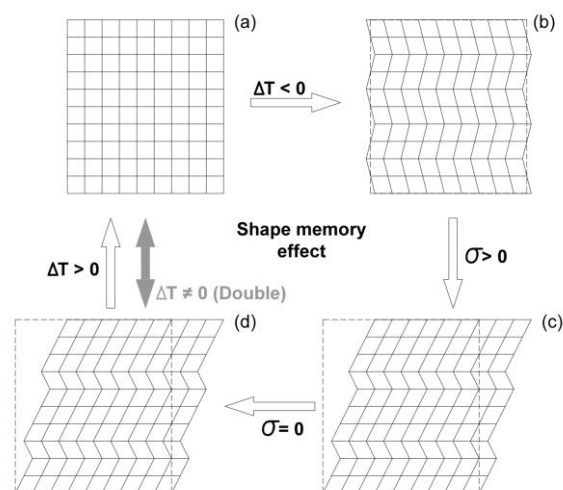


Figure 2.12. Diagram of the shape memory effect (white arrows) and the two-way shape memory effect (grey arrows). From (Santamarta et al. 2005)

If the deformations were totally impeded, these ones could not be cancelled out and recovery stresses would be produced in the alloy. Upon cooling and returning to ambient temperature, the alloy would remain in austenite, providing the ambient temperature was greater than M_s , maintaining the recovery stresses. This is what would be employed when using SMAs as active reinforcement. On the other hand, an alloy that is stable in martensite at ambient temperature ($T < M_f$) would not be appropriate for acting as permanent prestressing, as the recovery stresses would disappear on returning to ambient temperature (forward transformation), as it will be deeply commented in Section 2.4.3.

The macroscopic change in shape of the material would be negligible in this case upon the forward transformation taking place, as adjacent variants would develop opposing changes of shape and would form what is known as a group of self-accommodated variants, with recovery stresses disappearing (Cladera, Oller, et al. 2014).

If this recovery strain is constrained because the SMA is used, for example, to wrap a beam, the SMA will generate recovery stresses when heated and cooled afterwards, prestressing and/or confining the concrete member. With the adequate selection of the SMA, these stresses will remain applied throughout the service life of the structure. Some of these SMAs also possess a very high ductile behavior, which has been found to be essential for providing ductile shear failures when using them as internal reinforcement (Mas et al. 2016a).

2.3.2 THE PSEUDO-ELASTICITY

Another interesting property of SMAs is the pseudo-elasticity (or super-elasticity). It means that, despite high inelastic deformations SMAs may be able to undergo when loaded, they return to their original shape upon unloading. If the initial temperature is greater than A_f (figure 2.11), the stress-strain diagram may show a specific pattern known as **pseudo-elasticity**. This is made up of an initial elastic phase, with the initial elastic modulus of the austenite, a very horizontal pseudo-plastic phase, in which the phase transformation from austenite to martensite is mechanically induced, and another elastic phase with the initial modulus of the martensite. At any point of the stress-strain diagram represented in figure 2.11 paths 5 and 6, upon unloading, the material will return to the origin of the diagram without significant permanent deformations and performing a hysteresis loop that dissipates

energy. Different evolution of pseudo-elasticity in terms of variation of modulus of elasticity, location of pseudo-plastic phase, ultimate strength or energy dissipated when cyclic or dynamic loads are applied has been reported (Desroches et al. 2004).

2.3.3 THE DAMPING EFFECT

The third commented property, linked to the two previous ones, refers to the capacity to convert mechanical energy into thermal energy and, therefore, to the possibility of reducing the movements or vibrations of a structure. In case of pseudo-elastic behavior (original material in austenite at room temperature), permanent deformations are not produced at the end of the stress-strain loop and the material is able to dissipate energy producing a **damping effect**. If, in this latter case, the stress were to continue rising after the elastic phase of the martensite, a plastic branch of martensite would be produced that is irrecoverable upon unloading (a phenomenon not represented in figure 2.11). In the case in which the SMA is always in austenite for operating temperatures, pseudo-elasticity takes place perfectly, thus it would be the desired situation whenever it is wished to use the benefits of the deformations disappearing on eliminating the stress even if very large strains have been reached; for instance, in the case of Ni-Ti it would be possible to recover strains of up to 8 % as (Janke et al. 2005) mentioned, whilst other type of SMA may recover up to 3.5 %. Another aspect mentioned is the Specific Damping Effect (SDE) as a ratio of dissipated energy and applied energy. Ni-Ti alloys may have up to 20 % and other alloys may have upper values up to 85 %.

An interesting property of alloys in martensite phase to take into account for applications of damping is that they have a much larger hysteresis loop than in austenite when used in stress cycles of a different sign (figure 2.13), wherefore their use in applications in which damping is necessary is very interesting. However, probably due to the fact that these alloys lack the self-recentering capability upon elimination of the load, they have been less used in applications linked to structural concrete. Upon using alloys in martensite, self-recentering must be caused by the reverse transformation. This effect will be commented in the examples on joints in applications of shape memory effect, in which the damping effect is combined with the shape memory effect.

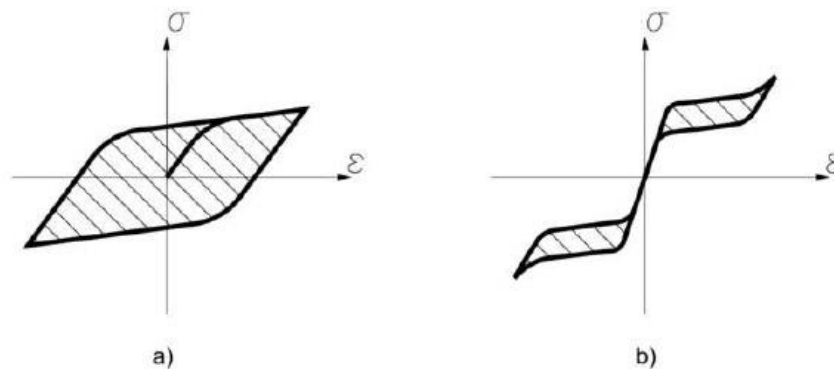


Figure 2.13. Stress-strain diagrams and dissipated energy: (a) martensitic damping ($T < A_s$); (b) damping in austenite (super elasticity) From (Cladera, Oller, et al. 2014)

2.4 REVIEW OF SOME SMAs FOR STRUCTURAL ENGINEERING APPLICATIONS

2.4.1 INTRODUCTION TO DIFFERENT SMAs

Different types of SMAs have been reported that show shape memory effect (SME), pseudo-elasticity (PE) and damping effect (DE). However, not all of them may be used in structural engineering (Janke et al. 2005), at least in the useful range of civil engineering temperatures (-20°C - $+60^{\circ}\text{C}$) or due to the special mechanical properties required. Production costs of industrial applications is another constrain to widen the use of SMAs. Basically, the referenced alloys could be classified in three main groups: copper (Cu) based, iron (Fe) based and niquel-titatum (Ni-Ti) based (table 2.3).

Schematic behaviors of different SMAs (stress-strain behavior), their relationship with phase transformation temperatures and engineering temperatures are depicted in figure 2.14. Actuator-like change of strain and stiffness against a constant force (fig. 2.14a, b); SME in the cases of free recovery and constrained recovery (fig. 2.14c, d); pseudo-elasticity (fig. 2.14e, f); and martensitic damping effect (fig. 2.14g, h).

Table 2.3. Some alloys exhibiting shape memory effect (SME), pseudo-elasticity (PE) and damping effect(DE). Adapted from (Janke et al. 2005) and (Cladera, Weber, et al. 2014)

Alloy	Composition (% weight)	Reported application
Cu-Al-Ni	66.5-69;28-29;3-4.5	SME
Cu-Al-Be	87.7;11.8;0.5	PE – DE
Fe-Mn-Si-Cr-Ni-(V,C)	63;17;5;10;4;1	SME
Fe-Ni-Co-Al-Ta-B	59.05;28;17;11.5;2.5;0.05	PE
Fe-Ni-Nb	62;31;7	SME
Ni-Ti	49-51	SME
Ni-Ti	49.2;50.8	SE - SME
Ni-Ti-Nb	47.45;37.86;14.69	SME

The behavior of different SMAs reported in the literature confirm that these materials have been widely used and applied, mainly Fe-based and Ni-Ti based SMAs. For Fe-based SMAs there are a lot of references from the discovery of SME in Fe-based SMAs (Sato et al. 1984). From the review of features of SME about low cost, good workability, good machinability and good weldability (Kajiwara 1999), and the review of applications from (Janke et al. 2005), (Sato et al. 2006), and (Maruyama & Kubo 2011), to the overview of (Cladera, Weber, et al. 2014) for the use of Fe-based SMAs for civil engineering structures, confirm this affirmation. The research about material properties has been focused on anti-corrosion, training effects, cyclic deformation and strengthening (Wang et al. 1995), (Kajiwara et al. 2001), (Stanford & Dunne 2006), (Stanford et al. 2008), (Baruj & Troiani 2008), (Druker et al. 2013).

In the case of Ni-Ti based SMAs, the next sub-chapters are devoted to review the main found references of the application of Ni-Ti based SMAs in structural engineering. There is also a specific sub-chapter focused on the main references about Ni-Ti-Nb SMA applications in structural engineering since it is one of the main objectives of this research.

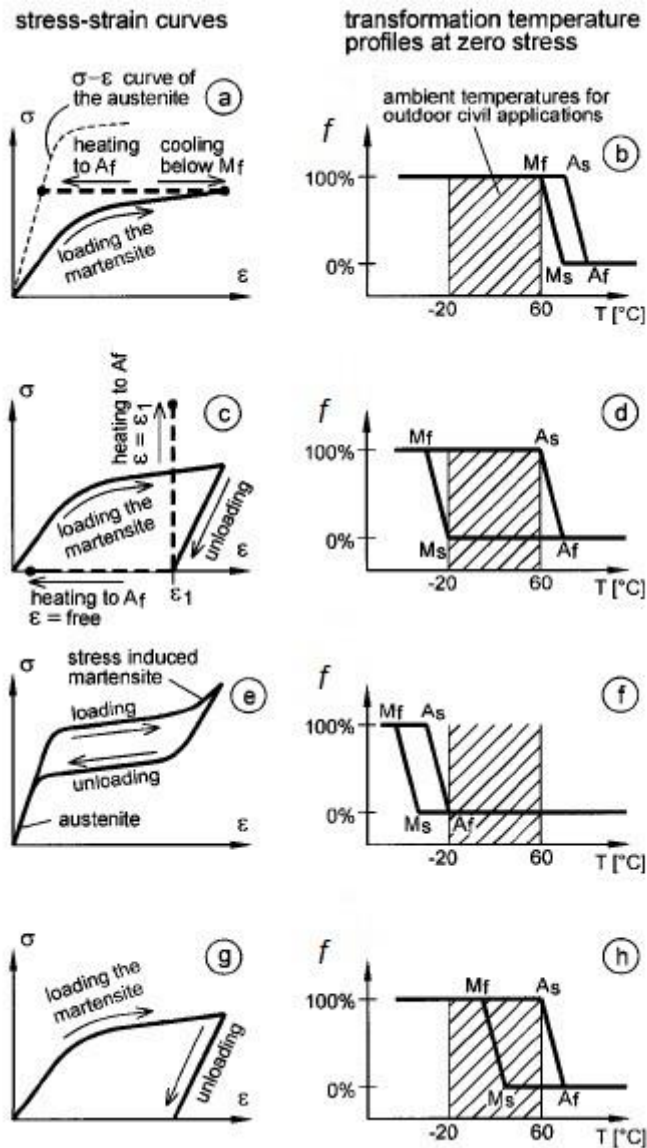


Figure 2.14. Schematic stress-strain curves of shape memory alloys (left) and associated transformation temperature profiles at zero stress (right) in terms of the martensitic phase fraction (f): a), b) Actuator-like change of strain and stiffness against a constant force; c), d) shape memory effect in the cases of free recovery and constrained recovery; e), f) pseudo-elasticity; and g), h) martensitic damping. From (Janke et al. 2005)

2.4.2 BINARY Ni-Ti ALLOYS

Binary Ni-Ti alloys are the current market-dominant alloys, with many applications across different fields. Nevertheless, most applications in structural engineering have recently been developed.

The properties related to SME are strongly dependent on material composition and on training process a SMA is submitted and this last aspect affects its applicability in structural engineering. For example, the variability of thermal hysteresis in martensitic transformation: the amplitude of the interval between transformation temperatures (austenite and martensite) depends on material composition and training process. Also, other properties like pseudo-elasticity, damping effect and ductility may be adequate for some specific issues. Although the properties of Ni-Ti alloys were former known, until the beginning of the 21st century these alloys were not applied to structural engineering. (Debbarna & Saha 2012a) reviewed SMA application in civil engineering and overviewed the properties to be integrated in civil structures summarizing as:

- The large force generated upon returning to its original shape.
- Repeated absorption of large amounts of strain energy under loading without permanent deformation.
- Excellent damping characteristics at temperature below the transition range.
- Excellent property of corrosion resistance and non-magnetic in nature.
- Low density and high fatigue resistance under large strain cycles.
- Ability to be heated electrically for recovery of shape.

Furthermore, they studied different possible applications of SMA: vibration control of structures, applications as an actuator, as tendons or external tensioning material in concrete structures and retrofitting of structures, and connectors between structural elements.

One of the first applications of SMA in actual structures was that of protecting historic buildings and cultural heritage (Dolce & Cardone 2001a). A real scale application of a super-elastic SMA device was the earthquake resistant retrofitting. The historic gable was connected with the main structure by a device using SMA. The Ni-Ti SMA rods were subjected to tension, although they were designed to take tension and compression forces. Another reinforcement project with external post-tensioning was executed to retrofit the earthquake resistant bell tower of the Church of San Giorgio, Italy (Auricchio et al. 2001). The intervention consisted of inserting 4 prestressed steel rebars in the internal vertices of the tower. A SMA device was put in place in series with each rebar, in order to keep the force applied to the masonry constant and below 20 kN and to dissipate energy from new quakes. A seismic episode in 2000 (4.5 on the Richter scale) was the best validation of the strengthening, as no damage at all was seen in the tower.

(Desroches & Delemont 2002) proposed increasing the position stability of simply supported bridges in earthquake prone regions through connection between the bearings of the bridge and the bridge deck slab using super-elastic bars. In 2003, (Sakai et al. 2003) presented the results of an experimental campaign of elements of cement mortar reinforced with a super-elastic SMA (Ni-Ti) in order to study the capacity of recovery from excessive strains caused by an earthquake. Static tests were conducted, revealing that super-elasticity allowed recovery from large deflections, reducing residual strains to 1/10 of the maximum strains. However, they also confirmed the problem of adherence between Ni-Ti wires and the mortar, as only a crack was formed in the midspan.

(Desroches et al. 2004) analyzed cyclic properties of wires and bars of different diameters of Ni-Ti SMA with a composition of Ni 56% by weight and Ti 44% like super-elastic behavior, forward transformation stress, damping, recentering capability and effect of dynamic loading, basic properties for seismic applications. They provided a valuable guide in determining the appropriate use of super-elastic SMA in seismic applications.

(Ocel et al. 2004) carried out a pilot study on beam-column joints in a metallic structure. The joints were materialized using 4 large diameter Ni-Ti rebars (35 or 36.5 mm) which connected the flanges of the beams and the columns. The alloy was initially in martensite, and showed a high degree of energy dissipation (damping in martensitic phase), a high ductility capability and did not suffer a degradation of resistance after cycles of up to 4% drift. Subsequently, the cables were heated to bring about the reverse transformation and recover the residual deformation (shape memory). The connections that had buckled under compression did not recover their original shape, partly because of the difficulty in providing a uniform heating temperature in the large diameter rebars used. A more recent study on a similar connection did not observe this shape recovery problem using 6 mm diameter SMA rebars (Wu et al. 2011), therefore the size effect on the phase transformation should be further studied.

The advantages of damping in martensitic phase (see Section 2.3.3) in passive seismic control devices were widely studied in the MANSIDE project (Dolce & Cardone 2001b; Dolce et al. 2007). The isolation devices against seismic vibration used the self-recentering capability of the austenite phase, and the large damping capacity of the martensite phase. The combination of alloys in austenite or martensite phase in different proportions made it

possible to obtain tailor-made devices to fit requirements. The same concept has been used for bracings to retrofit and damping in structures composed of multiple concrete frames (Cardone & Rossino 2014).

(Li et al. 2005) and (Song, Mo, et al. 2006) studied the change of resistance of the SMA in accordance with its elongation, finding that the value of electrical resistance decreased with the increase in elongation of the SMA and coming to measure variations of up to 27 %. Therefore, the value of electrical resistance of SMA wires or cables can be used to estimate the crack width and to determine, in the case of SMA post-tensioning, when to heat the alloy in order to achieve the rehabilitation of a certain structural element. Either way, the real potential of the use of this application has not been widely validated. In fact, other authors (Alam et al. 2012; Alam et al. 2009) based the monitoring of SMA reinforced structures on independent sensors (i.e. conventional strain gauges, piezoelectric sensors, inclinometers, optic fiber sensors).

(Torra et al. 2007) performed an experimental analysis and modeling in finite element simulation of SMA for built in dampers for family homes. Three different SMAs were studied: Cu-Al-Zn, Cu-Al-Be and Ni-Ti. The simulation results showed that the SMA dampers were capable of reducing the maximum oscillation amplitude by a factor of 2 and that they dissipate 50 % of the energy transmitted to the structure.

(Saiidi et al. 2007) carried out a pilot study on the behavior of concrete beams reinforced with super-elastic SMAs under cyclic loads. The experimental results showed that the mean residual deflections of the Ni-Ti reinforced beams were less than a fifth of the steel reinforced elements. However, the low elastic modulus of the alloy used produced a decrease in the rigidity of reinforced concrete elements, which could be desirable for some applications, such as earthquake resistance, but undesirable for others. For this reason, they complemented their research with an analytical study of hybrid elements, reinforced with high resistance steel or CFRP and SMAs, showing that in this case it was possible to have a greater rigidity and a partial deformation recovery.

(Li et al. 2008) reported a new repair method for a simple RC beam strengthened with CFRP plates in combination with SMA wires with a composition of Ni 50.8 % and Ti. It had a phase transformation plateau stress of about 200 MPa, an ultimate strength approximately equal to 920 MPa for a strain of around 19%. The test results indicated that the SMA wires

could reduce residual deformations of the specimens effectively when heated, thus, using the shape memory effect. An increase of the number of SMA wires led to a greater reduction in residual deformation.

(Kuang & Ou 2008) presented the possibility of reinforcing concrete beams with SMA wires in austenite combined with fragile fibers with adhesive materials, observing how these beams were capable of recovering practically the whole deflection, closing up the cracks, after the disappearance of external loads. The fragile fibers, on breaking due to the cracks, disperse adhesives inside the cracks, recovering the initial stiffness of the beams.

(Saiidi et al. 2009) studied and tested the incorporation of Ni-Ti super-elastic SMA in the plastic hinge zone in concrete bridge columns subjected to strong earthquakes to reduce permanent displacements and damage. It was reported a reduction of displacement between 67% and 83% depending on concrete configuration using Ni-Ti rods only in the plastic hinge zone to minimize costs. Couplers were used to connect the Ni-Ti to the steel. The diameter of the Ni-Ti rods was 15.9 mm but the middle of the rods was reduced to a diameter of 12.7 mm to match the diameter of the steel bars in an attempt to allow the Ni-Ti rods to yield instead of the steel and to prevent thread failure at the couplers.

Different studies and tests have been performed to assess the possibility of building a real bridge using SMAs in the plastic hinge zones. (Padgett et al. 2010) tested a four-span, one-quarter scale, concrete slab bridge, using Ni-Ti SMA restrainer cables connected at the deck abutment interface to evaluate the effectiveness in limiting the hinge opening, assessing a reduction of as-built openings by 47 and 32 % for low-level and high-level loading, respectively. Recently, (Varela & Saiidi 2017) performed a quarter-scale column models with engineered cementitious composite plastic hinges incorporating SMA bars (Ni-Ti and Cu-Al-Mn) to test them under simulated earthquakes. The design of the elements consisted of prefabricated plastic hinges and prefabricated tubes in a concept for resilient bridge columns comprising precast modules designed for disassembly. The results showed that the reassembled models reached the same capacity as original ones but were more flexible. Moreover, a real application of using super-elastic SMAs (Ni-Ti) and composite plastic hinges has been carried out in a real bridge already constructed, located in the new State route 99 exit ramp in Seattle and will become the first “flexible” bridge in the world built to sway with a strong earthquake and return to its original shape (WSDOT 2018). The bridge

construction finished in May 2017, but it is not already in service because it is included in a greater project, the Alaskan Way Viaduct Replacement Program, that will replace the Viaduct with a tunnel that is still under construction.

Other practical applications are also currently being developed. (Wierschem & Andrawes 2010) developed a SMA-FRP composite reinforcement for concrete structures, with the aim of improving ductility and the damping capacity of the FRP rebars. The experimental results revealed that by replacing 25% volume of the glass fibers with SMA wires, the ductility increased 64% and the elastic energy dissipated increased up to 2.6 times that of the FRP material alone. In a more recent paper, (Zafar & Andrawes 2013) have gone more in depth on the fabrication process and the cyclic behavior of this composite material to be used in seismic structural applications.

(Roh & Reinhorn 2010) presented the results of a test on a precast segmental bridge pier prototype, in which the connection between the footing and the first segment was carried out using super-elastic, non-adherent SMA rebars, which avoided damage caused by horizontal cyclic loads, and provided a significant self-recentering capability. This restoring capability ensured that the structure could sustain subsequent shocks after a main earthquake event.

(Speicher et al. 2011) built and tested interior beam-column connections in a metallic structure incorporating super-elastic Ni-Ti tendons also showing that this type of joints can have excellent ductility, energy dissipation and self-recentering capability. The joints were capable of returning to their original shape for drifts of up to 1%, and had a self-recentering capability, recovering 85% of their deformation, after cycles of up to 5% drift. It is worth noting that the authors reported that contrary to what happens in SMA joining elements in martensite phase, the diameter of the rebars used in austenite phase does not influenced the self-recentering capability (Desroches et al. 2004), which is of great interest for seismic response control devices.

(Shajil et al. 2012) performed an experimental study on self-centering and energy dissipation capabilities of pseudo-elastic Ni-Ti SMA fiber reinforced beams under cyclic loading. That SMA had a phase transformation upper plateau stress of about 550 MPa and a lower plateau stress of around 200 MPa. As qualitatively depicted in figure 2.15, the area inside a (loading–unloading) loop is the energy dissipated per cycle.

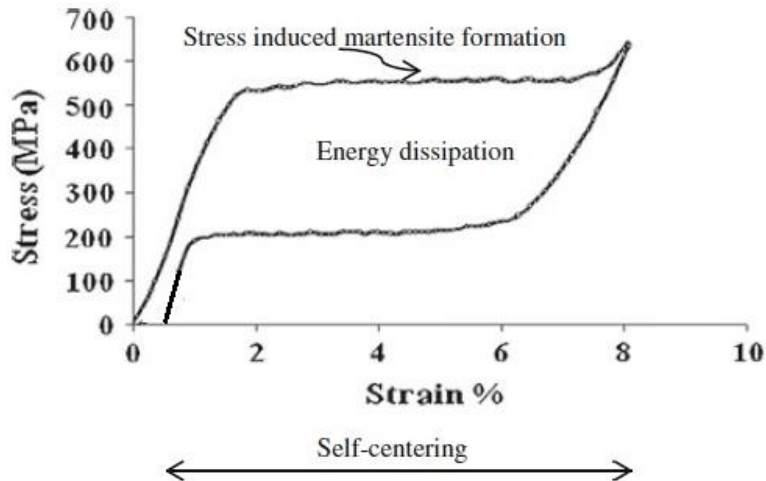


Figure 2.15. Pseudo-elastic stress-strain behavior of the Ni-Ti alloy 0.5 mm diameter wire used as fiber reinforcement of a beam. From (Shajil et al. 2012)

An interesting self-centering factor was introduced to quantify it, defined as the ratio of the difference between maximum deflection undergone and permanent deformation to the maximum deflection undergone during a cycle of loading ($[\delta_{ultimate} - \delta_{residual}]/\delta_{ultimate}$). Therefore, a self-centering factor of 1 indicates pure self-centering. Steel fiber reinforced case showed a self-centering factor of roughly 0.1 whereas Ni-Ti fiber reinforced case showed around 0.7. It was then reported significant self-centering characteristics in comparison to the steel fibers in post-cracked conditions, provided behavior of steel cannot regain its shape beyond yielding and the performance deteriorated enormously when subjected to a strong cyclic load and, thus, improving performance of SMA especially after a severe loading.

Ductility and seismic over-strength of steel and SMA reinforced concrete frames were studied analytically by (Alam et al. 2008; Alam et al. 2012; Alam et al. 2009). Specifically, in 2012 they studied the behavior of buildings with 3, 6 and 8 floors in an earthquake. The frames were made of reinforced concrete, in one case completely with steel rebars, in another case totally with SMAs, and in the last case a hybrid solution was used, in which the frame was reinforced with steel except for the use of SMAs in the plastic hinges. The results depended on the number of floors of the building studied. Up to 6 floors, the best results for ductility and over-strength were obtained with the SMA reinforced building, followed by the mixed SMA-steel building and lastly by the conventional steel one. On the other hand, for the building with 8 floors, the building with a conventional reinforced concrete frame obtained a better behavior, thanks to the greater elastic modulus of steel with respect to the

SMA, which made it possible to reduce drift. Therefore, the use of a SMA with a greater elastic modulus could improve the behavior of buildings in an earthquake for the case of 8 floors or higher. However, according to the authors these results must be taken with precaution due to a lack of a larger quantity of experimental and analytical results. In construction practice, the ideal case of a whole frame reinforced with SMAs does not make sense for reasons of cost. Thus, the localized use of SMAs where their properties are more necessary (plastic hinges) is an alternative that should be deeper studied.

Also, (Muntasir Billah & Alam 2012) analytically studied the combined use of FRP reinforced concrete columns and SMA or stainless steel plastic hinges at the base, with the aim of achieving columns highly resistant to corrosion and with the necessary ductility in earthquakes. The reduction of residual displacement in the columns with SMA plastic hinges was 87% higher than in the columns with stainless steel in the plastic hinge. However, the columns that only included stainless steel had greater ductility than the combined use of SMA-FRP.

(Zafar & Andrawes 2012) analyzed the use of hybrid FRP and SMA rebars in the areas where plastic hinges are formed (beam-column joints) in frames of 3 and 6 floors with one or two spans, respectively. From the dynamic incremental analysis of the prototypes, they concluded that the presence of these SMA rebars significantly improved ductility, dissipation energy and residual drifts compared to identical frames reinforced with fiberglass rebars (GFRP), whereby the use of SMAs brought about an improvement in seismic behavior.

(Abdulridha et al. 2013) also studied the recentering behavior and modelling of super-elastic SMA reinforced concrete beams and develop constitutive plastic models for SMA. In summary, they concluded that the use of Ni-Ti SMA that exhibits pseudo-elasticity as depicted in figure 2.16 with a composition of Ni at. 56% and Ti at. 44%, with a yield strength equal to 415 MPa, a modulus of elasticity of 60 GPa and ultimate strength equal to 800 MPa, is an alternative for longitudinal reinforcement, as re-shape or as partial substitution of steel in beam-column joints as it exhibits capacity to recover inelastic displacements, yielding and strain hardening, while sustaining large displacement ductility.

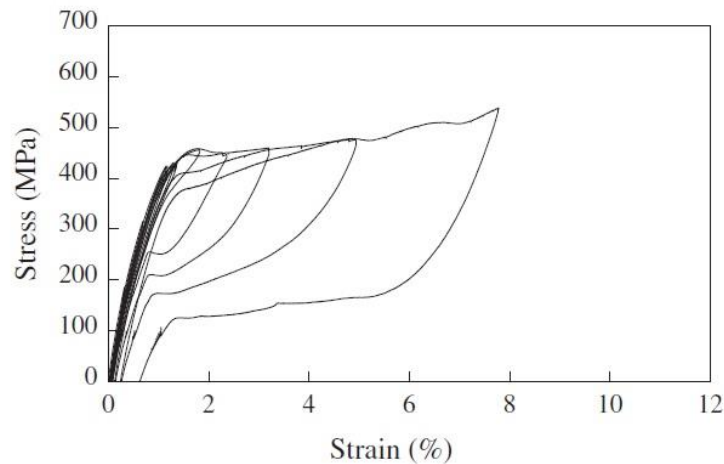


Figure 2.16. Cyclic stress-strain behavior of the Ni-Ti alloy. From (Abdulridha et al. 2013)

More recently, (Isalgue et al. 2015) experimented with Ni-Ti wires for dampers and actuators in extreme conditions (over-straining), to check the possibility to establish time life, fatigue and mechanical energy absorption. They concluded that the performance was reduced, but it was still useful for damping and actuators.

(Mas et al. 2016a) analyzed a binary Ni-Ti SMA with a composition of Ni at 51.80% and Ti at 48.20% and conclude its narrow thermal hysteresis made the alloy inappropriate for use in prestressing applications in civil engineering structures relying on the shape memory effect. This effect is quite common in this binary Ni-Ti alloys. Anyway, they used this alloy to shear strengthen reinforced concrete (RC) beams and tested them relying in other properties like pseudo-elasticity with an ultimate strength approximately equal to 1395 MPa for a strain of around 13.5-16 %, a modulus of elasticity of 41 GPa and a phase transformation from austenite to martensite starts due to mechanical induction, $\sigma^{Ms} = 505$ MPa and $\sigma^{Mf} = 590$ MPa (fig. 2.17). The most remarkable encountered effect was the sustainment of shear force for larger deflections. An effect of increment of ductility was also encountered in the reinforced beams as can be seen in figure 2.18 where a comparison between brittle and ductile shear failures is depicted. It can be seen in a shear force–deflection graph that, in cyclic load tests, in beams without shear reinforcement (01-Steel/f14/-/-2) or with steel shear reinforcement (02-Steel/f14/Steel/130/2), the deflection increment after maximum shear force is little (brittle shear failure), compared with beams shear reinforced with SMA (03-Steel/f14/Ni-Ti/130/2 and 04-Steel/f14/Ni-Ti/65/2), with more ductile shear failure.

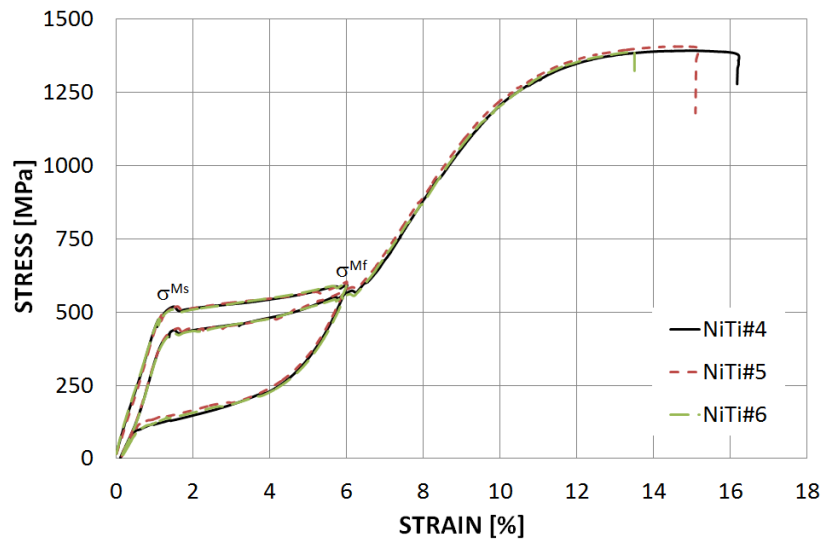


Figure 2.17. Stress-strain behavior of the Ni-Ti alloy tested by (Mas et al. 2016a)

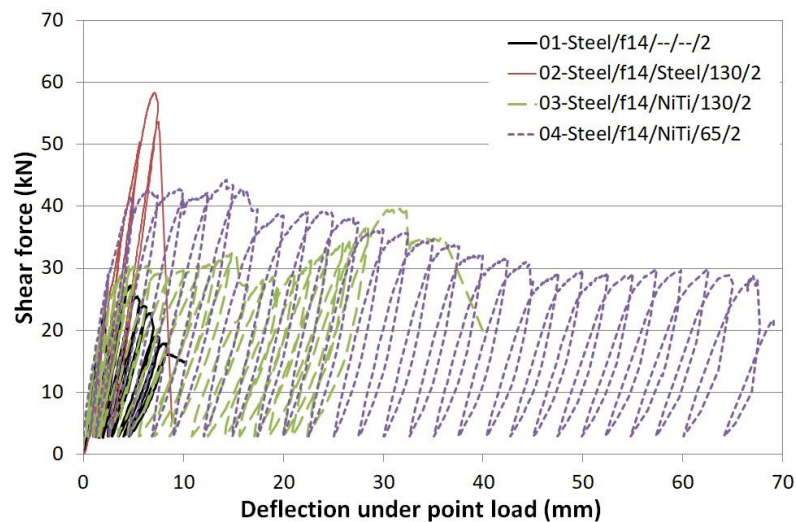


Figure 2.18. Comparison between brittle and ductile shear failures. (Mas et al. 2016a)

Recently, (Pereiro-Barceló & Bonet 2017) studied Ni-Ti SMA bars under compression. They provided a constitutive model that included instability since the low Young modulus of Ni-Ti, in comparison with steel, can significantly increase instability problems. Also, (Pereiro-Barceló et al. 2018) studied buckling of steel and Ni-Ti reinforcements in very high-performance concrete (VHPC) elements subjected to monotonic loading. The results of these tests were to extend their previous model which determined the buckling critical stress for any transverse reinforcement separation and considered the effect of the concrete cover.

2.4.3 Ni-Ti-Nb ALLOYS IN STRUCTURAL ENGINEERING

The addition of a third component (Nb) to a binary alloy (Ni-Ti) affects and widens the thermal hysteresis and makes these ternary alloys useful for prestressing applications in civil engineering. This topic is a key aspect in this research. Ni-Ti-Nb alloys were first reported in 1986 (Melton et al. 1986; Melton et al. 1989) and the main aspect to be highlighted is they are easier to handle and store owing to their larger temperature hysteresis. This allows the material to be prestrained at a low temperature at martensite state, be safely transported at ambient temperatures, be activated at a higher temperature with reverse transformation to austenite and retain high values of recovery stresses at ambient temperatures (fig. 2.14c-d).

(Cladera, Weber, et al. 2014) analyzed the distinct ranges of generation of recovery stresses for two different alloys as binary Ni-Ti and ternary Ni-Ti-Nb. It is schematically depicted in figures 2.19, 2.20 and 2.10. Figures 2.19a and 2.20a show a stress-strain path for a narrow hysteresis alloy (i.e. Ni-Ti) and figures 2.19b and 2.20b a wide hysteresis alloy (i.e. Ni-Ti-Nb). In these cases, the process starts with a pre-treatment with loading and the material being twinned martensite, evolving with an almost horizontal plateau, in which the detwinning process takes place and unloading with a prestrain maintained. For Ni-Ti alloys, in case of impeded strains, the recovery stress increases during heating but decreases during subsequent cooling (fig. 2.19a and 2.20a).

The recovery stress during heating may exceed the detwinning stress value (σ_s) because the energy (or stress) needed to detwin the martensite is significantly lower than the energy (temperature) needed to carry out the reverse transformation. However, when cooling, the recovery stress may drop down almost to zero because of forward transformation. To avoid any loss of recovery stress, the M_s temperature is often chosen to be below the ambient temperature (situation not represented in fig. 2.19, see fig. 2.14c-d). In this case, the SMA is typically cooled down below the M_f temperature for prestraining and stored at a temperature below A_s , by liquid nitrogen if needed. Throughout the service life, the SMA then remains in the high-temperature austenitic phase where it keeps the high recovery stress (Melton et al. 1986). For Ni-Ti-Nb alloys (fig. 2.20b), which have a larger hysteresis (fig. 2.14d), after the same treatment the prestraining is still done at cooled conditions, but storage can be at ambient temperature, if it is below A_s (Uchida et al. 2011).

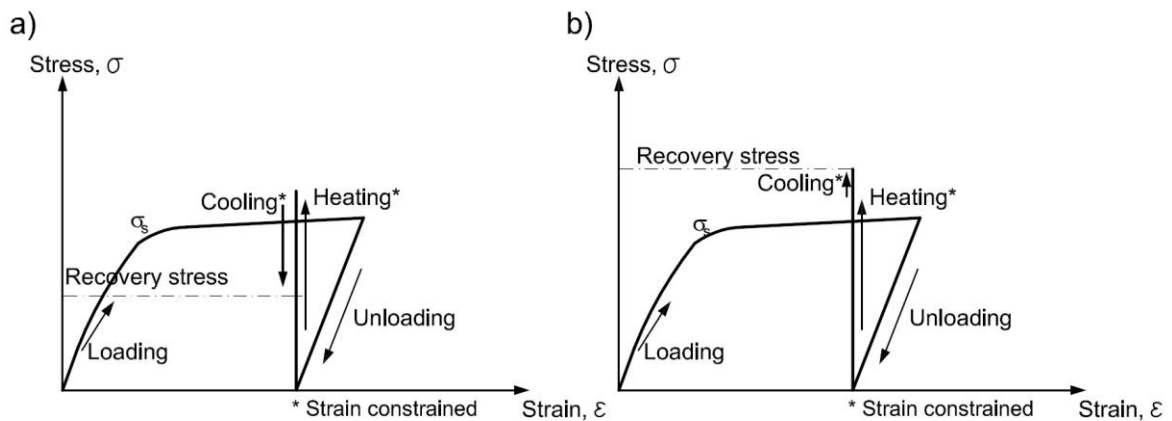


Figure 2.19. Schematic stress–strain diagrams of prestraining and generation of recovery stresses during the activation of the reverse transformation in a constrained SMA: a) Narrow hysteresis alloy, i.e., Ni–Ti; b) Wide hysteresis alloy, i.e., Ni–Ti–Nb. From (Cladera, Weber, et al. 2014)

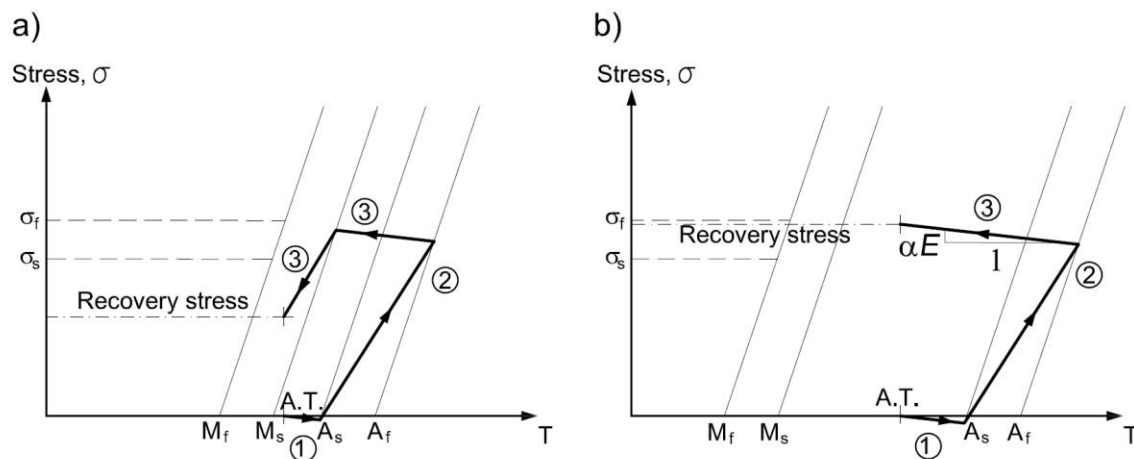


Figure 2.20. Schematic thermomechanical paths during the activation and cooling of a constrained SMA: a) narrow hysteresis alloy, i.e., Ni–Ti; b) wide hysteresis alloy, i.e., Ni–Ti–Nb. From (Cladera, Weber, et al. 2014)

Figure 2.20 shows the evolution of recovery stresses and temperature during heating and cooling of the two above mentioned alloys. During the heating step (path 1), the elastic stress in the SMA first decreases due to the suppressed thermal expansion. Once the stress-temperature path crosses the A_s boundary, a reverse transformation to the austenite phase occurs (path 2). This transformation activates the SME, which generates tensile stresses in the SMA, because the contraction is inhibited, until the complete transformation of the alloy into austenite. However, some of the stress is lost due to thermal expansion. The thermal expansion effect is recovered by thermal contraction during subsequent cooling (Lee et al. 2013). The slope of the stress variation due to pure thermal expansion/contraction varies

depending on the alloy and this slope can be obtained from Eqs. 2.23 to 2.26. The elongation of the sample due to the internal force is:

$$\Delta l_F = \frac{Fl}{EA} \quad (2.23)$$

where

- F is the force applied to the sample,
- l is the length of the sample,
- E is the elastic modulus of the sample, and
- A is the area of the cross-section of the sample.

The elongation due to the thermal expansion is:

$$\Delta l_T = \alpha_T \Delta T l \quad (2.24)$$

where

- ΔT is the temperature increment of the sample,
- α_T is the Coefficient of Thermal Expansion (CTE).

Since $\sigma = F / A$, and taking into account that the element is constrained, the elongation due to the thermal expansion must equal the elongation due to the internal force:

$$\Delta l_T = \Delta l_F \quad (2.25)$$

A relationship (slope) of stresses due to thermal increment is obtained:

$$\sigma = \alpha_T E \Delta T \quad (2.26)$$

Thus, for an austenite phase Ni–Ti alloy, considering $E = 60$ GPa and $\alpha_T = 11 \times 10^{-6}/^\circ\text{C}$, the slope would be $\alpha_T E = 0.66$ MPa/ $^\circ\text{C}$.

The behavior during cooling back to ambient temperature (AT) depends mainly on the width of the hysteresis (path 3). For a Ni–Ti SMA with a narrow hysteresis, the recovery stress drops down due to forward transformation (figs. 2.19a and 2.20a). For a wide hysteresis Ni–Ti–Nb alloy, the austenite remains stable as long as the AT is above the M_s boundary, maintaining a high recovery stress (figs. 2.19b and 2.20b). An alloy with AT between M_s and A_s and a narrow temperature hysteresis (fig. 2.20a, i.e., Ni–Ti) is not appropriate for acting as permanent prestressing because the recovery stresses decreases considerably after heating and cooling back to the AT. The recovery stresses would even become negligible if

the martensite finish temperature, M_f , was higher than the AT, a situation that is not shown in fig. 2.20a.

As stated before, in the absence of heating or cooling, the SMA is at AT and from civil engineering point of view, this temperature defines the phase in which the alloy should be stable in its structural applications. (Janke et al. 2005) proposed that, for external applications in outdoor structures, the ambient temperature can be assumed to be situated between $-20\text{ }^\circ\text{C}$ in winter and $60\text{ }^\circ\text{C}$ under intense solar radiation in summer. For this reason, high hysteresis SMAs are required for structural applications involving the SME.

2.5 ACTIVE STRENGTHENING OF REINFORCED CONCRETE BEAMS USING SHAPE MEMORY ALLOYS

2.5.1 PRESTRESSING THROUGH SMA WIRES

Prestressing RC structures is a well-known and widely developed technique to improve mechanical behavior of RC beams. (Maji & Negret 1998) carried out one of the first research studies in which Ni-Ti wires were used to create an additional prestressing force in elements of cement mortar. The cables were prestrained beyond their elastic limit in the martensite phase and, subsequently were embedded in the beams. Through electrical heating the transformation from martensite to austenite generated recovery stresses in the SMA and, therefore, compressive stresses in the mortar. Other references related to the use the SMA for prestressing are, among many others, (Soroushian et al. 2001), (Sawaguchi et al. 2006), or more recently (Czaderski et al. 2014), (Lee et al. 2015), (Shahverdi et al. 2016) or (Rojab & El-Hacha 2017).

Even though the adherence between SMA wires and concrete has been a technological problem of major concern (Czaderski et al. 2006), prestressing RC structures with SMA has the advantage that does not need hydraulic jacks and can be applied at any time during the lifetime of an element. These facts offer new possibilities, such as prestressing by stages in

order to avoid cracking. Moreover, there are no losses due to friction; it could be especially useful when the layout of the prestressing is particularly curved (Janke et al. 2005).

Improvement in wire bonding was studied in 2006 (Czaderski et al. 2006), using epoxy resins to fix quartz sand on the surface of the wires, although the chlorides in the resin caused unacceptable corrosion problems in the SMA. (Deng et al. 2006) used prestressing to produce counter-deflections in small concrete beams, also studying the effect of prestraining and the effect of variability of the diameter of the SMA rebars. They concluded that lower diameters provided a greater contact surface, wherefore it was advisable to use small diameters, a conclusion that was due to the problem of adherence above mentioned. (Reedlunn et al. 2013a; Reedlunn et al. 2013b) performed a characterization of super-elastic behavior of Ni-Ti SMA cables as structural elements investigating the tensile behavior for different cable configurations. (Mas et al. 2017) presented a study of the performance of Ni-Ti SMA cables for their use in reinforced concrete applications. It was concluded that the cables have huge possibilities due to its good super-elastic properties. Nevertheless, with respect to the bonding tests (figure 2.21), the cable presented a different behavior compared to the conventional rebars or cables for which these tests were designed. The low modulus of elasticity of the cable was a handicap for its application in reinforced concrete members. However, the modulus of elasticity could be increased by adjusting the alloy or heat treatment process to lower the transformation temperatures, in order to avoid excessive longitudinal and transverse deformations and to improve the bonding properties.

(El-Tawil & Ortega-Rosales 2004) investigated prestressing of beams with a standard Ni-Ti alloy and a Ni-Ti-Nb alloy. They concluded, for the particular case of the used SMAs, that the latter was able to maintain recovery stresses after cooling the SMA, thus it is much more appropriate for prestressing, as has been already discussed previously in this chapter.

(Li et al. 2008) used SMA wires combined with conventional steel in tensile reinforcement, carrying out temporary prestressing with the SMA in order to facilitate permanent reinforcement through CFRP laminates. They observed that SMA wires can effectively reduce residual strain of the beams after heating, but, by combining their use with steel, the recovery was impeded. The low modulus of elasticity of ordinary SMAs impedes their joint use with conventional steel arranged in the same direction, as the recovery stresses would be resisted by the steel with small deformations and would not be transmitted to the concrete.

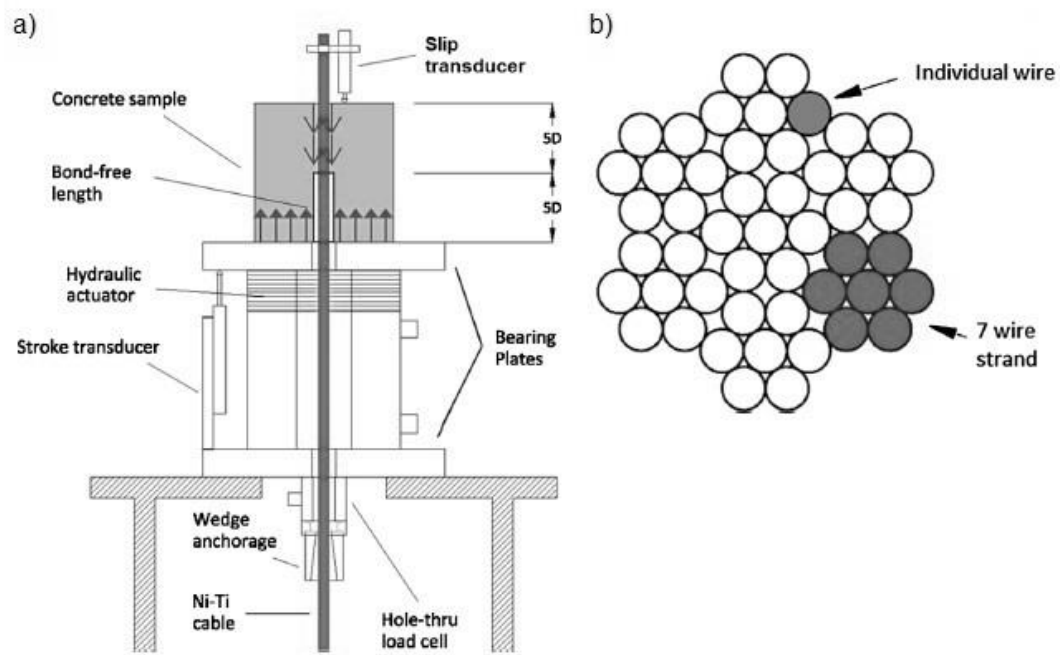


Figure 2.21. a) Schematic drawing of the bonding test set-up and b) Cross-section of the tested Ni-Ti wire.
From (Mas et al. 2017)

The use of SMAs as external prestressing for strengthening structures makes it possible to take advantage of the exceptional corrosion resistance characteristics of most of SMAs. Moreover, as the alloy is placed externally to the concrete, it can reach a high A_f temperature without damaging the concrete. However, there are fewer research studies in this field. It is worth noting the reinforcement of a bridge in Michigan through external post-tensioning performed with SMA rebars (Soroushian et al. 2001), after a laboratory research study on the possibilities of external reinforcement of shear cracks (figure 2.22).

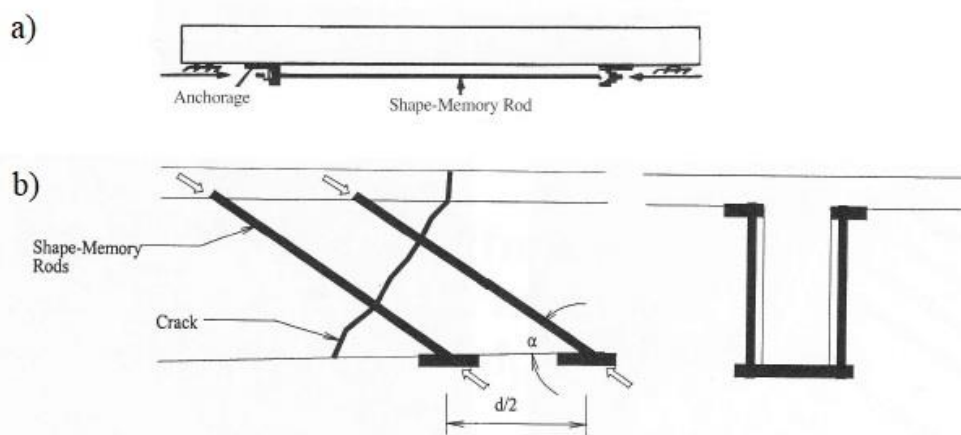


Figure 2.22. Some analyzed possibilities of external reinforcement from (Soroushian et al. 2001): a) longitudinal corrective force and b) local post-tensioning for enhancement of shear resistance

In this case a Fe-Mn-Si-Cr alloy was used which could develop recovery stresses of 255 MPa after heating it to 300°C. The effect that extreme external temperatures could have on the restrained recovery stresses of the selected iron-based alloy was also studied, concluding that the variations in stress were relatively small. The study showed that post-tensioning with SMAs enabled the shear crack to be closed to a large extent, recovering the initial ductility and the load capacity of the beam.

The possibility of prestressing concrete through the use of short active SMA fibers embedded in concrete structures has also been studied (Moser 2005), showing that it is a feasible process. The authors reported recovery stresses in the Ni-Ti fibers of 845 MPa when heated to 180 °C and the effective maximum prestress reached was estimated to be of the order of 7 MPa. However, the used SMA returned to the martensite phase upon cooling, whereby it lost much of the prestressing. Studies have also been conducted with intermediate solutions between short fibers and prestressed wires (Krstulovic-Opara & Thiedeman 2000), (Watanabe et al. 2002).

(Song, Ma, et al. 2006) used internal post-tensioning in a beam with self-rehabilitation capability, presenting the concept of reinforced concrete smart structure and its application in monitoring structural damage and rehabilitation, combining for this, the use of SMAs and piezoceramic sensors. The structure was reinforced with Ni-Ti in martensite phase inside post-tensioned sheaths, proceeding to tensioning up to a strain of 2 %. The piezometric elements detected cracking. Once the damage had been detected, the SMA cables were heated to 90 °C, producing the reverse transformation, adding a tensioning force to the SMA and consequently compressing the concrete.

In order to study the potential of smart concrete beams, in which prestressing is activated and modifies the behavior of the beams according to needs, for instance upon detecting heavy traffic, (Li et al. 2007) developed an experimental campaign with two bridge slab beams with embedded SMA cables analyzing the influence of temperature and the recovery force of the cables which depended on the initial conditions of each cable. Even though the recovery force was different in each bundle, their force increments in each activating time were almost the same. In addition, the effect of the environment was significant, because the displacement at midspan induced by the environmental temperature was about twelve times

the displacement of the recovery force of the SMA. Some other factors, such as the activating times, the length of the unbonded section, the length and prestrain of the SMA bundles, could also affect the behavior of the concrete beam and further investigation was needed. However, from their experimental program, the authors concluded that SMAs could be used in the future in practical civil engineering structures to resist overloads.

(Shahverdi et al. 2016) investigated the real performance of flexural behavior of RC beams strengthened and prestressed with Fe-SMA strips comparing externally bonded reinforcement with near surface strengthening (strips located in grooves and filled with mortar to bond) taking advantage of reduced probability of corrosion, fire, vandalism, mechanical damage and aging. The bond behavior was judged to be sufficient for strengthening applications with approximate recovery stresses of about 200 MPa although smaller than those obtained in the climate chamber of about 230 MPa in perfect conditions. The Near Surface Mounted (NSM) technique (figure 2.23) had already been researched and practical applications were developed, e.g. in case of FRP for RC structures (De Lorenzis & Teng 2007). Also, in case of Fe-based SMAs, the NSM technique has been tested (Czaderski et al. 2014) to longitudinally prestress RC structures.

(Rojob & El-hacha 2017) also worked on flexural strengthening of RC beams using the NSM technique, with the advantage of isolating SMA bars/strips from environ they were inserted in a groove (covered with mortar afterwards) on the tension side of the RC beam (figure 2.23) and then activated through heating to apply prestressing force to the beam by means of a Fe-SMA. The results showed increment of 20.3 %, 24.3 % and 18.3 % in cracking load, yielding load and ultimate load and 19.2 % in deflection at yielding from the strengthened beam to the unstrengthened one. They also reported maintained good contact of the Fe-SMA with the grout until debonding at about yielding load.

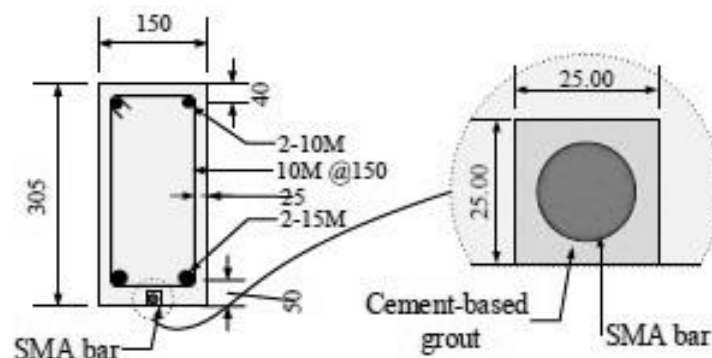


Figure 2.23. Section and detail of NSM SMA bar for prestressing technique. From (Rojob & El-hacha 2017)

2.5.2 ACTIVE CONFINEMENT

Active confinement of concrete columns through SMAs is a particular case of the prestressing technique, but with a conceptual difference of the function performed by the strengthening material (the SMA) with respect to the above-mentioned cases (figure 2.24).

Active confinement would make sense in the rehabilitation of existing structures, when it is necessary to gain ductility, but the cost of SMAs would hardly justify this application in planning new structures (Janke et al. 2005). The first tests on active confinement with SMAs date back to the year 2000 (Krstulovic-Opara & Thiedeman 2000), and it is in recent years that most experimental results have been published (Choi et al. 2008), (Andrawes et al. 2010), (Shin & Andrawes 2010), (Park et al. 2011), (Dommer & Andrawes 2012), (Shin & Andrawes 2012), (Shin & Andrawes 2013), (Shin & Andrawes 2014), (El-hacha & Abdelrahman 2015), (Tran et al. 2015) (Tavousi Tehrani et al. 2017), (Tazarv & Saiidi 2017), (Chen & Andrawes 2017a).

In 2008, (Choi et al. 2008) studied the behavior of concrete test specimens confined with 1 mm diameter wires. They used two Ni-Ti alloys: one in martensite phase with a prestrain of 3%, which actively compressed the test specimens upon heating through an electrical circuit; and a second Ni-Ti alloy in austenite phase. The active confinement of the first case slightly increased the concrete compressive strength, with a significant rise in ductility. The confinement effect produced with the austenite alloy was similar. It is worth noting that the geometrical imperfections of the wire produced significant losses after cooling of the martensite, which undoubtedly decreased the confining stress.

(Shin & Andrawes 2010) published the results of an experimental study on the feasibility of the use of Ni-Ti-Nb spirals to apply active confinement pressure. The used alloy enabled recovery stresses of 565 MPa to be mobilized at 108 °C with a prestrain of 6.4 %, maintaining a residual recovery stress of 460 MPa at ambient temperature. Uniaxial compression tests were carried out in actively (SMA) and passively (GFRP) confined concrete test specimens. Through active confinement, the ultimate strength increased 21% compared to identical plain concrete test specimens; with the ultimate strain rising 24 times (figure 2.25). In the experimental campaign, they also studied the use of GFRP fabrics with SMAs, which enabled delaying the rupture of the GFRP.

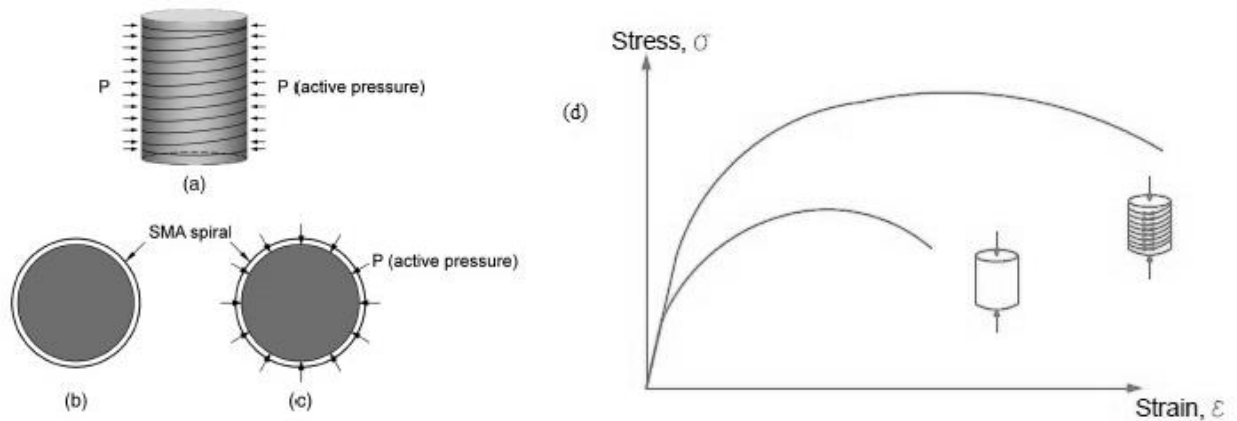


Figure 2.24. Schematic drawings of a confined concrete column uniaxial compressive test: a) Concrete element confined with SMA spirals, b) Cross-section before heating, c) Cross-section after heating, and d) Uniaxial compressive test stress–strain path comparison between confined and unconfined test. From (Cladera, Oller, et al. 2014), adapted from (Shin & Andrawes 2010)

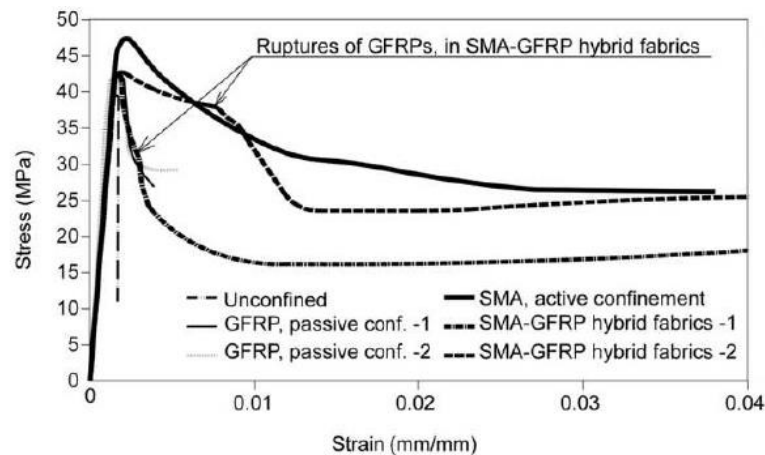


Figure 2.25. Stress-strain relationship for test specimens without confinement, confined with SMAs, GFRP, or SMA-GFRP hybrid fabrics (Cladera, Oller, et al. 2014)

A subsequent study (Park et al. 2011), also using a Ni-Ti-Nb alloy, revealed that the load and unload cycles that produced strains above the initial prestrain, led to the loss of residual stress of the prestressing upon unloading, therefore it was necessary to study this phenomenon in more depth. In 2012, (Choi, Nam, et al. 2012) reported a maximum recovery stress of 325 MPa for Ni-Ti-Nb wires (1 mm diameter and composition Ni - 47.75 %, Ti - 37.86 %, Nb - 14.69 %) with a hysteretic gap ($A_s - M_s$) of 122.5 °C ($M_s = -17.59$ °C) suitable for confining civil structures but concluded that not all Ni-Ti-Nb alloys are appropriate for post-tensioning applications, which is also likely to occur with different alloys, as when faced with load and unload cycles after initial prestressing, active confinement may be lost,

leaving only passive confinement, which would also give the concrete greater resistance and ductility, although to a lesser extent than active confinement.

In 2012, (Dommer & Andrawes 2012) reported a maximum recovery stress of 574 MPa for Ni-Ti-Nb wires with an acceptable level of stability within a range of -10 °C to 50 °C. Other SMAs could be also suitable for this purpose as (Leinenbach et al. 2012) reported recovery stresses of about 500 MPa for Fe-based SMAs.

Ni-Ti-Nb wires have been successfully used to actively confine circular and non-circular columns to improve their behavior under axial compression forces and bending. (Shin & Andrawes 2010; Dommer & Andrawes 2012) reported good performance on active confinement of RC columns (compression) by means of Ni-Ti-Nb spirals in retrofitting, i.e. seismic retrofit of highway bridge columns (figure 2.26a).

(Choi, Choi, et al. 2012) ascertained good performance in a study of application of Ni-Ti-Nb martensitic SMA wires to retrofit for reinforced concrete columns with lap splices using wire jackets (figure 2.26b). Also, they compared the results with those of Ni-Ti wires with the same application. Furthermore, the study investigated the recovery and the residual stresses of Ni-Ti-Nb wires and its behavior. The study showed that the Ni-Ti-Nb wire jackets were more adaptive for retrofit of RC columns than the Ni-Ti wire jackets since the Ni-Ti-Nb disposed of more appropriate temperature windows for the applications of SMAs in civil structures.

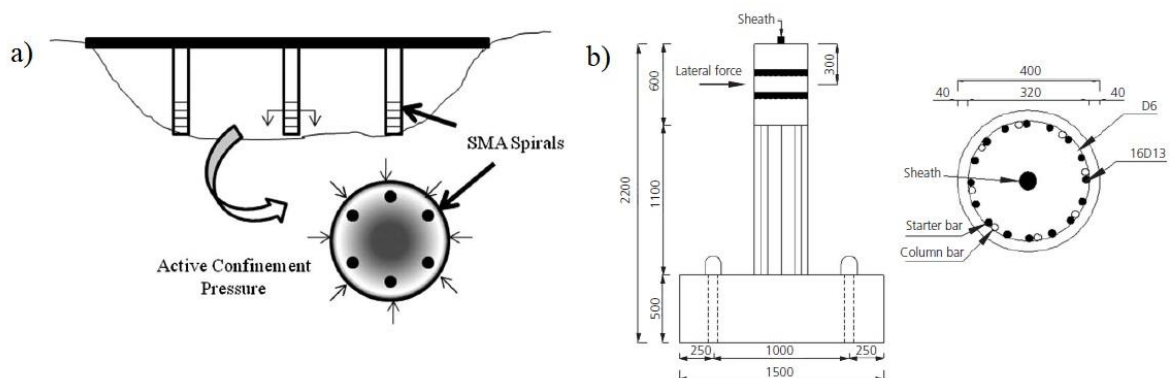


Figure 2.26. a) Example of application of SMA spirals for active confinement of bridge piers (Dommer & Andrawes 2012) and b) general view and cross section of lab specimen of RC columns retrofit by SMA wire jackets (Choi, Choi, et al. 2012)

Recently, (Chen & Andrawes 2017a) investigated the cyclic behavior of Ni-Ti-Nb SMA confined concrete performing a series of uniaxial cyclic tests on confined concrete cylinders. The test results showed that the effectiveness of Ni-Ti-Nb SMA confinement on strength and ductility enhancement increases as active confining pressure increases. Using the test results the authors developed an empirical stress-strain model for Ni-Ti-Nb SMA confined concrete, and proposed (Chen & Andrawes 2017b) a plasticity-based confined concrete constitutive model. This model is capable of predicting and simulating three-dimensional stress-strain behavior of Ni-Ti-Nb SMA confined concrete under both monotonic and cyclic loading. New hardening/softening function, dilation rate function, and damage parameters are derived and validated based on experimental results. The proposed model (figure 2.27) is able to closely simulate the axial and lateral stress-strain behaviors of the retrofitted cylinders. Therefore, novel confinement techniques using SMA spirals are proved to be promising for seismic retrofit of concrete structures.

(Chen et al. 2014) studied active confinement of concrete prisms using SMA wires. Their study focuses on developing a novel scheme for applying external active confinement to non-circular concrete elements that lack ductility using SMAs (figure 2.28). Concrete elements (prisms) were tested under monotonic and cyclic uniaxial compression loads. The compressive stress-strain relationships of the SMA confined concrete elements were examined and compared with the behaviors of elements confined with conventional GFRP jackets.

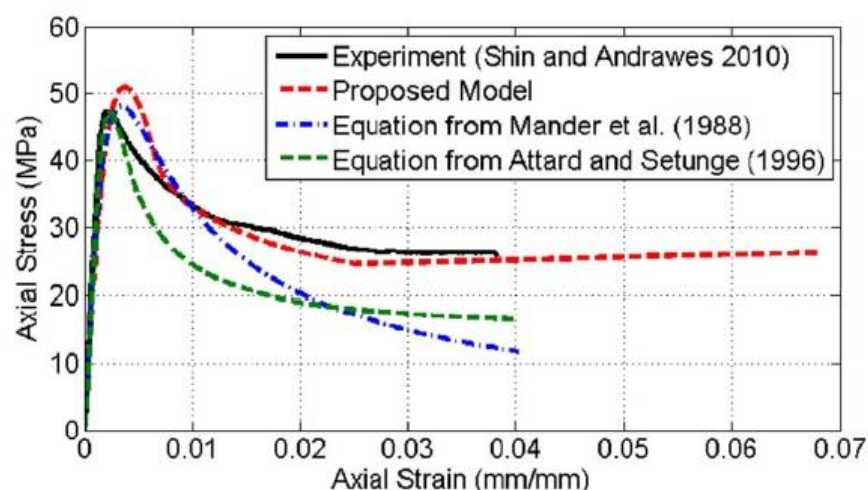


Figure 2.27. Comparison of Stress-strain relationship for proposed plasticity model and experimental results (Chen & Andrawes 2017b).

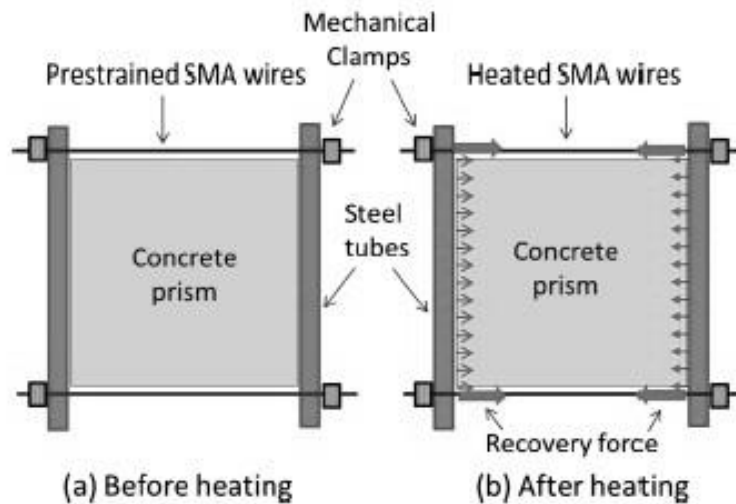


Figure 2.28. Scheme of active confinement of non-circular prisms in (Chen et al. 2014)

The results clearly showed a significant improvement in the ultimate strain and residual (post-peak) strength of concrete elements actively confined with SMA compared to that of GFRP confined elements. The new technique clearly showed effectiveness in delaying the damage of concrete, which helped significantly in improving the ductility of non-circular concrete members.

2.5.3 PERFORMANCE OF RECOVERY STRESSES

Different studies have been conducted with regard to the shape recovery and recovery stress formation in SMAs from a theoretical point of view, but most of them have been conducted in idealized conditions. Some practical issues have been shortly considered in the literature. One important issue is the development of the recovery stress under non-ideal restraints during the installing process or the activation of SMA components. The evolution of expected recovery stresses in the presence of an initial gap, initial imperfection in the contact between concrete surface and wires (non-circular RC elements) or elastic restraints could be reduced, and the effectiveness of the reinforcement could be affected or directly disabled if the strain initially lost reach certain value.

(Lee et al. 2015) studied the formation of recovery stresses in a restrained Fe-based SMA used for mechanical coupling. On the other hand, prestressing was investigated with special

emphasis on non-ideal restraints that might reduce the stress recovery. The evolution of recovery stresses in the presence of an initial gap and elastic restraints was experimentally investigated (figure 2.29). The results showed that the alloy could still produce substantial recovery stresses even under non-ideal restraining conditions and the final recovery stress decreases almost linearly with the shortening strain.

The performance of SMAs strengthening RC structures during the whole service life has been investigated taking into account creep and stress relaxation. (Leinenbach et al. 2016) systematically studied them in stress and strain controlled tensile tests carried out on Fe-based SMAs and concluded that, if strain is kept constant, a pronounced stress relaxation of up to 10 % of the initial stress occurred.

(Hosseini et al. 2018) also studied stress recovery and cyclic deformation behavior of Fe-based SMA strips and showed that the magnitude of the tensile stress during activation could have a significant effect on the recovery stress. Relaxation effects have also been investigated in the case of Ni-Ti-Nb wires (Varela et al. 2017) and the first results have shown that relaxation can be several times higher than conventional steel.

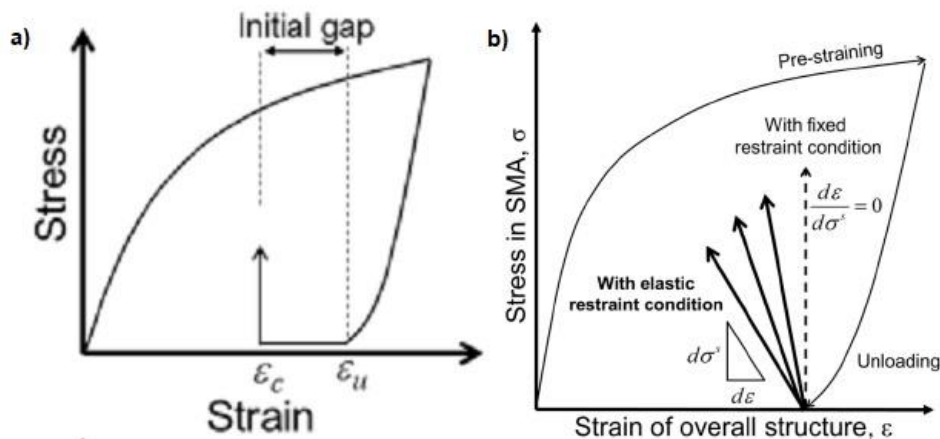


Figure 2.29. Schematic graphs of stress recovery developing under: a) initial gap and b) elastic constraint condition. From (Lee et al. 2015)

2.5.4 ACTIVE STRENGTHENING OF RC BEAMS USING Ni-Ti-Nb

As stated before, the SME of SMAs is an essential property for the featured strengthening technology. If a SMA is used as external reinforcement, for example, to wrap a beam, and the recovery strain when heating and cooling afterwards is constrained, the SMA will generate recovery stresses, prestressing and/or confining the concrete member. With the adequate selection of the SMA, these stresses will remain applied throughout the service life of the structure.

Ni-Ti alloys have already been used in many civil engineering applications, due to their pseudo-elastic behavior and their damping capacity. However, as has been analyzed before in this chapter, its narrow thermal hysteresis makes this alloy inappropriate for use in prestressing applications in civil engineering structures relying on the shape memory effect (Mas et al. 2016b).

The use of spirals has already shown important benefits as internal reinforcement for shear, using common materials or even shape memory alloys. (Mas et al. 2016a) reported that beams reinforced in shear with the Ni-Ti rectangular spiral could sustain a significant load after the full development of the critical shear crack, enhancing other resisting mechanisms at failure, such as the dowel effect, the shear transferred by the shear reinforcement and the arch effect.

The use of Ni-Ti-Nb wires as prestraining reinforcement for shear critical beams may overcome the limitation of a narrow hysteresis. Therefore, the use of external spirals of Ni-Ti-Nb to actively shear strength RC beams has been chosen as a practical application to be developed in this Ph.D. thesis. A simple method to install the wires has been looked for, as well as, the selection of an easy way for perform the SMA activation process.

In fact, some of the tasks and results carried out during this Ph.D. thesis have already been published in a paper and presented in 3 communications at two different international conferences:

- Rius, Joan M.; Cladera, Antoni; Ribas, Carlos; Mas, Benito 2018: ‘Shear Strengthening of Reinforced Concrete Beams Using Shape Memory Alloys’. *Construction and Building Materials*. In press (Rius et al. 2018).

- Rius, Joan M. ; Cladera, Antoni; Ribas, Carlos; Mas, Benito 2017: ‘Active external shear reinforcement using shape memory alloys’. ‘Refuerzo externo activo mediante aleaciones con memoria de forma’. VII congreso de ACHE. La Coruña (Spain), June 2017. Publication data: Hormigón y Acero. Volumen 68 - Especial Congreso. ISSN: 0439-5689. (Rius et al. 2017b).
- Varela, Fernando; Rius, Joan M.; Herrador, Manuel; Cladera, Antoni; Martínez, Fernando; Ribas, Carlos 2017: ‘Stress relaxation of Ni-Ti-Nb shape memory alloy wires’. ‘Relajación tensional en cables de aleaciones con memoria de forma Ni-Ti-Nb’. VII congreso de ACHE. La Coruña (Spain), June 2017. Publication data: Hormigón y Acero. Volumen 68 - Especial Congreso. ISSN: 0439-5689. (Varela et al. 2017).
- Rius, Joan M.; Cladera, Antoni, Ribas, Carlos; Mas, Benito 2017: ‘Active shear strengthening of RC beams using shape memory alloys’. SMAR 2017 – Fourth Conference on Smart Monitoring, Assessment and Rehabilitation of Civil Structures. Zurich (Switzerland), September 2017. Publication data: Proceedings of SMAR 2017 - ISBN: 978-3-905594-66-9. (Rius et al. 2017a).

Furthermore, a new patent has been granted in Spain entitled ‘Active reinforcement method against shear force or punching shear in structural supporting elements, and active reinforcement system’. ‘Método de refuerzo activo frente a esfuerzo cortante o punzonamiento en elementos portantes estructurales, y sistema de refuerzo activo’. ES 2592554 B1’. Authors: Cladera, Antoni; Ribas, Carlos; Mas, Benito; Rius; Joan M.; Montoya, Luis; Ruiz, Joaquín (Cladera, Ribas, et al. 2016).

3. RESEARCH OBJECTIVES

3.1. SHORT SUMMARY OF THE STATE OF THE ART

The use of SMAs for strengthening RC structures is a feasible technology to improve their behavior under different circumstances such as cyclic loads, large deformations and the repair of deteriorated structures, among many others. SMAs are materials with a relatively wide use in different fields such as aeronautical engineering and medicine. From a civil engineering point of view, they have been used in specific applications—at research level—although their use is not yet widespread.

In order to be used in civil and structural engineering, their special shape memory effect (SME) and pseudo-elasticity properties need to be useful in the temperature range of civil engineering. Many SMAs present difficulties when applied in such a temperature range where SME is the required special feature. One SMA with applicability in this range of temperatures is Ni-Ti-Nb alloys.

Strengthening of RC structures has already been undertaken with SMAs in specific applications, mostly for confining purposes in columns. With regard to shear strength reinforcement, a binary alloy such as Ni-Ti has been internally used to reinforce concrete beams, but a ternary alloy such as Ni-Ti-Nb has not been used, to the best of the author's knowledge, for external shear strengthening of critical RC members.

3.2. SPECIFIC OBJECTIVES

The main objective of this Ph.D. thesis is to expand knowledge of repair and strengthening in RC structures using SMAs in structural engineering. Specifically, an active external shear strengthening method using Ni-Ti-Nb SMA wires as external reinforcement in shear critical RC beams will be developed.

The suitability of this Ni-Ti-Nb SMA with a wide thermal hysteretic behavior will be studied for generating recovery stresses within the typical temperature range for outdoor civil engineering structural applications.

The practical procedure of the application of this SMA as shear strengthening of RC beams in an experimental campaign, as well as the improvement of shear strength of the tested beams, will lead to the development of a new technology for shear strengthening of RC structures using SMAs. The specific objectives for this purpose are:

- Physical and thermo-mechanical characterization of the available SMA (Ni-Ti-Nb), by means of different experimental tests to determine its properties.
- Experimental application of external strengthening of RC beams without internal shear reinforcement by means of spirals, or other configurations, made from Ni-Ti-Nb wires.
- Characterization of the Ni-Ti-Nb recovery stresses under non-idealized conditions.
- Validation and extension, if needed, of previously developed mechanical models for the determination of the shear strength to take into account the external strengthening in shear.

3.3. METHODOLOGY

To achieve the proposed specific objectives, the following methodology has been applied:

- For the physical and thermo-mechanical characterization of the available SMA, the following laboratory tasks were carried out:

- Determination of composition of the supplied material: 3 mm diameter Ni-Ti-Nb wires by means of Dispersive Energy X-ray Spectroscopy (EDX).
 - Thermal characterization of Ni-Ti-Nb. Determination of characteristic transformation temperatures for direct and reverse phase transformation by means of Differential Scanning Calorimetry (DSC) and resistivity tests.
 - Mechanical characterization of the Ni-Ti-Nb wires in martensite and austenite phases by means of tensile tests at different ambient temperatures.
 - Thermo-mechanical characterization of Ni-Ti-Nb wires by means of determination of recovery stresses during activation (reverse transformation) with constrained strains.
- For the experimental application of external strengthening of RC beams without internal shear reinforcement by means of spirals of Ni-Ti-Nb wires to improve their strength, the following laboratory tasks were carried out:
- Planning an experimental campaign of small-scale tests of RC beams with an external reinforcement of Ni-Ti-Nb wires: design of test specimens and concrete properties determination campaign, design of specific shear strengthening elements, design of test instrumentation and monitoring.
 - Fabrication of tests specimens, strengthening them and installing the instrumentation to carry out the experimental tests.
 - Conducting of the experimental tests.
 - Analysis of the behavior of the strengthened beams.
- For the characterization of the Ni-Ti-Nb recovery stresses under non-idealized conditions, a new campaign of laboratory tests was carried out, including:
- Additional recovery stress tests on Ni-Ti-Nb wires with activation by means of a heat gun.
 - Additional recovery stress tests on Ni-Ti-Nb wires with different initial imperfection on the sample.
 - Actual recovery stress determination on the wire links installed on the beams.

- For the validation and extension, if needed, of a previously developed mechanical model to take into account the external strengthening using SMAs the following analytical tasks were carried out:
 - Prediction of the shear strength of the tested beams using two different shear models: The Compression Chord Capacity Model (CCCM) and the shear design equations included in Eurocode-2.
 - Comparison of the predictions by the applied shear models and the experiment results to assess the performance and applicability of the models.

4. CHARACTERIZATION OF THE Ni-Ti-Nb WIRES

4.1 OBJECTIVES AND BRIEF SUMMARY OF THE TESTS

An experimental campaign was planned with the main objective of characterizing the supplied material, as well as determining its composition. This experimental campaign was initially designed with a flexible planning, and it evolved taking into account the results of the previous tests.

The supplied material, a SMA of nickel, titanium, and niobium (Ni-Ti-Nb) had these characteristics:

- 3 mm-diameter wires, without ribs or indentation of any type, manufactured by Memry (Saes Group Company),
- material supplied in martensite phase with a 6 % pre-strain in a forward transformation from austenite to martensite, and
- 267 cm long wires. A total amount of 45 samples of 30 cm long (figure 4.1) were obtained cutting them by using a manual shear.



Figure 4.1. 300 mm long Ni-Ti-Nb samples ready to be tested

The main properties of the Ni-Ti-Nb wires to be found were physical and mechanical ones. Physical properties were material composition of the alloy and the transformation temperatures (M_s , M_f , A_s and A_f temperatures). The mechanical properties to be determined were the modulus of elasticity (E), yield strength (f_y), ultimate strength (f_u), and ultimate strain (ε_u) from both austenite and martensite solid phases. The stresses related to the stress-induced martensite transformation (martensite starts, σ^{M_s} , and martensite finish, σ^{M_f}) were also analyzed. Additionally, it was considered important to investigate the relationship between these properties and the test ambient temperature, and the type of applied load (monotonic or cyclic).

The tests were carried out following own protocols of the Construction and Structural Engineering (ConStruct) Group at the UIB. This group had previously conducted different experimental campaigns on super-elastic Ni-Ti alloys. The corresponding Standards: for the determination of transformation temperatures (ASTM F2082-06 2006), and for tensioning testing (ASTM-F2516-07 2007) were taken as a basis for some tests, although with test speeds adapted to the conditions of the equipment for tension testing, as will be explained later in this chapter.

4.2 MATERIAL COMPOSITION

The determination of the material composition was carried out by means of an energy dispersive X-ray spectroscopy (EDX) test. The EDX test equipment used was a Hitachi S-

3400N Scanning Electron Microscope (figure 4.2a) located at the *Servei Científico-Tècnic* (SCT) laboratory of the University of Balearic Islands (UIB).

The determined composition of the alloy was: Ti atw.45.81 %, Ni atw.45.76 %, and Nb atw.8.43 %.

4.3 TRANSFORMATION TEMPERATURES

Since the available SMA was a Ni-Ti-Nb alloy, a wide hysteretic behavior was expected to be found. That meant that the difference between martensite start and austenite start temperatures ($M_s - A_s$, see figure 4.3) was expected to be much higher than that of a binary Ni-Ti alloy (about tens of degrees).

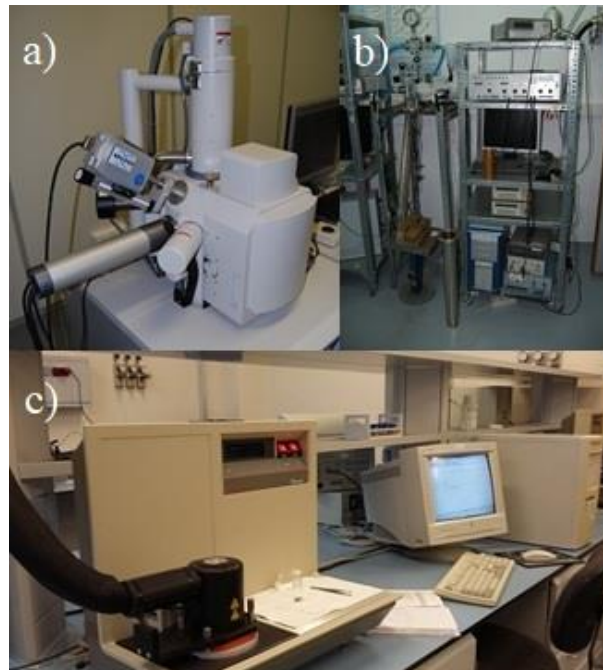


Figure 4.2. Test equipment at UIB laboratories employed for the SMA physical characterization: a) EDX equipment at SCT lab, b) resistance test equipment at the Material Science lab of the Dept. of Physics of the UIB, and c) DSC test equipment at SCT lab

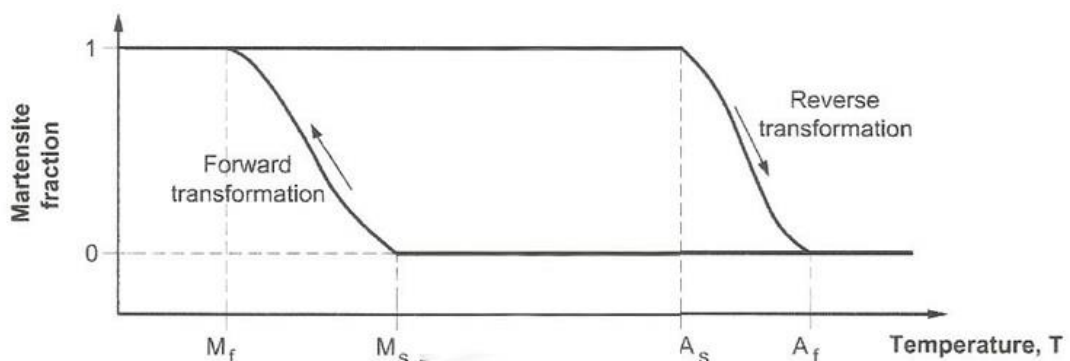


Figure 4.3. Schematic graph of phase transformation in SMAs according to temperature with a wide hysteretic behavior. Adapted from (Cladera, Weber, et al. 2014)

The determination of transformation temperatures for martensite phase transformation can be carried out by means of different laboratory techniques:

- Differential scanning calorimetry (DSC) test, and
- Resistivity test

DSC is an experimental technique used to measure crystalline transition temperatures of metallic samples. These temperatures are estimated by measuring the variation of the amount of heat required to increase the temperature of the sample. The used DSC test equipment was a TA INSTRUMENTS DSC-2920 (figure 4.2c).

The results of the Differential Scanning Calorimetry (DSC) test carried out to determine the phase transformation temperatures can be seen in figure 4.4. From the DSC, the detected phase transformation temperatures were $A_s = 72\text{ °C}$ and $A_f = 85\text{ °C}$.

The martensite start (M_s) and finish (M_f) temperatures were not detected in the DSC tests because of the minimum temperature of the used test equipment was -100 °C . Thus, resistance tests were carried out to determine the phase transformation temperatures, since the minimum temperature of the used equipment could go down to -190 °C . The main used experimental technique was four wire alternating current (a.c.) impedance measurements at a frequency of 686 Hz (Kustov et al. 2012). The real part of the impedance (R) was measured by means of a lock-in amplifier, which provided high resolution measurements. The temperature range was from -190 °C to 120 °C and both martensite and austenite temperatures were determined with this second technique. The resistance test equipment was developed by Dr. Sergey Kustov (figure 4.2b) and it is located at the Material Science laboratory of the Department of Physics of UIB.

The measured values of transformation temperatures in the resistivity test reached the next: $M_f = -135\text{ °C}$, $M_s = -105\text{ °C}$, $A_s = 69\text{ °C}$, and $A_f = 74\text{ °C}$ (figure 4.5). A second thermal cycle was carried out, obtaining the same M_f and M_s temperatures, but different ones for the two others in the second cycle, $A_s = -45\text{ °C}$ and $A_f = -21\text{ °C}$. This was coincident with the reported wide thermal hysteresis of Ni-Ti-Nb for the first thermal cycle. The reduction of the thermal hysteresis in the second cycle was not detrimental for the envisaged application of this alloy in structural engineering, as once the SMA has been transported to the working place, installed and activated, the alloy will remain always in austenite, except for the case that

ambient temperatures decrease to $-100\text{ }^{\circ}\text{C}$, not a normal case for most outdoor civil engineering structures.

The measured phase transformation by the resistance tests (fig. 4.6) for the first cycle had a large thermal hysteresis ($\Delta_{s1} = M_s - A_s = 174\text{ }^{\circ}\text{C}$) but for the second cycle has a lower thermal hysteresis ($\Delta_{s2} = M_s - A_s = 60\text{ }^{\circ}\text{C}$).

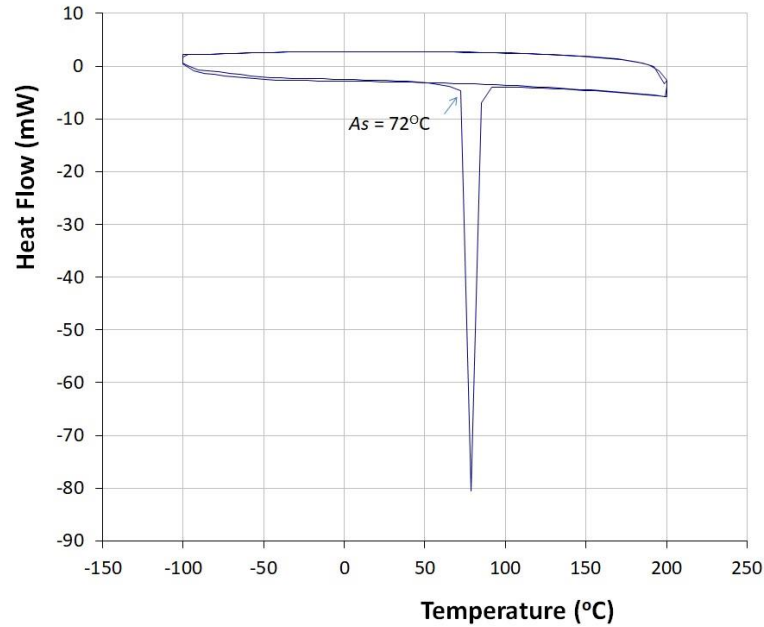


Figure 4.4. Differential Scanning Calorimetry (DSC) result of Ni-Ti-Nb test carried out

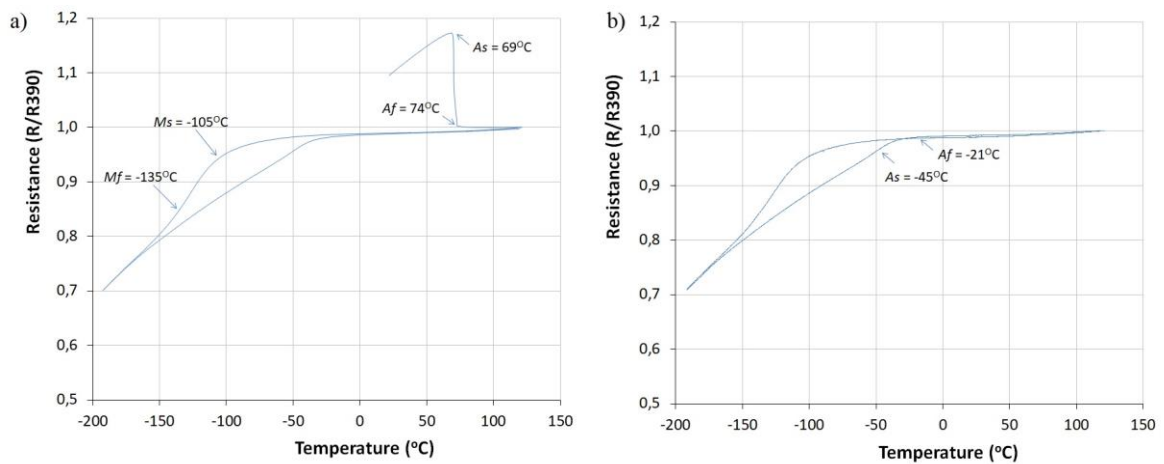


Figure 4.5. Temperature dependence of resistance for a Ni-Ti-Nb sample. Data are normalized to the value of resistance at $390\text{ }^{\circ}\text{K}$: a) first cycle, and b) second cycle

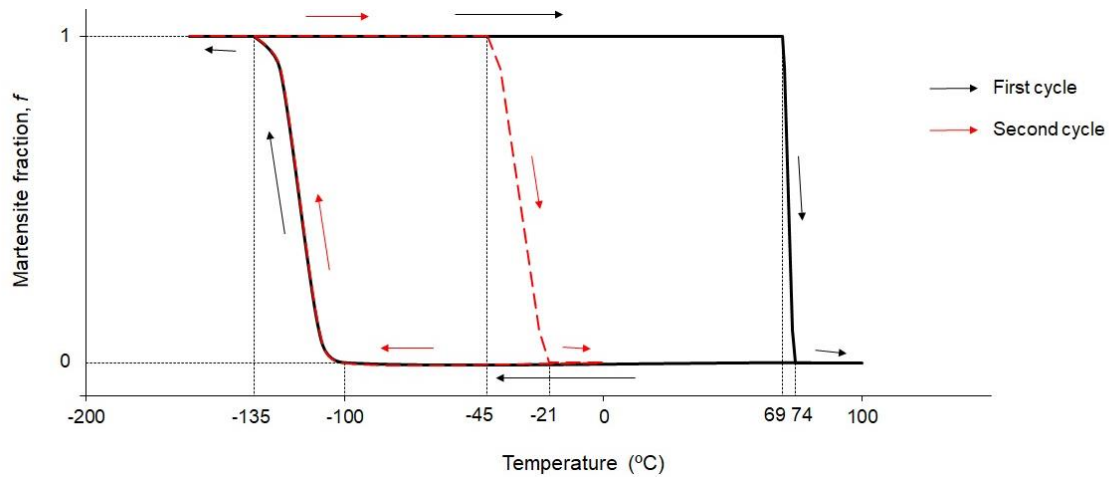


Figure 4.6. Martensite fraction-temperature graph of the two cycles of the tested Ni-Ti-Nb alloy samples from resistance tests

4.4 THERMO-MECHANICAL CHARACTERIZATION

4.4.1 TEST EQUIPMENT AND INSTRUMENTATION

The test equipment for the thermo-mechanical characterization was a Zwick Z100 load frame with thermal chamber located at the SCT laboratory of the UIB. The main equipment and instrumentation can be seen in figure 4.7.

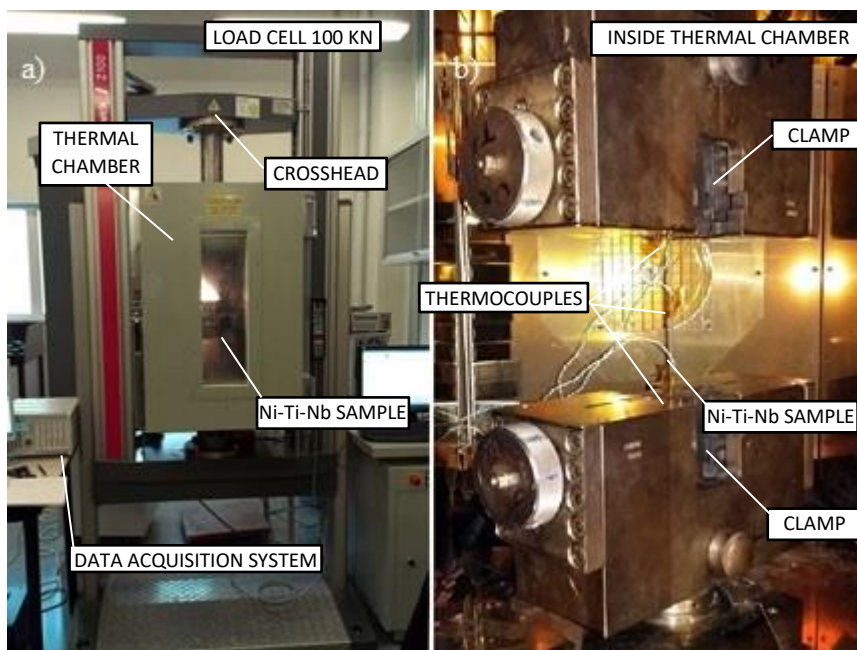


Figure 4.7. Experimental set-up for tensile tests: a) Load frame and b) inside view of thermal chamber

For the monitoring of the temperature during the tests, 3 or 5 thermocouples (type K) were used, uniformly distributed along the samples (figure 4.8a) and connected to a HBM data acquisition system (figure 4.8b) to verify that the target temperature was reached throughout the sample. The temperature in the air of the thermal chamber was monitored by its own control system. However, because of the high thermal inertia of the clamps due to their large mass (figure 4.7b), the air temperature and the sample temperatures differed during the tests. In fact, the temperature in the sample was not uniform until the clamps reached the air temperature, as will be seen in the test results. Hence, the thermal tests carried out in thermal chamber were done keeping constant the chamber temperature until the temperature in the sample, measured with the thermocouples, was practically uniform throughout the sample.

4.4.2 PLANNING OF THE TESTS

The experimental campaign was planned considering that the mechanical properties of the Ni-Ti-Nb wires depend on the alloy phase (martensite or austenite) and on the alloy temperature. The general planning of these tests can be seen in table 4.1. The first column of table 4.1 is the test number. The second one is the type of test carried out (named group of tests from 1 to 4) as 4 different tensile tests were carried out in the Zwick Z-100 load frame. The third column is the date when the test was carried out. The fourth to sixth columns indicate the initial phase of the sample, intermediate phase (if it exists depending on the type of test) and the final phase of the sample, respectively. As can be seen in the table 4.1 only group 4 starts from austenite with a previous treatment of a martensite sample. The seventh column is a short description of the type of test and the eighth column is the temperature of the sample during the test (if more than one temperature appears, they indicate the variation of temperatures during the whole test).

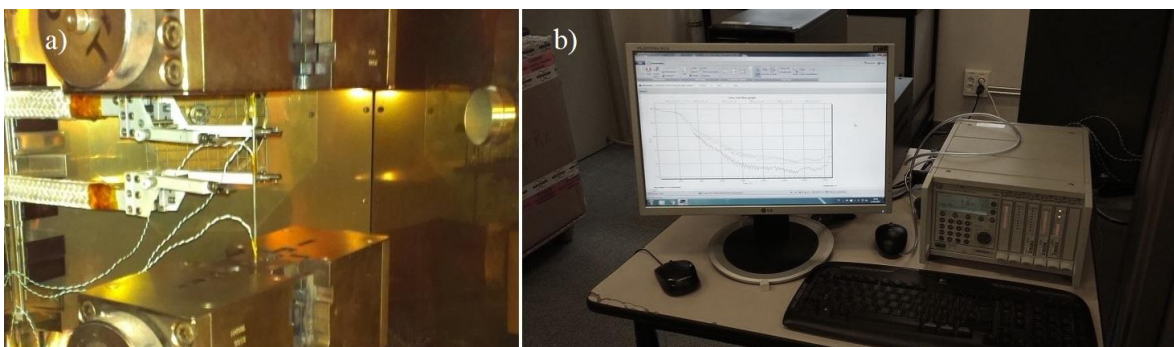


Figure 4.8 a) thermocouples along a sample and b) HBM data acquisition system for the thermocouples

The 4 groups of tests are:

- GROUP 1. OPTIMUM TEMPERATURE DETERMINATION (#1-#3): Recovery stress tests in constrained sample with different maximum temperatures (160 °C, 185 °C, and 200 °C). The objective of these tests was to determinate the recovery stresses for different maximum temperatures up to 200 °C. It is assumed that this temperature was sufficient for the phase transformation to have occurred in a significant percentage and it will be confirmed later. Higher temperatures were not tested to avoid damaging the concrete during the strengthening of the concrete beams. This action is called activation of the SMA sample.
- GROUP 2. MECHANICAL CHARACTERIZATION IN MARTENSITE PHASE (#4-#9 & #19): Tensile test at different temperatures. The objective of these tests was the determination of the stress-strain curve in tension up to failure in martensite phase. Monotonic and cyclic tests were performed. Test temperatures: 0 °C, room temperature (RT) about 20 °C, and 40 °C.
- GROUP 3. THERMO-MECHANICAL CHARACTERIZATION AFTER GENERATION OF RECOVERY STRESSES (#10-#15). Tests including the following actions: 1) Activation of the sample, and 2) tensile test at a prefixed temperature without releasing the recovery stresses generated during the activation. The objective of these tests was the determination of the stress-strain curve in tension up to failure after stress recovery. Monotonic and cyclic tests were performed. Tensile test temperatures: 0 °C, RT, and 40 °C.
- GROUP 4. MECHANICAL CHARACTERIZATION IN AUSTENITE PHASE (#16-#18 and #27-#35). These tests included the following actions: 1) Thermal test (heating up to phase change from martensite to austenite) without constraining the sample (free sample), and 2) tensile test at 0 °C, RT, and 40 °C. The objective of these tests was the determination of the stress-strain curve in tension up to failure, starting with the material in austenite and producing a phase change from austenite to martensite induced by stresses. Monotonic and cyclic tests were performed.

Table 4.1. List of main characteristics of planned tests of Ni-Ti-Nb wires

TEST N.	GROUP	DATE	INITIAL PHASE	INTERM. PHASE	FINAL PHASE	TYPE	TEMP. (°C)
1	1	17/12/2014	M	-	A	RECOVERY STRESS	RT-160-RT
2	1	17/12/2014	M	-	A	RECOVERY STRESS	RT-185-RT
3	1	18/12/2014	M	-	A	RECOVERY STRESS	RT-200-RT
4	2	10/12/2014	M	-	M	MONOTONIC	RT
5	2	11/12/2014	M	-	M	CYCLIC	RT
6	2	11/12/2014	M	-	M	MONOTONIC	40
7	2	11/12/2014	M	-	M	CYCLIC	40
8	2	17/12/2014	M	-	M	MONOTONIC	0
9	2	22/01/2015	M	-	M	CYCLIC	0
19	2	28/08/2015	M	-	M	CYCLIC ASTM2516	RT
10	3	16/02/2015	M	A	M	MONOTONIC FROM REC. STRESS	RT-200-RT-RT
11	3	13/04/2015	M	A	M	CYCLIC FROM REC. STRESS	RT-200-RT-RT
12	3	11/03/2015	M	A	M	MONOTONIC FROM REC. STRESS	RT-200-RT-40
13	3	26/03/2015	M	A	M	CYCLIC FROM REC. STRESS	RT-200-RT-40
14	3	17/02/2015	M	A	M	MONOTONIC FROM REC. STRESS	RT-200-RT-0
15	3	30/03/2015	M	A	M	CYCLIC FROM REC. STRESS	RT-200-RT-0
16	4	16/07/2015	A (M)	-	M	MONOTONIC	RT
17	4	28/08/2015	A (M)	-	M	ONE-CYCLE	RT
18	4	28/08/2015	A (M)	-	M	CYCLIC	RT
27	4	09/12/2016	A (M)	-	M	MONOTONIC	RT
28	4	09/12/2016	A (M)	-	M	ONE-CYCLE	RT
28a	4	21/12/2016	A (M)	-	M	ONE-CYCLE	RT
29	4	08/02/2017	A (M)	-	M	CYCLIC	RT
30	4	20/12/2016	A (M)	-	M	MONOTONIC	40
31	4	20/12/2016	A (M)	-	M	ONE-CYCLE	40
32	4	23/12/2016	A (M)	-	M	CYCLIC	40
32a	4	03/03/2017	A (M)	-	M	CYCLIC	40
33	4	11/01/2017	A (M)	-	M	MONOTONIC	0
34	4	11/01/2017	A (M)	-	M	ONE-CYCLE	0
35	4	27/02/2017	A (M)	-	M	CYCLIC	0

4.4.3 TEST PROCEDURE

A total length sample of 300 mm was used (figure 4.9): 150 mm between clamps plus 75 mm within each clamp. Different test procedures were performed depending on the test group: activation (heating), tensile test (monotonic or cyclic), or a combination of activation and tensile test (monotonic or cyclic).

ACTIVATION (RECOVERY STRESS TEST)

Once the sample was correctly placed and fixed with the clamps, thermocouples correctly located and protected with thermal tape, and the thermal chamber closed, the next step was to introduce a small prestress of 8 MPa, to ensure the correct installation of the sample. Afterwards, it was performed the activation of the sample by means of heating it, rising the temperature in the thermal chamber up to the target temperature to ensure the phase reverse transformation (from martensite to austenite). The displacement of the clamps was impeded, so the sample generated recovery stresses.

Three different activation tests were performed to study the generation of recovery stresses (160 °C, 185 °C, and 200 °C). Thus, once reverse transformation started, the sample tried to recover its initial shape (the wire had been previously prestrained up to 6 % by the manufacturer). As the movement of the clamps was prevented, recovery stresses developed. After several tests it was found that the heating of the samples in the thermal chamber had to be maintained up to 90 minutes and the cooling to room temperature (RT) up to 24 hours. As mentioned above, this procedure was monitored by means of different (3 or 5) thermocouples located along the sample.

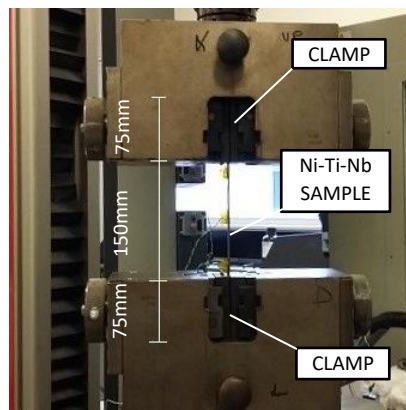


Figure 4.9. A Ni-Ti-Nb sample between clamps (150 mm tested sample and 75 mm within each clamp) ready to be tested

TENSILE TEST

The tensile tests started after the installation of the sample. A small prestress of 8 MPa was introduced to the sample to ensure its correct installation. The tensile tests were performed at different typical temperatures of civil structures' conditions: 0 °C, RT (about 20 °C), and 40 °C. These temperatures were kept constant inside the thermal chamber during 1 hour before starting the tensile test.

For a complete characterization three distinct types of tensile tests were performed:

- Monotonic: loading up to failure with a deformation speed of 7.5 mm/min.
- 1 cycle loading-unloading and load up to failure: a first load up to 6% strain, unload to initial prestress (8 MPa) and a second load up to failure in compliance with (ASTM-F2516-07 2007) Standard. Although this standard is intended for superelastic materials, it was followed only to verify whether the used SMA in austenite phase presented the superelastic behavior. This standardized test procedure limits the crosshead speed for the first cycle and for the second cycle with different values. For the first cycle, it is limited to a maximum of 0.01 mm/min per mm of length of sample between clamps, for a sample diameter higher than 2.5 mm. Consequently, for a 3 mm diameter and 150 mm length sample, there is a speed limit of 1.5 mm/min. Likewise, two tests with speeds of 3 mm/min and 1.5 mm/min were performed (tests #28 and #28a), showing almost identical results. Therefore, a speed limit of 3 mm/min was selected for these tensile tests. For the second cycle, the crosshead speed is limited to a value of 0.1 mm/min per mm of length of sample between clamps. Therefore, a maximum value of 15 mm/min may be selected. Anyway, a speed limit of 3 mm/min was selected for the two cycles.
- Cyclic with 2 % strain increment steps: different load and unload cycles of a 2% additional strain each load increment and unload to prestress (8 MPa). Deformation speed equal to 7.5 mm/min.

ACTIVATION AND TENSILE TEST

This test procedure consisted in performing an activation test (recovery stress test) followed by a tensile test, both previously defined. In this case, the activation of the sample was done

heating it up to a temperature of 200 °C, cooling it, and, afterwards, a tensile test without releasing the clamps was carried out (keeping the developed recovery stresses). The tensile tests were also performed at different temperatures: 0 °C, RT (≈ 20 °C), and 40 °C.

Two distinct types of tensile tests were performed: monotonic and cyclic.

- Monotonic: loading up to failure with a deformation speed of 7.5 mm/min.
- Cyclic: different load and unload cycles of 2% strain each load increment and unload to initial prestress (8 MPa) up to sample failure (deformation speed of 7.5 mm/min).

4.4.4 SUMMARY OF THE TEST RESULTS

The test results are summarized in table 4.2 and the complete results are presented in table 4.3. Note that the properties differ depending on the phase of the sample: austenite or martensite. The reported mechanical properties are the modulus of elasticity (E), yielding strength ($f_{y,0.002}$) and ultimate strength (f_u), ultimate strain (ϵ_u), recovery stresses (σ_R , in table 4.3) as well as martensite initial (σ^{Ms}) and final (σ^{Mf}) stresses of direct transformation.

The modulus of elasticity was computed as the slope of the stress-strain curve computed between 100 MPa and 350 MPa. The yielding strength was computed as the stress value that induce a remnant strain of 0.002 when unloading. The ultimate strength and strain were computed as the maximum reached stress and the strain in this maximum stress. The recovery stress was computed as the final value of stress recovery test. The martensite initial and final stresses were computed as the stress values at the inflection points of the stress-strain curve when stress induced martensite was produced.

Table 4.2. Summary of average thermo-mechanical properties of the Ni-Ti-Nb wires at RT

Property	Martensite	Austenite
E (GPa)	25	33
$f_{y,0.002}$ (MPa)	591	451
f_u (MPa)	1002	935
ϵ_u	0.37	0.55
σ^{Ms} (MPa)	-	494
σ^{Mf} (MPa)	-	543

Table 4.3. Summary of the Ni-Ti-Nb characterization test results

TEST	GROUP	PHASE	TYPE	TEMP. (°C)	σ_R (MPa)	E (MPa)	$f_{y,0.002}$ (MPa)	f_u (MPa)	ϵ_u
1	1	M	RECOVERY STRESS	RT-160-RT	356	-	-	-	0
2	1	M	RECOVERY STRESS	RT-185-RT	486	-	-	-	0
3	1	M	RECOVERY STRESS	RT-200-RT	585	-	-	-	0
4	2	M	MONOTONIC	RT	-	25012	591	1002	0.37
5	2	M	CYCLIC	RT	-	22311		996	0.31
6	2	M	MONOTONIC	40	-	22930	580	982	0.43
7	2	M	CYCLIC	40	-	23344		976	0.33
8	2	M	MONOTONIC	0	-	36618	599	1024	0.24
9	2	M	CYCLIC	0	-	25835		997	0.25
19	2	M	ONE-CYCLE	RT	-	18263	518	769	0.58
10	3	M	MONOTONIC FROM REC. STRESS	RT-200-RT-RT	569	25138	-	965	0.28
11	3	M	CYCLIC FROM REC. STRESS	RT-200-RT-RT	590	26712	-	1164	0.40
12	3	M	MONOTONIC FROM REC. STRESS	RT-200-RT-40	611	26164	-	971	0.32
13	3	M	CYCLIC FROM REC. STRESS	RT-200-RT-40	586	20980	-	959	0.36
14	3	M	MONOTONIC FROM REC. STRESS	RT-200-RT-0	550	22622	-	1013	0.38
15	3	M	CYCLIC FROM RECOVERY STRESS	RT-200-RT-0	518	10749	-	1010	0.33
16	4	A	MONOTONIC	RT	-	21205	417	860	0.55
17	4	A	ONE-CYCLE	RT	-	24650	376	795	0.79
18	4	A	CYCLIC	RT	-	36478	503	982	0.49
27	4	A	MONOTONIC	RT	-	43911	484	1010	*
28	4	A	ONE-CYCLE	RT	-	47941	483	991	*
28a	4	A	ONE-CYCLE	RT	-	45469	482	996	*
29	4	A	CYCLIC	RT	-	33980	479	957	*
30	4	A	MONOTONIC	40	-	50934	508	1040	*
31	4	A	ONE-CYCLE	40	-	48257	543	1006	*
32	4	A	CYCLIC	40	-	32673	521	777	*
32a	4	A	CYCLIC	40	-	38202	529	755	*
33	4	A	MONOTONIC	0	-	31685	423	980	*
34	4	A	ONE-CYCLE	0	-	35644	413	990	*
35	4	A	CYCLIC	0	-	25554	416	980	*

* No significant value obtained due to cross-head maximum span reached during test

4.4.5 RECOVERY STRESS-TEMPERATURE PHASE DIAGRAM

To determine the stress-temperature phase diagram it is necessary to determine the transformation temperatures (Section 4.3), to study the development of the recovery stresses (Group 1), and to obtain the martensite initial (σ^{Ms}) and final stresses (σ^{Mf}) of direct transformation (Tests #27, #30, and #33 of Group 4).

RECOVERY STRESSES. GROUP 1

The results of these tests showed different recovery stresses for the different target temperatures (160 °C, 185 °C, and 200 °C) as can be seen in figures 4.10 and 4.11.

The information of the exact sample temperature during the tests was obtained by the 5 thermocouples installed on the samples (figure 4.7). The main difficulty of these tests was to ensure a uniform temperature in the sample at maximum test temperature. As anticipated, the parts of the samples closest to the heavy clamps had a slower rising of the temperature than the middle parts of them (figure 4.12). This can be explained by thermo-inertial effects of the clamps mass. The same procedure was repeated for all recovery stress tests, but in subsequent ones, 3 thermocouples were used instead: one in the middle of the sample and two others at the ends.

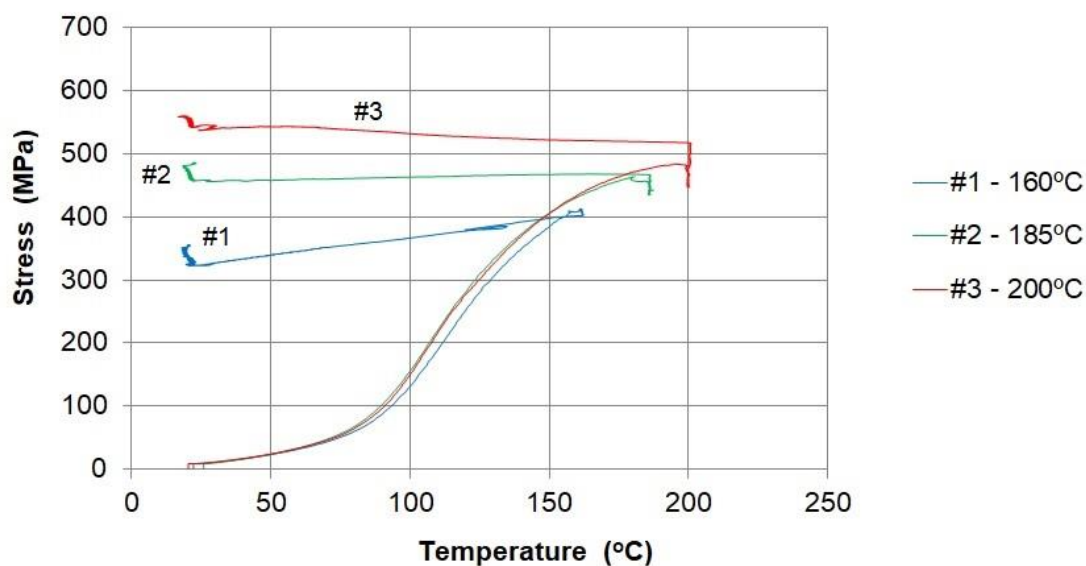


Figure 4.10. Recovery stress tests at different temperatures (stress-temperature curve)

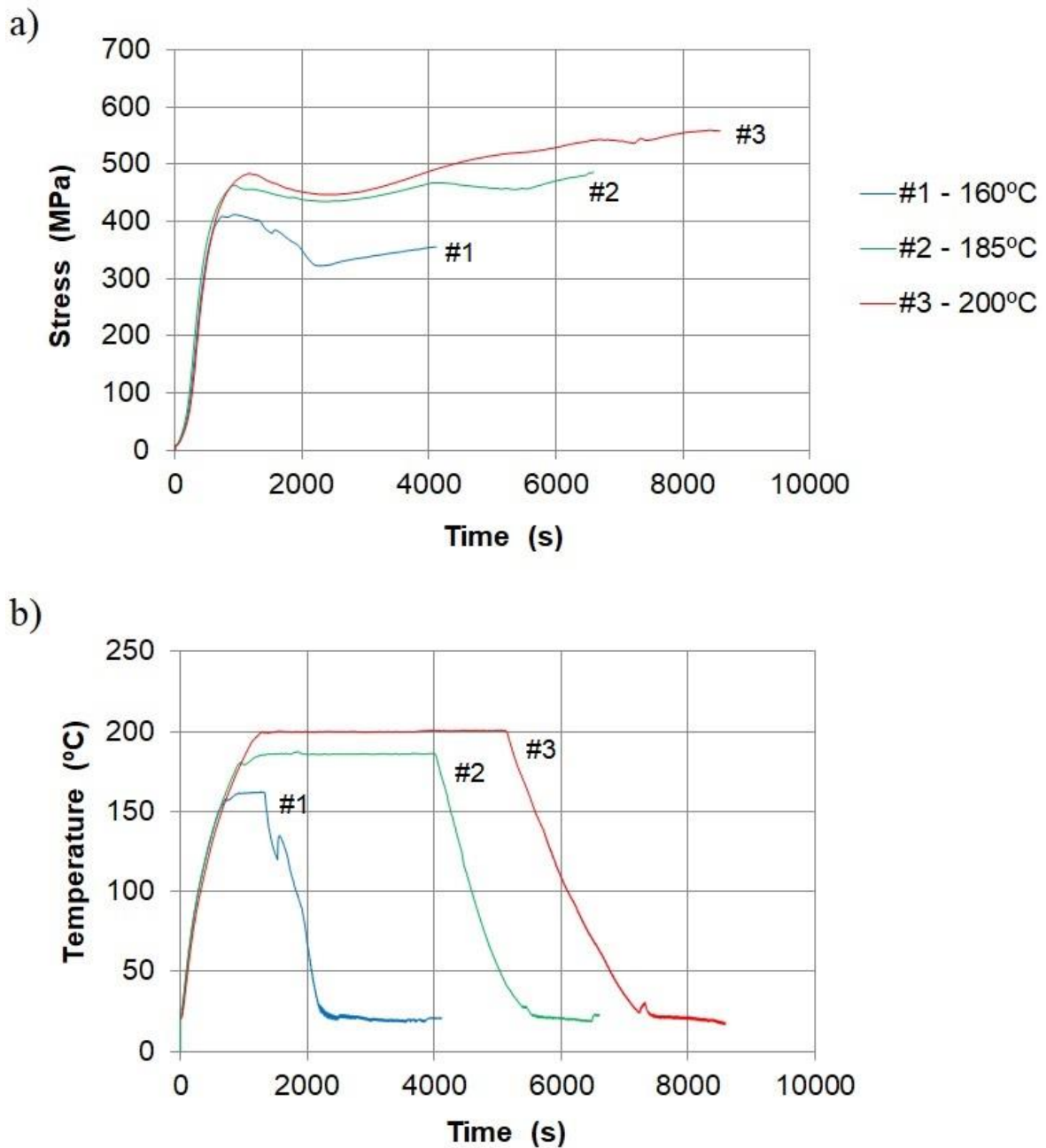


Figure 4.11. Recovery stress tests: a) Stress-time curve and b) temperature-time curve

The main conclusion of these three tests was that the higher temperature reached, up to 200 °C, the higher the recovery stresses obtained. No higher temperatures were tested to take into account that during the envisaged application the concrete of the beams should not be damaged. A maximum value of 584.6 MPa of recovery stress was obtained for an activation temperature of 200 °C, whilst lower values were obtained from lower activation temperatures (486.0 MPa for 185 °C and 356.0 MPa for 160 °C).

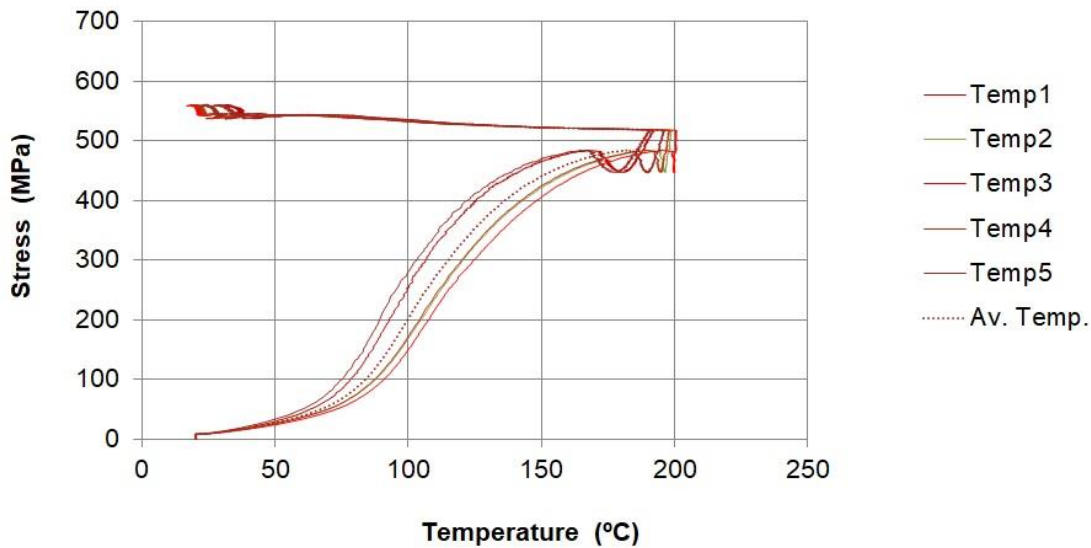


Figure 4.12. Recovery stress test #3 (5 points temperature logging uniformly distributed on the sample: temp1 upper part of the sample to temp5 lower part of it)

CHARACTERIZATION IN AUSTENITE PHASE. GROUP 4 (Tests #27, #30, and #33)

The austenite samples were obtained heating martensite samples as provided by the manufacturer with free deformation, but in this case the samples were heated by a heat gun. The activation method does not make any difference, provided that the predicted temperature was reached throughout the sample and it was verified by thermocouples.

The results of the tests #27, #30, and #33 will be used for the construction of the phase diagram, and they are presented here. The results of the tensile tests are depicted in figure 4.13. The rest of the tests of the Group 4 will be discussed later on this chapter.

The martensite initial (σ^{Ms}) and final stresses (σ^{Mf}) of direct transformation are shown in figure 4.13 for 0 °C, RT, and 40 °C.

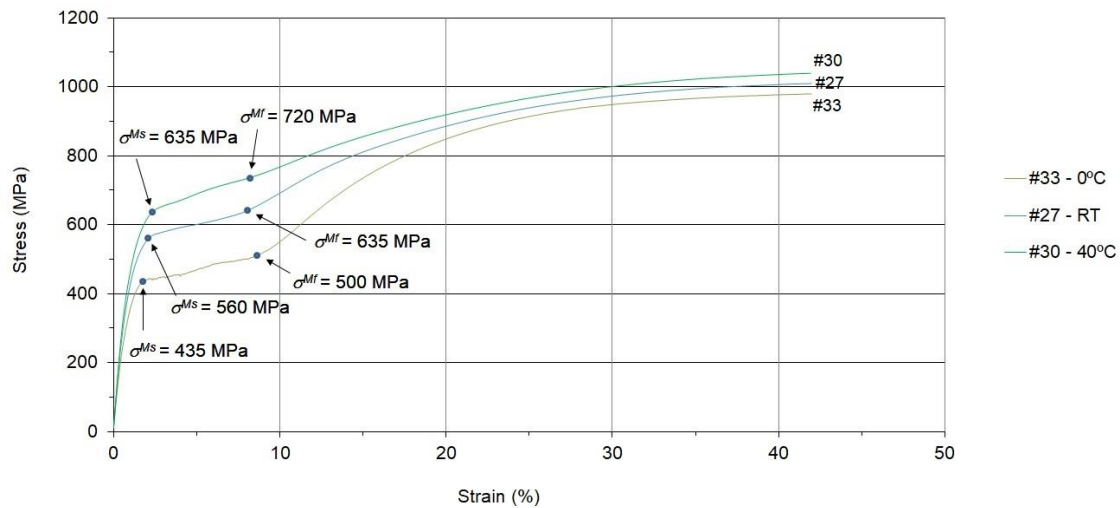


Figure 4.13. Monotonic tensile tests for austenite samples at different test temperatures

RECOVERY STRESS – TEMPERATURE PHASE DIAGRAM

Since the forward and reverse transformations occur over a range of temperatures (M_s to M_f , A_s to A_f) and the transformation temperatures strongly depend on the magnitude of the applied load (Lagoudas 2008), the transformation regions in a stress-temperature space can be constructed from data of different recovery stress tests and, data from the resistance or DSC tests carried out. The region of the martensite transformation is limited by the starting phase transformation (M_s) and the finishing phase transformation (M_f). From the tensile tests in austenite phase at different temperatures, different values of σ^{M_s} and σ^{M_f} were obtained. Thus, the slope of the region could be determined. The data of the tests used to approximate the transformation area can be seen in table 4.4.

A quite good agreement has been obtained for the region of martensite transformation of the available Ni-Ti-Nb, representing the phase transformation for this SMA. The slopes of the lines interpolated with the available data are: 4.39 MPa/°C for M_s and 4.05 MPa/°C for M_f . This relationship is depicted in figure 4.14. The relationships of stress-temperature for the austenite transformation of the Ni-Ti-Nb have, then, been adjusted by means of an average slope of 4.22 MPa/°C starting from the average values of A_s and A_f obtained from DSC and resistivity tests. They are depicted in figure 4.15. Furthermore, the recovery stress tests for different temperatures achieved are also shown in figure 4.15 and the recovery stress test at

200 °C seems to have achieved a complete transformation of the sample from martensite to austenite since the reverse transformation region ($A_s - A_f$) has been exceeded.

Table 4.4. Tests data for phase transformation regions of NI-Ti-Nb wires (stress-temperature)

Test	Temp (°C)	σ^{M_s} (MPa)	σ^{M_f} (MPa)
Resistance (M_f)	-135		0
Resistance (M_s)	-105	0	
#33	0	435	500
#27	20	560	635
#30	40	635	720

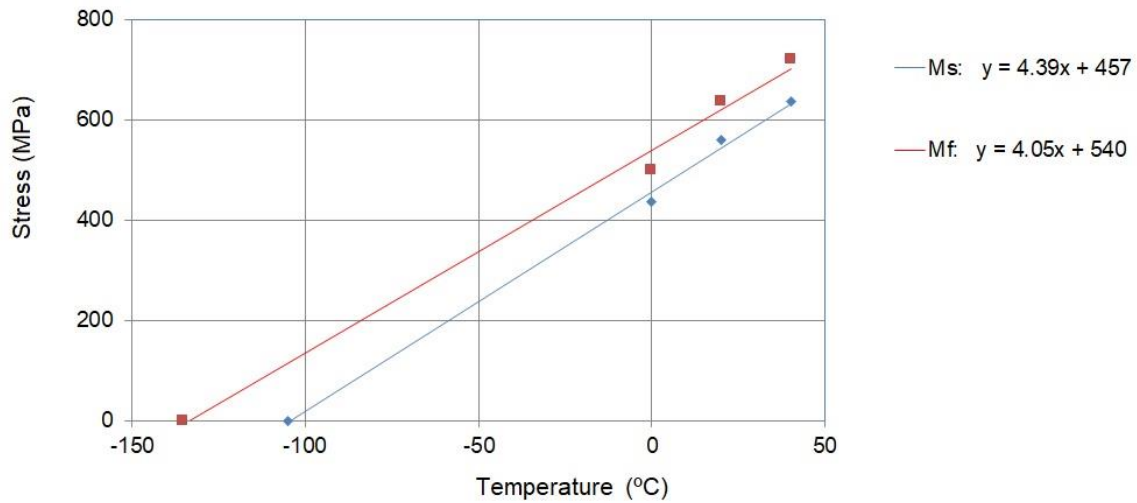


Figure 4.14. Adjusted diagram for phase transformation M_s and M_f

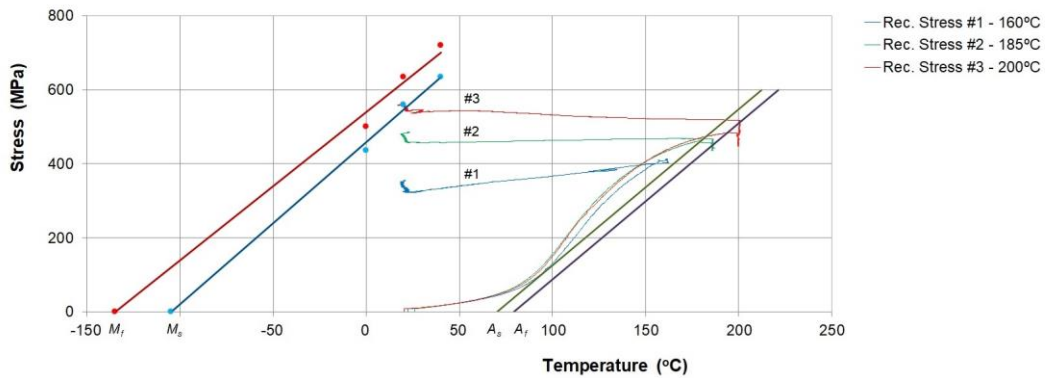


Figure 4.15. Calculated phase transformation diagram for Ni-Ti-Nb and recovery stress tests.

4.4.6 OTHER DETAILED RESULTS

CHARACTERIZATION IN MARTENSITE PHASE. GROUP 2

The mechanical characterization of the samples in martensite phase (as provided by the manufacturer) was performed by means of tensile tests at different temperatures, approximately covering the service temperatures of common civil engineering structures: 0 °C, RT, and 40 °C.

For the monotonic tensile tests, failure stresses up to around 1000 MPa were achieved. The behavior of the samples has two different stress-strain slopes. The first one, at the beginning of the tests, is the elastic one up to 5 – 6 % strain. After this elastic phase, there is a plateau with a non-significant increment of stresses, with strains up to 23 and 58 % at failure. These tests at different temperatures are depicted in figure 4.16. The lower the temperature the higher the elastic modulus, and both yielding and ultimate strengths are. This group includes a one cycle test (explained in section 4.4.3) that shows lower values of E and f_u but higher value of ε_u . This last test (one-cycle) was carried out with different deformation speed than previous ones. Actually, its deformation speed of 3 mm/min is clearly lower than others, 7.5 mm/min, and this would have had a significant influence in lowering the values involved. The properties values obtained from these tests are shown in table 4.5.

For the cyclic tensile tests, the values of f_u obtained as the maximum reached stress have shown less difference between them. In this case, the effect of the higher the temperature the lower the ultimate strength is less obvious, since the values are quite similar, even the modulus is higher in the sample at 40 °C than 20°C. The modulus of elasticity has been computed as the slope of the stress-strain curve computed between 100 MPa and 350 MPa in the first loading cycle. The stress-strain graphs are depicted in figure 4.17. The values are shown in table 4.6.

As can be seen in figure 4.17 one additional effect related to cyclic loading and unloading can be highlighted. The slope of loading and unloading branches (in stress-strain graph) decreases during the test. Thus, at the first stages of the tests these slopes are almost like the one found in the monotonic test, but in the last stages the slope has decreased significantly.

For example, at test #7, the modulus decreases to a value of about 15 GPa in the last cycle while it was about 23 GPa in the first cycle.

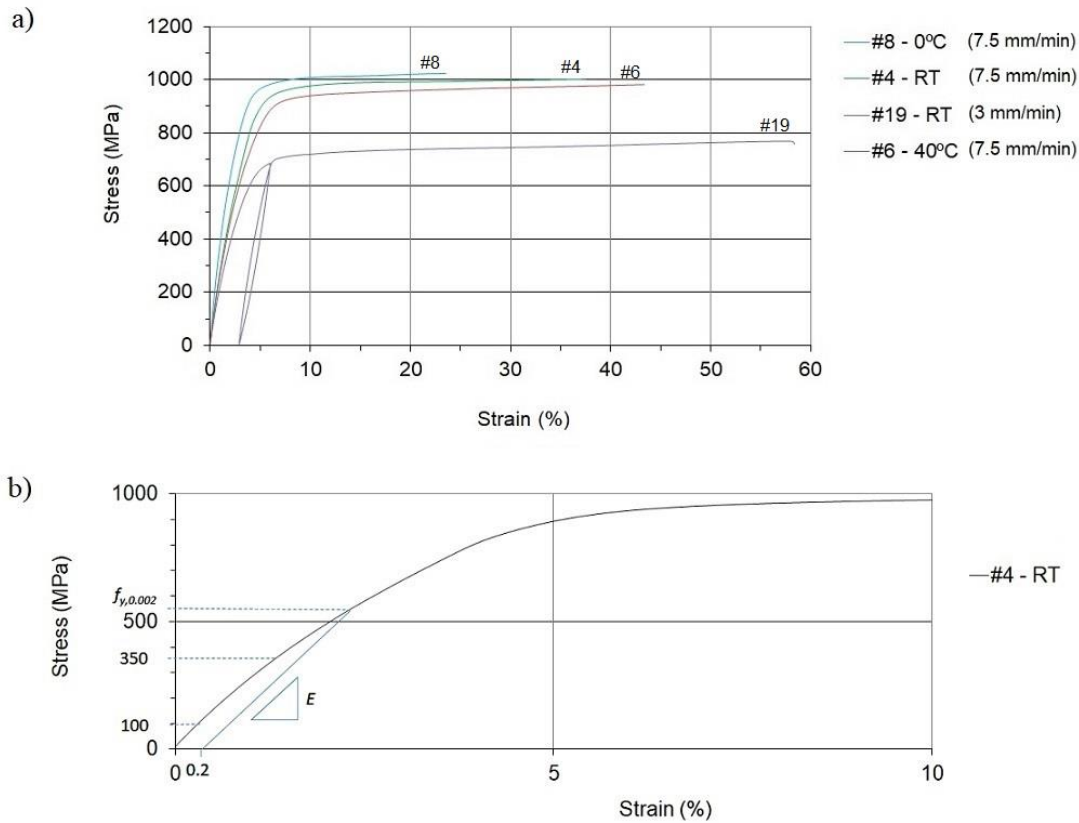


Figure 4.16. a) Monotonic tensile tests of Ni-Ti-Nb wires in martensite phase. b) Schematic graph of determination of elastic modulus (E) and yield strength ($f_{y,0.002}$) for test #4 at RT (strain depicted up to 10 %).

Table 4.5. Properties of Ni-Ti-Nb wires in monotonic tensile tests

Sample #	Def. speed (mm/min)	Test temp. (°C)	E (MPa)	$f_{y,0.002}$ (MPa)	f_u (MPa)	ϵ_u (%)
8	7.5	0	36618	659	1024	24
4	7.5	RT (20)	25012	550	1002	37
6	7.5	40	22930	600	982	43
19	3	RT (20)	18263	400	769	58

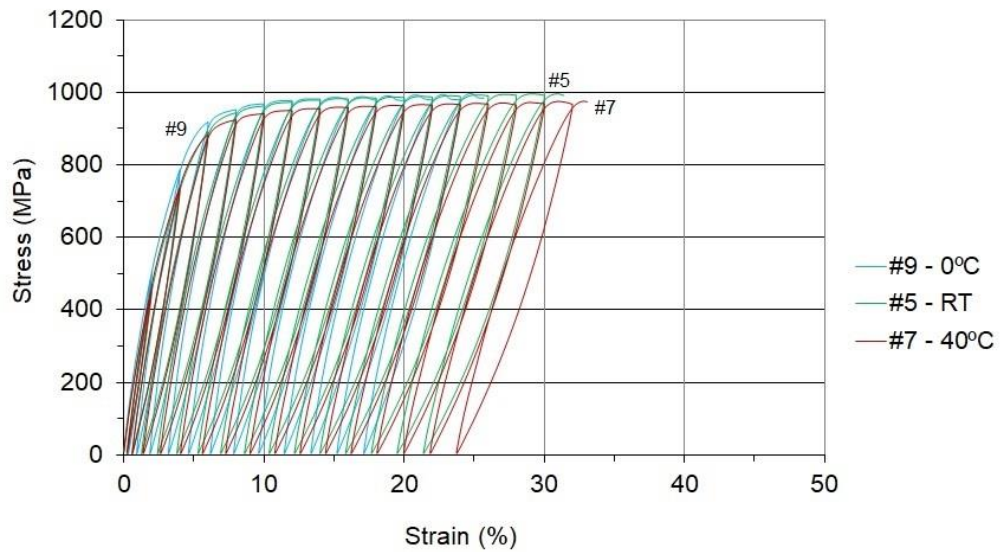


Figure 4.17. Cyclic tensile tests of Ni-Ti-Nb wires in martensite phase

Table 4.6. Properties of Ni-Ti-Nb wires in cyclic tensile tests in martensite phase

Sample #	Test temp. (°C)	E (MPa)	f_u (MPa)	ϵ_u (%)
9	0	25834	997	25
5	RT (20)	22311	996	31
7	40	23344	976	33

CHARACTERIZATION AFTER GENERATION OF RECOVERY STRESSES. GROUP 3

The mechanical characterization of the samples in austenite phase after activating the samples with prevented deformation (recovery stresses test) was achieved by means of tensile tests at different temperatures. The recovery stress values of the samples at the end of the previous recovery stress test are shown in table 4.7.

Note that the recovery stress test starts rising the temperature up to 200 °C, maintaining it between 3000 and 5000 seconds, and cooling down to RT during around 24 hours. If any additional change of temperature had to be done (RT to 40 °C or RT to 0 °C), the temperature was changed around 2 hours before the tensile test.

Immediately after the previous heat treatment (recovery stress test) on the samples #10, #12 and #14, and without releasing the stresses, monotonic tensile tests up to failure were carried out, as depicted in figure 4.18 which show stress-strain and stress-time graphs of the tests. The failure stresses were up to 1000 MPa, and even higher for test at 0 °C, and the samples developed strains between 28 and 38 %. The main results are shown in table 4.8.

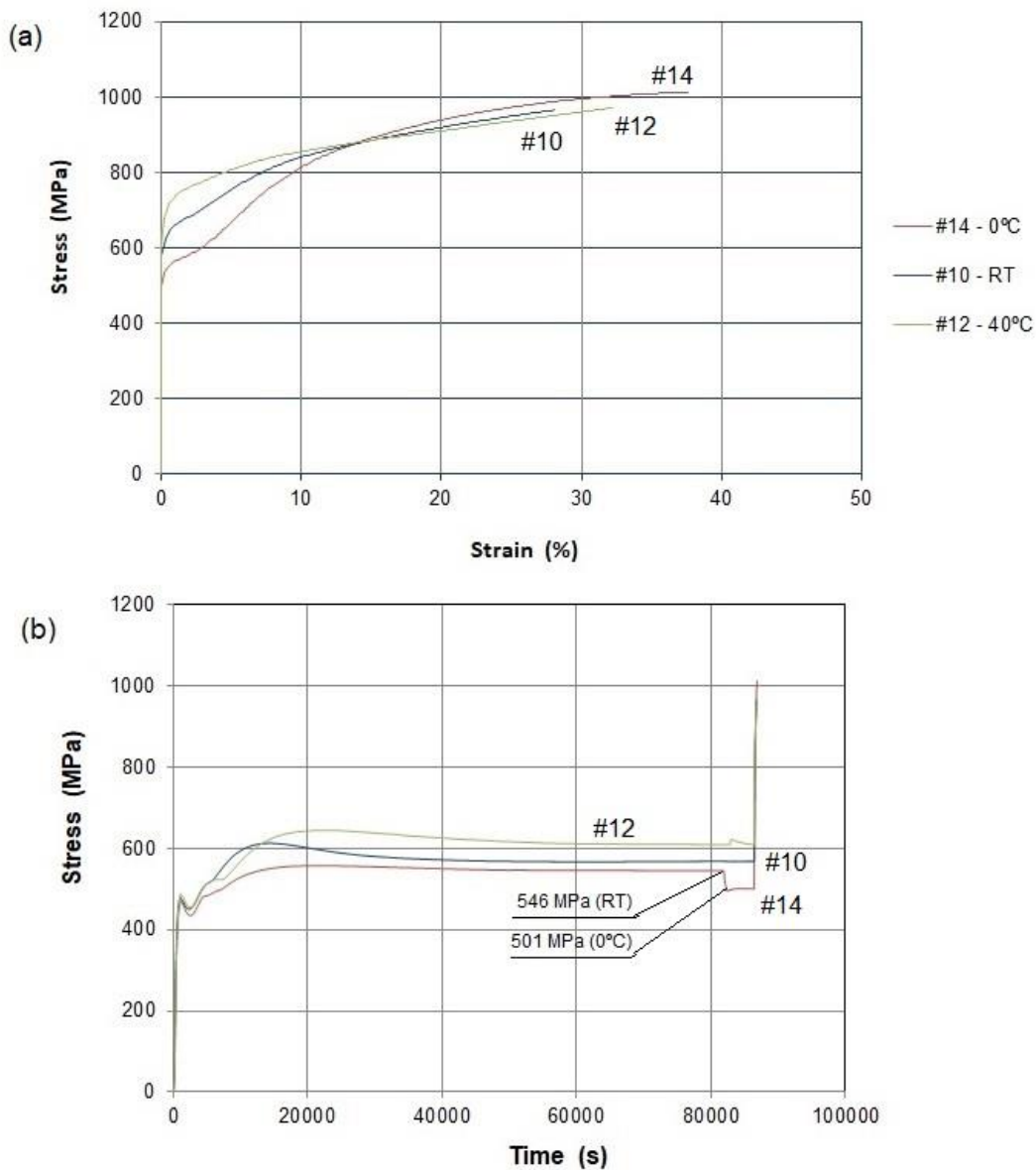


Figure 4.18. Monotonic tensile tests at different temperatures carried out immediately after recovery stresses generation: a) stress-strain graph and b) Stress-time graph. Note stress drop during cooling down to 0 °C on sample #14

Table 4.7. Final recovery stresses values on the samples in the previous recovery stress test

Sample #	Recovery stresses (MPa)	Temperature at measured recovery stresses (°C)
10	569	RT
11	590	RT
12	611	40
13	690	40
14	501	0
15	517	0
Average	580	-

Table 4.8. Properties of Ni-Ti-Nb wires in monotonic tensile tests after recovery stresses generation

Sample #	Test temperature (°C)	E (MPa)	f_u (MPa)	ϵ_u (%)
14	0	22622	1013	38
10	RT (20)	25138	965	28
12	40	26163	971	32

As depicted in figure 4.18b, whilst cooling down the confined sample from RT to 0 °C, the recovery stress dropped from 546 MPa to 501 MPa. This behavior could be explained as a coupling effect between the change of modulus of elasticity with the temperature (the higher the temperature, the higher the modulus of elasticity), the thermal contraction/dilation of the sample and the clamps, and, very important, the crossing of the M_s temperature line under stress (figure 4.19). A minor increase in the recovery stress when the sample was heated to 40 °C can also be seen in figures 4.18 and 4.19, in this case due to the two previous described effects (thermal contraction and crossing of M_s temperature line under stress).

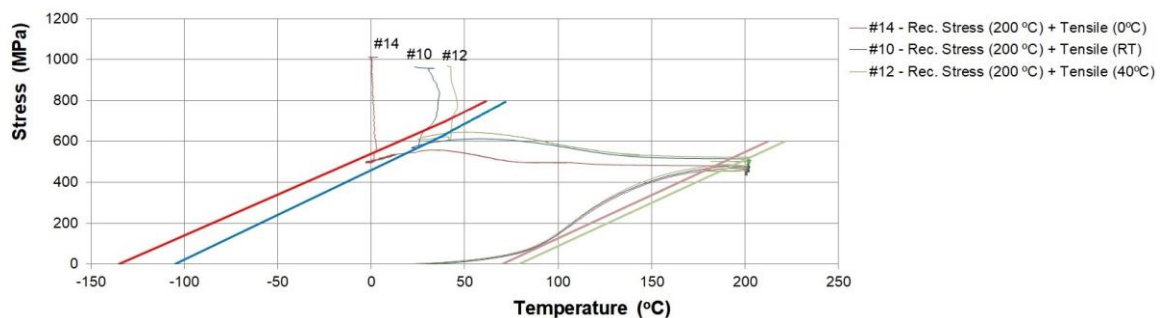


Figure 4.19. Stress-time graph of monotonic tensile tests at different temperatures carried out immediately after recovery stresses generation and calculated phase transformation diagram for Ni-Ti-Nb

The modulus of elasticity (E) was computed in a different way in these tensile tests after recovery stresses since the reached stresses were significantly higher than 350 MPa at the starting point of loading. Also, as can be seen in figure 4.18, the slope of the stress-strain curve is very sensitive to the loading from the very first stages of load. Therefore, a new criterion was adopted: the slope of the stress-strain curve was computed from the first stages of load with a stress increment range between 10 and 50 MPa and a strain increment between 0.1 and 0.3 %. Note that the modulus of elasticity for tests in group 2 (table 4.5) decreased when the test temperature was increased. However, after the recovery stress generation, the modulus of elasticity experienced the opposite behavior (table 4.8). This very complex behavior is due to the different fraction of martensite and austenite phases after the recovery stress test, and it is depending on the temperature (the location of the stress-temperature point in figure 4.15).

As it was done for the characterization of the samples in the original phase (martensite) the same cyclic tests were carried out for the samples after the recovery stress tests. The results of the tests are shown in table 4.9 and figure 4.20.

As can be seen in figure 4.21, whilst cooling down the confined sample from RT to 0 °C, the recovery stress dropped from 595 MPa to 517 MPa. However, when the temperature was raised to 40 °C, the recovery stress increased from 586 MPa until 691 MPa. This behavior could be explained, as before, as a coupling effect between the change of modulus of elasticity with the temperature (the higher the temperature, the higher the modulus of elasticity), the thermal contraction/dilation of the sample and the clamps, and the distinct martensite/austenite fraction depending on the temperature.

Table 4.9. Properties of Ni-Ti-Nb wires in cyclic tensile tests after recovery stresses generation

Sample #	Test temperature (°C)	E (MPa)	f_u (MPa)	ε_u (%)
15	0	10749	1010	33
11	20	26712	1161	39
13	40	20980	959	35

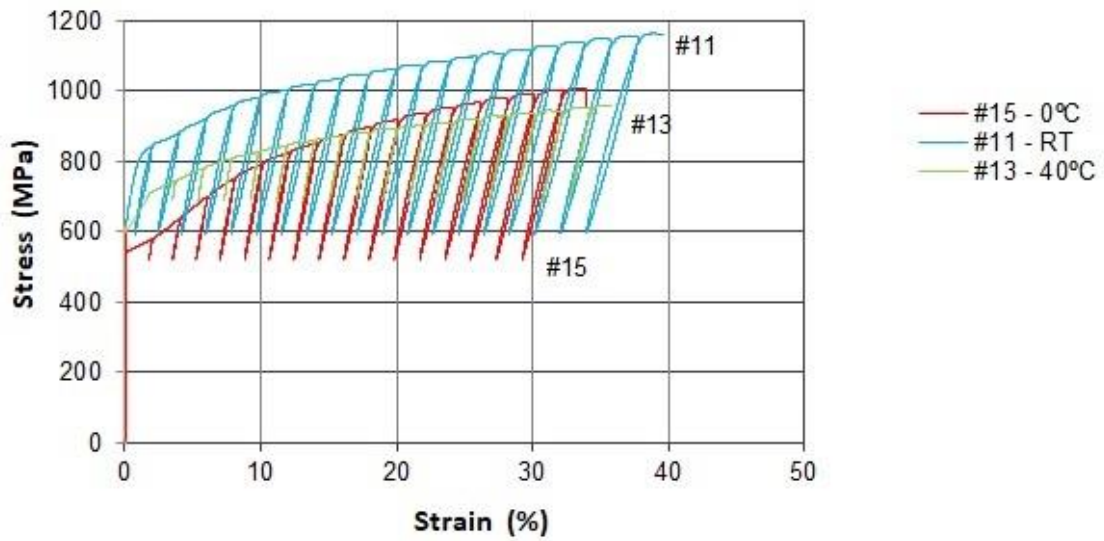


Figure 4.20. Cyclic tensile tests after recovery stresses generation

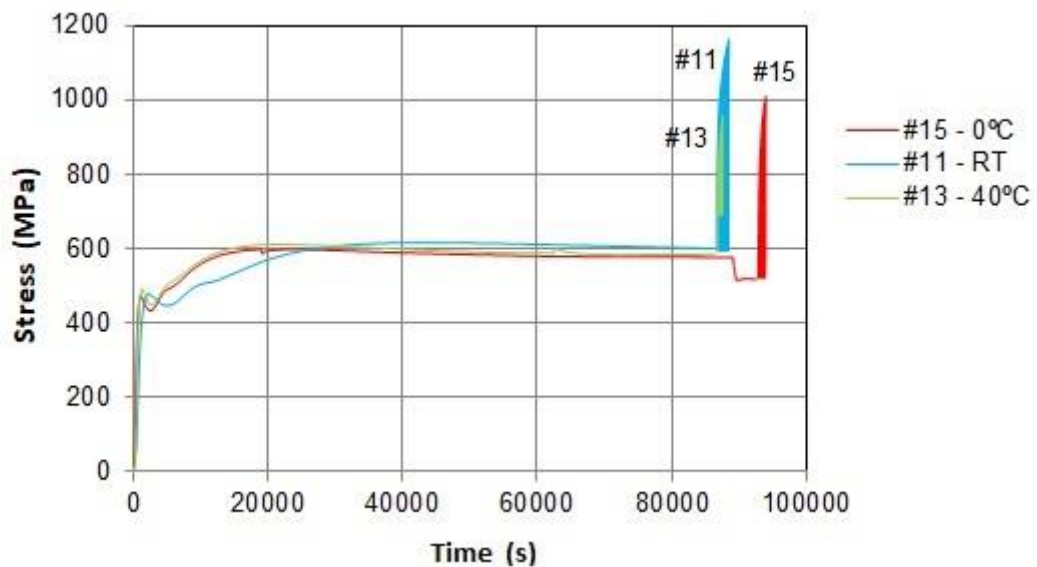


Figure 4.21. Stress-time graph of cyclic tensile tests with previous heat treatment tests. Note stress drop during cooling down to 0 °C on sample #15 and stress increment during heating to 40 °C on sample #13

CHARACTERIZATION IN AUSTENITE PHASE. GROUP 4

At first, three tensile tests were performed after heating the samples, under free shape recovery. This meant that no stresses developed in the previous heat treatment and recovery strains developed. The manufacturer declared an initial prestrain of 6 %. Table 4.10 shows

the recovery strains measured in three different samples, being the average of the recovery strain equal to 6 %.

For these samples a different behavior was expected and σ^{Ms} and σ^{Mf} could be obtained. As for the tensile tests in group 2, a monotonic tensile test (figure 4.22), one-cycle test (figure 4.22), and cyclic tests (figure 4.23) were carried out. The results are shown in table 4.11.

Table 4.10. Recovery strains on the samples with the previous treatment

Sample #	Recovery strains (mm - %)
16	17 - 5.7
17	18 - 6.0
18	19 - 6.3

Table 4.11. Properties of austenite samples (stress free) in monotonic and cyclic tensile tests

Sample #	Type	Def. speed (mm/min)	E (MPa)	ϵ_u (%)	$f_{y,0.002}$ (MPa)	f_u (MPa)	σ^{Ms} (MPa)	σ^{Mf} (MPa)
16	Monotonic	7.5	21205	55	417	860	427	450
17	One cycle	3	24650	79	376	795	360	380
18	Cyclic	7.5	36478	49	503	982	-	-

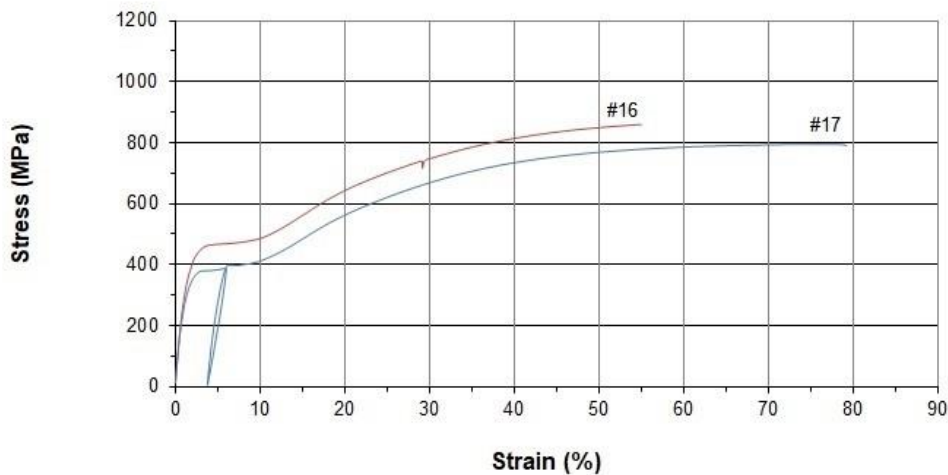


Figure 4.22. Monotonic tensile test of the austenite sample #16 and one-cycle tensile test of the austenite sample #17 obtained by heating a martensite sample (strain free).

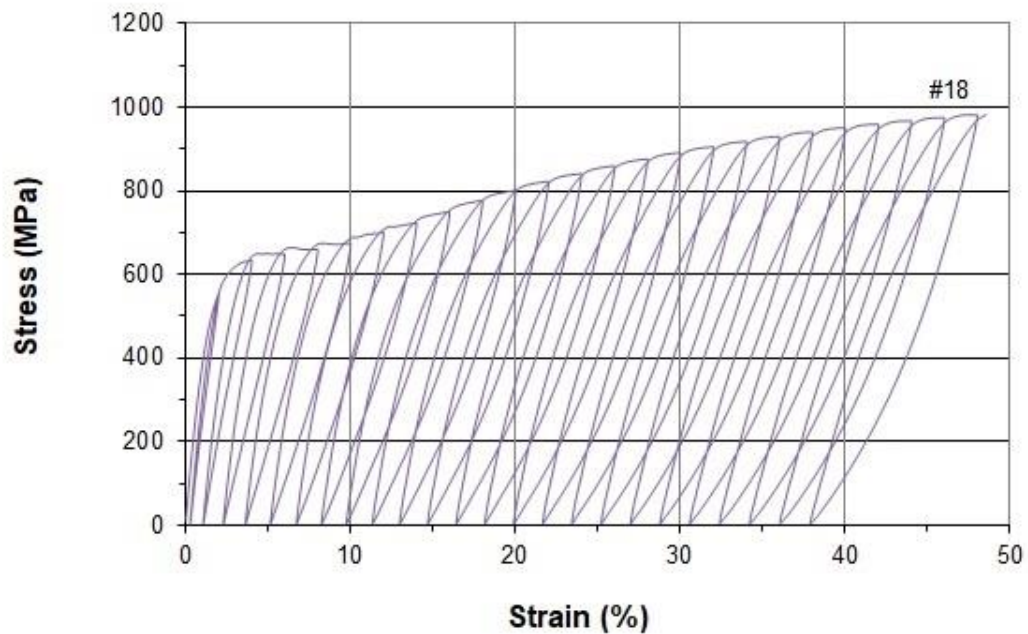


Figure 4.23. Cyclic tensile test of the austenite sample #18 obtained by heating a martensite sample (strain free).

Some more tensile tests were carried out at different temperatures (0 °C, RT, and 40°C). Monotonic, one cycle and cyclic tests were also carried out. The austenite samples were obtained heating martensite samples as provided by the manufacturer with free deformation, but in this case the samples were heated by means of a heat gun. The activation method, provided that the predicted temperature was reached throughout the sample which was checked by thermocouples, did not make any difference. The main conclusions of this group of tests are values of up to $f_u = 1000$ MPa of ultimate strength were obtained and an initial modulus of elasticity of about $E = 40$ GPa. The results of the tensile tests are depicted in figures 4.24, 4.25 and 4.26. The results presented in figure 4.24 were already presented (figure 4.13) for the construction of the stress-temperature phase diagram, but they are repeated here for clarity. From the one-cyclic tensile tests (figure 4.25) it can be seen that the alloy does not present pseudo-elastic properties when unloaded at a tensile stress between σ^{Ms} and σ^{Mf} .

As can be seen in these figures the effect of martensite phase transformation induced by stress is shown in all graphics by means of a plateau with lower increment of stresses and large increment of strains between two values of stress: martensite start (σ^{Ms}) and martensite

finish (σ^{Mf}). The values of these stresses, elastic limit (f_e) and ultimate strength (f_u) are shown in table 4.12.

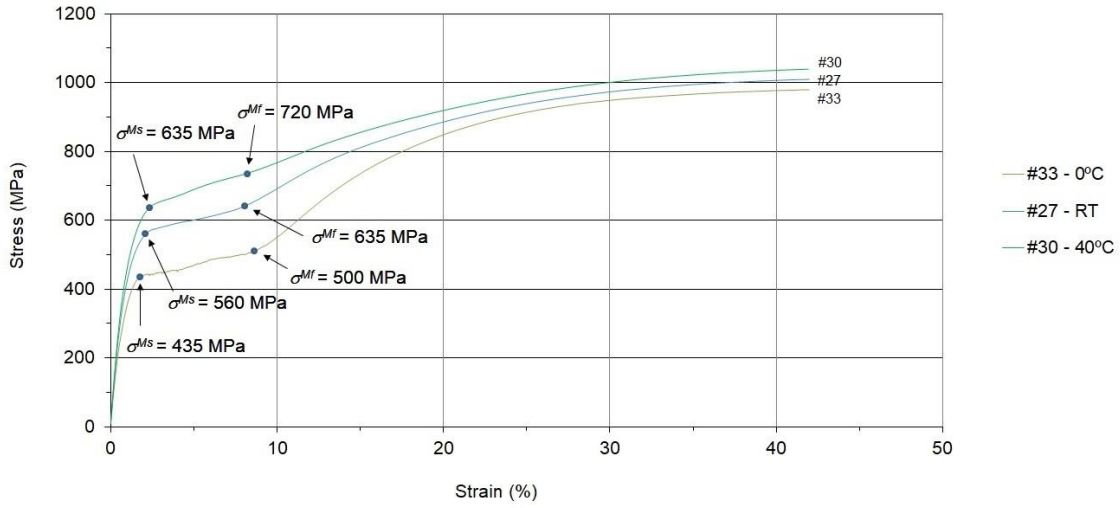


Figure 4.24. Monotonic tensile tests for austenite samples at different test temperatures

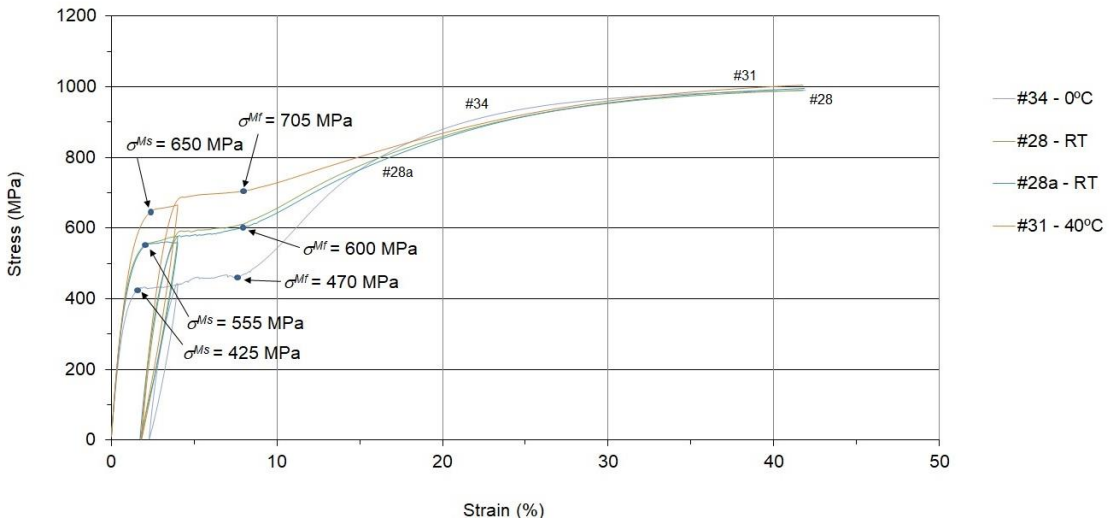


Figure 4.25. One cycle tensile tests for austenite samples at different test temperatures

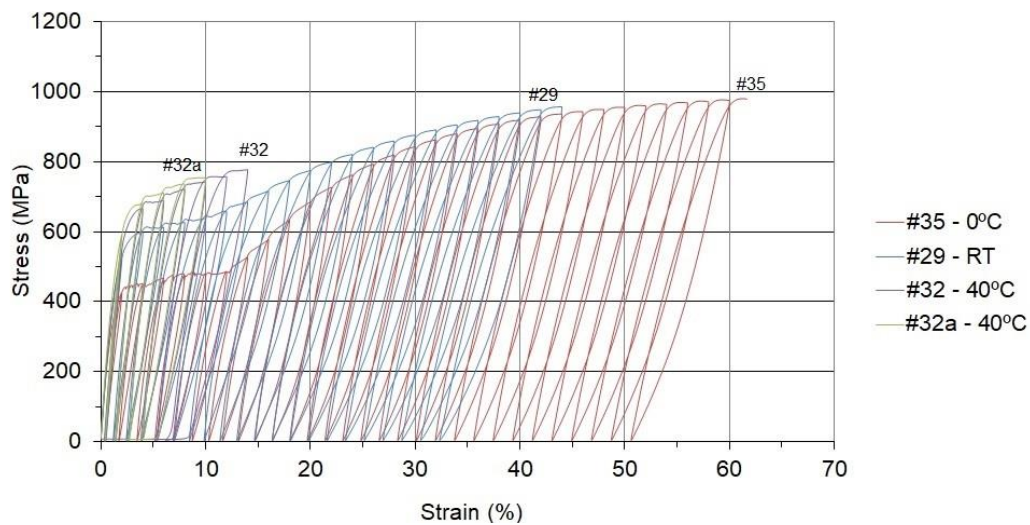


Figure 4.26. Cyclic tensile tests for austenite samples at different test temperatures

Table 4.12. Mechanical properties of austenite samples in monotonic and cyclic tensile tests

Sample #	Type	Temperature (°C)	E (GPa)	$f_{y,0.002}$ (MPa)	σ^{Ms} (MPa)	σ^{Mf} (MPa)	f_u (MPa)
33	Monotonic	0	32	423	435	485	980
34	One cycle	0	36	413	425	470	990
35	Cyclic	0	26	416	440	485	980
27	Monotonic	RT	44	484	560	635	1010
28	One cycle	RT	48	483	555	600	991
28a	One cycle	RT	45	482	555	605	996
29	Cyclic	RT	34	479	580	640	957
30	Monotonic	40	51	508	635	720	1039
31	One cycle	40	48	543	650	705	1006
32	Cyclic	40	33	521	650	720	-
32a	Cyclic	40	38	529	650	-	-

From the tests carried out, it can be stated that, related to the stress plateau, the higher the test temperature, the higher the values of stresses of martensite start and martensite finish. Thus, at a test temperature of 0 °C the plateau takes place at values of around 400 MPa, while at test temperature of 40 °C it takes place at values of around 600 MPa.

The test #28 was carried out at a deformation speed of 1.5 mm/min and the test #28a at a speed of 3 mm/min to assess practical applicability of ASTM2516 standard as commented in Section 4.4.3 (one cycle tests). The tests carried out show almost identical results, so all one cycle tests were carried out at 3 mm/min speed.

The sample in the cyclic test #32 carried out at 40 °C failed due to buckling when unloading it after reaching 12 % strain. The test was repeated with the same result. The reason could not be determined, hence more research would be needed.

4.5 CONCLUSIONS ON Ni-Ti-Nb CHARACTERIZATION

With regard to the characterization of the supplied SMA (3 mm diameter wires of Ni-Ti-Nb), proper results have been attained. Basic physical properties have been determined and material thermo-mechanical characterization has been performed by means of different laboratory tests planned with an active experimental campaign. This was updated during the planned tests, taking into account the results and interpretation of earlier tests. The main conclusions were:

- The composition of the material supplied resulted in Ti atw.45.81 %, Ni atw.45.76 % and Nb atw.8.43 %.
- The transformation temperatures have been determined from DSC and resistivity tests. The average obtained values were: $A_s = 70.5$ °C, $A_f = 79.5$ °C, $M_s = -105$ °C and $M_f = -135$ °C. Therefore, a hysteretic behavior ($A_s - M_s$) of 175.5 °C has been obtained for the first cycle.
- Values between 500 – 700 MPa of recovery stresses have been reached in optimal laboratory conditions (minimum value of 501 MPa, maximum of 690 MPa and average of 580 MPa). These values are comparable to the values of the yield strength of the conventional steel used in reinforced concrete structures.
- A stress-temperature phase diagram for the Ni-Ti-Nb samples has been adjusted. Moreover, when looking at the recovery stress tests, it has been observed that the test carried out at a maximum temperature of 200 °C suffices for a practical complete phase transformation to austenite.
- Values of 1002 MPa for ultimate strength, 591 MPa for yield strength, and 25 GPa for modulus of elasticity have been obtained for martensite SMA at RT. For austenite SMA at RT, values of 935 MPa for ultimate strength, 451 MPa for yield strength, and 33 GPa for modulus of elasticity have been found. Stresses for start (σ^{M_s}) and

finish (σ^{Mf}) direct transformation of 494 MPa and 543 MPa have been obtained, respectively.

- The ultimate strains obtained in the tensile tests were very high for Ni-Ti-Nb (30-50%). These values are not reached in steel that is usually used as reinforcement in RC structures
- Characterization tests have been carried out at different test temperatures: 0 °C, room temperature (RT, about 20 °C) and 40 °C, to cover the typical range of temperatures for civil engineering structures. Slightly different behavior has been observed when test temperatures vary between this range. In addition, the tests were carried out applying different load conditions: monotonic and cyclic tests. Similar values in terms of ultimate strength and elastic modulus have been obtained when comparing monotonic and cyclic tests.
- Additional tests with monotonic and cyclic loads after activation have also been carried out to consider practical performance conditions for real post-stressing structures with Ni-Ti-Nb wires. Values of 965 MPa for ultimate strength and 25 GPa for modulus of elasticity have been obtained after activation (austenite) with recovery stresses of more than 569 MPa at RT test.

The supplied Ni-Ti-Nb SMA is an adequate material for structural strengthening applications. For active strengthening, it can be used with recovery (active confinement) stresses but once converted to austenite, it has been observed that there is no more pseudo-elastic behavior.

Finally, from a functional point of view, the cost of Ni-Ti-Nb is very high, but recent research on iron-based shape memory alloys envisages the application of cheaper shape memory alloys with similar behavior. Nonetheless, an advantage of the Ni-Ti-Nb wires should be highlighted: the tested Ni-Ti-Nb wires have a wide range of available strain to be recovered under ‘activation’ process (up to 6%) while other SMA materials have a narrow range. Despite the high cost of Ni-Ti-Nb, the amount of material needed is small and needs to be placed only in critical regions of the beams meaning this application promises to be a very interesting technology for strengthening key civil infrastructures.

5. EXPERIMENTAL CAMPAIGN ON ACTIVE SHEAR STRENGTHENING OF RC BEAMS USING Ni-Ti-Nb WIRES

5.1 OBJECTIVE OF THE EXPERIMENTAL CAMPAIGN

The main objective of the experimental campaign is the validation of a new active shear external strengthening technology for RC beams by means of Ni-Ti-Nb SMA wires. The activation of the Ni-Ti-Nb alloy is produced by heating the wires, generating tensile recovery stresses in the wires and confining/prestressing forces on the RC beams.

The experimental campaign was developed into two different phases of tests. The first one, composed of 12 tests in 10 beams, was planned to verify the feasibility of active shear strengthening of RC beams by means of Ni-Ti-Nb external spirals, with different pitch and different pre-testing conditions (without pre-load, pre-load up to the appearance of the shear cracking, or pre-load up to beam collapse). With the main results of the first phase of tests, the second one, with 10 more tests in 10 different beams, was planned with other different types of shear strengthening (vertical stirrups or compression chord strengthening) and other spiral variants (with grooves to try to improve the contact between the longitudinal reinforcement and the external strengthening spirals). This configuration was tested to study the possible increase in the dowel effect transfer action.

5.2 DESIGN OF THE TEST SPECIMENS

In real engineering practice, the objective of strengthening a RC beam in shear would be to avoid the shear failure, forcing the shear strength to be higher than the flexural strength and, consequently, inducing a more ductile flexural failure. However, to be able to quantify the shear strengthening effect with the proposed technology, the objective in this experimental campaign was to raise the shear strength but without reaching the flexural strength.

Twenty small scale RC beam specimens were produced, all with the same geometry and longitudinal reinforcement. A rectangular cross-section of 80-mm wide (b), and 150-mm deep (h), is shown in figure 5.1. The total length of the beam specimens was 900 mm and the tests were carried out by loading the beams at a central point, testing both sides identically and at the same time. The longitudinal reinforcement was calculated to ensure enough bending strength to trigger shear failure and it was composed of one $\phi 16$ mm steel rebar ($A_s = 201 \text{ mm}^2$) in beam. To achieve good anchorage conditions in such small beam specimens, both ends of the bars were welded to a plate. The beams were not internally shear reinforced. The desired concrete compressive strength was 40 MPa.

Considering a central point load configuration (figure 5.1b) for the tests and an ultimate strength for the steel longitudinal reinforcement $f_u = 642 \text{ MPa}$, as it will be shown later, the ultimate bending moment in conventional flexural analyses is $M_u = 13.76 \text{ kN}$ and, consequently, a maximum load of $P_{bending} = 80.94 \text{ kN}$, and a maximum shear force of $V_{bending} = 40.47 \text{ kN}$. Considering the shear analysis in compliance with (Comisión Permanente del Hormigón 2008) Standard, the maximum load is $P_{shear} = 34.7 \text{ kN}$ and shear force $V_{shear} = 17.3 \text{ kN}$, without taking into account the coefficients of reduction of the material considered in the cited standard. Therefore, a shear failure is expected for the reference beams (not strengthened beams) and this failure load will be raised thanks to the addition of the external strengthening.

The 20 beam specimens, as well as the test cubes and test cylinders for the determination of concrete compressive and splitting strength, respectively, were cast from two different concrete batches, that define the two phases.

The shear span, a , was equal to 340 mm (figure 5.1c) and the effective depth, d , was calculated from Eq. 5.1:

$$d = h - r - \frac{\phi_{long}}{2} = 150 - 15 - 8 = 127 \text{ mm} \quad (5.1)$$

where,

- h is overall depth,
- r is covering of longitudinal reinforcement, and
- ϕ_{long} is longitudinal reinforcement diameter.

Thus, the effective depth of the beams is $d = 127$ mm, with a/d approximately equal to 2.68. The characteristics of the beam specimens of the 2 phases are summarized in table 5.1.

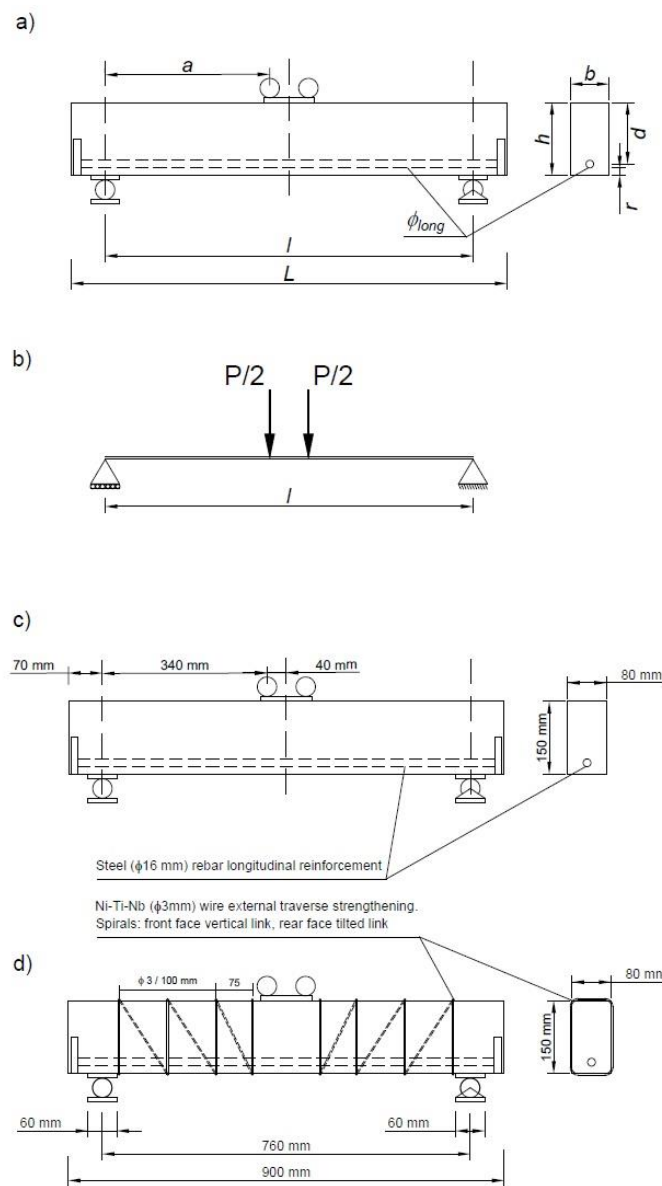


Figure 5.1. a) Main RC beam geometry characteristics, b) schematic drawing of central point load configuration, c) geometry and dimensions for reference beams (without external strengthening), and d) geometry and dimensions for specimens with external strengthening (SMA wires).

Table 5.1. Characteristics of the tested beam specimens

Phase 1 beams	Age at testing (days)	f_{cm} (MPa)	f_{sp} (MPa)	Shear strengthening				Comments
				ϕ /spacing (mm)	<i>Ni-Ti-Nb state</i>	ϕ_{front} (°)	ϕ_{back} (°)	
1.1 – Reference	49	41.4	3.2	-	-	-	-	-
1.2 – Reference	56	41.7	3.2	-	-	-	-	-
2.1 - S ϕ 3/100/UCR/A	63	41.9	3.2	ϕ 3/100	Activated	90	56	Un-cracked
2.2 - S ϕ 3/100/UCR/A	68	42.1	3.2	ϕ 3/100	Activated	90	56	Un-cracked
3.1a - S ϕ 3/100/UCR/NA	102	42.6	3.3	ϕ 3/100	Non-Activated	90	56	Un-cracked
3.1b - S ϕ 3/100/COL/A	130	42.8	3.3	ϕ 3/100	Activated	90	56	Tested after collapse 3.1a
3.2a - S ϕ 3/100/UCR/NA	102	42.6	3.3	ϕ 3/100	Non-Activated	90	56	Un-cracked
3.2b - S ϕ 3/100/COL/A	116	42.7	3.3	ϕ 3/100	Activated	90	56	Tested after collapse 3.2a
4.1 - S ϕ 3/100/PCR/A	175	43.0	3.3	ϕ 3/100	Activated	90	56	Pre-cracked V_{cr} =17.79 kN
4.2 - S ϕ 3/100/PCR/A	182	43.0	3.3	ϕ 3/100	Activated	90	56	Pre-cracked V_{cr} =18.08 kN
5.1 - S ϕ 3/075/UCR/A	263	43.2	3.4	ϕ 3/75	Activated	90	63	Un-cracked
5.2 - S ϕ 3/075/UCR/A	272	43.2	3.4	ϕ 3/75	Activated	90	63	Un-cracked

Phase 2 beams	Age at testing (days)	f_{cm} (MPa)	f_{sp} (MPa)	Shear strengthening				Comments
				ϕ /spacing (mm)	<i>Ni-Ti-Nb state</i>	ϕ_{front} (°)	ϕ_{back} (°)	
6.1 – Reference	202	39.7	3.4	-	-	-	-	-
6.2 – Reference	202	39.7	3.4	-	-	-	-	-
7.1 - S ϕ 3/100/UCR/A/G	279	39.8	3.5	ϕ 3/100	Activated	90	56	Un-cracked / Grooved
7.2 - S ϕ 3/100/UCR/A/G	279	39.8	3.5	ϕ 3/100	Activated	90	56	Un-cracked / Grooved
8.1 - U ϕ 3/100/UCR/A	224	39.7	3.4	ϕ 3/100	Activated	90	90	Un-cracked / U-shape
8.2 - U ϕ 3/100/UCR/A	244	39.7	3.4	ϕ 3/100	Activated	90	90	Un-cracked / U-shape
9.1 - S ϕ 3/100/UCR/A/S	272	39.8	3.5	ϕ 3/100	Activated	90	37	Un-cracked / Confinement of compression chord
9.2 - S ϕ 3/100/UCR/A/S	279	39.8	3.5	ϕ 3/100	Activated	90	37	Un-cracked / Confinement of compression chord
10.1 - U ϕ 3/075/UCR/A	321	39.8	3.5	ϕ 3/075	Activated	90	90	Un-cracked / U-shape
10.2 - U ϕ 3/075/UCR/A	325	39.8	3.5	ϕ 3/075	Activated	90	90	Un-cracked / U-shape

The nomenclature for the different beam specimens (e.g., 7.1 - S ϕ 3/100/UCR/A/G) is as follows: the nomenclature begins with a short test code (1.1 to 10.2) for fast identification.

If this code is followed by “a” or “b”, it means that the beam specimen was tested twice, “a” indicating the first test. Next, S ϕ 3 (3-mm diameter spiral) or U ϕ 3 (3-mm diameter U-shape stirrup) indicates the type of shear strengthening used, followed by “100” or “075”, indicating the pitch in mm of the Ni-Ti-Nb pseudo-rectangular spiral or U-shape stirrup. The next field consists of three letters, “UCR”, “PCR” or “COL”, indicating that the beam specimen was un-cracked when the strengthening spiral was placed and activated (UnCRacked), that it had been previously loaded until a shear crack appeared (Pre-CRacked), or that the beam specimen had already been tested until collapse, and, after the collapse, the strengthening spiral had been activated (COLlapsed). Note that the placement of the spiral or U-shape stirrup was always performed before carrying out any test or pre-cracking. The next term indicates whether the strengthening spiral had been activated before the beam test (A) or had been placed but not activated before the beam test (NA). Some of the beams have a last term indicating an additional characteristic for the specimen: if the lower part of the spiral is placed in a groove, this term is a (G) and if the spiral is wrapping only the compression chord of the beam (approximately the upper mid part of the cross section of the beam specimen), this term is a (S). To ensure the repeatability of the findings, two identical beams were tested for each set of criteria testing both sides identically and at the same time (for example, beams 2.1 and 2.2, where the second number indicates the first and the second tested beam specimens of beam type 2).

The first column of table 5.1 is the test number and its nomenclature designation, the second one is the age of concrete in days at testing, and the third and fourth columns are the concrete compressive strength, f_{cm} (MPa) and the splitting strength, f_{sp} (MPa), respectively. The fifth to eighth columns are referred to shear strengthening: 5th is diameter and spacing of stirrups (or pitch for spiral strengthening) in mm, 6th is the state of the wire (activated or not activated), 7th and 8th are the inclination angles in degrees of front and rear links (angle between longitudinal axis of the beam and the direction of the link). Finally, the ninth column is a comment about test performance and/or about geometry of strengthening.

Figures 5.2 and 5.3 depict beam geometry, strain gauge location and characteristics of every tested beam in phase 1 (fig. 5.2) and phase 2 (fig. 5.3). Note that the spacing of the external reinforcement (or pith for the spiral) near the point of load application is reduced so that it does not overlap with the load application plate.

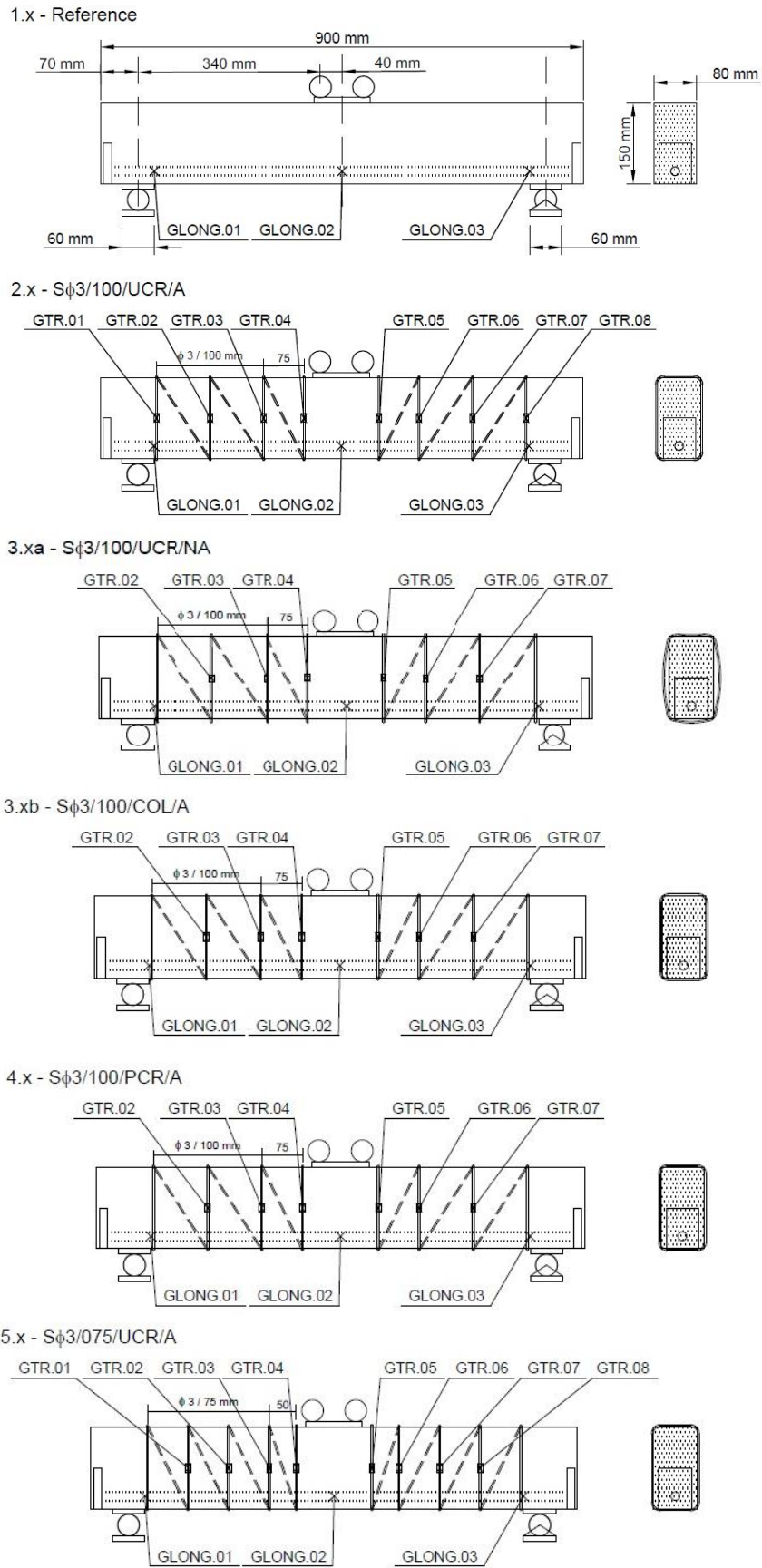


Figure 5.2. Beams 1 to 5 geometries and strain-gauge locations of the beam specimens for phase 1

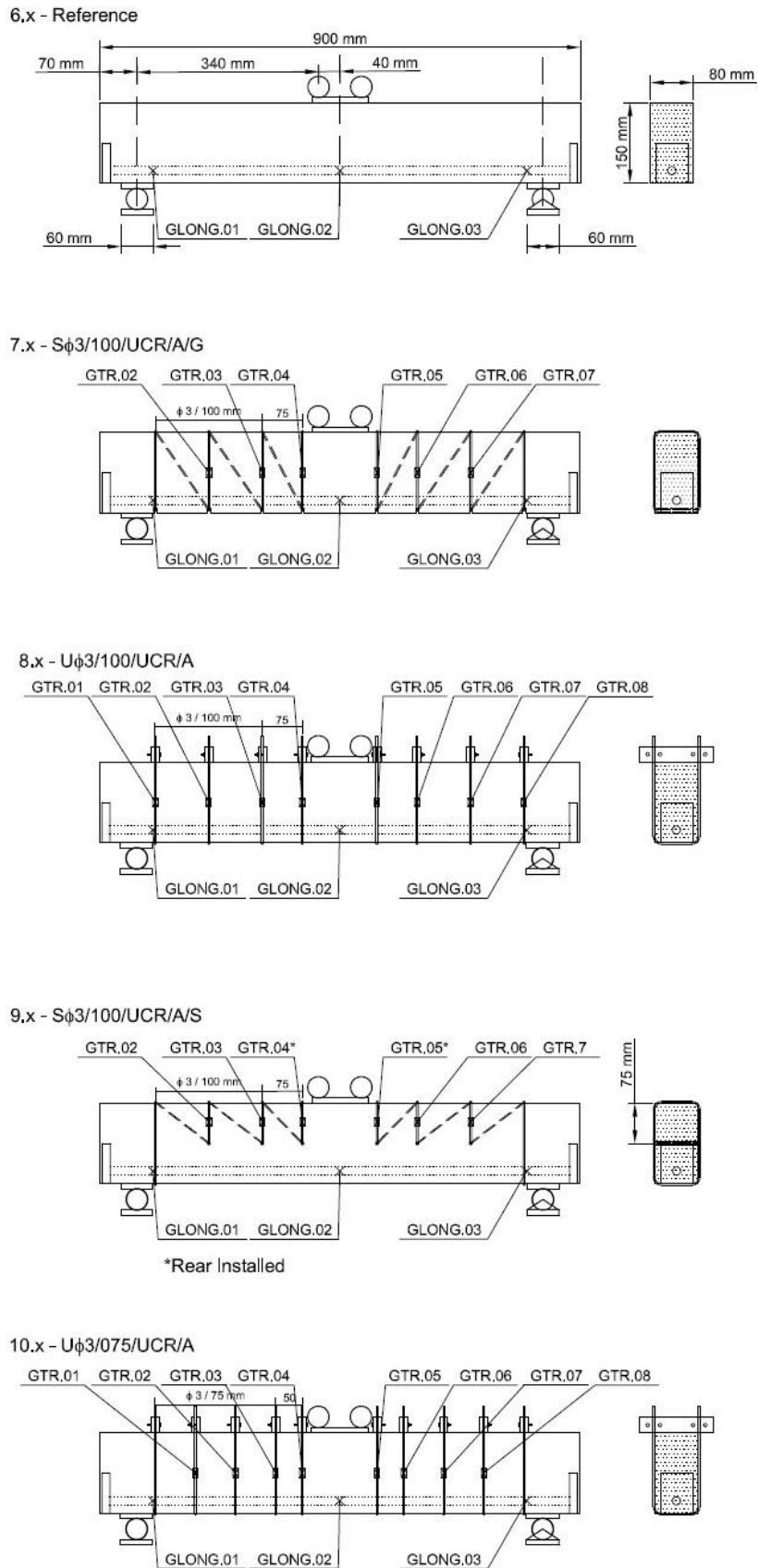


Figure 5.3. Beams 6 to 10 geometries and strain-gauge locations of the beam specimens for phase 2

5.3 FABRICATION OF THE TEST SPECIMENS. CONCRETE AND STEEL PROPERTIES

The beams were cast at a precast concrete plant, named Pastor, located in Santa Margalida (Mallorca, Spain). The 20 beam specimens, as well as the test cubes and test cylinders for the determination of concrete compressive and splitting strength, were cast from two different concrete batches in dates October 16th 2015 (phase 1 beams) and October 23rd 2015 (phase 2 beams). Different steps of the fabrication of the test specimens are depicted in figure 5.4. A maximum aggregate size of 14 mm was used. Standard 150 mm cubes (fig. 5.5a) and 150 mm × 300 mm cylinders (fig. 5.5b) were cast with the specimens to obtain the compressive strength, f_{cm} , and the splitting strength, f_{sp} , in compliance with UNE-EN-12390-3 Standard (AENOR 2009) and UNE-EN-12390-6 Standard (AENOR 2010), respectively, and tested at 28 days in compliance with EHE Code (Comisión Permanente del Hormigón 2008). These cubes and cylinders were kept under the same environmental conditions as the beam specimens until the time of testing of the beams in the laboratory with a temperature typically 20 °C. The f_{cm} and f_{sp} estimations are derived from the results of 23 cube tests for the compressive strength and 25 cylinder tests for the splitting strength, tested at 28 days and at the age of each beam specimen at the time of testing. The results of cube and cylinder tests are summarized in table 5.2.

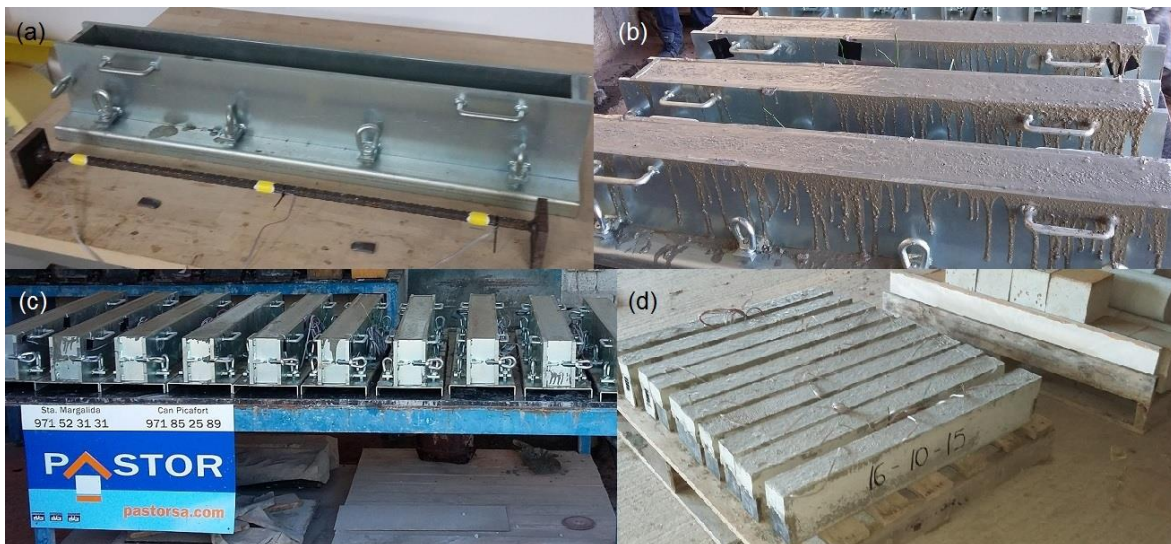


Figure 5.4. a) Instrumented longitudinal reinforcement of a beam before casting, b) fresh concrete, c) the first concrete batch, and d) concrete beams ready to be tested

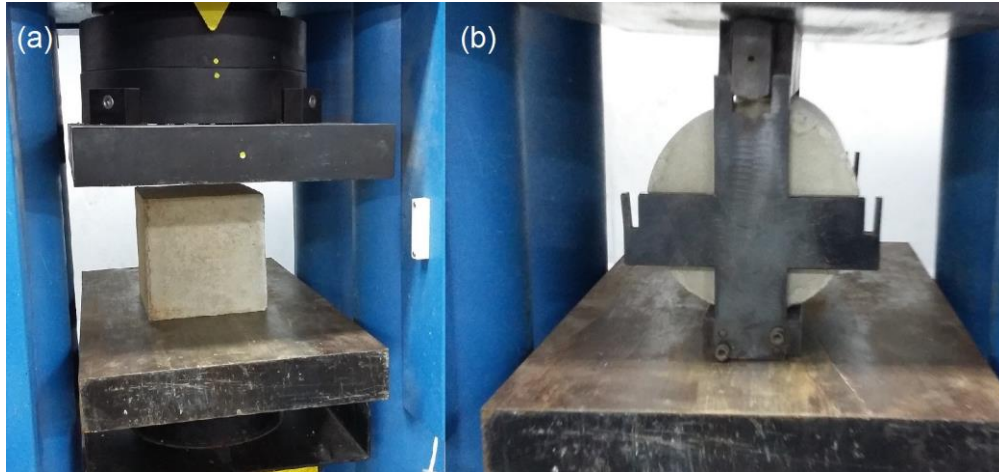


Figure 5.5 a) Standard cubes and, b) cylinders in the test frame

For the determination of the compressive and splitting strength, an homogenization procedure was followed to ensure that the small scatter in the results did not influence the final values adopted for each beam specimen, according to the batch and the age of testing. The first column of table 5.2 is the test number and its nomenclature designation, the second one is the age of concrete in days at testing, the third (number of samples), fourth (average), and fifth (estimated) are data related to compressive strength, f_{cm} (MPa), and the sixth (number of samples), seventh (average), and eighth (estimated) are data related to splitting strength, f_{sp} (MPa).

Regarding to Spanish standards (Comisión Permanente del Hormigón 2008), the compressive strength evolution of the concrete is given by Eq. 5.2:

$$f_{cm}(t) = e^{\left\{s \left[1 - \left(\frac{28}{t}\right)^{\frac{1}{2}}\right]\right\}} f_{cm}(28) \quad (5.2)$$

where,

$f_{cm}(t)$ is compressive strength at t days,

$f_{cm}(28)$ is compressive strength at 28 days,

s coefficient dependent on cement type. According to the evolution observed of the compression strength, a coefficient $s = 0.15$ has been adopted (very fast cement).

The evolution of the splitting strength is given by Eq. 5.3:

$$f_{sp}(t) = \left\langle e^{\left[1 - \left(\frac{28}{t}\right)^{\frac{1}{2}}\right]} \right\rangle^{\alpha_E} f_{sp}(28) \quad (5.3)$$

where,

$f_{sp}(t)$ is compressive strength at t days,

$f_{sp}(28)$ is compressive strength at 28 days,

α_E coefficient dependent on concrete age and characteristic strength at 28 days
($\alpha_E = 2/3$ for normal strength concrete at $t > 28$ days).

Thus, taking into account the previous equations and all the strength values at different ages, an adjustment had been done for the two batches. The results obtained have a good agreement with the experimental data: obtained average value of the relationship Average strength/Estimated strength of 1.002 and coefficient of variation of 3.4 % for both batches for compressive strength, and average of 0.997 and coefficient of variation of 5.5 % for splitting strength. The application of this procedure allowed to estimate the compressive and splitting strengths taking into account all the available information. This way, some inconsistencies have been corrected. Initially, some strength average data were slightly inconsistent, with some higher values of average strength for younger samples with respect to the strength of older ones, as can be seen in table 5.2 (see for instance the average compressive strength and the estimated strength of beams 9.1 and 10.1)

As can also be seen in the data from table 5.2, the variability is higher in the results of splitting tests than those of compression tests. This is due to different factors: a higher degree of difficulty for the correct installation of the specimens in the test frame for the splitting test than those of the compression test and the higher natural scatter of the tensile strength compared to the compressive strength.

Longitudinal reinforcement of the RC beams was composed of one $\phi 16$ mm standard B500SD rebar ($A_s = 201 \text{ mm}^2$) in each beam specimen. Both ends of the bars were welded to a plate to guarantee sufficient anchorage in such small beam specimens, as previously mentioned. The mechanical properties of the longitudinal bars are: $f_y = 513 \text{ MPa}$, $f_u = 642 \text{ MPa}$, $\varepsilon_u = 20.5\%$ and $E = 213 \text{ GPa}$ (mean value of two tests reported). Figure 5.6 depicts stress-strain curves for the $\phi 16$ mm bars, tested at an external laboratory, LABARTEC,

located in Palma (Mallorca, Spain) in compliance to current UNE36065 (AENOR 2011) and UNE-EN-ISO15630 (AENOR 2003) Standards.

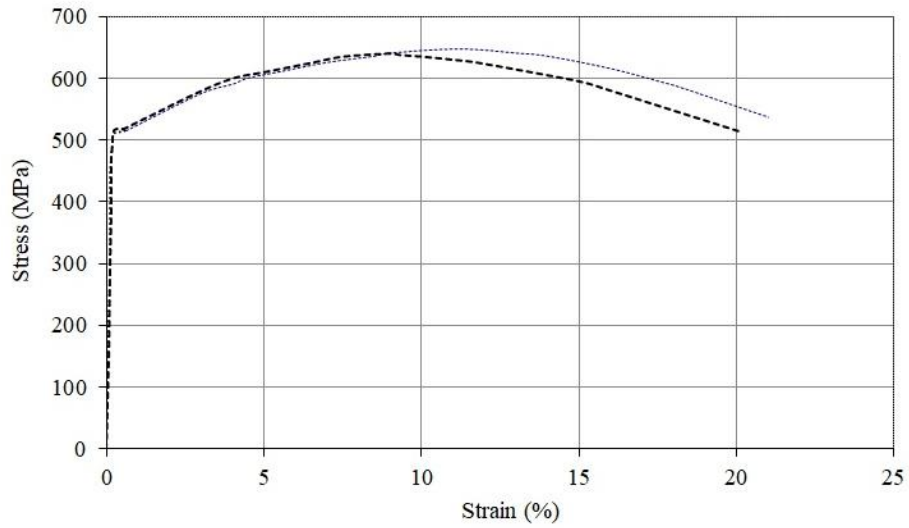


Figure 5.6. Stress-strain curves for $\phi 16$ mm bars used as longitudinal reinforcement

Table 5.2. Results of compressive and splitting strength tests performed

Phase 1 beams	Age at testing (days)	Compressive			Splitting		
		Samples tested	Average (MPa)	Estimated f_{cm} (MPa)	Samples tested	Average (MPa)	Estimated f_{sp} (MPa)
None	28	3	37.5	37.5	3	3.3	3.1
1.1 – Reference	49	2	40.9	41.4	2	3.1	3.2
1.2 – Reference	56	2	42.5	41.7	2	3.0	3.2
2.1 - S ϕ 3/100/UCR/A	63	2	42.3	41.9	2	3.4	3.2
2.2 - S ϕ 3/100/UCR/A	68	2	41.6	42.1	2	3.1	3.2
3.1a - S ϕ 3/100/UCR/NA	102	2	43.3	42.6	2	3.3	3.3
3.1b - S ϕ 3/100/COL/A	130	-	-	42.8	-	-	3.3
3.2a - S ϕ 3/100/UCR/NA	102	2	43.3	42.6	2	3.3	3.3
3.2b - S ϕ 3/100/COL/A	116	-	-	42.7	-	-	3.3
4.1 - S ϕ 3/100/PCR/A	175	2	45.6	43.0	2	3.0	3.3
4.2 - S ϕ 3/100/PCR/A	182	2	44.7	43.0	2	3.3	3.3
5.1 - S ϕ 3/075/UCR/A	263	2	44.1	43.2	3	3.6	3.4
5.2 - S ϕ 3/075/UCR/A	272	2	46.5	43.2	3	3.4	3.4
Phase 2 beams	Age at testing (days)	Compressive			Splitting		
		Samples tested	Average (MPa)	Estimated f_{cm} (MPa)	Samples tested	Average (MPa)	Estimated f_{sp} (MPa)
None	28	3	34.5	34.5	3	2.7	2.7
6.1 – Reference	202	3	40.0	39.7	3	3.5	3.4
6.2 – Reference	202	3	40.0	39.7	3	3.5	3.4
7.1 - S ϕ 3/100/UCR/A/G	279	2	39.4	39.8	3	3.5	3.5
7.2 - S ϕ 3/100/UCR/A/G	279	2	39.4	39.8	3	3.5	3.5
8.1 - U ϕ 3/100/UCR/A	224	2	39.0	39.7	3	3.0	3.4
8.2 - U ϕ 3/100/UCR/A	244	2	38.4	39.7	2	3.3	3.4
9.1 - S ϕ 3/100/UCR/A/S	272	3	39.4	39.8	3	3.4	3.5
9.2 - S ϕ 3/100/UCR/A/S	279	2	39.4	39.8	3	3.5	3.5
10.1 - U ϕ 3/075/UCR/A	321	2	37.4	39.8	2	3.8	3.5
10.2 - U ϕ 3/075/UCR/A	325	2	37.4	39.8	2	3.7	3.5

5.4 STRENGTHENING OF THE BEAM SPECIMENS

The strengthening of the RC beams was performed by means of four different configurations:

- Pseudo-rectangular spirals (fig. 5.7) with vertical links on the front face (fig. 5.7a) and inclined links on the back face (fig. 5.7b).
- U-shape stirrups (fig. 5.8a) with vertical links clamped in the upper part of the beams with bolted steel plates.
- Pseudo-rectangular spirals with embedment of wires, in grooves, in the lower part of the beams to improve contact between longitudinal reinforcement and the spirals (fig. 5.8b). This configuration was tested to study the possible increase in the dowel effect transfer action.
- Confinement of concrete compression chord using mid-section rectangular spirals (fig. 5.8c), with drills in mid-section to allow wire pass through the beams. This configuration was tested to study the behavior of the beam improving the confinement of the compression chord but without adding the full contribution of the shear reinforcement (without links crossing the first branch of the critical crack).

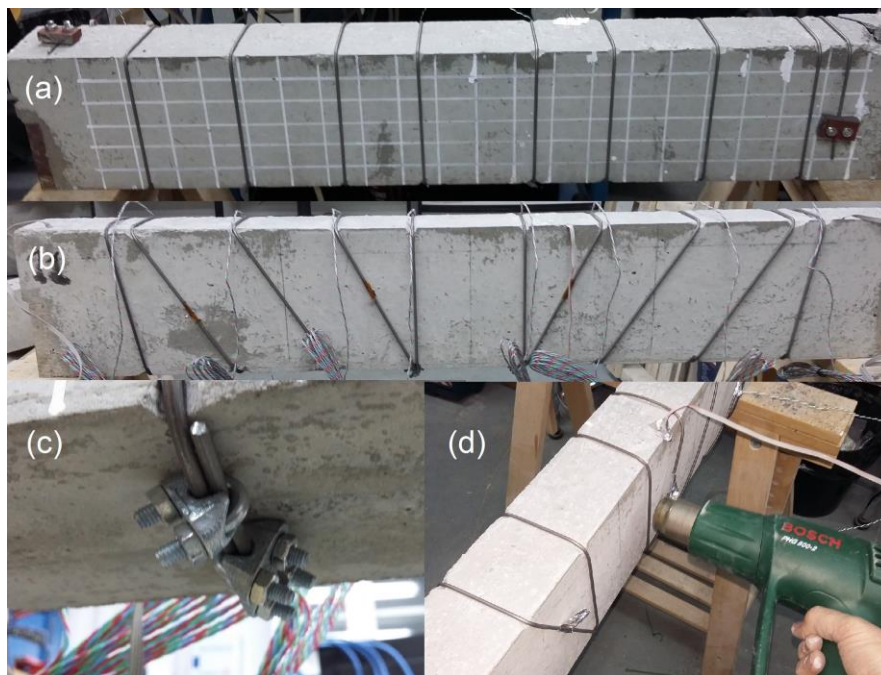


Figure 5.7 a) Front view, and b) rear view of a beam specimen, c) detail of the anchoring using U-Bolt saddle clamps, and d) activation process with heat gun

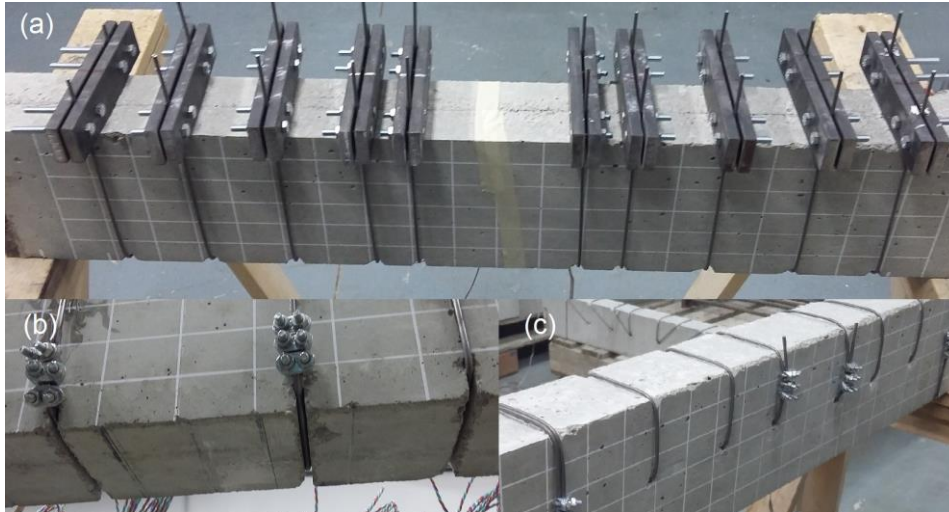


Figure 5.8. a) Strengthened beam with U-shape stirrups, b) detail of grooves in a beam, and c) spiral confining only the concrete compression chord of a beam.

For creating the pseudo-rectangular spirals, the prestained Ni-Ti-Nb wire was placed wrapping around the beam specimens. It was vertically located on the front side (fig. 5.7a) and tilted on the back side (fig. 5.7b). Note that small and short grooves or indentations were made at the corners of the rectangular cross-section, to ensure a proper rotation of the wires and to minimize the initial imperfections during their placement. The anchoring of the wires was performed using two different configurations: 1) the external end of the wire was anchored to the concrete by means of bolts and a small steel plate (fig. 5.7a), and 2) the internal end of the wire was self-anchored by means of U-bolt saddle clamps (fig. 5.7c). The placement of the wire into the small grooves at the corners (fig 5.9) avoided the slippage of the wires during the activation and minimize the initial imperfection. During the experimental campaign, and after verifying the low level of strains at the external end of the wires, the external anchorage was changed to self-anchorage by means of U-bolt saddle clamps as well with correct results (fig. 5.9).

The wires were activated using a heat gun (fig. 5.7d) in a sequence procedure starting from the external end of the wire and following the wire spirals to the internal end of it, producing the reverse martensitic transformation. As a result, the Ni-Ti-Nb wire attempted to shorten but it was restrained because of the presence of the RC beam. Thus, the wire transmitted the stresses induced by its transformation to the beam in the form of confining stresses (fig. 5.9). No slippage of the wires occurred since the turn of the wires at the small grooves at the cross-section corners was maintained fixed. Note that there is no bonding between the external

shear strengthening and the concrete, except for the friction concentrated at the corners of the cross-section of the beams.

The use of external spirals was chosen because the spiral geometry had already shown important benefits as internal reinforcement for shear, using common materials or even shape memory alloys (Azimi et al. 2016; Mas et al. 2016a; De Corte & Boel 2013; Karayannis & Chalioris 2013; Yang et al. 2011), as it was commented in chapter 2.

Regarding specifically to every RC beams, beams 1.1 and 1.2 were reference beams for phase 1 tests, so Ni-Ti-Nb spirals were not used. In beams 2.1, 2.2, 5.1, and 5.2, the activation of the Ni-Ti-Nb spirals was carried out before loading the beams (no preexisting cracks). Different pitches were used: 100 mm in beams 2.1 and 2.2, and 75 mm in beams 5.1 and 5.2. In beams 4.1 and 4.2, they were pre-cracked by a shear force of around 18 kN (see table 5.1), which represents approximately 98% of the maximum shear strength of the reference beams.

In beams 3.1 and 3.2, the Ni-Ti-Nb spiral was placed and anchored around the beams but not activated. The beams were, then, tested to collapse in tests 3.1a and 3.2a (note in fig. 5.2, 3xa, that the spiral wire is depicted with a curvature in the cross section, indicating that the strengthening wire had not been activated). After the collapse and the unloading of the beams, the Ni-Ti-Nb wires were activated, generating the recovery stresses, then the beams were retested in tests 3.1b and 3.2b.



Figure 5.9. Comparison of wire reinforcement in beam: before activation on left hand side wire and after activation on right hand side

Beams 6.1 and 6.2 were reference beams for phase 2, so Ni-Ti-Nb wires were not used. In all other beams, the activation of the Ni-Ti-Nb reinforcement was carried out before loading the beams (no preexisting cracks). The decision not to pre-crack anymore of the beams was taken upon seeing the results of the first phase, where the behavior of pre-cracked beams and even of pre-collapsed ones were very similar to that of the not pre-cracked. This fact will be explained later. Beams 7.1 and 7.2 were indented with grooves in the lower part of each spiral to test the influence of embedment of the wires and a possible increase in the dowel transfer action.

Beams 8.1, 8.2, 10.1 and 10.2 were strengthened with U-shape stirrups of Ni-Ti-Nb clamped in the upper part of the beams with bolted steel plates. This is a variant of a successful method used in (Chen et al. 2014) that show the effectiveness applied in non-circular (prismatic) concrete members in improving their ductility. Two different stirrup spacing configurations were used, i.e. 100 mm for beams 8.1 and 8.2 and 75 mm for beams 10.1 and 10.2.

The configuration for beams 9.1 and 9.2, using a spiral strengthening only the upper mid-section of the beam, was selected in order to study the behavior of the beams with only the compression chord confined.

5.5 INSTRUMENTATION AND TESTING PROCEDURE

A sketch of the test set-up is depicted in figure 5.10. The simply supported beams were loaded following a three-point bending scheme, with a span length $L = 760$ mm. The tests were carried out under control displacement using a hydraulic actuator (IBERTEST) with a maximum load capacity of 100 kN, located at the Building Engineering Laboratory of the University of Balearic Islands (fig. 5.11). The supporting plates were 60 mm long in the direction of the longitudinal axis of the beam, and the loading plate was 105 mm wide. The load was applied by two cylinders with centers spaced 80 mm apart. A sliding pin bearing was placed at the west side and a fixed pin bearing was placed at the east side. The displacement at the loading plate was monotonically increased until failure.

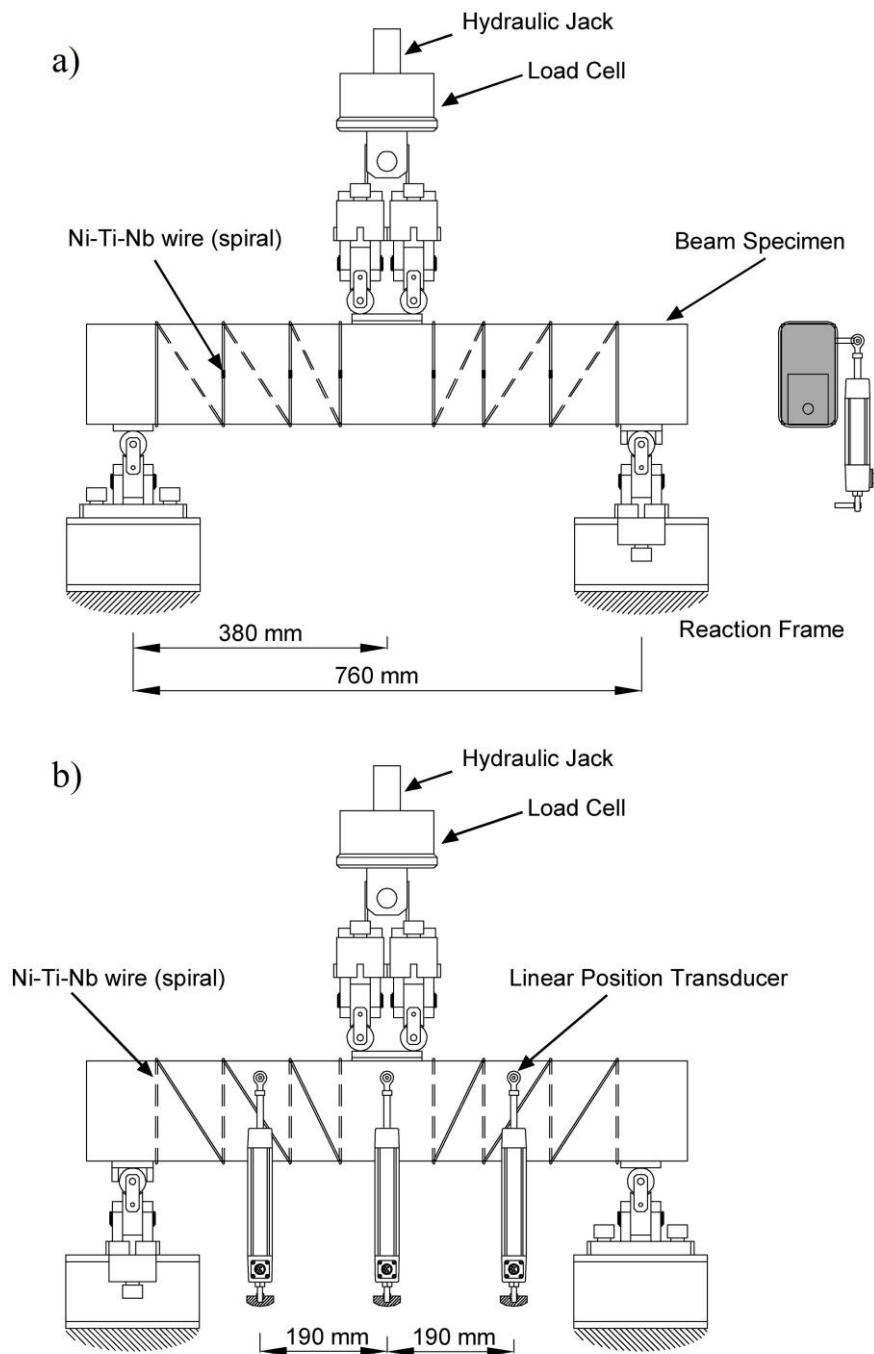


Figure 5.10. Test set-up with instrumentation devices: a) front view and b) back view.

To monitor the behavior of the tested beam specimens, the applied load, the strains in the wires, and the displacements of the beams different instrumentation was installed.

The strains in longitudinal reinforcement were measured with three strain gauges (named GLONG) located in central rebar and close to each support. The strains in the Ni-ti-Nb wires

were measured by means of eight strain gauges placed in central location of vertical links (named GTR). The numbering of the gauges (longitudinal and transverse) followed a sequential order from left to right (front view). The locations of the strain gauges in each beam are shown in figures 5.2 and 5.3.

Three magnetostrictive transducers (Linear Position Transducers, see fig. 5.12) were located at the rear side of the beams: one at mid-span and two others at half mid-span of the beams to monitor deflections of the beams. Video and photography (twin cameras) equipment was also used to record the tests (fig. 5.11). All parameters recorded from gauges, transducers and from the load cell were acquired continuously by a HBM data acquisition system (fig. 5.13).

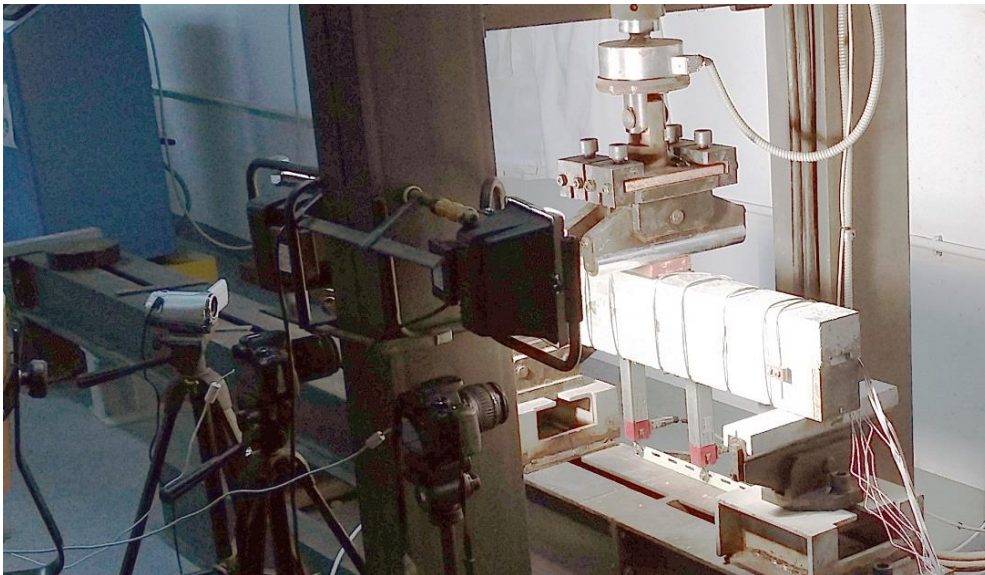


Figure 5.11. Load cell during a test with photography twin cameras and video equipment recording

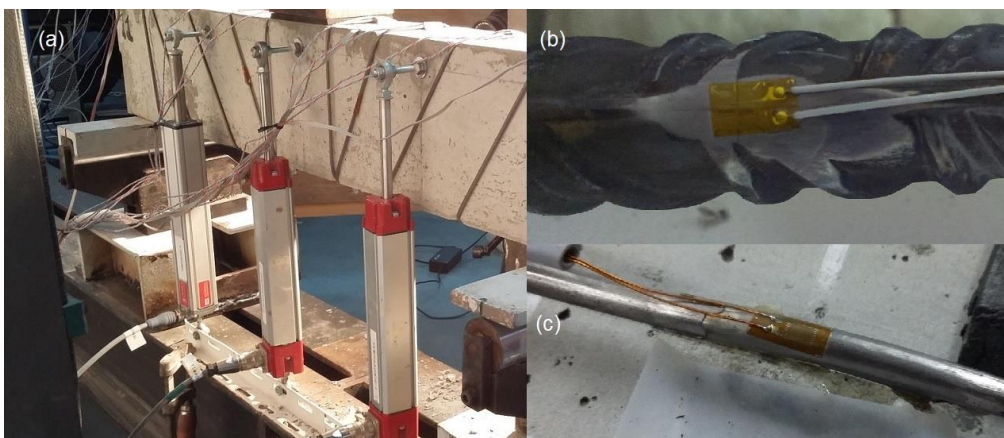


Figure 5.12. Monitoring devices: a) Linear position transducers located in a beam, b) strain gauge for longitudinal reinforcement, and c) strain gauge installed on Ni-Ti-Nb wire

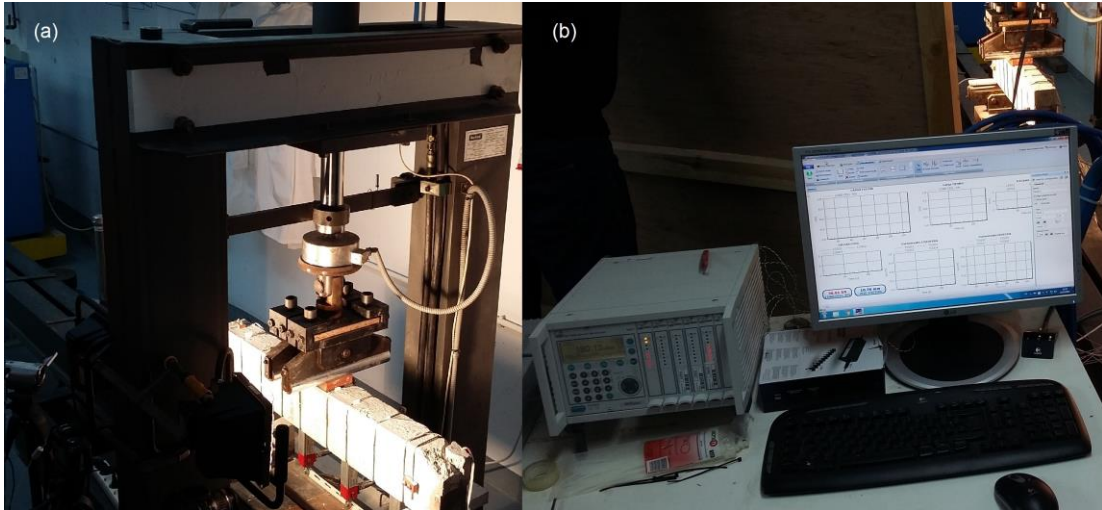


Figure 5.13. a) Hydraulic actuator carrying out a test and b) data acquisition system.

5.6 RESULTS OF EXPERIMENTAL TESTS AND DISCUSSION

5.6.1 OBSERVED BEHAVIOR AND SHEAR STRENGTH

All the tested beams of the two phases failed in shear, except for beam 5.2 which failed in bending, although shear critical cracks had already developed in its two shear spans. As it was mentioned above, the objective in this experimental program was to raise the shear strength but without reaching the flexural strength, if possible, to assess the shear strength of the strengthened RC beams. Table 5.3 summarize the test results.

The first column of table 5.3 is the test number and its nomenclature designation, the second column is the maximum shear strength in the test, V_{test} (kN), half of maximum applied load by the load cell in this case. The third column is the effectiveness of the shear strengthening as a ratio between shear strength over average shear strength of non-reinforced beams ($E_{ff} = \frac{V_{test}}{V_{no\ reinf.}}$). The fourth column is the deflection at maximum shear force, δ at V_{test} , (mm). The fifth column is the ratio $\frac{\delta}{l}$, ($\frac{1}{l}$) between deflection and beam span ($l= 760$ mm).

Table 5.3. Summary of beam test results

Phase 1 beams	V_{test} (kN)	E_{ff}	δ at V_{test} (mm)	δ/l (1/l)
1.1 – Reference	18.30	-	1.59	1/479
1.2 – Reference	18.41	-	1.64	1/462
2.1 - S ϕ 3/100/UCR/A	35.41	1.93	4.26	1/178
2.2 - S ϕ 3/100/UCR/A	35.95	1.96	4.94	1/154
3.1a - S ϕ 3/100/UCR/NA	18.23	-	1.67	1/456
3.1b - S ϕ 3/100/COL/A	27.14	1.48	3.46	1/220
3.2a - S ϕ 3/100/UCR/NA	21.47	-	1.69	1/450
3.2b - S ϕ 3/100/COL/A	35.21	1.92	3.83	1/198
4.1 - S ϕ 3/100/PCR/A	34.35	1.87	3.82	1/199
4.2 - S ϕ 3/100/PCR/A	35.60	1.94	4.10	1/185
5.1 - S ϕ 3/075/UCR/A	37.04	2.02	3.82	1/199
5.2 - S ϕ 3/075/UCR/A	41.82*	2.28	6.95	1/109
Phase 2 beams	V_{test} (kN)	E_{ff}	δ at V_{test} (mm)	δ/l (1/l)
6.1 – Reference	19.71	-	2.505	1/303
6.2 – Reference	18.50	-	1.692	1/449
7.1 - S ϕ 3/100/UCR/A/G	25.36	1.33	2.560	1/297
7.2 - S ϕ 3/100/UCR/A/G	35.51	1.86	6.039	1/126
8.1 - U ϕ 3/100/UCR/A	37.74	1.98	5.347	1/142
8.2 - U ϕ 3/100/UCR/A	34.75	1.82	5.148	1/148
9.1 - S ϕ 3/100/UCR/A/S	20.54	1.08	3.007	1/253
9.2 - S ϕ 3/100/UCR/A/S	22.03	1.15	3.695	1/206
10.1 - U ϕ 3/075/UCR/A	36.79	1.93	5.310	1/143
10.2 - U ϕ 3/075/UCR/A	33.65	1.76	4.736	1/160

*Failed in bending

The effectiveness of the proposed strengthening method can be shown by means of the increment of maximum shear force of a strengthened beam respect to the maximum shear force of non-strengthened beams (E_{ff}). This ratio has been calculated from average values of the non-reinforced beams of the same phase. The average value of non-reinforced beams of the first phase of tests, taken from beams 1.1 and 1.2, was $V_{no\ reinf.} = 18.36$ kN and the average value of non-reinforced beams of the second phase, taken from beams 6.1 and 6.2, was $V_{no\ reinf.} = 19.11$ kN. The effectiveness of the method is shown since the average value of this ratio calculated for strengthened beams of the first phase was ($E_{ff,average} = 1.92$) and the average value of this ratio calculated of strengthened beams of the second phase was ($E_{ff,average} = 1.85$), since beams 9.1 and 9.2, with a different strengthening scheme, were not accounted for the average. Therefore, an average increment of shear force of 89% has been achieved for this shear strengthening method.

In the case of deflection increments, more scattered values were encountered, although a clear trend is achieved in δ/l relationship: non-strengthened beams display values between 1/300 and 1/500 and strengthened beams values between 1/100 and 1/200, except for beams 9.1 and 9.2 with a different strengthening scheme and two other beams with relatively high previous damage (3.1 and 7.1). In the next paragraphs, a discussion of these beam test results will clarify their behavior.

Figure 5.14 shows the shear force-deflection curves of the reference beams of the phase 1 (1.1 and 1.2), the beams with the non-activated spiral (3.1a and 3.2a), the strengthened beams with pitch equal to 100 mm (2.1 and 2.2), and the strengthened beams with pitch equal to 75 mm (5.1 and 5.2). It can be seen that when the pseudo-spiral was placed around the beam without being activated, it was negligibly effective, thus the results for beams 3.1a and 3.2a were very similar to the results for the reference beams. This is because, due to the relatively high initial strengthening imperfection before activating, the wires did not start collaborating during the test (figure 5.15). However, when the spiral was activated (beams 2.1, 2.2, 5.1, and 5.2), the strengthening method was clearly effective in all cases, providing the highest shear strengths with the reduced-pitch (75 mm) spiral.

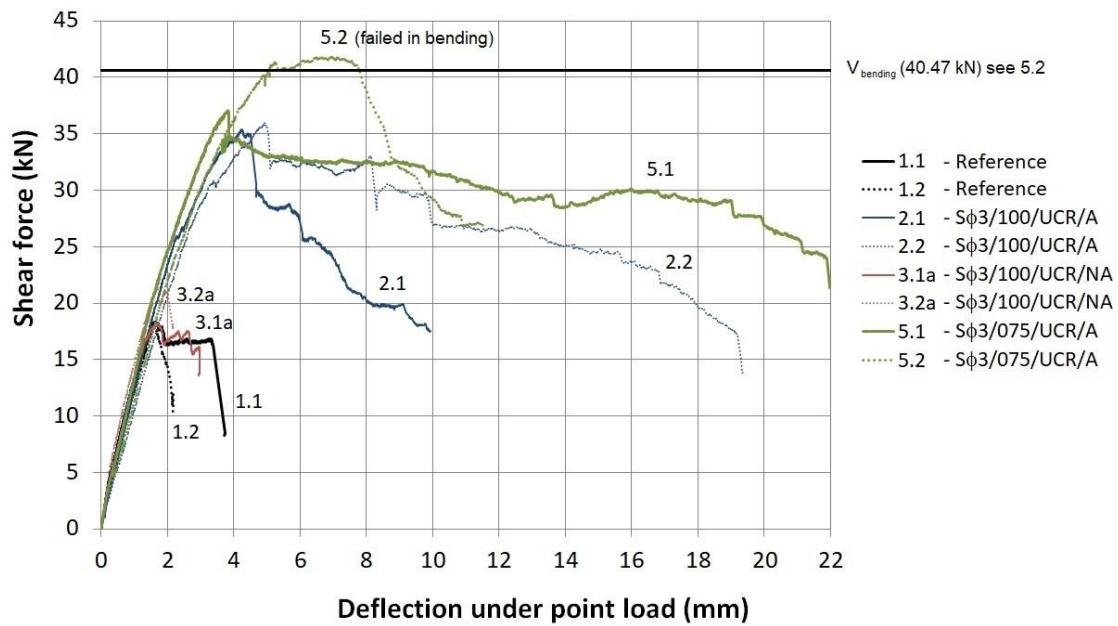


Figure 5.14. Shear force-deflection for reference beams (1.1 and 1.2), strengthened beams with pitch equal to 100 mm (2.1 and 2.2), beams with the spiral un-activated (3.1a and 3.2a), and strengthened beams with pitch equal to 75 mm (5.1 and 5.2)

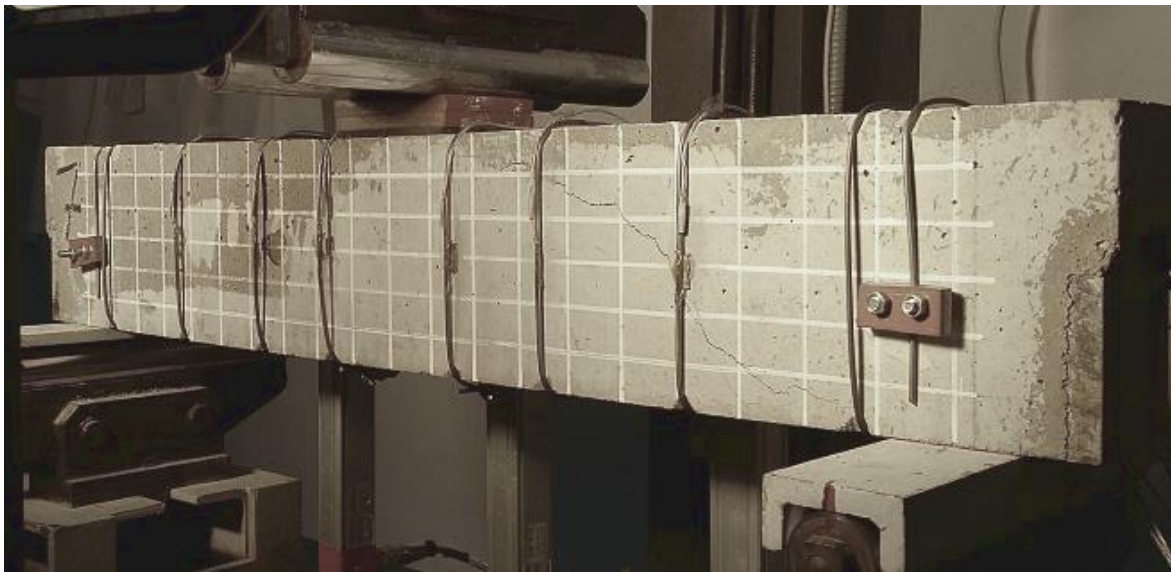


Figure 5.15. Beam 3.1a after peak load. Note that even after peak load, the wires already show some gap (vertical links)

Figure 5.16 compares the shear force-deflection curves for the reference beams (1.1 and 1.2), strengthened beams with pitch equal to 100 mm and activated without initial cracking (2.1 and 2.2), and beams with similar strengthening activated with preexisting shear cracking (4.1 and 4.2). Beams 4.1 and 4.2 had previously been loaded to approximately 98% of the maximum shear force determined for the reference beams, and the alloy had been activated

afterwards. The behavior of these beams, in terms of maximum shear force and deflection, was very similar, and it seemed that pre-cracking the beams did not affect the results. It must be highlighted that shear cracks developed during pre-load tests were almost closed during unloading, and therefore, these pre-cracked beams behave practically equal to intact ones after subsequent prestressing before the test.

Two beams were loaded until collapse (3.1a and 3.2a) and then they were strengthened and tested again (3.1b and 3.2b). The results (table 5.3 and fig. 5.17) show that the strengthening method was able to increase the shear strength of the beam even after it had already collapsed, without conducting any additional rehabilitation work. Beam 3.2b showed a very similar response to the other strengthened specimens with the same wire pitch (2.1, 2.2, 4.1, and 4.2), although beam 3.1b exhibited a lower degree of shear strength increase.

Note that beam 3.1a had been observed to suffer higher damage levels than those incurred by beam 3.2a after initial collapse. As can be seen in figure 5.17, beam 3.1a was initially led to further post-peak deflections in order to observe if the final strength of the element varied. Figure 5.17 shows that the higher the damage caused by the post-peak deflection, the lower the resistance of the element.

As a conclusion of the results for beams 2.1, 2.2, 3.2b, 4.1 and 4.2, as the shear strength (V_{test}) is very similar for all of them, no more beams of the second phase were pre-cracked.

Figure 5.18 shows the shear force-deflection curves of the reference beams of the phase 2 (6.1 and 6.2), the beams with the grooves (7.1 and 7.2), the strengthened beams with U-shape stirrups 100 mm pitch (8.1 and 8.2), the strengthened beams with spirals confining only the compression chord (9.1 and 9.2). The pitch was in all these cases equal to 100 mm and the wires were activated before performing the tests.

It can also be seen in figure 5.18 that the different strengthening methods (U-shaped stirrups in beams 8.1 and 8.2 or spirals in beams 7.1 and 7.2) were effective, except for beam 7.1 (later explained). For beams 9.1 and 9.2, the beams with only the compression chord confined, the shear strength increased around 16% with respect to the reference beams, but the increment of ultimate deflection is more significant. Therefore, the ductility of the shear failure has been improved by confining only the compression chord.

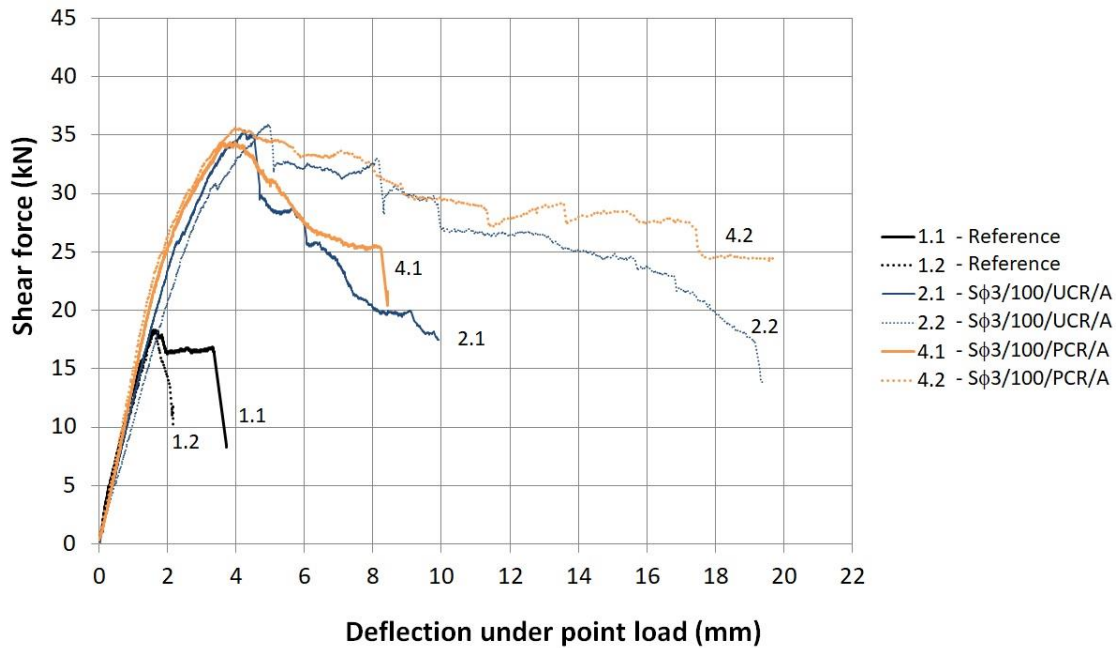


Figure 5.16. Shear force-deflection for reference beams (1.1 and 1.2), strengthened beams (2.1 and 2.2) and strengthened beams after pre-cracking (4.1 and 4.2). All strengthened beams with pitch equal to 100 mm

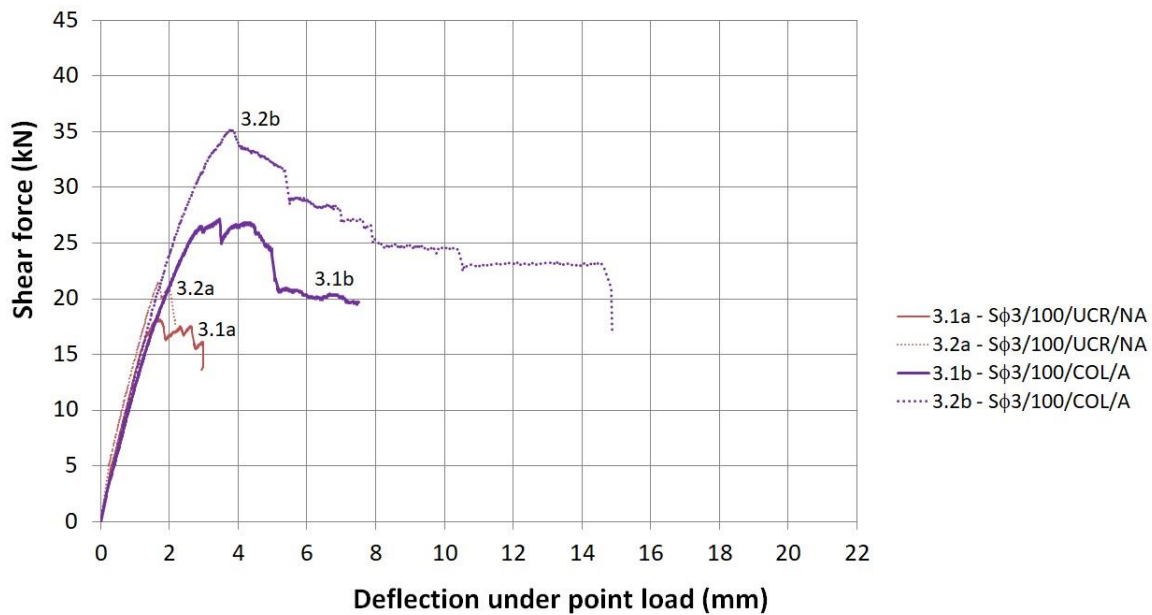


Figure 5.17. Shear force-deflection for reference beams with the spiral un-activated (3.1a and 3.2a) and the same beams with the spiral activated after the first collapse (3.1b and 3.2b)

Figure 5.19 compares the shear force-deflection curves for the reference beams (6.1 and 6.2), strengthened beams with U-shape stirrups with pitch equal to 100 mm (8.1 and 8.2), and beams with U-shape stirrups with pitch equal to 75 mm (10.1 and 10.2). The behavior of these last beams, in terms of maximum shear force and deflection, was very similar. Anyway, some considerations must be done. At first, beams strengthened with spirals were

expected to have a higher value of shear strength than beams strengthened with U-shape stirrups (vertical) with the same pitch, even taking into account that splitting strength of the concrete of the second batch was slightly higher (table 5.2). Thus, higher values of shear strength for beams 2.1 and 2.2 (35.68 kN) were expected than for beams 8.1 and 8.2 (36.25 kN), and also higher values for beams 5.1 and 5.2 (38.63 kN) than for beams 10.1 and 10.2 (35.22 kN). As this fact was not confirmed in the first case, other aspects could have affected the tested beams, like initial imperfections of the initial installation of the Ni-Ti-Nb wires around the beams or the fact that the U-shape stirrups do not weaken the compression chord, as will be explained in chapter 6.

Beam 7.1 presented an outlier result. This test may be considered as not representative due to its unexpected low shear strength. Actually, as can be seen in figure 5.20m, the shear critical crack has been forced to reach a groove in the lower part of the beam triggering a more rapid failure. The behavior of beam 7.2 seems more predictable and this beam will be taken into account to analyze the results of performing grooves. In any case, the use of grooves does not suppose an increment of shear strength: the dowel effect of the longitudinal reinforcement is not affected by the fact that the spiral is practically in contact with the bar, or not, like in the other tests with the totally external spiral. Anyway, due to the observed behavior of beams 7.1 and 7.2, the increment of work in order to retrofit the beam (performing of grooves) is not recommended.

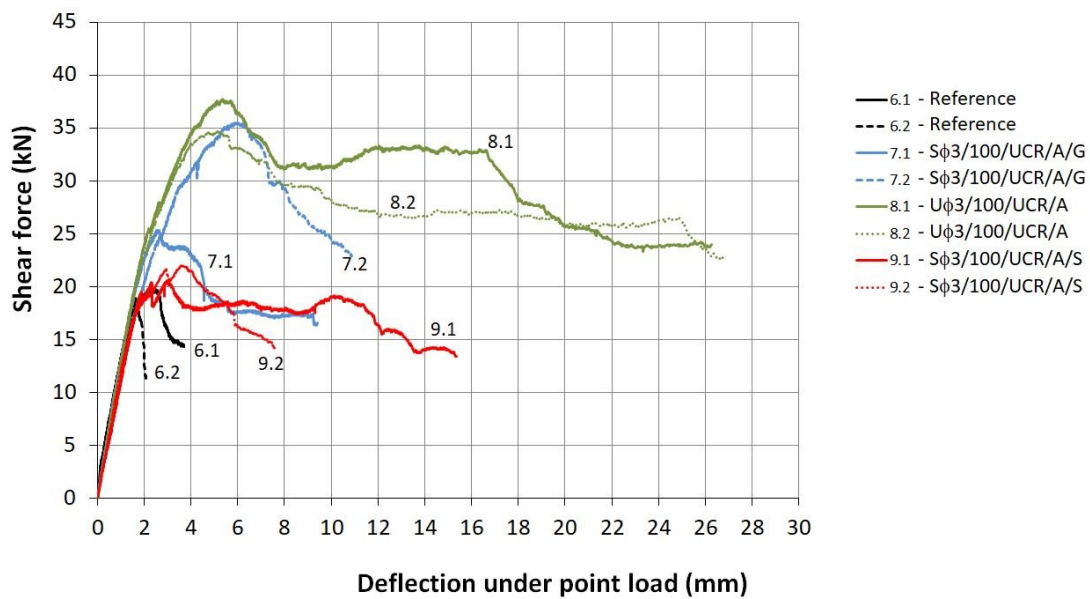


Figure 5.18. Shear force-deflection for reference beams (6.1 and 6.2), strengthened beams with grooved wires (7.1 and 7.2), beams with U-shape stirrups (8.1 and 8.2), and beams with spirals confining only the concrete compression chord (9.1 and 9.2)

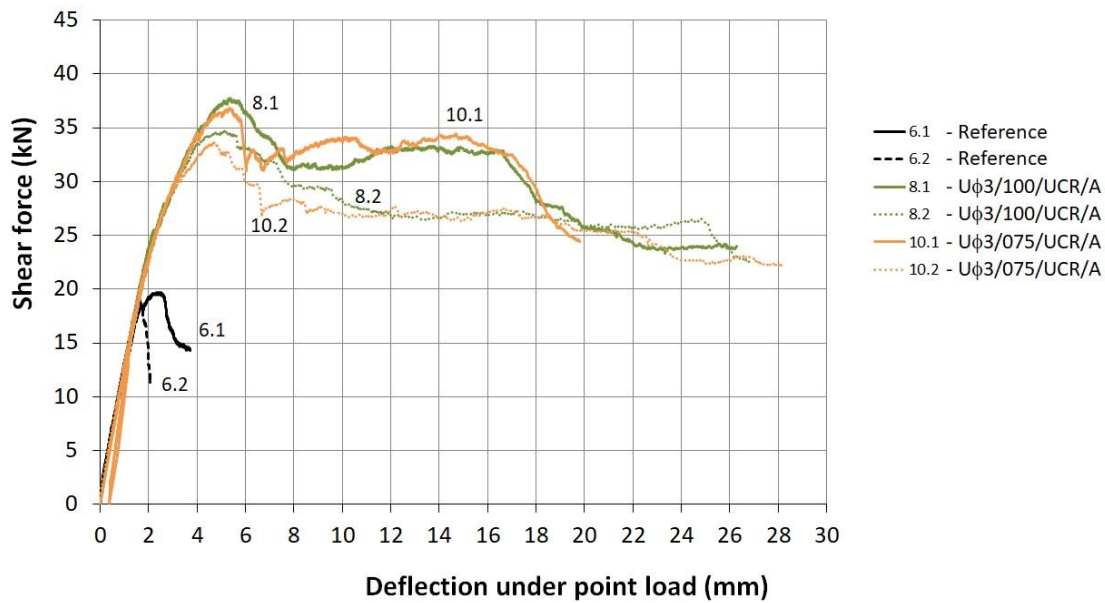


Figure 5.19. Shear force-deflection for reference beams (6.1 and 6.2), strengthened beams with U-shape stirrups with pitch equal to 100 mm (8.1 and 8.2), and with pitch equal to 75 mm (10.1 and 10.2)

As will be seen in the chapter 6, for beams strengthened with U-shape stirrups lower values of initial imperfection are expected and, therefore, higher values of recovery stresses could develop. Anyway, this increment of recovery stress is small enough so that the effect of shear force increment cannot be confirmed in all cases.

The crack patterns in the reference beams and in the strengthened beams were very similar for the beam tests of the two phases. It can be seen in figure 5.20, where crack pattern of all beams just after their maximum applied load is depicted. For clarity, only one side of the beam, the critical one, is shown. For most of the tested beams, a typical shear crack pattern is detected with a first branch and a second branch of the critical shear crack. The first branch developed inclined with an average value of 47° , but with a relatively high scatter from around 30° to 60° , from the lower part of the beam to the vicinity of the neutral axis. A second branch developed from the tip of the first branch to the point of load application, crossing the compression chord.

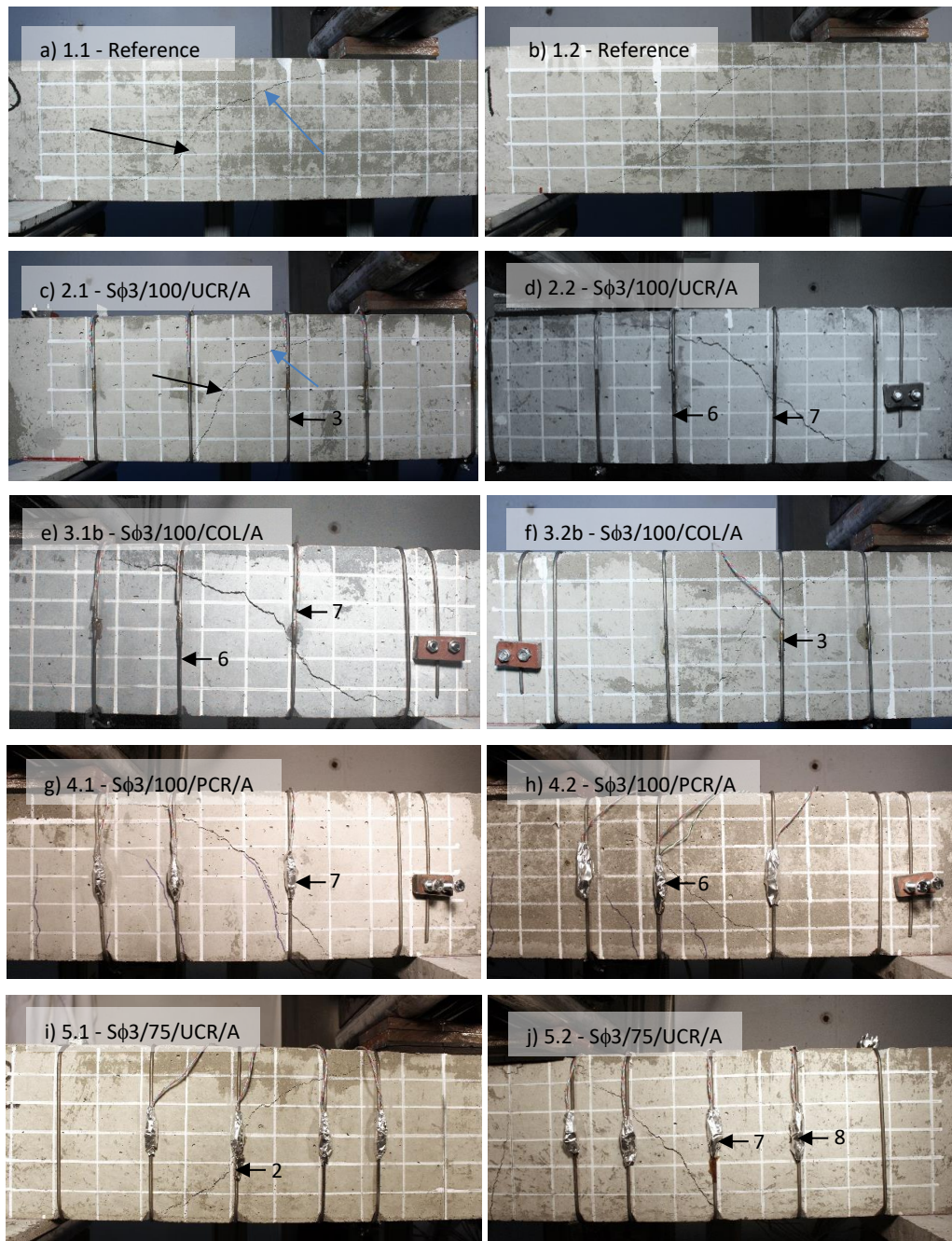


Fig. 5.20 a) – j) Photographs of first phase beam specimens just after their maximum load was achieved and their crack patterns, with the numbering of the vertical links crossing the critical crack (except for beam 5.2 failed in bending)

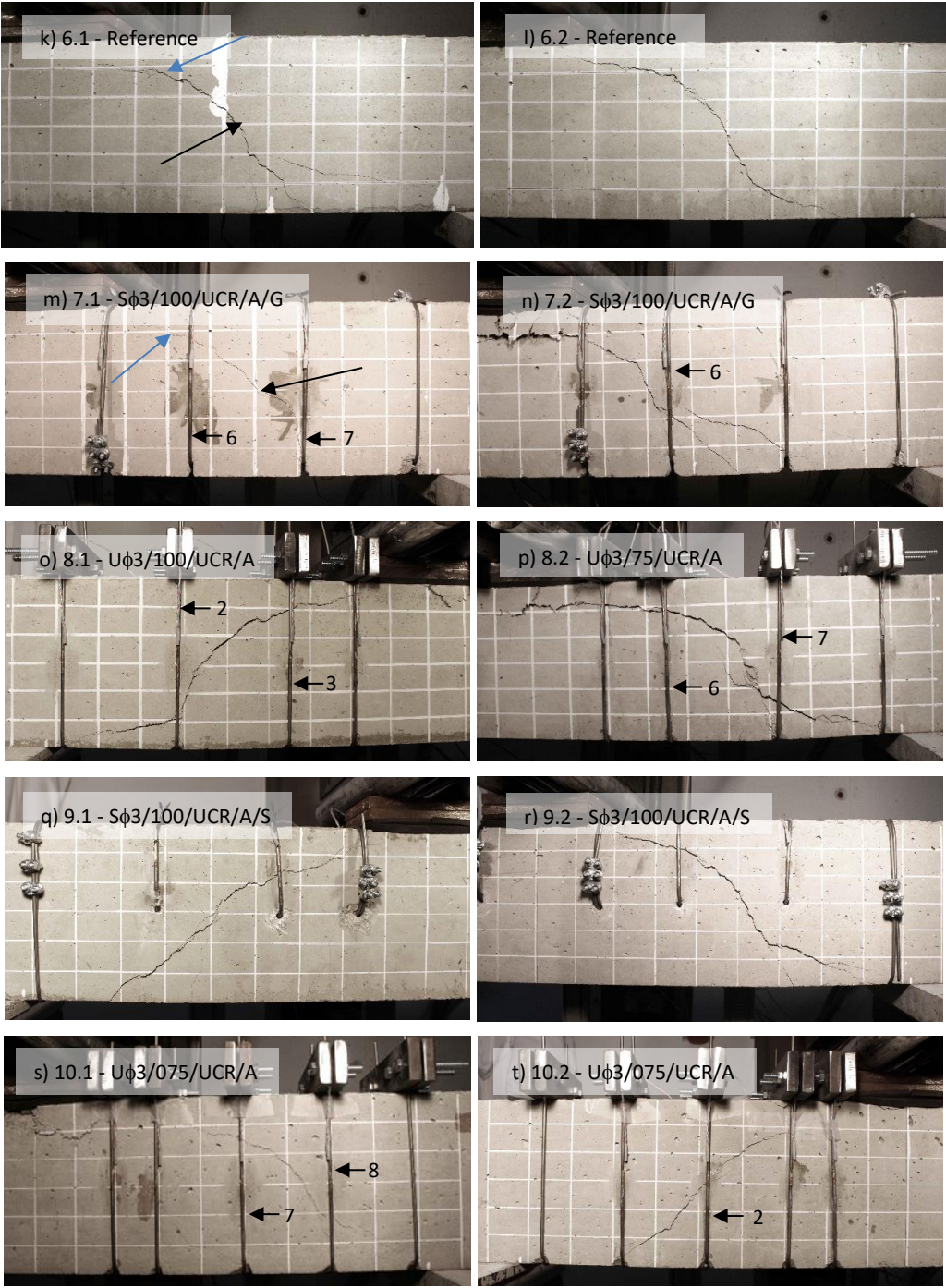


Fig. 5.20 k) – t). Photographs of second phase beam specimens just after their maximum load was achieved and their crack patterns, with the numbering of the vertical links crossing the critical crack

Two branches of the critical shear crack can be detected as indicated with arrows in figures 5.20a and 5.20k for reference beams, and figures 5.20c and 5.20m for not pre-cracked (UCR), and shear strengthened, activated SMA, (A) beams. The black arrows correspond to the first branch and the blue arrows correspond to the second branch which have different inclination. The applied load that develop the whole first branch of the critical shear crack during the reference tests (figures 5.20a and 5.20b) was useful to approximate value of the pre-load to be applied for beams 4.1 and 4.2, the pre-cracked beams. Thus, the pre-cracking procedure for beams 4.1 and 4.2 (figures 5.20g and 5.20h) had to be carried out with an applied load approximately 98% of the maximum load of the reference beams, as stated before.

The commented fact that the shape of the critical crack was similar in non-strengthened and strengthened beams is shown in the form of the critical crack in the PCR (4.1 and 4.2) and in the UCR (2.1 and 2.2) beams, that is very similar. This involved that the same number of links (segments of the wire) were mobilized due to the crack opening and that the strengths of PCR and UCR beams were very similar. Note that each inclined link that runs the rear face, not visible in the figure 5.20, contributed better to crack closure and hence, to shear strengthening, since they were more perpendicular to the first branch of the critical crack. It can be also seen that pitch of the pseudo-rectangular spiral was different for the link close to the load application point due to the need for space for the loading plate. Thus, for the spiral pitch equal to 100 mm, the last pitch, close to loading plate, was reduced to 75 mm. For the spiral pitch equal to 75 mm, the last pitch was reduced to 50 mm close to loading plate. This adaptation did not affect the development of the first branch of critical crack.

An important aspect to be considered, regarding shear strengthening, was the number of activated links of the spirals crossed by the first branch of critical crack. The higher the number of links crossed, the higher the contribution of the wire to the shear strength. Therefore, for beams 2.1, 2.2, 3.2b, 4.1, 4.2, 5.1 and 7.2, quite similar values of shear strength were achieved regardless of the pitch. As can be seen in figures 5.20, almost in all cases up to 3 links (adding both front-vertical and rear-inclined links) were crossed by the first branch of the shear critical crack. Note the for beams 8.1, 8.2, 10.1 and 10.2 only with vertical U-shape stirrups, the same comment can be made.

Regarding to beams 5.1 and 5.2, with activated spiral pitch of 75 mm, the beam 5.2, although with the same configuration of beam 5.1, developed bending failure, as can be seen in fig. 5.20j (bending crack on the left-hand side of the picture). This may be due to the fact that the starting point of the critical shear crack in the beam 5.2 was forced by the small groove in the vertical of the link 7, relatively close to the point of load application. For this reason, in the two sides of the beam 5.2, direct struts could be developed connecting the load application point to the support without passing through cracked concrete, enhancing the arch effect and thus increasing the shear strength. However, in beam 5.1, the critical shear crack developed closer to the support. Since the shear force needed to reach the ultimate bending moment at the beam was 40.47 kN (as stated in chapter 5.1), beam 5.2 failed in bending with a shear force equal to 41.82 kN (see table 5.3).

Regarding the grooves of beams 7.1 and 7.2, in figure 5.20m and 5.20n a significant difference can be seen in the development of the first branch of critical crack. Thus, for beam 7.1 this branch reached the third groove, and because of that, only one link (inclined rear face) was crossed until failure. On the contrary, beam 7.2 developed a first branch crossing 3 spiral sections (one vertical and two inclined). This could explain the low shear strength of beam 7.1, with a shear strength increment due to strengthening over the base value of reference beams 6.1 and 6.2 (fig. 5.18) of one third of the shear strength increment of beam 7.2.

In the case of beams 9.1 and 9.2, as can be seen in figures 5.20q and 5.20r, the confinement achieved due to spiral strengthening only influenced the development of the second branch of critical crack and the post-peak behavior. As will be seen in Chapter 6, the level of initial imperfection of the spiral was high for these beams, due to the difficulty in placing the spiral and the shorter length of the links.

5.6.2 MEASURED STRAINS

The installed gauges are capable to give interesting information about the behavior of the tested beams. Strain gauges installed in both, the longitudinal reinforcement and the traverse strengthening, gave quantitative information about strains and they were capable to show where the failure of the beam developed, and whether the beam failed in shear or bending. Figures 5.21 and 5.22 show the strain measured in the gauges of the longitudinal

reinforcement of all tests. A schematic drawing of the locations of the gauges is depicted on graph of beam 1.1 and in figs. 5.2 and 5.3. Almost all longitudinal strain gauges worked properly recording strains except for the gauge GLONG.02 of beam 5.1 where an unexpected rupture was detected close to the failure load of the test.

The approximate yielding strain is shown in the graphs by means of a vertical dashed line. It is taken from the measured yielding strength of the tested steel rebars ($f_y = 513 \text{ MPa}$) as previously shown in subchapter 5.3 and it is given from Eq. 5.4:

$$\varepsilon = \frac{f_y}{E} = \frac{513}{200,000} = 0.002565 \quad (5.4)$$

It can be seen that in beam 5.2 (which failed in bending), the longitudinal reinforcement yielded at mid-span (Gauge GLONG.02, see fig. 5.21). However, in the other beams, the longitudinal reinforcement did not yield at mid-span, but instead the longitudinal bar yielded close to the support in the shear span where the critical crack developed.

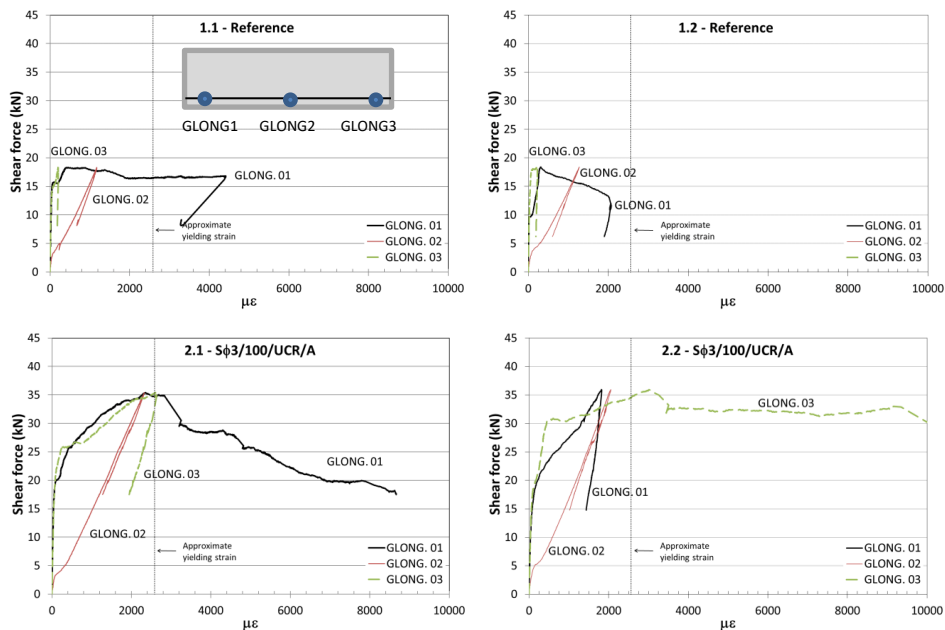


Figure 5.21a. Strains measured in the longitudinal reinforcement of beams 1.1, 1.2, 2.1 and 2.2. A schematic drawing of the locations of the gauges is depicted on graph of beam 1.1

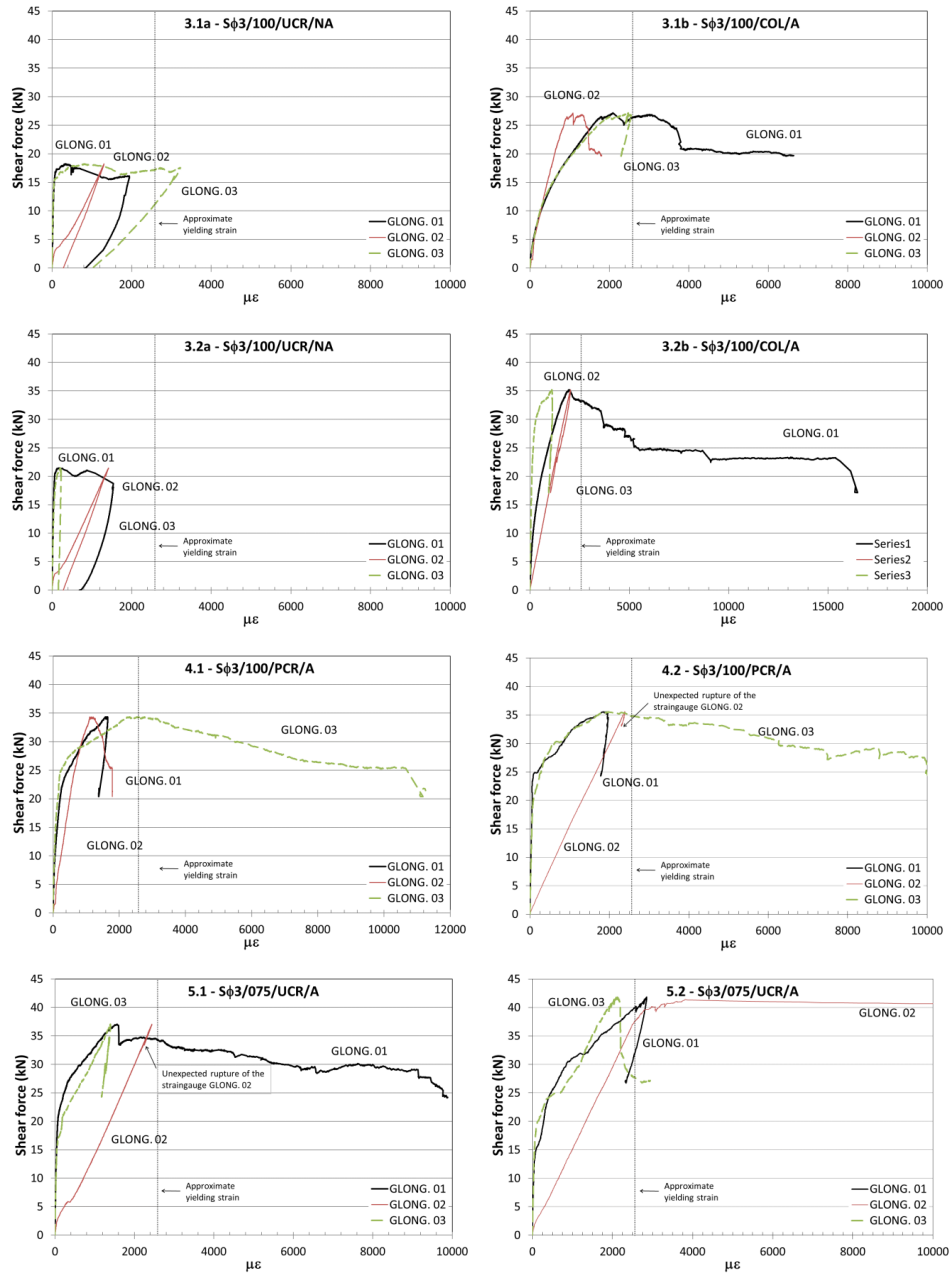


Figure 5.21b. Strains measured in the longitudinal reinforcement of beams: 3.1a, 3.1b, 3.2a, 3.2b, 4.1, 4.2, 5.1 and 5.2

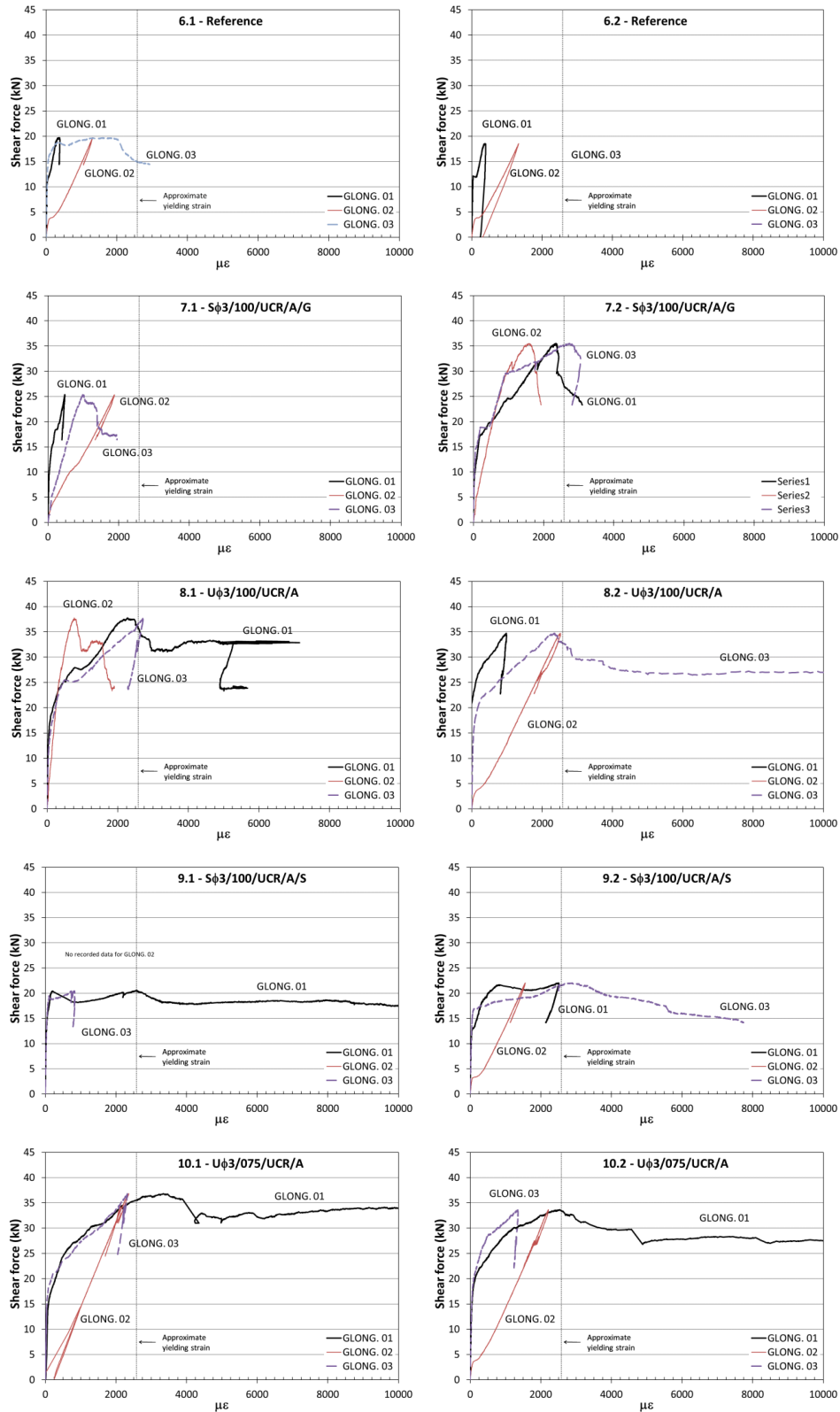


Figure 5.22. Strains measured in the longitudinal reinforcement of beams of the second phase

The strain measured in the vertical links of the Ni-Ti-Nb pseudo-rectangular spiral are represented for the beam tests in fig. 5.23 and fig. 5.24. A schematic drawing of the locations of the gauges are depicted on graphs of beams 2.1 and 2.2, and in figs. 5.2 and 5.3. For clarity, only the strain measured in the gauges located in the critical span, where the failure took place, are represented.

The strain in the vertical links remained negligible until the shear cracks propagated. The values of the measured strains of the gauges were directly related to crack openings since the configuration of the spirals, with no adherence between concrete and Ni-Ti-Nb wires and only contact between them in the turn of the wires in each edge of the faces of the beams, made that all strain in each wire crossed by a crack, and consequently wire elongation, was a consequence of the opening of the crack.

At failure, different strain values were measured by the strain gauges attached at each vertical link. This ensures that there had been no general wire slippage around the corners of the cross sections. Visual inspection throughout all tests also confirmed that the slippage of the wires was avoided. Table 5.4 shows the strains at failure measured in all gauges of the beams.

Table 5.4. Strains ($\mu\varepsilon$) at beam failure measured in the gauges of the vertical links of the beams. In bold gauges in links of spans that failed in shear

Beam	GTR.01 ($\mu\varepsilon$)	GTR.02 ($\mu\varepsilon$)	GTR.03 ($\mu\varepsilon$)	GTR.04 ($\mu\varepsilon$)	GTR.05 ($\mu\varepsilon$)	GTR.06 ($\mu\varepsilon$)	GTR.07 ($\mu\varepsilon$)	GTR.08 ($\mu\varepsilon$)
2.1	-50	1137	3148	-1168	378	1271	4148	-8
2.2	-11	1799	430	137	5	4645	4675	-83
3.1a	-	-48	-89	-38	-4	-389	-139	-
3.1b	-	*	-42	-5	*	4	*	-
3.2a	-	-9	70	61	-94	-49	-43	-
3.2b	-	32	2016	5	2	-87	27	-
4.1	-	759	131	-230	-20	60	1968	-
4.2	-	3982	2568	-103	305	2686	1214	-
5.1	26	2371	784	84	-23	32	-490	-661
5.2	2070	83	67	13	31	-72	18	667
7.1	-	-226	-244	-386	-353	1167	1711	-
7.2	-	-308	-2842	2159	909	3870	2311	-
8.1	-1	2207	3031	1041	410	3417	3491	-47
8.2	-48	112	2519	-340	1083	5575	3191	-35
9.1	-	-34	-2354	-661	-410	77	-18	-
9.2	-	*	15	*	-127	*	-101	-
10.1	-33	1829	1332	-124	532	2	2794	1944
10.2	2913	5091	1610	1452	1000	2143	1321	443

-No strain gauge used in positions GTR.01 and GTR.08

*Gauges did not provide proper data due to an error in the test set-up

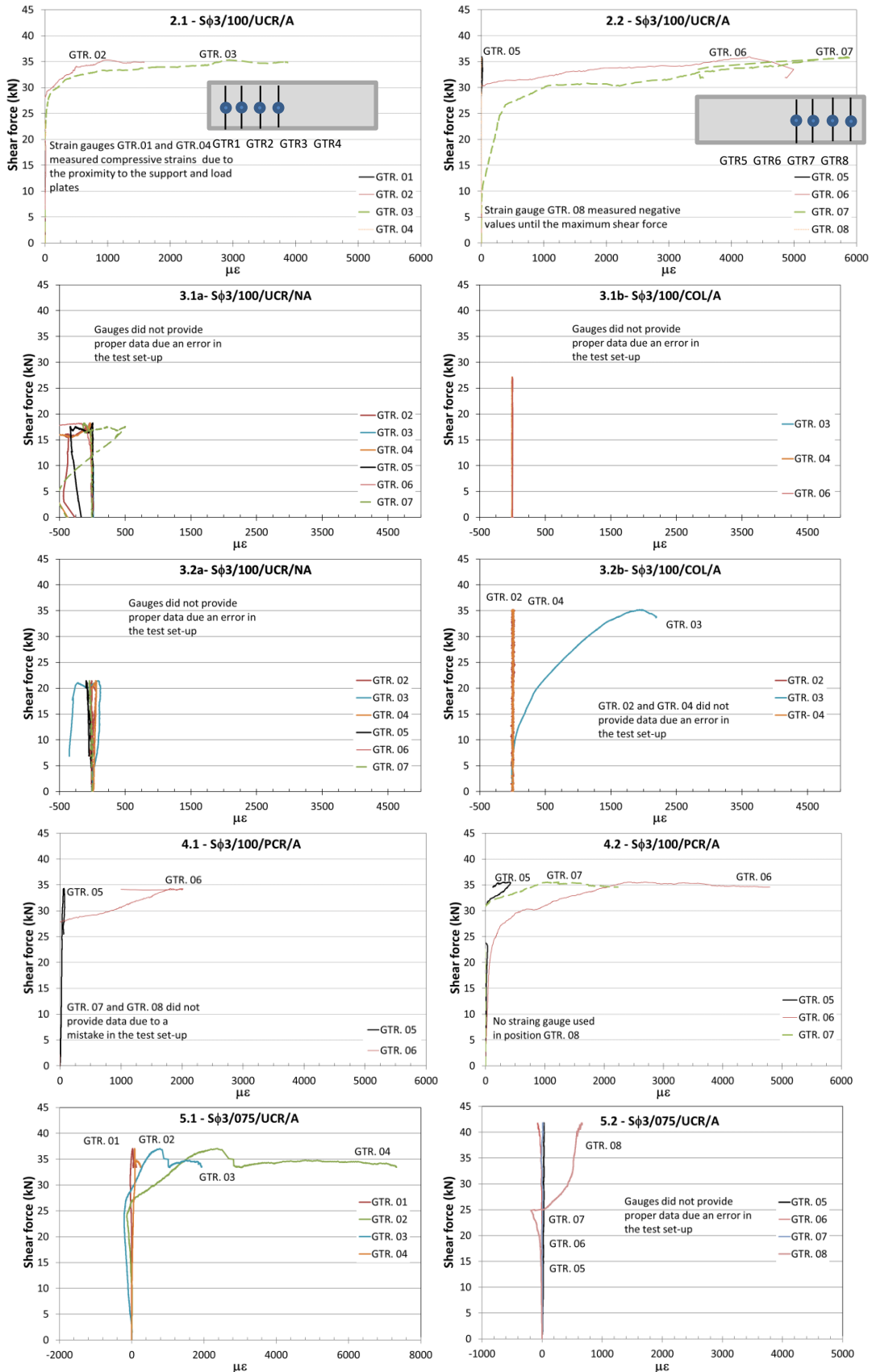


Figure 5.23. Strains measured in the spiral vertical links in beams 2.1, 2.2, 3.1a, 3.1b, 3.2a, 3.2b, 4.1, 4.2, 5.1, and 5.2. Schematic drawings of the locations of the gauges are depicted on graphs of beams 2.1 and 2.2

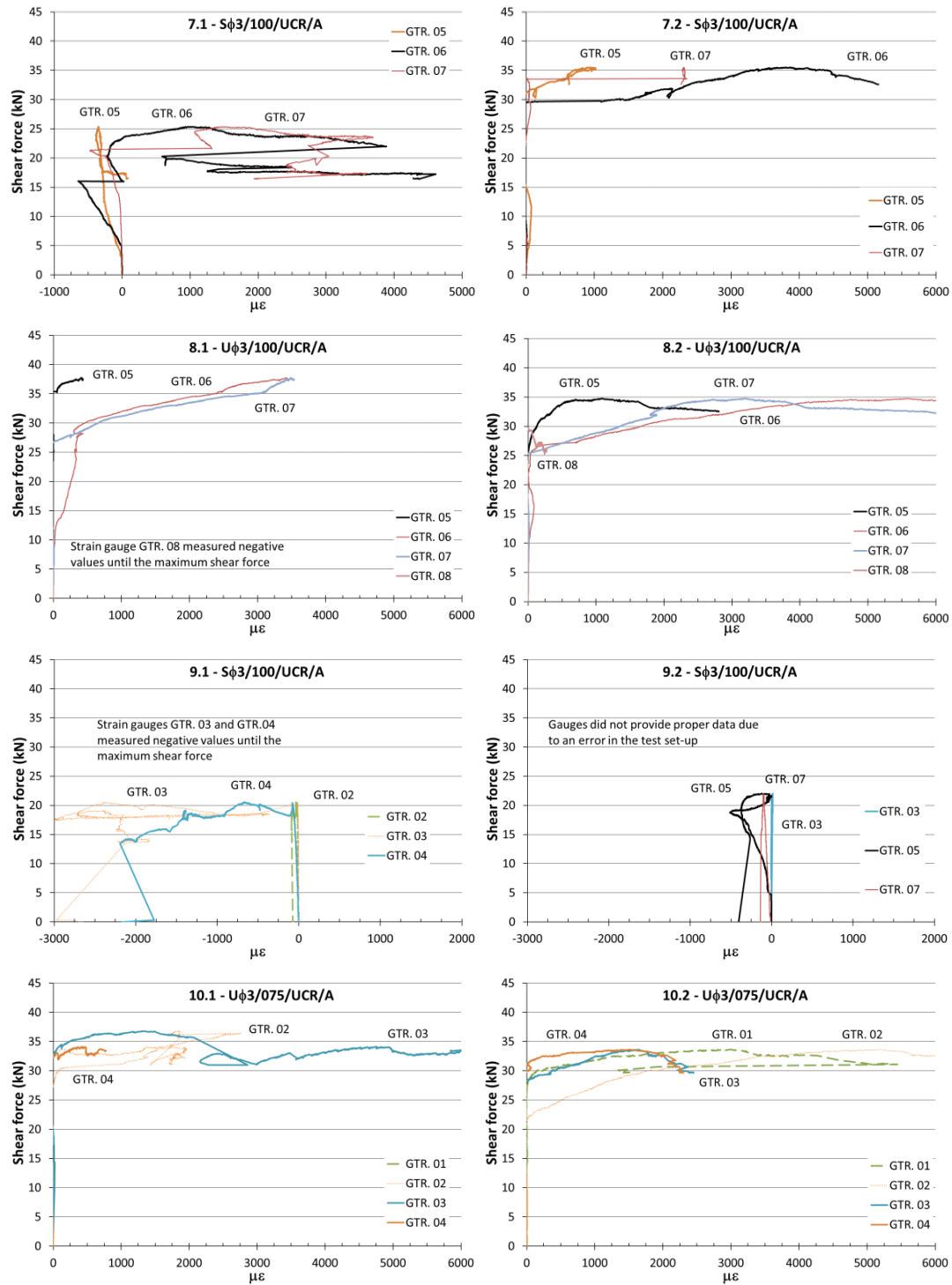


Figure 5.24. Strains measured in the vertical links of the spirals in beams 7.1, 7.2, 8.1, 8.2, 9.1, 9.2, 10.1 and 10.2

For beams 3.1 and 3.2 some difficulties in the set-up for the strain gauges were encountered, since the gauges were installed previously to the activation process with a heat gun and, although the gauges were attached with special thermal adhesive (for temperatures up to 300 °C), during the activation process some gauges were disabled and only one gauge in beam 3.2 worked correctly, measuring strains up to 3000 $\mu\epsilon$. This encountered difficulty was overcome with an additional protection of the gauges of beams 4.1 and 4.2, protecting them with special butyl wrap and external thermal tape (figure 5.25).

The stresses at failure in the vertical links may be obtained from the measured strains, taking into account the links crossing the first branch of the critical crack. For example, in beam 2.2, the first branch of the critical crack crossed the vertical link in which GTR.07 was attached (fig. 5.20d). Taking into account the tangent modulus of elasticity of Ni-Ti-Nb after the generation of recovery stresses (25 GPa), see table 4.8, the increase of stress in the Ni-Ti-Nb wire is given by Eq. 5.5:

$$\sigma = E \cdot \varepsilon = 25,000 \cdot 4,675 \cdot 10^{-6} = 116.87 \text{ MPa} \quad (5.5)$$



Figure 5.25. Beam 4.2 with shear strengthening ready to be activated after the application of a pre-load (highlighted fissures) with specially protected strain gauges

This value will have to be added to the recovery stress developed due to activation when considering the stresses developed in the strengthening wires (for predicting the shear strength of the tested specimens, see Chapter 7). Also, crack opening in the first branch developed at failure can be approximated although the crack widths were not monitored during the tests. Considering, that the length of 150 mm of spiral link that developed such strain had an elongation of 0.70 mm ($0.004675 \cdot 150$), all this elongation is due to the shear crack width in the vertical direction, which is a reasonable value. This aspect can be considered only in the cases where only one crack crosses the vertical link. This happens in most of the cases (see fig. 5.20).

To obtain a reasonable value of stresses developed at failure in all tested beams, the strains measured in the vertical cracks crossed by the first branch of critical crack have been analyzed and they are shown in table 5.5. Note that in some cases the first branch of critical crack did not develop exactly in the location of a vertical wire, and in those cases more than one strain gauge has been taken into account. Therefore, for modelling purposes, average values may be considered.

Considerable scatter had been encountered and values between 1000 $\mu\epsilon$ and 5000 $\mu\epsilon$ were obtained. Anyway, the average value of 3007 $\mu\epsilon$ with a standard deviation of 1221 $\mu\epsilon$ and covariance of 41 % for all tested beams are reasonable values in such test measurements.

The crack widths were not monitored during the tests. However, the considered average strain value of 3000 $\mu\epsilon$ of Ni-Ti-Nb spiral link is equivalent, assuming one single shear crack (as may be seen in figure 5.20), leads to a shear crack width in the vertical direction of 0.45 mm at failure (length of 150 mm of spiral branch), what is a reasonable value. For reference: 2000 $\mu\epsilon$ involves a shear crack width in the vertical direction of 0.30 mm at failure, and 5000 $\mu\epsilon$ involves a shear crack width in the vertical direction of 0.75 mm at failure.

Table 5.5. Strains ($\mu\epsilon$) measured in strain gauges attached to vertical links crossed by the first branch of the critical crack.

Beam	Failure type	V_u (kN)	Gauges in links crossing the critical crack				Average $\mu\epsilon$	σ (MPa)
			GTR	$\mu\epsilon$	GTR*	$\mu\epsilon$		
2.1	Shear	35.41	3	3148	-	-	3148	79
2.2	Shear	35.95	6	4645	7	4675	4660	116
3.1b	Shear	27.14	6	#	7	#	#	#
3.2b	Shear	35.21	3	2016	-	-	2016	50
4.1	Shear	34.35	7	1968	-	-	1968	49
4.2	Shear	35.60	6	2686	-	-	2686	67
5.1	Shear	37.04	2	2371	-	-	2371	59
5.2	Bending	41.82	1	1303	-	-	\$	\$
			Average	2806			Average	70
			St. Dev.	1003			St. Dev.	25
			Cov.(%)	36			Cov.(%)	36
7.1	Shear	25.36	6	1167	7	1711	1439	29
7.2	Shear	35.51	6	3870	-	-	3870	97
8.1	Shear	37.74	2	2207	3	3031	2619	55
8.2	Shear	34.75	6	5575	7	3191	4383	139
9.1	Shear	20.54	#	#	#	#	#	#
9.2	Shear	22.03	#	#	#	#	#	#
10.1	Shear	36.79	7	2794	8	1944	2369	70
10.2	Shear	33.65	2	5091	-	-	5091	127
			Average	3208			Average	86
			St. Dev.	1439			St. Dev.	43
			Cov.(%)	45			Cov.(%)	49

* Second gauge crossed by first branch of critical crack

Gauges did not provide proper data due to an error in the test set-up

\$ Not considered strain and stress (bending failure)

5.7 COMPARATIVE ANALYSIS OF THE BEAM TESTS

The results of the experimental campaign carried out within the two phases of beam tests show the effectiveness of this active shear strengthening of RC beams using Ni-Ti-Nb wires methodology. Different configurations of shear strengthening of RC beams were used to validate the experimental campaign. The main results of the whole experimental program in terms of average data are summarized in table 5.6. These average values for all types of shear strengthened beams show a significant increment of shear force (%) and deflection increment (times) for the strengthened beams with respect to non-strengthened ones.

Table 5.6. Summary of average test results of the whole experimental campaign

Average beams with...	V_{test} (kN)	E_{ff}	δ at V_{test} (mm)	δl (l/l)	Shear force increment (%)	Deflection increment (times)
Non-strengthened (1.1, 1.2, 3.1a, 3.2a, 6.1, 6.2)	19.10	-	1.80	1/433	-	-
100 mm spiral pitch (2.1, 2.2, 3.2b, 4.1, 4.2, 7.1, 7.2)	33.07	1.73	4.13	1/195	73	2.3
75 mm spiral pitch (5.1, 5.2)	39.43	2.06	5.38	1/154	106	3.0
Spirals (2.1, 2.2, 3.2b, 4.1, 4.2, 5.1, 5.2, 7.1, 7.2)	34.34	1.80	4.38	1/187	80	2.4
100 mm U-shape stirrup (8.1, 8.2)	36.25	1.90	5.25	1/145	90	2.9
75 mm U-shape stirrup (10.1, 10.2)	35.22	1.84	5.02	1/152	84	2.8
U-shape stirrups (8.1, 8.2, 10.1, 10.2)	35.73	1.87	3.98	1/225	87	2.2
Compression chord confinement (9.1, 9.2)	21.29	1.11	3.35	1/229	11	1.9
100 mm pitch (2.1, 2.2, 3.2b, 4.1, 4.2, 7.1, 7.2, 8.1, 8.2)	33.70	1.76	4.35	1/185	76	2.4
75 mm pitch (5.1, 5.2, 10.1, 10.2)	37.33	1.95	5.20	1/153	95	2.9
Strengthened (2.1, 2.2, 3.2b, 4.1, 4.2, 5.1, 5.2, 7.1, 7.2, 8.1, 8.2, 10.1, 10.2)	34.74	1.82	4.59	1/176	82	2.6

5.8 CONCLUSIONS OF THE BEAM EXPERIMENTAL CAMPAIGN

With regard to the experimental campaign, the effectiveness of the methodology of using Ni-Ti-Nb wires as pseudo-spirals (generating recovery stresses as a prestressing system) for active external shear strengthening of RC beams was confirmed. An average increase of 82 % in shear force and an increase of 2.6 times deflection at maximum shear force were measured in the instrumented beams of the experimental campaign. The other main conclusions of the experimental campaign are:

- The negligible effect of the pseudo-spiral placed around the beam without being activated can be seen. However, when the spiral is activated, the strengthening method is clearly effective in all cases.
- The behavior of the activated beams, in terms of shear strength and maximum deflection, is very similar and pre-cracking the beams does not affect the results if the pre-crack load is removed before activating the Ni-Ti-Nb wires.
- The strengthening method was able to increase the shear strength of the beams even after they had already collapsed and unloaded in a previous test, without conducting any additional rehabilitation work.
- The use of grooves does not represent an increase in shear strength in these beams. In addition, its use is not recommended since additional works are required to perform the grooves and they can initiate unwanted cracks.
- Non-significant differences between spirals and U-shape stirrups in shear strength and deflection at the maximum shear force were detected. However, lower values were expected from U-shape stirrups compared to spirals but only encountered for 75 mm pitch. Unexpected high values in comparison with those obtained with spirals were reached. Other aspects could have affected the tested beams, like initial imperfections of the initial installation of the Ni-Ti-Nb wires around the beams and the fact that the U-shape stirrups do not weaken the compression chord.
- The measured strains in vertical links ranged between 1000 $\mu\epsilon$ and 5000 $\mu\epsilon$. Anyway, the average value of 3007 $\mu\epsilon$ with a standard deviation of 1221 $\mu\epsilon$ and covariance of 41 % for all tested beams are reasonable values in such test measurements. An average

strain value of $3007 \mu\epsilon$ is equivalent to a vertical shear crack width of 0.45 mm at failure, which is a reasonable value.

- The configuration of the RC beams, with or without strengthening, was intended to obtain shear failures of the tested beams and, indeed, these were obtained in almost all instances: only for beam 5.2 with a spiral pitch of 75 mm was bending failure achieved. Note that beam 5.1, with the same spiral pitch of 75 mm as beam 5.2, failed in shear.
- The methodology followed in the experimental campaign to externally strengthen the specimens is simple to put in practice: rectangular spirals are installed by hand, anchored by U-shape saddle clamps and activated using a heat gun.

6. EXPERIMENTAL STUDY OF THE Ni-Ti-Nb RECOVERY STRESSES UNDER NON-IDEALIZED CONDITIONS

6.1 PLANING OF THE TESTS AND TEST PROCEDURE

The Ni-Ti-Nb alloy wires, characterized in Chapter 4, were used to strengthen shear critical RC beams tested up to failure (Chapter 5). The wires were initially tested under idealized conditions (universal testing machine with thermal chamber, in Chapter 4). However, during the strengthening of the beams, it was seen that the performance of the wires on the RC beams took place under non-idealized conditions: activation by means of a heat gun, and the links of the pseudo-rectangular spirals were not perfectly straight before the activation). Therefore, a new experimental campaign to study the behavior of the Ni-Ti-Nb wires under non-idealized conditions was carried out.

The general planning of this campaign can be seen in table 6.1. The first column of table 6.1 is the test number. The second one is the group of tests from 1 to 4 (already defined in chapter 4). The third column is the date when the test was carried out. The fourth to sixth columns indicate the initial phase of the sample, intermediate phase (if it exists depending on the type of test) and the final phase of the sample, respectively. The seventh column is a short description of the type of test. The eighth column is the temperature of the sample during the test (if more than one temperature appears, they indicate the variation of temperatures during the whole test). The ninth column is the applied preload to the sample and the tenth column is the initial imperfection of the sample.

For this experimental campaign, there were tests included into the groups 1 and 4 (only one test). Those included into the group 1, differ from those of the Chapter 4 in the way of heating of the sample and the initial pre-load. The activation heat treatment for this second set of tests was done by mean of a heat gun ensuring the prescribed temperature of 200 °C (optimum temperature as seen in Chapter 4). The temperature of the sample was monitored by means of thermocouples. The heat gun was a Bosch PHG 500-2 (figure 6.1a).

Different configurations were considered for the tests included in Group 1 (table 6.1): different pre-loads of the samples (8 or 40 MPa – Tests #21-#26), and different initial imperfection of the sample (samples tested with initial imperfection-curvature, tests #36-#41). The test procedure followed the same basic steps as seen in Chapter 4, except for the aspects already commented: once the sample was placed between the clamps, the displacement between them was restrained, and the sample was heated (activated), generating recovery stresses. In the case of the samples with initial curvature (figure 6.1b), they recovered some strain (to become straight) prior to developing recovery stresses. Based on those tests, with different initial curvatures, the actual recovery stresses on the pseudo-rectangular spirals installed wrapping the beams were evaluated for calculating the shear strength of the retrofitted beams (Chapter 7).

Moreover, additional tests were planned to study the behavior of the self-anchorage of the wire by means of U-bolt saddle clamps. Also, a recovery stress test (test #42 in table 6.1) and a tensile test (#43, group 4) with the same test procedure as defined in Chapter 4 were carried out.



Figure 6.1. a) Heating with a heat gun during activation of a sample, and b) installed sample between clamps with initial curvature

Table 6.1. List of planned tests under non-idealized conditions

TEST N.	GROUP	DATE	INITIAL PHASE	INTERM. PHASE	FINAL PHASE	TYPE	TEMP. (°C)	PRE-LOAD (MPa)	INITIAL IMPERFECTION (%)
21	1	30/11/2016	M	-	A	RECOVERY STRESS	RT-200-RT	8	0
22	1	30/11/2016	M	-	A	RECOVERY STRESS	RT-200-RT	8	0
23	1	01/12/2016	M	-	A	RECOVERY STRESS	RT-200-RT	8	0
24	1	01/12/2016	M	-	A	RECOVERY STRESS	RT-200-RT	40	0
25	1	09/12/2016	M	-	A	RECOVERY STRESS	RT-200-RT	40	0
26	1	09/12/2016	M	-	A	RECOVERY STRESS	RT-200-RT	40	0
36	1	02/01/2017	M	-	A	REC. STRESS - INITIAL IMPERFECTION	RT-200-RT	8	0.54
37	1	02/01/2017	M	-	A	REC. STRESS - INITIAL IMPERFECTION	RT-200-RT	8	2.34
38	1	17/01/2017	M	-	A	REC. STRESS - INITIAL IMPERFECTION	RT-200-RT	8	4.12
39	1	17/01/2017	M	-	A	REC. STRESS - INITIAL IMPERFECTION	RT-200-RT	8	10.99
40	1	08/02/2017	M	-	A	REC. STRESS - INITIAL IMPERFECTION	RT-200-RT	8	4.94
41	1	08/02/2017	M	-	A	REC. STRESS - INITIAL IMPERFECTION	RT-200-RT	8	5.92
42	1	10/02/2017	M	-	A	RECOVERY STRESS U-BOLT UNION	RT-200-RT	8	-
43	4	22/02/2017	A (M)	-	M	MONOTONIC U-BOLT UNION	RT	8	-

6.2 TEST RESULTS

RECOVERY STRESSES. ACTIVATION WITH A HEAT GUN

Tests #21, #22, and #23 were performed with an initial pre-load of around 8 MPa as in Chapter 4. The results of these tests are presented in figure 6.2 and table 6.2. An average value of 452 MPa of recovery stress (σ_R) was obtained at the end of the test (minimum 25 min), with a maximum value, just after heating the sample, up to 520 MPa.

Additional tests were performed with an initial pre-load of 40 MPa. Slightly lower values of the recovery stresses were obtained in this case, with an average value of 435 MPa of recovery stress (σ_R) at the end of the test, with a maximum value, just after heating the sample, up to 503 MPa.

These results indicate that the higher the preload, the lower the stress recovery. Nevertheless, in the tested beams, when they were strengthened without any preload in the wires, those ones did not develop this reduction of stress at all, since the activation started from zero stress.

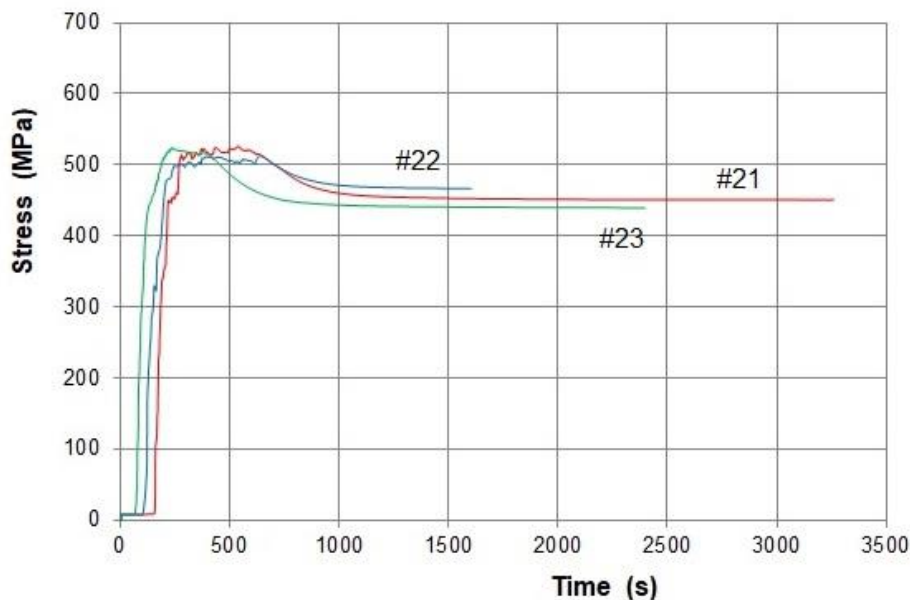


Figure 6.2. Recovery stress tests (stress-time). Pre-load of 8 MPa

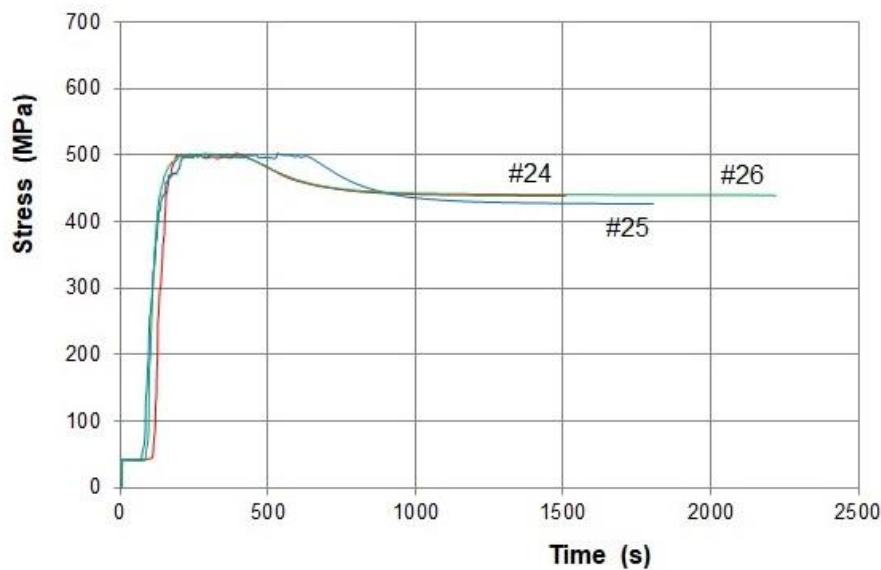


Figure 6.3. Recovery stress tests (stress-time). Pre-load of 40 MPa

Table 6.2. Recovery stresses of the samples with the heat gun activation treatment

Sample	Pre-load (MPa)	Maximum σ_R (MPa)	Average maximum σ_R (MPa)	Final σ_R (MPa)	Average final σ_R (MPa)
21	8	525		450	
22	8	512	520	466	452
23	8	523		439	
24	40	503		438	
25	40	503	503	426	435
26	40	504		440	

The results of these tests, with lower values of recovery stresses, are different from that of figure 4.11 (sample activated in thermal chamber). The duration of the heating process, and the thermal inertia of the heavy clamps, have probably affected the results. In any case, the values of recovery stresses to be used for predicting the shear strength (Chapter 7) will conservatively be those obtained with the activation with the heat gun.

RECOVERY STRESSES WITH DIFFERENT INITIAL IMPERFECTION ON THE SAMPLES AND ACTIVATION WITH A HEAT GUN

In the recovery stress tests presented in former paragraphs, the sample was perfectly straight before heating. However, the links of the pseudo-rectangular spirals placed around the beams

(Chapter 5) were not perfectly straight since some imperfections occurred. Thus, the initial length of the spiral links was slightly greater due to some initial curvature of the wire wrapping the beams (figure 6.4c). For this reason, recovery stress tests with different initial degrees of imperfection due to curvature were performed (figures 6.4 and 6.5).

Measures were taken of the retrofitted beams, as will be seen later in this section, and the initial curvature imperfections were characterized. The values of the different tests carried out can be seen in table 6.3. An initial imperfection is defined by Eq. 6.1, as the unit increment of length before activation (l_f) compared to a perfectly straight sample (l_o), see fig. 6.4e.

The length of the sample after activation, if all the initial imperfection is corrected, will be also equal to l_o .

$$i_0 = \frac{(l_f - l_o)}{l_o} \quad (6.1)$$

The Ni-Ti-Nb wires supplied had an initial prestrain of 6 %, and this value was confirmed heating some samples and measuring their strain recovery without any constrain or acting force, as was shown in table 4.10. Thus, the samples with an initial curvature lower than 6 %, will generate recovery stresses during activation, as can be seen in table 6.3 and in figure 6.6. It can be seen two tendencies of recovery stress values: values up to 4 % of initial imperfection where recovery stresses slowly decrease from 450 MPa to 370 MPa and values from 4 % up to 6 % of initial imperfection where recovery stresses rapidly decrease to a value of 170 MPa. Therefore, reasonable values of initial curvature (or initial imperfection) have to be established to obtain an adequate level of recovery stresses. Similar behavior was obtained by (Lee et al. 2015) in an application for prestressing of joining with the formation of recovery stresses in a Fe-based SMA obtaining substantial recovery stresses under non-ideal restraining conditions.

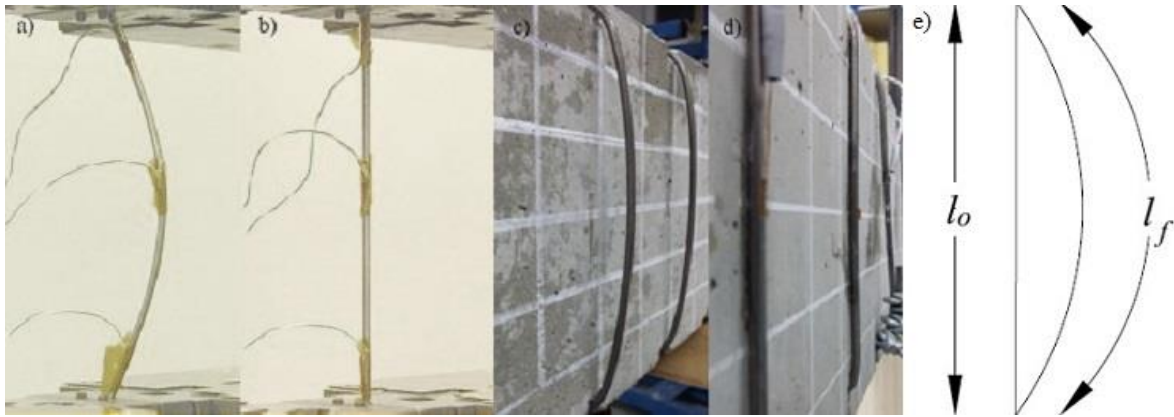


Figure 6.4. Initial imperfection (curvature) of SMA wires: a) before activation at tensile test, after activation at tensile test, c) before activation on a beam, d) after activation on a beam, and e) schematic drawing of the length before (l_f) and after activation (l_o)

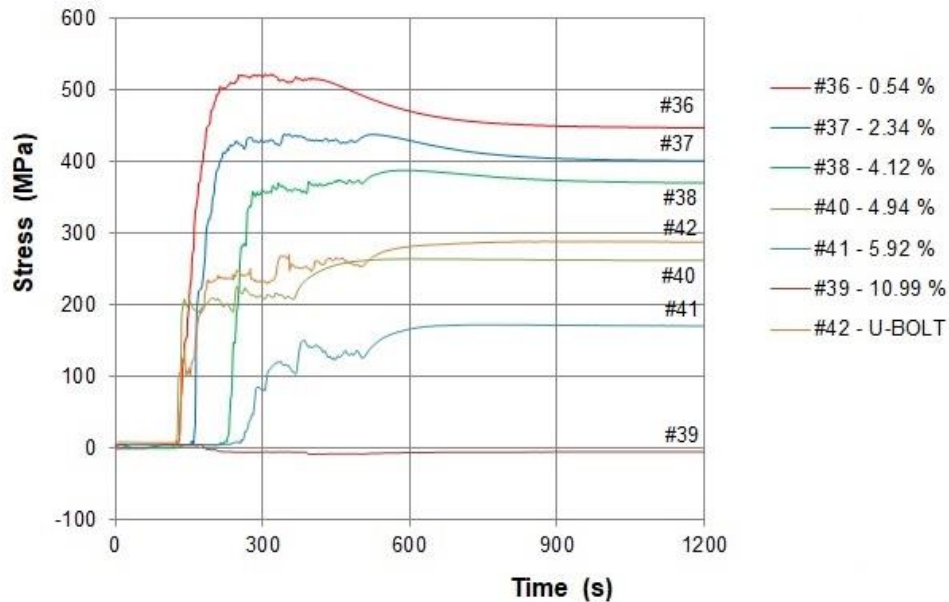


Figure 6.5. Recovery stress tests with initial imperfection

It is very important to characterize the relationship between recovery stress and initial imperfection. As will be commented later, the initial length (l_f) of the vertical links of the wires wrapping the RC beams was measured. The obtained lengths involved initial imperfections (i_o) between 0.6 % and 2.0 % for most cases. As shown in figure 6.6, an approximate safety-side performance curve was proposed by Eq. (6.2):

$$\sigma_R(i_o) = -7.6829 i_o^2 + 443 \quad (6.2)$$

where σ_R (MPa) is the recovery stress and i_o (%) is the initial imperfection. This curve was used to determine the recovery stress in each vertical link from the measured initial imperfection.

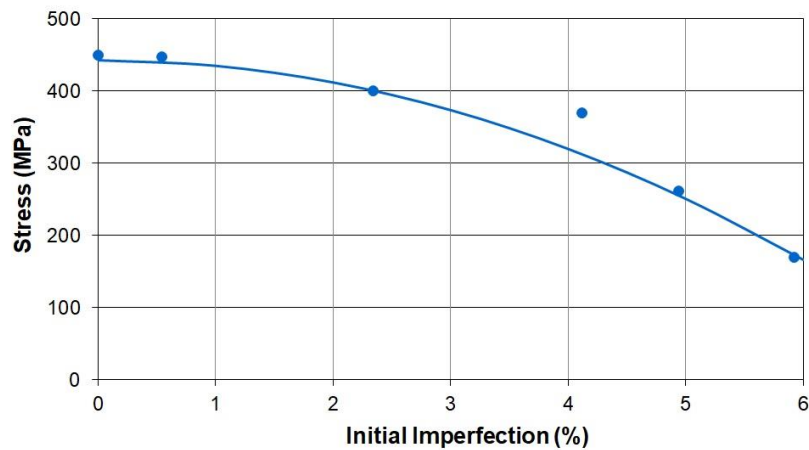


Figure 6.6 Recovery stress-initial imperfection relationship for different tests carried out and adjusted curve for modeling purposes

Table 6.3. Measured recovery stresses on the samples with initial imperfection (curvature)

Sample	Type of curvature	i_0 (%)	σ_R (MPa)
21	Straight	0	450
36	Curved	0.54	447
37	Curved	2.34	400
38	Curved	4.12	370
39	Curved	10.99	-5
40	Curved	4.94	262
41	Curved	5.92	170
42	U-bolt union	0	283

U-BOLT ANCHORAGE TESTS

An additional recovery stress test (#42) was carried out considering the union of the two wires by means of 3 U-bolts (figure 6.7). The same type of union was used as self-anchorage in the pseudo-rectangular spirals. The recovery stresses reached 283 MPa. This self-anchorage was placed in the soffit of the beam. In that location, very high recovery stresses are not needed. Afterwards a monotonic tensile test (#43) was carried out. A maximum tensile strength of 408 MPa was obtained (figure 6.8). In this test, after an initial elastic behavior with a maximum stress value of 310 MPa, slippage of the anchorage was produced and stresses between 300 MPa and 400 MPa were kept until strain of about 32 %, when a sudden drop of stress was produced.

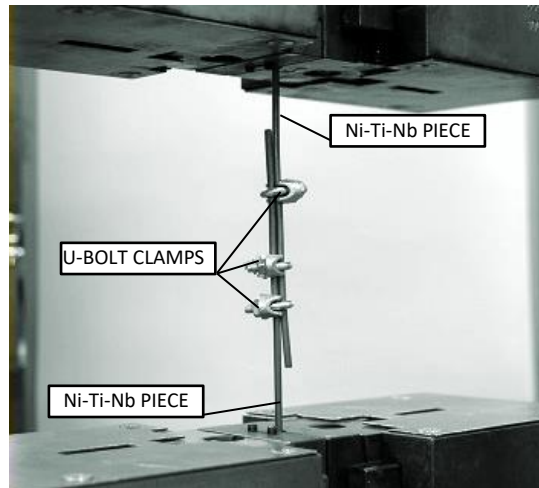


Figure 6.7. Two wires with U-bolt union sample between clamps ready to be tested

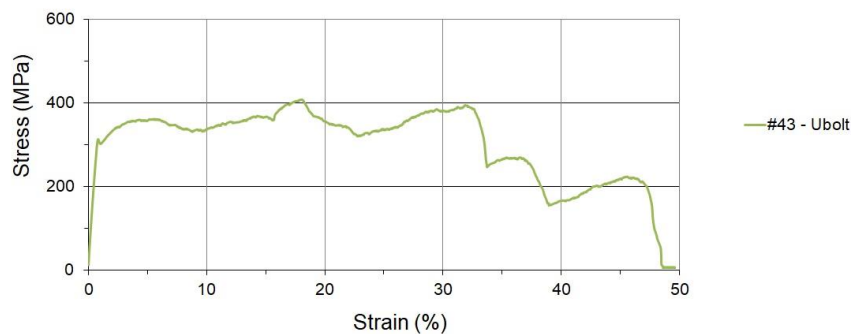


Figure 6.8. Monotonic tensile test on U-bolt anchorage sample

6.3 RECOVERY STRESS OF THE STRENGTHENING WIRES

The determination of recovery stresses of the wires wrapping the RC beams in the tests presented in Chapter 5 is an important issue because the strengthening effect in every beam depends on them. As previously explained, the higher the initial imperfection (curvature), the lesser the stress recovery are (eq. 6.2 and fig. 6.6). The recovery stresses were not directly measured in the tests, as the direct measure is not easy.

The installation procedure of the wires was intended to be accurate enough to produce a minimum loss of recovery stress due to the imperfections, but a slightly different imperfection was produced in each spiral link. It was also seen that the initial wire

configuration had an ellipse-like shape. The initial curvature length (l_f) was adjusted to an elliptical curve with main axes: height of the beam (considering the small grooves or the full transversal grooves), and the gap (g) between maximum separation of wire before activation of the beam (figure 6.9). Figures 6.10 and 6.11 show the strengthened beams at installation of wires but, before activation, and the imperfection of wire installation can be seen.

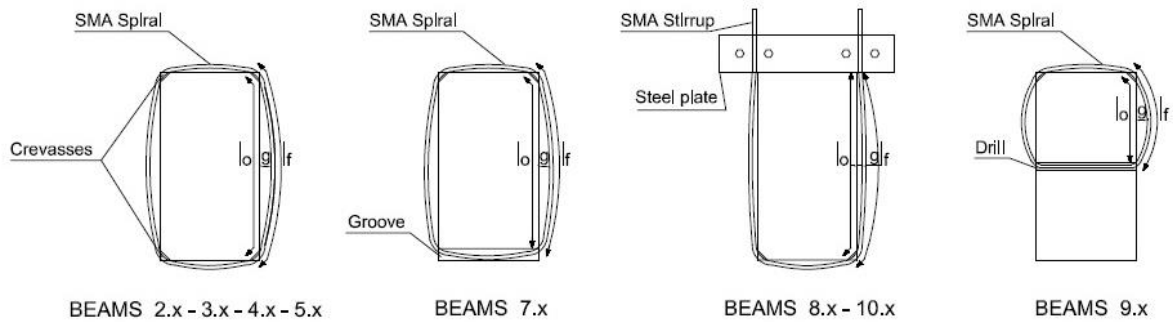


Figure 6.9. Schematic picture of beam cross-section and the wire installation



Figure 6.10. Beams 2.1, 2.2, 3.1a, 3.2a, 4.1, 4.2, 5.1, and 5.2 during spiral installation (initial imperfection before activation)



Figure 6.11. Beams 7.1, 7.2, 8.1, 8.2, 9.1, and 10.1 during wire installation (initial imperfection before activation).

The summary of the measured imperfection by means of the mentioned gap (g) and the obtained stress recovery of the selected branch (crossed by critical crack) of each beam can be seen in table 6.4. The first column shows the beam nomenclature, the second column shows the measured gap (g), the third column shows the estimated wire length of the spiral vertical link before activation (l_f), the fourth column shows the length of the wire after activation (l_o), and the fifth column shows the initial imperfection or length increment in percentage (i_o , Eq. 6.1). The estimated recovery stresses (σ_R) predicted by Eq. 6.2 are shown in the sixth column.

Table 6.4. Measured imperfection (i_o) and obtained recovery stresses (σ_R) for tested beams

Beam	g (mm)	l_f (mm)	l_o (mm)	i_o (%)	σ_R (MPa)
2.1 - S ϕ 3/100/UCR/A	11.2	159.5	156.6	1.83	417
2.2 - S ϕ 3/100/UCR/A	8.1	158.5	156.6	1.20	432
3.1a - S ϕ 3/100/UCR/NA	7.2	158.2	156.6	1.03	435
3.2a - S ϕ 3/100/UCR/NA	9.2	158.8	156.6	1.37	428
4.1 - S ϕ 3/100/PCR/A	7.0	158.1	156.6	0.94	436
4.2 - S ϕ 3/100/PCR/A	11.3	159.6	156.6	1.90	415
5.1 - S ϕ 3/075/UCR/A	8.1	158.4	156.6	1.14	433
5.2 - S ϕ 3/075/UCR/A	7.0	158.2	156.6	1.00	435
Beam	g (mm)	l_f (mm)	l_o (mm)	i_o (%)	σ_R (MPa)
7.1 - S ϕ 3/100/UCR/A/G	12.0	144.6	140.8	2.66	389
7.2 - S ϕ 3/100/UCR/A/G	10.0	143.8	140.8	2.09	409
8.1 - U ϕ 3/100/UCR/A	5.7	154.3	153.3	0.64	440
8.2 - U ϕ 3/100/UCR/A	5.1	154.1	153.3	0.53	441
9.1 - S ϕ 3/100/UCR/A/S	9.0	81.5	78.3	4.07	316
9.2 - S ϕ 3/100/UCR/A/S	8.5	81.2	78.3	3.69	338
10.1 - U ϕ 3/075/UCR/A	5.0	154.0	153.3	0.45	441
10.2 - U ϕ 3/075/UCR/A	5.1	154.1	153.3	0.53	441

For the beams 7.1 and 7.2, with spirals located in grooves in the lower part, the initial imperfection encountered was significantly higher than for other spirals. This strengthening configuration should be improved to reduce the encountered initial imperfection. Anyway, maximum values of initial imperfection reached 2.66 % for these two beams.

For beams 8.1, 8.2, 10.1 and 10.2, with U-shape stirrups, the initial imperfection was lower, due to the straight fixation in the upper part of the cross-section. So the beams are not weakened in the compression chord. In this case, maximum values of initial imperfection

reached 0.64 %. This fact could explain the observed increase in shear strength of these beams compared to beams 2.1 and 2.2, presented in chapter 5.6.1 of this document.

In the case of beams 9.1 and 9.2, with spirals wrapping only the concrete compression chord of the beam, the initial imperfection was higher due to the reduced spiral length. Values around 4 % of initial imperfection were estimated for these two beams.

Comparing the measured values of imperfections and the strengthened depth of the beams (full depth, reduced depth due to grooves, and compression chord depth), it can be stated that the lower the strengthened depth, the higher the imperfection. This is an interesting aspect to be taken into account because the application of this strengthening method to real beams, with greater depth, would perform better than the actual tests.

The calculated values of recovery stresses will be taken into account for the prediction of the shear strength of the strengthened beams (Chapter 7). These stresses will be added to the increase of stresses that took place during the beam tests.

6.4 CONCLUSIONS OF THE Ni-Ti-Nb RECOVERY STRESSES UNDER NON-IDEALIZED CONDITIONS

With regard to the characterization of Ni-Ti-Nb recovery stresses under non-idealized conditions, a further experimental campaign was planned and performed in order to improve and complete the characterization of the Ni-Ti-Nb alloy; it was carried out once the experimental campaign of strengthened beams had been finished. Two different objectives were set: the determination of actual recovery stresses under realistic conditions by means of activation with a heat gun and the study of the influence of the initial imperfections (curvature) of the wires in the generation of recovery stresses. The main conclusions are:

- The results of the performed tests with activation by means of heat gun show that recovery stresses with practical conditions are slightly lower, with an average value of recovery stresses equal to 452 MPa with an initial pre-load of 8 MPa and 435 MPa in the case of an initial pre-load of 40 MPa.
- The imperfect installation of the wires on the beams was assessed by means of increased wire length due to initial curvature or initial imperfection (%). For most

beams with spiral wires and U-shape stirrups as shear strengthening, the initial imperfection was assessed to be between 0.5 and 2 %.

- The stress recovery tests with initial imperfection show that for an initial imperfection of 0.54 % a value of 447 MPa of recovery stress was obtained. For initial imperfections equal to 2.34 %, the recovery stress equaled 400 MPa. Lower values for higher initial imperfection up to 6% were also obtained.
- A relationship was observed between initial imperfection (i_o) and recovery stresses (σ_R), to be used in the prediction of recovery stresses of the strengthened beams. Values of recovery stresses higher than 400 MPa have been obtained for the range of reasonable imperfections, lower than 2%.
- It has been observed that the lower the strengthened beam depth, the higher the observed imperfection. Therefore, the application of this strengthening method to real beams, with greater depth, would perform better.

7. COMPARISON OF THE RC BEAM TESTS RESULTS WITH THE PREDICTIONS BY TWO DIFFERENT SHEAR STRENGTH MODELS

One of the specific objectives of this Ph.D. thesis is the validation and extension, if needed, of a previously developed mechanical model for the determination of the shear strength to take into account the external shear strengthening. Hence, a first task was the selection of the models to be used since there are few mechanical models intended to consider external shear strengthening for RC beams. Nevertheless, some of the existing ones can be applied as no constrain in considering external shear strengthening is envisaged. In the chapter 2, two of them have been selected and the main equations have been introduced: the Compression Chord Capacity Model (CCCM) (Cladera, Marí, et al. 2016), and the shear provisions included in Eurocode 2 (CEN 2002).

The determination of the stresses in the Ultimate Limit States (ULS) in the external shear strengthening wires is required for computing the shear strength using the two selected models. The recovery stresses in the Ni-Ti-Nb wires for the tested beams have been calculated in the chapter 6. The value of the stress increment in the Ni-Ti-Nb wires during the beam tests have also been calculated from the experimentally measured strains in the wires in chapter 5.

In this chapter, the shear strength predictions using the experimentally derived tensile stresses in the strengthening wires will be presented and discussed. Finally, reasonable conservative values for the tensile stresses of the strengthening wires will be proposed in a

general way for each strengthening procedure. These values could be useful for designing the strengthening system in real structures, although more research is still needed. The shear strength predictions based in these suggested tensile stresses will also be presented and discussed.

7.1 STRESSES IN STRENGTHENING WIRES DERIVED FROM THE EXPERIMENTAL CAMPAIGNS

The stresses developed in the Ni-Ti-Nb wires of the tested beams, for modeling and prediction purposes, can be obtained by the addition of the recovery stresses produced at activation (σ_R) and the stress increments ($\Delta\sigma_\varepsilon$) developed in the wires at ULS measured by means of strain during the RC beam tests. The recovery stresses (σ_R) have been calculated in chapter 6 (table 6.4), and the stress increments ($\Delta\sigma_\varepsilon$) have been calculated from strains measured in the wires crossed by the first branch of the critical crack in chapter 5 (table 5.5). The stresses developed in the strengthening wires in all tested beams are shown in table 7.1.

Note that the stress increment for beams 9.1 and 9.2 (only compression chord wrapping) has been taken equal to 0, as these spirals are not crossed by the first branch of the critical crack. In this case, the stress in the wires will increase only during the propagation of the second branch of the critical crack, after the softening of the concrete in the compression chord.

The stress developed in the shear strengthening Ni-Ti-Nb wires in the RC beam tests are schematically depicted in figure 7.1. Figure 7.1a shows the paths in stress-strain diagram of the SMA performance in the beam tests. Previous treatment (path 1) lead the wires to a prestrain value of 6 % to be installed on the beams. The imperfect installation of the wires on the beams involves some recovery strain at the beginning of the activation (path 2). The continuation of the activation (heating and cooling) of the constrained wires involves stress recovery (path 3) up to a certain value depending on the initial imperfection. For simplicity, only one path is depicted but different stress recovery values are obtained for each wire. Finally, the strengthened RC beam failure tests involve tension stresses in wires crossing critical cracks and, subsequently, stress increment develops in those wires (path 4). Note that no rupture of wires has been observed during the failure of the beams. Thus, this aspect is not depicted in figure 7.1. Figure 7.1b shows the observed values of recovery stresses for

wires with initial imperfections (see chapter 6) in the same stress-strain graph and the obtained adjustment curve.

Table 7.1. Recovery stresses and final developed stresses in the strengthening wires at beam failure for tested beams

BEAM	FAILURE	V_u (kN)	σ_R (MPa)	$\Delta\sigma_\varepsilon$ (MPa)	$\sigma_R + \Delta\sigma_\varepsilon$ (MPa)
2.1	Shear	35.10	417	79	496
2.2	Shear	35.75	432	116	548
3.1a	Shear	18.02	-	-	-
3.1b	Shear	27.14	435	70*	505
3.2a	Shear	21.38	-	-	-
3.2b	Shear	35.02	428	50	479
4.1	Shear	34.27	436	49	485
4.2	Shear	35.51	415	67	482
5.1	Shear	37.05	433	59	492
5.2	Bending	41.82	435	70*	505
Average			429	70	499
* No measurements. Stress increment averaged					
BEAM	FAILURE	V_u (kN)	σ_R (MPa)	$\Delta\sigma_\varepsilon$ (MPa)	$\sigma_R + \Delta\sigma_\varepsilon$ (MPa)
7.1	Shear	25.27	389	29	418
7.2	Shear	35.51	409	97	506
8.1	Shear	37.74	440	55	495
8.2	Shear	34.75	441	139	580
9.1	Shear	20.53	316	0	316
9.2	Shear	22.03	338	0	338
10.1	Shear	36.79	441	70	511
10.2	Shear	33.60	441	127	568
Spiral groove average			399	63	462
U-shape average			441	98	539
Compression chord spiral average			327	0	327

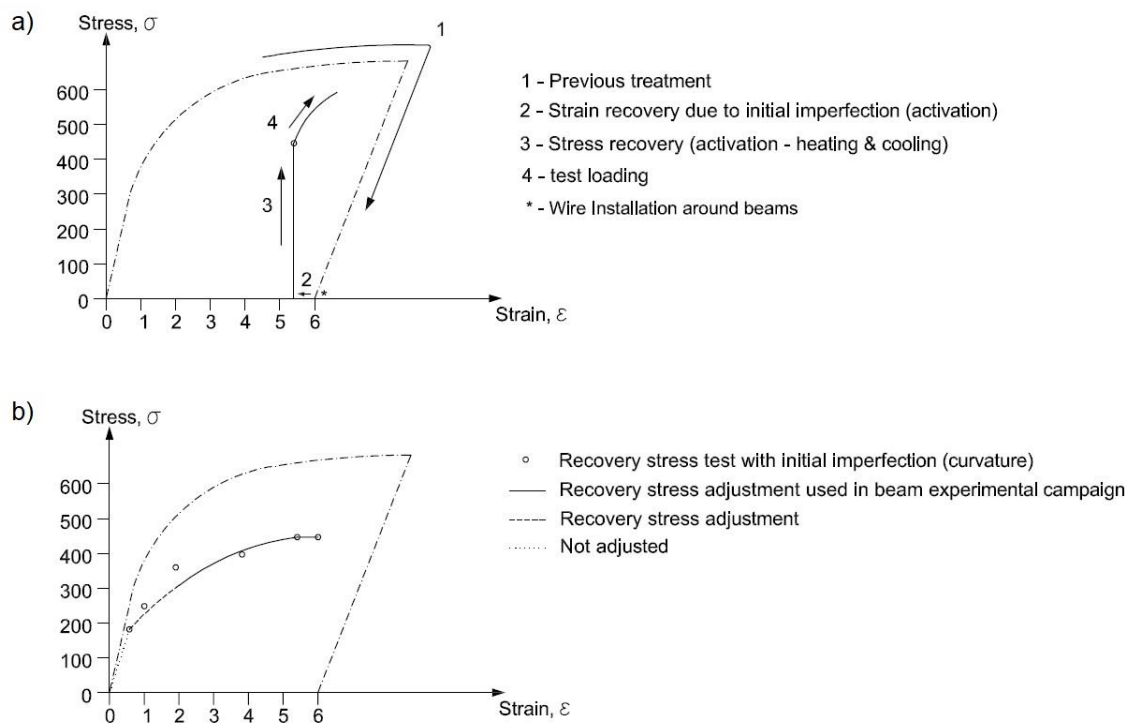


Figure 7.1. a) Schematic stress-strain path of Ni-Ti-Nb wires installed in the tested strengthened RC beams, and b) stress-strain graph of observed recovery stresses in tested wires

7.2 PREDICTIONS CONSIDERING THE EXPERIMENTALLY OBTAINED STRESSES IN THE STRENGTHENING Ni-Ti-Nb WIRES

7.2.1 PREDICTIONS BY THE COMPRESSION CHORD CAPACITY MODEL (CCCM)

The Compression Chord Capacity Model (CCCM) (Cladera, Marí, et al. 2016), introduced in chapter 2, is a design-oriented model for the shear strength of reinforced concrete (RC) and prestressed concrete (PC) beams. It was developed under the premise that the shear transferred by the compression chord is the main resisting action in the considered failure state. The main equations of the CCCM were also presented in chapter 2 (Eqs. 2.18 - 2.22).

In the case of active externally strengthened RC beams, it is advisable to write separately the strength increment of the compression chord due to the externally strengthening wires.

Moreover, the material strength parameters adopted are average laboratory values and not design values. Therefore, the shear strength of a RC beam, with rectangular cross-section, and externally confined may be considered as the sum of the concrete contribution, the concrete contribution increment due to external confinement, and the shear reinforcement contribution:

$$V_R = V_{cu} + V_{cu}^{confinement} + V_{su} \leq V_{R,max} \quad (7.1)$$

where strut crushing is given by Eq. (7.2):

$$V_{R,max} = bzv f_{cm} (\cot \theta + \cot \alpha) / (1 + \cot^2 \theta) \quad (7.2)$$

The concrete contribution is given by Eq. (7.3):

$$V_{cu} = 0.3\zeta \frac{x}{d} f_{cm}^{2/3} bd \leq V_{cu,min} = 0.25 \left(\zeta K_c + \frac{20}{d_0} \right) f_{cm}^{2/3} bd \quad (7.3)$$

where $K_c = \frac{x}{d} \geq 0.2$.

The increase of the concrete contribution due to the confinement done by the external shear reinforcement is given by Eq. (7.4):

$$V_{cu}^{confinement} = \frac{A_{sw}}{s} f_s (d - x) \sin \alpha (\cot \theta + \cot \alpha) \Delta V_{cu} \quad (7.4)$$

The contribution of the shear reinforcement, without including the previously commented confinement effect, is given by Eq. (7.5):

$$V_{su} = \frac{A_{sw}}{s} f_s (d - x) \sin \alpha (\cot \theta + \cot \alpha) \quad (7.5)$$

The special configuration of shear strengthening wires of the tested beams, with pseudo-spirals with front links in vertical direction and back links with inclined direction depending on spiral-pitch can, thus, be considered in CCCM model since the contribution of each link with different inclination can be obtained separately and the global shear resistance can be obtained by the sum of each link contribution.

The predictions made by the CCCM are presented in table 7.2. The first column of table 7.2 is the test number and its nomenclature. The second column is the concrete compression strength of the cylinder specimens. The third column is the shear strength of the test. The

fourth column is the yield strength of the shear strengthening material. The fifth to ninth columns are the predictions of the Compression Chord Capacity Model.

The concrete compression strength of the cylinder specimens is taken equal to $0.9 \cdot f_{c,cube}$ (Comisión Permanente del Hormigón 2008). The compression strength varied slightly depending on the age of the specimen at testing, slightly affecting the concrete contribution V_{cu} (table 7.2). The average value of x , the neutral axis depth, is 49 mm according to Eq. (2.16). It can be seen in figure 5.20 that this is a very close estimation of the separation between the first branch of the critical crack (more vertical) and the second branch (more horizontal, through the compression chord). For reference, in fig. 5.20 the spacing of the horizontal guidelines painted on the beam specimens is 25 mm.

No partial safety coefficients were used in the calculations presented in table 7.2. The yield strength of the material, f_s , was substituted by the stress in the spiral at failure, $\sigma_R + \Delta\sigma_\varepsilon$ (MPa) in table 7.1. The pitch or spacing of the vertical links of the spiral was constant in the tested beams (nominally 100 mm or 75 mm), except for the vertical links closest to the loading plate (75 mm and 50 mm, see Fig. 5.2). For the application of the CCCM, the nominal spacing has been taken into account, as this is the distance between the links in the first branch of the critical crack (figure 7.2), and this is the value required to obtain V_{su} (table 7.2).

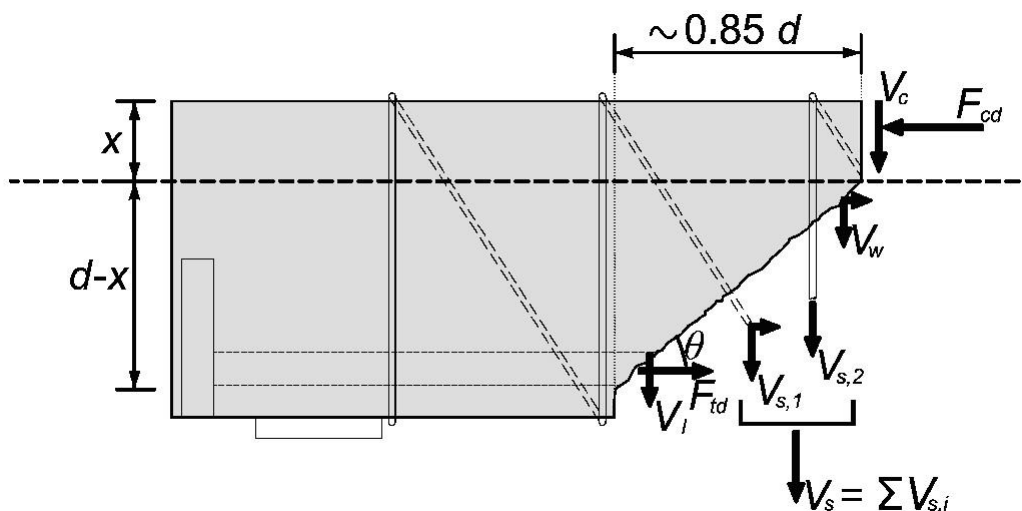


Figure 7.2. First branch of the critical crack and stirrup contribution. From (Marí et al. 2015)

Table 7.2. Predictions by the CCCM: a) for phase 1 beams, and b) for phase 2 beams

a) Phase 1 beams	$f_{em,cyl}$ (MPa)	V_{test} (kN)	f_s (MPa)	<i>Compression Chord Capacity Model</i>				
				V_{cu} (kN)	$V_{cu}^{confinement}$ (kN)	V_{su} (kN)	V_R (kN)	V_{test}/V_R
1.1 - Reference	37.3	18.30	-	16.85	-	-	16.85	1.09
1.2 - Reference	37.5	18.41	-	16.92	-	-	16.92	1.09
2.1 - S ϕ 3/100/UCR/A	37.7	35.41	496	16.96	4.19	8.45	29.60	1.20
2.2 - S ϕ 3/100/UCR/A	37.9	35.95	548	17.01	4.62	9.34	30.97	1.16
3.1a - ϕ 3/100/UCR/NA	38.3	18.23	-	17.12	-	-	17.12	1.06
3.1b - S ϕ 3/100/COL/A	38.5	27.14	505	17.17	4.25	8.61	30.03	0.90
3.2a - ϕ 3/100/UCR/NA	38.3	21.47	-	17.12	-	-	17.12	1.25
3.2b - S ϕ 3/100/COL/A	38.4	35.21	479	17.14	4.03	8.15	29.32	1.20
4.1 - S ϕ 3/100/PCR/A	38.7	34.35	485	17.21	4.08	8.27	29.56	1.16
4.2 - S ϕ 3/100/PCR/A	38.7	35.60	482	17.21	4.06	8.22	29.49	1.21
5.1 - S ϕ 3/075/UCR/A	38.9	37.04	492	17.25	5.49	11.11	33.85	1.09
5.2 - S ϕ 3/075/UCR/A	38.9	41.82	505	17.25	5.63	11.41	34.29	1.22
Average								1.14 (1.16)
Standard deviation								0.10 (0.07)
Coefficient of Variation (%)								8.4 (5.6)

b) Phase 2 beams	$f_{em,cyl}$ (MPa)	V_{test} (kN)	f_s (MPa)	<i>Compression Chord Capacity Model</i>				
				V_{cu} (kN)	$V_{cu}^{confinement}$ (kN)	V_{su} (kN)	V_R (kN)	V_{test}/V_R
6.1 - Reference	35.73	19.71	-	16.47	-	-	16.47	1.20
6.2 - Reference	35.73	18.50	-	16.47	-	-	16.47	1.12
7.1 - ϕ 3/100/UCR/A/G	35.82	25.36	418	16.49	3.55	7.12	27.16	0.90
7.2 - ϕ 3/100/UCR/A/G	35.82	35.51	506	16.49	4.29	8.62	29.40	1.21
8.1 - U ϕ 3/100/UCR/A	35.73	37.74	495	16.47	3.76	7.56	27.79	1.36
8.2 - U ϕ 3/100/UCR/A	35.73	34.75	580	16.47	4.41	8.85	29.73	1.17
9.1 - ϕ 3/100/UCR/A/S	35.82	20.54	316	16.49	2.61	-	19.10	1.08
9.2 - ϕ 3/100/UCR/A/S	35.82	22.03	338	16.49	2.80	-	19.29	1.14
10.1 - U ϕ 3/075/UCR/A	35.82	36.79	511	16.49	5.19	10.40	32.08	1.15
10.2 - U ϕ 3/075/UCR/A	35.82	33.65	568	16.49	5.76	11.56	33.81	1.00
Average								1.13 (1.16)
Standard deviation								0.12 (0.10)
Coefficient of Variation (%)								10.3 (8.6)

Average								1.14 (1.16)
Standard deviation								0.10 (0.08)
Coefficient of Variation (%)								9.1 (6.9)

The predictions given by the model without any modification with respect to the procedure established to evaluate internal reinforcement are excellent (see table 7.2) for the two phases, with an average value of the ratio V_{test}/V_R equal to 1.14, a standard deviation of 0.10 and a coefficient of variation of 9.1 %. The average value of the ratio V_{test}/V_R is similar to the ratios for the shear strength of 784 RC beams without stirrups ($V_{test}/V_R = 1.17$) and 170 RC beams with stirrups ($V_{test}/V_R = 1.16$) (Cladera, Marí, et al. 2016).

The reference beams (1.1 – Reference, 1.2 – Reference, 6.1 – Reference, 6.2 – Reference) and the non-activated strengthened beams (3.1a – S ϕ 3/100/UCR/NA, 3.2a – S ϕ 3/100/UCR/NA) are modelled taking into account only the concrete contribution and they have excellent agreement as the rest of the beams with V_{test}/V_R between 1.09 and 1.20. Only 3.2a – S ϕ 3/100/UCR/NA beam has a value of 1.25 and there could be some non-activated reinforcement contribution.

The pseudo-spiral shear strengthened beams with different shear reinforcement configurations (2.1 – S ϕ 3/100/UCR/A, 2.2 – S ϕ 3/100/UCR/A, 3.1b - S ϕ 3/100/COL/A, 3.2b - S ϕ 3/100/COL/A, 4.1 – S ϕ 3/100/PCR/A, 4.2 – S ϕ 3/100/PCR/A, 5.1 – S ϕ 3/075/UCR/A, 5.2 – S ϕ 3/075/UCR/A, 7.1 - S ϕ 3/100/UCR/A/G, 7.2 - S ϕ 3/100/UCR/A/G) are modelled taking into account both concrete and shear strengthening contributions and they have excellent agreement with V_{test}/V_R between 1.09 and 1.22. Note that only the prediction for beams 3.1b - S ϕ 3/100/COL/A and 7.1 - S ϕ 3/100/UCR/A/G are unsafe ($V_{test}/V_R < 1.0$). As previously commented, the beam 3.1 had previously suffered a very high damage level in test 3.1a, and in real engineering, this beam specimen would have not probably been strengthened after its collapse. Also, in beam 7.1 unexpected low maximum load test was encountered and its results may be considered as not representatives. Hence, such values have been removed from model calculations in the values given in brackets in table 7.2.

The U-shape stirrup shear strengthened beams (8.1 – U ϕ 3/100/UCR/A, (8.2 – U ϕ 3/100/UCR/A, 10.1 – U ϕ 3/075/UCR/A, 10.2 – U ϕ 3/075/UCR/A) are modelled taking into account both concrete and shear strengthening contributions and they have some dispersion with V_{test}/V_R between 1.00 and 1.36. Actually, one of the V_{test} obtained value for 100 pitch stirrup beams (8.1) is higher than the V_{test} values obtained for 75 mm pitch beams, and one of the V_{test} obtained value for 75 mm pitch stirrup beams (10.2) is lower than the

V_{test} values obtained for 100 mm pitch beams. Thus, the modelled values confirm these unexpected results of such beams.

The compression chord spiral shear strengthened beams (9.1 - S ϕ 3/100/UCR/A/S, 9.2 - S ϕ 3/100/UCR/A/S) are modelled taking into account both concrete and shear strengthening contributions, but in the case of shear strengthening only the term affecting the concrete contribution increase due to confinement, since the shear reinforcement does not wrap longitudinal reinforcement. The agreement is excellent with V_{test}/V_R between 1.08 and 1.14.

In next subsections, two examples are presented to illustrate the CCCM detailed calculation procedure.

EXAMPLE OF CALCULATION OF THE SHEAR STRENGTH BY THE CCCM OF REFERENCE BEAM 1.1

The reference beam 1.1 (fig. 7.3) tested in the experimental program (chapter 5) is presented here to show the detailed calculation using the CCCM. The values of the main geometric parameters of the beam 1.1 are: $b = 80$ mm, $h = 150$ mm, $d = 150 - 15 - 16/2 = 127$ mm, and $a = 340$ mm. The values of the main material parameters of the beam 1.1 are:

$$f_{cm,cyl} = 0.9 f_{cm,cub} = 0.9 \cdot 41.4 = 37.3 \text{ MPa}$$

$$E_{cm} = 22000 \sqrt[3]{\frac{f_{cm,cyl}}{10}} = 22000 \sqrt[3]{\frac{37.3}{10}} = 32643 \text{ MPa}$$

$$\alpha_e = \frac{E_s}{E_{cm}} = \frac{200000}{32643} = 6.13$$

$$\rho_l = \frac{A_{slong}}{bd} = \frac{\pi \frac{\phi^2}{4}}{bd} = \frac{\pi \frac{16^2}{4}}{80 \cdot 127} = 0.0198$$

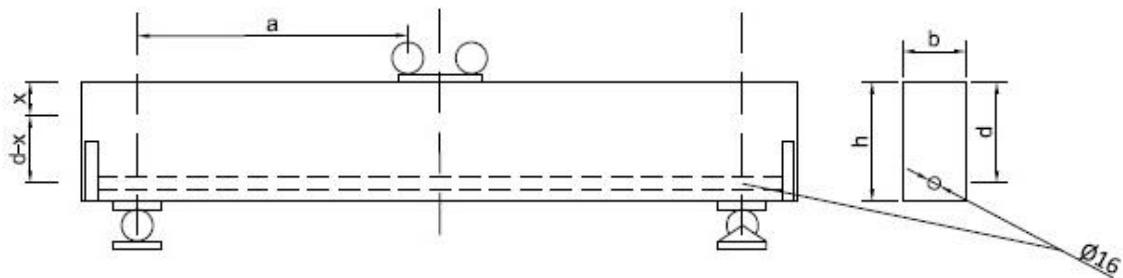


Figure 7.3. Main geometric parameters for reference beam 1.1

Note that no partial safety coefficients are used in the calculations. The values of the main CCCM model parameters for beam 1.1 are:

$$\frac{x}{d} = \alpha_e \rho_l \left(-1 + \sqrt{1 + \frac{2}{\alpha_e \rho_l}} \right) = 6.13 \cdot 0.0198 \left(-1 + \sqrt{1 + \frac{2}{6.13 \cdot 0.0198}} \right) = 0.386$$

$$x = d \frac{x}{d} = 127 \cdot 0.386 = 49.003 \text{ mm}$$

$$\xi = \frac{2}{\sqrt{1 + \frac{d_0}{200}}} \left(\frac{d}{a} \right)^{0.2} = \frac{2}{\sqrt{1 + \frac{127}{200}}} \left(\frac{127}{340} \right)^{0.2} = 1.285 \quad (d_0 = d \ll 100)$$

$$V_{cu} = 0.3 \xi \frac{x}{d} f_{cm}^{2/3} b d = 0.3 \cdot 1.285 \cdot 0.386 \cdot 37.3^{2/3} \cdot 80 \cdot 127 = 16.85 \text{ kN}$$

EXAMPLE OF CALCULATION OF THE SHEAR STRENGTH BY THE CCCM OF EXTERNALLY STRENGTHENED BEAM 2.1

As example of application of the CCCM model, the calculations for beam 2.1 (figure 7.4) are presented below. The values of the main geometric parameters of the beam 2.1 are: $b = 80 \text{ mm}$, $h = 150 \text{ mm}$, $d = 150 - 15 - 16/2 = 127 \text{ mm}$, $a = 340 \text{ mm}$, $z = 0.9 \cdot d = 0.9 \cdot 127 = 114.3 \text{ mm}$, $\nu = 0.6$, $s = 100 \text{ mm}$, $\alpha_f = 90^\circ$, and $\alpha_b = \arctan \frac{h}{s} = \arctan \frac{150}{100} = 56^\circ$. Note that the pseudo-spiral has two different branch inclinations: front branch inclination (α_f) and back branch inclination (α_b). Therefore, the contribution to the shear strength of the transverse reinforcement will be considered as the sum of the contribution of each branch.

The values of the main material parameters of the beam 2.1 are:

$$f_{cm,cyl} = 0.9 f_{cm,cub} = 0.9 \cdot 41.9 = 37.7 \text{ MPa}$$

$$E_{cm} = 22000 \sqrt[3]{\frac{f_{cm,cyl}}{10}} = 22000 \sqrt[3]{\frac{37.7}{10}} = 32761 \text{ MPa}$$

$$\alpha_e = \frac{E_s}{E_{cm}} = \frac{200000}{32761} = 6.10$$

$$\rho_l = \frac{A_{slong}}{bd} = \frac{\pi \frac{\phi^2}{4}}{bd} = \frac{\pi \frac{16^2}{4}}{80 \cdot 127} = 0.0198$$

$$f_s = 496 \text{ MPa}$$

$$A_{sw} = \pi \frac{\phi_{sw}^2}{4} = \pi \frac{3^2}{4} = 7.07 \text{ mm}^2$$

The values of the main CCCM model parameters of the beam 2.1 are:

$$\frac{x}{d} = \alpha_e \rho_l \left(-1 + \sqrt{1 + \frac{2}{\alpha_e \rho_l}} \right) = 6.10 \cdot 0.0198 \left(-1 + \sqrt{1 + \frac{2}{6.10 \cdot 0.0198}} \right) = 0.385$$

$$x = d \frac{x}{d} = 127 \cdot 0.385 = 48.94 \text{ mm}$$

$$\xi = \frac{2}{\sqrt{1 + \frac{d_0}{200}}} \left(\frac{d}{a} \right)^{0.2} = \frac{2}{\sqrt{1 + \frac{127}{200}}} \left(\frac{127}{340} \right)^{0.2} = 1.285 \quad (d_0 = d \neq 100)$$

$$V_{cu} = 0.3 \zeta \frac{x}{d} f_{cm}^{2/3} b d = 0.3 \cdot 1.285 \cdot 0.385 \cdot 37.7^{2/3} \cdot 80 \cdot 127 = 16.96 \text{ kN}$$

$$\cot \theta = \frac{0.85d}{d-x} = \frac{0.85 \cdot 127}{127-49} = 1.38 \leq 2.5 \quad (\theta = 35.5^\circ)$$

$$\Delta_{V_{cu}} = \zeta \frac{x}{d} = 1.285 \cdot 0.385 = 0.495$$

$$V_{cu}^{confinement} = \left(\frac{A_{sw}}{s} f_s (d-x) \sin \alpha_f (\cot \theta + \cot \alpha_f) + \frac{A_{sw}}{s} f_s (d-x) \sin \alpha_b (\cot \theta + \cot \alpha_b) \right) (\Delta_{V_{cu}})$$

$$V_{cu}^{confinement} = \left(\frac{7.07}{100} 496 \cdot 78 \cdot \sin 90 (1.4 + \cot 90) + \frac{7.07}{100} 496 \cdot 78 \cdot \sin 56 (1.4 + \cot 56) \right) 0.495$$

$$V_{cu}^{confinement} = (3.786 + 4.669) 0.495 = 4.19 \text{ kN}$$

$$V_{su} = \left(\frac{A_{sw}}{s} f_s (d-x) \sin \alpha_f (\cot \theta + \cot \alpha_f) + \frac{A_{sw}}{s} f_s (d-x) \sin \alpha_b (\cot \theta + \cot \alpha_b) \right)$$

$$V_{su} = \left(\frac{7.07}{100} 496 \cdot 78 \cdot \sin 90 (1.4 + \cot 90) + \frac{7.07}{100} 496 \cdot 78 \cdot \sin 56 (1.4 + \cot 56) \right)$$

$$V_{su} = (3.786 + 4.669) = 8.45 \text{ kN}$$

$$V_R = V_{cu} + V_{cu}^{confinement} + V_{su} = 16.96 + 4.19 + 8.45 = 29.60 \text{ kN}$$

$$V_{R,max} = b z v f_{cd} \frac{\cot \theta + \cot \alpha}{1 + \cot^2 \theta} = 80 \cdot 114.3 \cdot 0.6 \cdot 37.7 \frac{1.4}{1 + 1.4^2} = 99.80 \text{ kN}$$

$$V_R = 29.60 \text{ kN} \leq 99.80 \text{ kN} = V_{R,max}$$

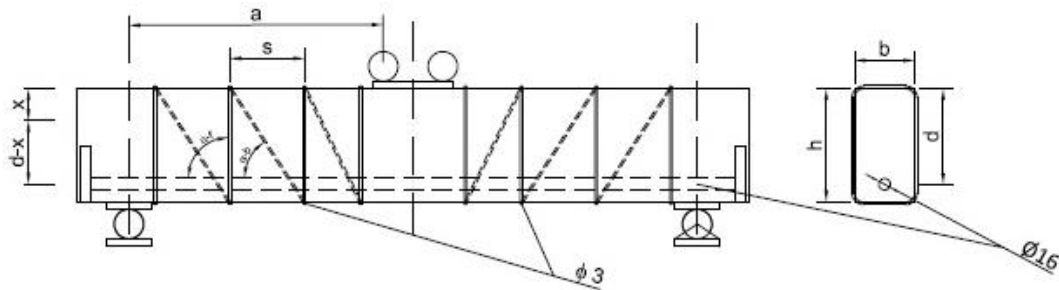


Figure 7.4. Main geometric parameters for strengthened beam 2.1

7.2.2 PREDICTIONS BY THE SHEAR DESIGN EQUATIONS IN EUROCODE 2 (EC2)

The European Standard for concrete, Eurocode 2 (CEN 2002) presents, as it was introduced in chapter 2, two different models: an empirical equation for members without stirrups, and a variable angle truss model without concrete contribution for elements with stirrups. The main shear equations of the EC-2 were also presented in chapter 2 (Eqs. 2.2 - 2.8).

The special configuration of shear reinforcement of the tested beams, with pseudo-spirals with a front link in vertical direction and a back link with inclined direction depending on spiral-pitch can, thus, be considered in EC2 model since the contribution of each link can be obtained with the adequate equations and the shear resistance can be obtained considering the maximum between the concrete contribution and the shear contribution.

The final shear resistance of the member is the addition of both contributions: the vertical branch and the inclined one of the shear reinforcement and it has to be higher than the strength of a similar beam without the external strengthening. The predictions when using the current Eurocode 2 are also presented in table 7.3. The first column of table 7.3 is the test number and its nomenclature. The second column is the concrete compression strength of the cylinder specimens. The third column is the shear strength of the test. The fourth column is the yield strength of the shear strengthening material. The fifth to eighth columns are the predictions of the shear equations of the EC 2.

Note that EC 2 presents two different models for elements without and with stirrups: an empirical equation for members without stirrups, and a variable angle truss model without concrete contribution for elements with stirrups. It must be also noted that EC2 model is not intended for calculating the shear strength of externally strengthened beams.

Table 7.3. Predictions by the EC 2: a) for phase 1 beams and b) for phase 2 beams

a) Phase 1 beams	$f_{cm,cyl}$ (MPa)	V_{test} (kN)	f_s (MPa)	Eurocode 2			
				$V_{R,c}$ (kN)	$V_{R,s}$ (kN)	V_R (kN)	V_{test}/V_R
1.1 – Reference	37.3	18.30	-	15.34	0	15.34	1.19
1.2 – Reference	37.5	18.41	-	15.37	0	15.37	1.20
2.1 – S ϕ 3/100/UCR/A	37.7	35.41	496	15.40	20.57	20.57	1.72
2.2 – S ϕ 3/100/UCR/A	37.9	35.95	548	15.42	22.73	22.73	1.58
3.1a – S ϕ 3/100/UCR/NA	38.3	18.23	-	15.48	0	15.48	1.18
3.1b – S ϕ 3/100/COL/A	38.5	27.14	505	15.51	20.94	20.94	1.30
3.2a – S ϕ 3/100/UCR/NA	38.3	21.47	-	15.48	0	15.48	1.39
3.2b – S ϕ 3/100/COL/A	38.4	35.21	479	15.49	19.82	19.82	1.78
4.1 – S ϕ 3/100/PCR/A	38.7	34.35	485	15.53	20.11	20.11	1.71
4.2 – S ϕ 3/100/PCR/A	38.7	35.60	482	15.53	19.99	19.99	1.78
5.1 – S ϕ 3/075/UCR/A	38.9	37.04	492	15.56	27.47	27.47	1.35
5.2 – S ϕ 3/075/UCR/A	38.9	41.82	505	15.56	28.19	28.19	1.48
Average							1.47 (1.49)
Standard deviation							0.24 (0.24)
Coefficient of Variation (%)							16.0 (16.2)
b) Phase 2 beams	$f_{cm,cyl}$ (MPa)	V_{test} (kN)	f_s (MPa)	Eurocode 2			
				$V_{R,c}$ (kN)	$V_{R,s}$ (kN)	V_R (kN)	V_{test}/V_R
6.1 – Reference	35.73	19.71	-	15.12	0	15.12	1.30
6.2 – Reference	35.73	18.50	-	15.12	0	15.12	1.22
7.1 - S ϕ 3/100/UCR/A/G	35.82	25.36	454	15.14	17.22	17.22	1.47
7.2 - S ϕ 3/100/UCR/A/G	35.82	35.51	522	15.14	20.85	20.85	1.70
8.1 - U ϕ 3/100/UCR/A	35.73	37.74	505	15.12	20.00	20.00	1.89
8.2 - U ϕ 3/100/UCR/A	35.73	34.75	589	15.12	23.43	23.43	1.48
9.1 - S ϕ 3/100/UCR/A/S	35.82	20.54	436	15.14	0	15.14	1.36
9.2 - S ϕ 3/100/UCR/A/S	35.82	22.03	436	15.14	0	15.14	1.46
10.1 - U ϕ 3/075/UCR/A	35.82	36.79	520	15.14	27.53	27.53	1.34
10.2 - U ϕ 3/075/UCR/A	35.82	33.65	577	15.14	30.60	30.60	1.10
Average							1.43 (1.43)
Standard deviation							0.23 (0.24)
Coefficient of Variation (%)							16.0 (17.0)
Average							1.45 (1.46)
Standard deviation							0.23 (0.24)
Coefficient of Variation (%)							15.7 (16.2)

The results are quite conservative and present a high scatter, with an average value of the ratio V_{test}/V_R equal to 1.45, a standard deviation of 0.23 and a coefficient of variation of 15.7 %. As previously commented, the values of beams 3.1b and 7.1 have been removed from average model calculations in the values given in brackets in table 7.3. The results predicted by EC-2 correlate worse with the experimental results than the predictions by the CCCM, as can be seen comparing tables 7.3 and 7.2.

EXAMPLE OF CALCULATION OF THE SHEAR STRENGTH BY THE EC-2 OF REFERENCE BEAM 1.1

As it was done with the CCCM, two examples of application of the EC2 model are presented in the next pages. The results of application of the model for beam 1.1 are listed below. The values of the main geometric parameters of the beam 1.1 are: $b = 80$ mm, $h = 150$ mm, and $d = 150 - 15 - 16/2 = 127$ mm.

The concrete compressive strength considered for the calculation is:

$$f_{cm,cyl} = 0.9 f_{cm,cub} = 0.9 \cdot 41.4 = 37.3 \text{ MPa}$$

Note that no partial safety coefficients are used in the calculations.

The shear resistance is given by:

$$V_{R,c} = \left[\frac{0.18}{\gamma_c} k (100 \rho_l f_{ck})^{1/3} \right] b d = [0.18 \cdot 2 \cdot (100 \cdot 0.0198 \cdot 37.3)^{1/3}] 80 \cdot 127 = 15.34 \text{ kN}$$

$$k = 1 + \sqrt{\frac{200}{d}} = 1 + \sqrt{\frac{200}{127}} = 2.3 > 2 \Rightarrow k = 2$$

$$\rho_l = \frac{A_{stong}}{b d} = \frac{\pi \frac{\phi^2}{4}}{b d} = \frac{\pi \frac{16^2}{4}}{80 \cdot 127} = 0.0198$$

with a minimum given by:

$$V_{R,min} = \left[0.035 k^2 (f_{ck})^{1/2} \right] b d = \left[0.035 \cdot 2^2 (37.3)^{1/2} \right] 80 \cdot 127 = 6.08 \text{ kN}$$

EXAMPLE OF CALCULATION OF THE SHEAR STRENGTH BY THE EC-2 OF EXTERNALLY STRENGTHENED BEAM 2.1

The results of application of the model for beam 2.1 are listed below. The values of the main geometric parameters of the beam 2.1 are: $b = 80$ mm, $h = 150$ mm, $d = 150 - 15 - 16/2 = 127$ mm, $z = 0.9 \cdot d = 0.9 \cdot 127 = 114.3$ mm $\nu = 0.6$ as for f_{ck} 60 MPa (see 2.1.2), $s = 100$ mm, $\alpha_f = 90^\circ$, and $\alpha_b = \arctan \frac{h}{s} = \arctan \frac{150}{100} = 56^\circ$.

Note that the pseudo-spiral defined for shear reinforcement has two different branch inclinations: front branch inclination (α_f) and back branch inclination (α_b). Therefore, the contribution to the shear strength of the transverse reinforcement will be considered as the sum of the contribution of each branch. The values of the main calculation parameters for beam 1.1 are:

$$f_{cm,cyl} = 0.9 f_{cm,cub} = 0.9 \cdot 41.9 = 37.7 \text{ MPa}$$

$$k = 1 + \sqrt{\frac{200}{d}} = 1 + \sqrt{\frac{200}{127}} = 2.3 > 2 \Rightarrow k = 2$$

$$\rho_l = \frac{A_{slong}}{bd} = \frac{\pi \frac{\phi^2}{4}}{bd} = \frac{\pi \frac{16^2}{4}}{80 \cdot 127} = 0.0198$$

$$f_s = 496 \text{ MPa}$$

$$A_{sw} = \pi \frac{\phi_{sw}^2}{4} = \pi \frac{3^2}{4} = 7.07 \text{ mm}^2$$

$$\cot \theta = 2.5$$

The shear resistance of this strengthened shear reinforced 2.1 beam is given in EC2 by the higher value between the concrete contribution and the shear reinforcement contribution based on a truss model.

The values of the EC2 model parameters for concrete contribution of the beam 2.1 are:

$$V_{R,c} = \left[\frac{0.18}{\gamma_c} k (100 \rho_l f_{cm})^{1/3} \right] bd = \left[0.18 \cdot 2 \cdot (100 \cdot 0.0198 \cdot 37.7)^{1/3} \right] 80 \cdot 127 = 15.40 \text{ kN}$$

with a minimum given by:

$$V_{R,cmin} = \left[0.035 k^2 (f_{cm})^{1/2} \right] bd = \left[0.035 \cdot 2^2 (37.7)^{1/2} \right] 80 \cdot 127 = 6.08 \text{ kN}$$

The values of the EC2 model parameters for shear reinforcement contribution of the beam 2.1 are:

$$V_{R,s} = \frac{A_{sw}}{s} z f_s (\cot \theta + \cot \alpha_f) \sin \alpha_f + \frac{A_{sw}}{s} z f_s (\cot \theta + \cot \alpha_b) \sin \alpha_b$$

$$V_{R,s} = \frac{7.07}{100} 114.3 \cdot 496 \cdot (2.5 + 0) \cdot 1 + \frac{7.07}{100} 114.3 \cdot 496 \cdot \left(2.5 + \frac{1}{\tan 56}\right) \cdot \sin 56$$

$$V_{R,s} = 10.02 + 10.54 = 20.57 \text{ kN}$$

$$V_R = \text{Maximum}(V_{R,c}, V_{R,s}) = 20.57 \text{ kN}$$

$$V_{R,max} = b z v f_{cm} (\cot \theta + \cot \alpha) / (1 + \cot^2 \theta) = 80 \cdot 114.3 \cdot 0.6 \cdot 37.7 / (2.5 + \frac{1}{2.5})$$

$$V_{R,max} = 71.32 \text{ kN}$$

7.2.3 COMPARISON BETWEEN THE TEST RESULTS AND THE PREDICTIONS OF CCCM AND EC2

The results of the experimental campaign carried out within two phases of beam tests have also been compared with those of the applied models. The main results of this comparison in terms of average data are summarized in table 7.4. The first column of table 7.4 indicates the beams considered in the average. The second (V_{test}) and the third (SSI_{test} -Shear Strength Increment) columns indicate average values related to experimental results. The fourth (V_{CCCM}), the fifth (V_{test}/V_{CCCM}), the sixth (SSI_{CCCM}), and seventh (SSI_{test}/SSI_{CCCM}) columns indicate average values related to CCCM. The eighth (V_{EC2}), the ninth (V_{test}/V_{EC2}), the tenth (SSI_{EC2}), and the eleventh (SSI_{test}/SSI_{EC2}) columns indicate average values related to EC2 model. The SSI_{test} , SSI_{CCCM} , and SSI_{EC2} are the Shear Strength Increments (%) related to experimental values, CCCM and EC2 models, respectively. Hence, the ratio SSI_{test}/SSI_{CCCM} and SSI_{test}/SSI_{EC2} indicate the goodness of each model in predicting increments of the shear strength. As can be seen in the table 7.4 the CCCM has an excellent agreement in predicting those increments of shear strength.

The correlation in terms of both shear strength and shear strength increments between the CCCM predictions and the experimental results are excellent. However, the correlation is not so good for the EC2 predictions. For this reason, in next section design suggested stresses in the strengthening wires will be proposed only for the CCCM.

Comparison of the RC beam tests results with the predictions by different shear strength models

Table 7.4. Summary of average comparison values of the whole experimental program and predicted shear strengths.

Average beams with...	Experimental		CCCM				EC2			
	V_{test} (kN)	SSI_{test} (%)	V_{CCCM} (kN)	$\frac{V_{test}}{V_{CCCM}}$	SSI_{CCCM} (%)	$\frac{SSI_{test}}{SSI_{CCCM}}$	V_{EC2} (kN)	$\frac{V_{test}}{V_{EC2}}$	SSI_{EC2} (%)	$\frac{SSI_{test}}{SSI_{EC2}}$
Non-strengthened (1.1, 1.2, 3.1a, 3.2a, 6.1, 6.2)	19.10	-	16.82	1.14	-	-	15.32	1.25	-	-
100 mm spiral pitch (2.1, 2.2, 3.2b, 4.1, 4.2, 7.2)	33.07	73	29.44	1.12	75	0.97	20.28	1.63	32	2.25
75 mm spiral pitch (5.1, 5.2)	39.43	106	34.07	1.16	103	1.04	27.83	1.42	82	1.30
Spirals (2.1, 2.2, 3.2b, 4.1, 4.2, 5.1, 5.2, 7.2)	34.34	80	30.37	1.13	80	0.99	22.30	1.54	46	1.75
100 mm U-shape stirrup (8.1, 8.2)	36.25	90	28.76	1.26	71	1.26	21.72	1.67	42	2.15
75 mm U-shape stirrup (10.1, 10.2)	35.22	84	32.93	1.07	96	0.88	29.06	1.21	90	0.94
U-shape stirrups (8.1, 8.2, 10.1, 10.2)	35.73	87	30.85	1.16	83	1.04	25.39	1.41	66	1.32
Compression chord confinement (9.1, 9.2)	21.29	11	19.19	1.11	14	0.81	15.14	1.41	0	-
100 mm spacing (2.1, 2.2, 3.2b, 4.1, 4.2, 7.2, 8.1, 8.2)	33.70	76	29.54	1.14	76	1.01	20.94	1.61	37	2.08
75 mm spacing (5.1, 5.2, 10.1, 10.2)	37.33	95	33.50	1.11	99	0.96	28.45	1.31	86	1.11
Strengthened (2.1, 2.2, 3.2b, 4.1, 4.2, 5.1, 5.2, 7.2, 8.1, 8.2, 10.1, 10.2)	34.74	82	30.76	1.13	83	0.99	23.25	1.49	52	1.58
				Average		1.00		Average		1.61
				Standard deviation		0.12		Standard deviation		0.48
				Coefficient of variation (%)		11.9		Coefficient of variation (%)		29.7

7.3 DESIGN SHEAR STRENGTH OF STRENGTHENED BEAMS

Once it has been observed that the predictions of the shear strength by the CCCM satisfactorily correlate with the experimental results, some simplifications have been performed for design purposes. Conservative recovery stresses for the strengthening wires are proposed for design purposes (approximately the minimum value obtained in the experimental program for each beam configuration). The following values are proposed:

- $\sigma_R = 415$ MPa. Value corresponding to an initial imperfection of 1.9 % for spirals.
- $\sigma_R = 440$ Mpa. Value corresponding to an initial imperfection of 0.6 % for U-shape stirrups.
- $\sigma_R = 400$ Mpa. Value corresponding to an initial imperfection of 2.4 % for spirals inside grooves in the lower part of the beams.
- $\sigma_R = 315$ Mpa. Value corresponding to an initial imperfection of 4.1 % for spirals located in the compression chord of the beams.

It is also proposed a simplified design value for the stress increment of the wires at beam failure: increment of strain equal to 0.2%, corresponding to an average increase of stresses at failure equal to 50 MPa (Eq. 7.6), except for the case of the spiral only wrapping the compression chord of the beam, where a value of 0 MPa is proposed for the increment of the stresses at failure, since the spiral is not crossed by the second branch of the critical crack.

$$\Delta\sigma_\varepsilon = E \cdot \varepsilon = 25,000 \cdot 2,000 \cdot 10^{-6} = 50 \text{ MPa} \quad (7.6)$$

The general proposed value of 50 MPa also corresponds to a shear crack width of 0.3 mm in the strengthened beams (no bonding between concrete and wire), as explained in chapter 5. The increment of strain value (0.2%) is similar to the strain at failure assumed for internal steel shear reinforcement by different codes (Comisión Permanente del Hormigón 2008) and (CEN 2002).

The yielding strength of the shear reinforcement must be substituted by the addition of $\sigma_R + \Delta\sigma_\varepsilon$.

Both proposed design values are conservative (see figure 6.11 and table 6.4). Note that the considered initial imperfection may be considered as an upper boundary for each

configuration, because the greater the depth of the beam, the less imperfection will be produced during the assembly process. The use of small scale members makes it more difficult to place the wire around the beam. Also, the U-shape stirrups are easier to place since the upper part of the links are not rounded and less imperfection is expected.

The suggested stress values have been used for predicting the shear strength of the tested beams using the CCCM (table 7.5). The different parameters shown in the columns of the table 7.5 are those already shown in table 7.2, but for designed beams. The EC-2 equations are not used in this section since the predictions in the previous section were significantly worse.

The CCCM model shows an average value of the ratio V_{test}/V_{Rd} equal to 1.16, a standard deviation of 0.11 and a coefficient of variation of 9.5 %. As previously commented, the values of beams 3.1b and 7.1 have been removed from average model calculations in the values given in brackets in table 7.5. The results confirm that for design purposes the use of the CCCM with the suggested stresses in the strengthening wires leads to excellent results. In any case, more research is needed, since other aspects have not been considered, e.g. the long-term wire relaxation or the actual strengthening effect in real scale beams.

Table 7.5. CCCM predictions of designed beams and comparison with average test values

Design phase 1 beams	V_{test} (kN)	f_s (MPa)	Compression Chord Capacity Model					V_{test}/V_{Rd}
			V_{cu} (kN)	$V_{cu}^{confinem}$ (kN)	V_{su} (kN)	V_{Rd} (kN)		
1.1 - Reference	18.30	-	16.85	-	-	16.85	1.09	
1.2 - Reference	18.41	-	16.92	-	-	16.92	1.09	
2.1 - S ϕ 3/100/UCR/A	35.41	465	16.96	3.92	7.93	28.81	1.23	
2.2 - S ϕ 3/100/UCR/A	35.95	465	17.01	3.92	7.93	28.86	1.25	
3.1a - S ϕ 3/100/UCR/NA	18.23	-	17.12	-	-	17.12	1.06	
3.1b - S ϕ 3/100/COL/A	27.14	465	17.17	3.91	7.93	29.01	0.94	
3.2a - S ϕ 3/100/UCR/NA	21.47	-	17.12	-	-	17.12	1.25	
3.2b - S ϕ 3/100/COL/A	35.21	465	17.14	3.92	7.93	28.99	1.21	
4.1 - S ϕ 3/100/PCR/A	34.35	465	17.21	3.91	7.93	29.05	1.18	
4.2 - S ϕ 3/100/PCR/A	35.60	465	17.21	3.91	7.93	29.05	1.23	
5.1 - S ϕ 3/075/UCR/A	37.04	465	17.25	5.18	5.18	32.94	1.12	
5.2 - S ϕ 3/075/UCR/A	41.82	465	17.25	5.18	5.18	32.94	1.27	
Average							1.16 (1.18)	
Standard deviation							0.10 (0.08)	
Coefficient of Variation (%)							8.7 (6.4)	
Design phase 2 beams	V_{test} (kN)	f_s (MPa)	Compression Chord Capacity Model					V_{test}/V_{Rd}
			V_{cu} (kN)	$V_{cu}^{confinem}$ (kN)	V_{su} (kN)	V_{Rd} (kN)		
6.1 - Reference	19.71	-	16.47	-	-	16.47	1.20	
6.2 - Reference	18.50	-	16.47	-	-	16.47	1.12	
7.1 - S ϕ 3/100/UCR/A/G	25.36	450	16.49	3.81	7.67	27.97	0.91	
7.2 - S ϕ 3/100/UCR/A/G	35.51	450	16.49	3.81	7.67	27.97	1.27	
8.1 - U ϕ 3/100/UCR/A	37.74	490	16.47	3.72	7.48	27.67	1.36	
8.2 - U ϕ 3/100/UCR/A	34.75	490	16.47	3.72	7.48	27.67	1.26	
9.1 - S ϕ 3/100/UCR/A/S	20.54	315	16.49	2.61	-	19.10	1.08	
9.2 - S ϕ 3/100/UCR/A/S	22.03	315	16.49	2.61	-	19.10	1.15	
10.1 - U ϕ 3/075/UCR/A	36.79	490	16.49	4.97	9.97	31.43	1.17	
10.2 - U ϕ 3/075/UCRA	33.65	490	16.49	4.97	9.97	31.43	1.07	
Average							1.16 (1.19)	
Standard deviation							0.13 (0.10)	
Coefficient of Variation (%)							10.9 (8.1)	
Average							1.16 (1.18)	
Standard deviation							0.11 (0.08)	
Coefficient of Variation (%)							9.5 (7.0)	

7.4 CONCLUSIONS OF APPLICATION OF SHEAR MODELS

The specific objective of this chapter was the validation and extension, if needed, of a previously developed mechanical model for the determination of the shear strength to take into account the external strengthening in shear. In order to achieve it, two different shear models have been used: the CCCM (Cladera, Marí, et al. 2016) and the shear equations of the Eurocode 2 (CEN 2002). Although, these models are not intended for external shear strengthening, they have been applied since no constrain in considering external shear strengthening has been encountered. Taking into account the predictions of the CCCM, the main conclusion on its application is the validation in considering active shear strengthening of RC beams using Ni-Ti-Nb SMA wires, and no additional extension is needed for this purpose.

With regard to the validation of the two existing shear design models (the Compression Chord Capacity Model and the shear design equations of Eurocode 2), the main conclusions are:

- The active external shear strengthening of RC beams has been modelled taking into account two contributions: the recovery stresses developed during the activation process and the stresses developed during the tests as elastic deformations of the Ni-Ti-Nb wires measured with the strain gauges. The activation process developed different recovery stresses depending on the initial imperfection due to installation of Ni-Ti-Nb wires ranges from around 316 MPa, at 4 % initial imperfection, to 441 MPa at 0.5 % initial imperfection in the installed wires. The increment of developed stress ranges from 29 MPa to 127 MPa. The addition of these values can be applied directly as the yield strength of the transverse reinforcement on shear models, and the obtained values range from 402 MPa to 568 MPa.
- In terms of the CCCM, the predictions given by the model without any modification with regard to the procedure established to evaluate internal reinforcement are excellent and the correlation with the experiment results is satisfactory, with an average value of the ratio V_{test}/V_R equal to 1.14, a standard deviation of 0.10, and a coefficient of variation equal to 9.1 %. It should be noted that the model has an excellent agreement taking into account that the model considers concrete

contribution, concrete contribution increase due to confinement of shear strengthening, and shear strengthening contribution.

- The predictions when using the shear equations of the current Eurocode 2 are quite conservative and present a high scatter, with an average value of the ratio V_{test}/V_R equal to 1.45, a standard deviation of 0.23 and a coefficient of variation of 15.7 %.
- Comparing the two used shear models, the CCCM predicts an increase of 83 % in shear strength of the strengthened beams compared to the reference beams. Note that the actual observed average increase of shear strength in the tested strengthened beams is 82 % compared to the reference beams. Nevertheless, the Eurocode prediction is that the strengthened beams should resist 49 % higher shear force compared to the reference beams.
- Since the predictions of shear strength of CCCM are excellent and the correlation with the experiment results is satisfactory, new predictions for design purposes with some simplifications have been performed. Different values of initial stresses after activation are suggested: 415 MPa for spirals (initial imperfection of 1.9 %); 440 MPa for U-shape stirrups (initial imperfection of 0.6 %); 400 MPa for spirals inside grooves in the lower part of the beams (initial imperfection of 2.4 %); and 315 MPa for spirals located in the upper mid-section of the beams (initial imperfection of 4.1 %). The strain increment of the wire at beam failure criterion has been selected to be the value at which yields conventional steel in internal shear reinforcement (strain of 0.2 %). For this reason, an average increase of stress at failure of 50 MPa has been considered.
- The predictions of the CCCM model for design purposes show an average value of the ratio V_{test}/V_R equal to 1.16, a standard deviation of 0.11 and a coefficient of variation of 9.5 %.
- The results confirm that for design purposes the considered criteria applied to active shear strengthening of RC beams using Ni-Ti-Nb wires have good performance. In any case, more research is needed, since other aspects have not been considered, e.g. the long-term wire relaxation or the actual strengthening effect in real scale beams.

8. CONCLUSIONS AND FUTURE WORK

This Ph.D. thesis was planned with the main objective of expanding knowledge in the repair and strengthening of RC structures using SMAs in structural engineering. An active external shear strengthening method using Ni-Ti-Nb SMA wires as external reinforcement in shear critical RC beams has been developed.

Specifically, an experimental campaign assessing the possibility of strengthening shear-critical beams using a SMA relying on the shape memory effect has been presented. The experiment results show a promising performance of the proposed technology, which increased both the shear strength of the retrofitted beams and the deflection at failure. The effectiveness of the method has been clearly shown, since strengthened beams show significant shear strength increment when compared to non-strengthened beams. Furthermore, the tests have shown that pre-cracked beams, having been loaded to approximately 98% of their maximum shear force, unloaded (equivalent to prop up), and actively strengthened by means of the proposed technology afterwards, perform similarly to beams strengthened prior to cracking.

The experimental campaign carried out has been an initial phase of a broader experimental program and has confirmed the effectiveness of the new methodology of active shear strengthening of RC beams using SMAs. These results have been the basis to plan other strengthening configurations for a further experimental campaign using a different SMA.

This research was planned as a proof-of-concept experimental campaign to demonstrate the feasibility of using externally placed SMA wires to increase the shear strength of RC members, but further research is still required.

The specific objectives were planned across four main topics:

- Physical and thermo-mechanical characterization of the available SMA: Ni-Ti-Nb wires.
- The experimental campaign of active external strengthening of RC beams without internal shear reinforcement by means of external spirals (and other configurations) of Ni-Ti-Nb wires to improve their strength.
- Characterization of the Ni-Ti-Nb recovery stresses under non-idealized conditions.
- Validation and extension, if needed, of previously developed mechanical models to take into account the external strengthening using Ni-Ti-Nb wires.

With regard to the characterization of the supplied SMA (3 mm diameter wires of Ni-Ti-Nb), proper results have been attained. Basic physical properties have been determined and material thermo-mechanical characterization has been performed by means of different laboratory tests planned with an active experimental campaign. This was updated during the planned tests, taking into account the results and interpretation of earlier tests. The main conclusions were:

- The composition of the material supplied resulted in Ti atw.45.81 %, Ni atw.45.76 % and Nb atw.8.43 %.
- The transformation temperatures have been determined from DSC and resistivity tests. The average obtained values were: $A_s = 70.5$ °C, $A_f = 79.5$ °C, $M_s = -105$ °C, and $M_f = -135$ °C. Therefore, a hysteretic behavior ($A_s - M_s$) of 175.5 °C has been obtained for the first cycle.
- Values between 500 – 700 MPa of recovery stresses have been reached in optimal laboratory conditions (minimum value of 501 MPa, maximum of 690 MPa, and average of 580 MPa). These values are comparable to the values of the yield strength of the conventional steel used in reinforced concrete structures.

- A stress-temperature phase diagram for the Ni-Ti-Nb samples has been adjusted. Moreover, when looking at the recovery stress tests, it has been observed that the test carried out at a maximum temperature of 200 °C suffices for a practical complete phase transformation to austenite.
- Values of 1002 MPa for ultimate strength, 591 MPa for yield strength, and 25 GPa for modulus of elasticity have been obtained for martensite SMA at RT. For austenite SMA at RT, values of 935 MPa for ultimate strength, 451 MPa for yield strength, and 33 GPa for modulus of elasticity have been found. Stresses for start (σ^{Ms}) and finish (σ^{Mf}) direct transformation of 494 MPa and 543 MPa have been obtained, respectively.
- The ultimate strains obtained in the tensile tests were very high for Ni-Ti-Nb (30-50%). These values are not reached in steel that is usually used as reinforcement in RC structures
- Characterization tests have been carried out at different test temperatures: 0 °C, room temperature (RT, about 20 °C) and 40 °C, to cover the typical range of temperatures for civil engineering structures. Slightly different behavior has been observed when test temperatures vary between this range. In addition, the tests were carried out applying different load conditions: monotonic and cyclic tests. Similar values in terms of ultimate strength and elastic modulus have been obtained when comparing monotonic and cyclic tests.
- Additional tests with monotonic and cyclic loads after activation have also been carried out to consider practical performance conditions for real post-stressing structures with Ni-Ti-Nb wires. Values of 965 MPa for ultimate strength and 25 GPa for modulus of elasticity have been obtained after activation (austenite) with recovery stresses of more than 569 MPa at RT test.

The supplied Ni-Ti-Nb SMA is an adequate material for structural strengthening applications. For active strengthening, it can be used with recovery (active confinement) stresses but once converted to austenite, it has been observed that there is no more pseudo-elastic behavior.

Finally, from a functional point of view, the cost of Ni-Ti-Nb is very high, but recent research on iron-based shape memory alloys envisages the application of cheaper shape memory

alloys with similar behavior. Nonetheless, an advantage of the Ni-Ti-Nb wires should be highlighted: the tested Ni-Ti-Nb wires have a wide range of available strain to be recovered under ‘activation’ process (up to 6%) while other SMA materials have a narrow range. Despite the high cost of Ni-Ti-Nb, the amount of material needed is small and needs to be placed only in critical regions of the beams meaning this application promises to be a very interesting technology for strengthening key civil infrastructures.

With regard to the experimental campaign, the effectiveness of the methodology of using Ni-Ti-Nb wires as pseudo-spirals (generating recovery stresses as a prestressing system) for active external shear strengthening of RC beams was confirmed. An average increase of 82 % in shear force and an increase of 2.6 times deflection at maximum shear force were measured in the instrumented beams of the experimental campaign. The other main conclusions of the experimental campaign are:

- The negligible effect of the pseudo-spiral placed around the beam without being activated can be seen. However, when the spiral is activated, the strengthening method is clearly effective in all cases.
- The behavior of the activated beams, in terms of shear strength and maximum deflection, is very similar and pre-cracking the beams does not affect the results if the pre-crack load is removed before activating the Ni-Ti-Nb wires.
- The strengthening method was able to increase the shear strength of the beams even after they had already collapsed and unloaded in a previous test, without conducting any additional rehabilitation work.
- The use of grooves does not represent an increase in shear strength in these beams. In addition, its use is not recommended since additional works are required to perform the grooves and they can initiate unwanted cracks.
- Non-significant differences between spirals and U-shape stirrups in shear strength and deflection at the maximum shear force were detected. However, lower values were expected from U-shape stirrups compared to spirals but only encountered for 75 mm pitch. Unexpected high values in comparison with those obtained with spirals were reached. Other aspects could have affected the tested beams, like initial imperfections

of the initial installation of the Ni-Ti-Nb wires around the beams and the fact that the U-shape stirrups do not weaken the compression chord.

- The measured strains in vertical links ranged between 1000 $\mu\epsilon$ and 5000 $\mu\epsilon$. Anyway, the average value of 3007 $\mu\epsilon$ with a standard deviation of 1221 $\mu\epsilon$ and covariance of 41 % for all tested beams are reasonable values in such test measurements. An average strain value of 3007 $\mu\epsilon$ is equivalent to a vertical shear crack width of 0.45 mm at failure, which is a reasonable value.
- The configuration of the RC beams, with or without strengthening, was intended to obtain shear failures of the tested beams and, indeed, these were obtained in almost all instances: only for beam 5.2 with a spiral pitch of 75 mm was bending failure achieved. Note that beam 5.1, with the same spiral pitch of 75 mm as beam 5.2, failed in shear.
- The methodology followed in the experimental campaign to externally strengthen the specimens is simple to put in practice: rectangular spirals are installed by hand, anchored by U-shape saddle clamps and activated using a heat gun.

With regard to the characterization of Ni-Ti-Nb recovery stresses under non-idealized conditions, a further experimental campaign was planned and performed in order to improve and complete the characterization of the Ni-Ti-Nb alloy; it was carried out once the experimental campaign of strengthened beams had been finished. Two different objectives were set: the determination of actual recovery stresses under realistic conditions by means of activation with a heat gun and the study of the influence of the initial imperfections (curvature) of the wires in the generation of recovery stresses. The main conclusions are:

- The results of the performed tests with activation by means of heat gun show that recovery stresses with practical conditions are slightly lower, with an average value of recovery stresses equal to 452 MPa with an initial pre-load of 8 MPa and 435 MPa in the case of an initial pre-load of 40 MPa.
- The imperfect installation of the wires on the beams was assessed by means of increased wire length due to initial curvature or initial imperfection (%). For most

beams with spiral wires and U-shape stirrups as shear strengthening, the initial imperfection was assessed to be between 0.5 and 2 %.

- The stress recovery tests with initial imperfection show that for an initial imperfection of 0.54 % a value of 447 MPa of recovery stress was obtained. For initial imperfections equal to 2.34 %, the recovery stress equaled 400 MPa. Lower values for higher initial imperfection up to 6% were also obtained.
- A relationship was observed between initial imperfection (i_o) and recovery stresses (σ_R), to be used in the prediction of recovery stresses of the strengthened beams. Values of recovery stresses higher than 400 MPa have been obtained for the range of reasonable imperfections, lower than 2%.
- It has been observed that the lower the strengthened beam depth, the higher the observed imperfection. Therefore, the application of this strengthening method to real beams, with greater depth, would perform better.

Another specific objective was the validation and extension, if needed, of a previously developed mechanical model for the determination of the shear strength to take into account the external strengthening in shear. In order to achieve it, two different shear models have been applied: the CCCM (Cladera, Marí, et al. 2016) and the shear equations of the Eurocode 2 (CEN 2002). Although, these models are not intended for external shear strengthening, they have been applied since no constrain in considering external shear strengthening has been encountered. Taking into account the predictions of the CCCM, the main conclusion on its application is the validation in considering active shear strengthening of RC beams using Ni-Ti-Nb SMA wires, and no additional extension is needed for this purpose.

With regard to the validation of the two existing shear design models (the Compression Chord Capacity Model and the shear design equations of Eurocode 2), the main conclusions are:

- The active external shear strengthening of RC beams has been modelled taking into account two contributions: the recovery stresses developed during the activation process and the stresses developed during the tests as elastic deformations of the Ni-Ti-Nb wires measured with the strain gauges. The activation process developed different recovery stresses depending on the initial imperfection due to installation of Ni-Ti-Nb wires ranges from around 316 MPa, at 4 % initial imperfection, to 441 MPa

at 0.5 % initial imperfection in the installed wires. The increment of developed stress ranges from 29 MPa to 127 MPa. The addition of these values can be applied directly as the yield strength of the transverse reinforcement on shear models, and the obtained values range from 402 MPa to 568 MPa.

- In terms of the CCCM, the predictions given by the model without any modification with regard to the procedure established to evaluate internal reinforcement are excellent and the correlation with the experiment results is satisfactory, with an average value of the ratio V_{test}/V_R equal to 1.14, a standard deviation of 0.10, and a coefficient of variation equal to 9.1 %. It should be noted that the model has an excellent agreement taking into account that the model considers concrete contribution, concrete contribution increase due to confinement of shear strengthening, and shear strengthening contribution.
- The predictions when using the shear equation of the current Eurocode 2 are quite conservative and present a high scatter, with an average value of the ratio V_{test}/V_R equal to 1.45, a standard deviation of 0.23 and a coefficient of variation of 15.7 %.
- Comparing the two used shear models, the CCCM predicts an increase of 83 % in shear strength of the strengthened beams compared to the reference beams. Note that the actual observed average increase of shear strength in the tested strengthened beams is 82 % compared to the reference beams. Nevertheless, the Eurocode prediction is that the strengthened beams should resist 49 % higher shear force compared to the reference beams.
- Since the predictions of shear strength of CCCM are excellent and the correlation with the experiment results is satisfactory, new predictions for design purposes with some simplifications have been performed. Different values of initial stresses after activation are suggested: 415 MPa for spirals (initial imperfection of 1.9 %); 440 MPa for U-shape stirrups (initial imperfection of 0.6 %); 400 MPa for spirals inside grooves in the lower part of the beams (initial imperfection of 2.4 %); and 315 MPa for spirals located in the upper mid-section of the beams (initial imperfection of 4.1 %). The strain increment of the wire at beam failure criterion has been selected to be the value at which yields conventional steel in internal shear reinforcement (strain of 0.2 %). For this reason, an average increase of stress at failure of 50 MPa has been considered.

- The predictions of the CCCM model for design purposes show an average value of the ratio V_{test}/V_R equal to 1.16, a standard deviation of 0.11 and a coefficient of variation of 9.5 %.
- The results confirm that for design purposes the considered criteria applied to active shear strengthening of RC beams using Ni-Ti-Nb wires have good performance. In any case, more research is needed, since other aspects have not been considered, e.g. the long-term wire relaxation or the actual strengthening effect in real scale beams.

This research was planned as a proof-of-concept experimental campaign to demonstrate the feasibility of using externally placed SMA wires to increase the shear strength of RC members, and more research is still required in various aspects for a complete development of this methodology:

- The experimental beam campaign has been performed through 20 tests. Further tests with different beam and reinforcement configurations, beam geometry and applied loads will serve to confirm the effectiveness of active external shear strengthening of RC beams using Ni-Ti-Nb wires as pseudo-spirals (generating recovery stresses as a pre-stressing system).
- Small-scale tests on RC beams have been carried out. Size effects have not been studied. For this reason, beam tests taking into account significantly higher dimensions need to be undertaken to confirm that the strengthening technology may be successfully applied to a broad range of civil engineering structures. The initial losses in the wires due to incorrect placement is related to the size of the beams: in all likelihood, the larger the beams the smaller the initial imperfections.
- With regard to the characterization of Ni-Ti-Nb SMA wires, long-term behavior is an important factor to constrain. Relaxation tests would be worthwhile to assess the loss of long-term recovery stress.
- The applied installation and activation technique of shear strengthening wires was intended to be an easy methodology to carry out in engineering practice that implies some initial imperfection. Although the available recovery strain of the used SMA is 6% and the initial imperfection of the applied technique is around 2 %, the use of other strengthening and installation techniques could help to improve the practical application of the actual methodology.

- A similar strengthening system could be adapted for use with different SMAs. The research group has recently performed a new experimental campaign beyond the scope of this Ph.D. thesis related to the shear strengthening of RC beams using a Fe-SMA.

REFERENCES

- Abdulridha, A. et al., 2013. Behavior and modeling of superelastic shape memory alloy reinforced concrete beams. *Engineering Structures*, 49, pp.893–904.
- Adhikary, B.B. & Mutsuyoshi, H., 2006. Shear strengthening of reinforced concrete beams using various techniques. *Construction and Building Materials*, 20(6), pp.366–373.
- AENOR, 2009. UNE-EN-12390-3. Testing hardened concrete - Part 3: Compressive strength of test specimens.
- AENOR, 2010. UNE-EN-12390-6. Testing hardened concrete - Part 6: Tensile splitting strength of test specimens.
- AENOR, 2003. UNE-EN-ISO15630-1. Aceros para el armado y el pretensado del hormigón. Métodos de ensayo. Parte 1: Barras, alambres y alambrón para hormigón armado.
- AENOR, 2011. UNE36065. Ribbed bars of weldable steel with special characteristics of ductility for the reinforcement of concrete.
- Alam, M.S., Moni, M. & Tesfamariam, S., 2012. Seismic overstrength and ductility of concrete buildings reinforced with superelastic shape memory alloy rebar. *Engineering Structures*, 34, pp.8–20.
- Alam, M.S., Nehdi, M. & Youssef, M.A., 2009. Seismic performance of concrete frame structures reinforced with superelastic shape memory alloys. *Smart*, 5(5), pp.565–585.
- Alam, M.S., Nehdi, M. & Youssef, M.A., 2008. Shape memory alloy-based smart RC bridges: overview of state-of-the-art. *Smart Structures and Systems*, 4(3), pp.367–389.
- Alam, M.S., Youssef, M.A. & Nehdi, M., 2007. Utilizing shape memory alloys to enhance the performance and safety of civil infrastructure: a review. *Canadian Journal of Civil Engineering*, 34(9), pp.1075–1086.
- Andrawes, B., Shin, M. & Wierschem, N., 2010. Active Confinement of Reinforced Concrete Bridge Columns Using Shape Memory Alloys. *Journal of Bridge*

-
- Engineering*, 15(1), pp.81–89.
- ASCE-ACI Committee 426, 1973. Shear strength of reinforced concrete members. *ASCE J Struct Div*, pp.1091–1197.
- ASCE-ACI Committee 445, 1998. Recent Approaches to Shear Design of Structural Concrete. , pp.1375–1417.
- ASTM-F2516-07, 2007. *Standard test method for tension testing of nickel-titanium superelastic materials* ASTM International, ed., West Conshohocken, PA: ASTM International.
- ASTM F2082-06, 2006. Standard test method for determination of transformation temperature of nickel–titanium shape memory alloys by bend and free recovery.
- Auricchio, F. et al., 2001. *Shape memory alloys : advances in modelling and applications* F. Auricchio et al., eds., Barcelona: CIMNE.
- Azimi, M. et al., 2016. Evaluation of new spiral shear reinforcement pattern for reinforced concrete joints subjected to cyclic loading. *Advances in Structural Engineering*, 19(5), pp.730–745.
- Baggio, D., Soudki, K. & Noël, M., 2014. Strengthening of shear critical RC beams with various FRP systems. *Construction and Building Materials*, 66, pp.634–644.
- Bairán, J.M., Marí, A. & Cladera, A., 2018. Analysis of shear resisting actions by means of optimization of strut and tie models taking into account crack patterns. *Hormigón y Acero*, (In press), p.10.
- Bairan, J.M. & Mari, A.R., 2006. Coupled model for the non-linear analysis of anisotropic sections subjected to general 3D loading. Part 1: Theoretical formulation. *Computers and Structures*, 84(31–32), pp.2254–2263.
- Bakis, C. et al., 2002. Fiber-reinforced polymer composites for construction state-of-the-art review. *Journal of Composites for Construction*, 6(2), pp.73–87.
- Baruj, A. & Troiani, H.E., 2008. The effect of pre-rolling Fe – Mn – Si-based shape memory alloys : Mechanical properties and transmission electron microcopy examination. *Materials Science and Engineering A*, 482, pp.574–577.

- Bentz, E.C., 2000. *Sectional analysis of reinforced concrete members (Doctoral Thesis)*. University of Toronto.
- Buehler, W.J., Gilfrich, J. V. & Wiley, R.C., 1963. Effect of Low-Temperature Phase Changes on the Mechanical Properties of Alloys near Composition TiNi. *Journal of Applied Physics*, 34(5), pp.1475–1477.
- Cardone, D. & Rossino, M., 2014. Fragility Curves of Pre-70 RC Frame Buildings Considering Different Performance Limit States. *Soil Dynamics and Earthquake Engineering*, (Dec. 2014).
- CEN, 2002. *Eurocode 2: Design of Concrete Structures: Part 1: General Rules and Rules for Buildings*. European Committee for Standardization; 2002,
- Chalioris, C.E., Thermou, G.E. & Pantazopoulou, S.J., 2014. Behaviour of rehabilitated RC beams with self-compacting concrete jacketing - Analytical model and test results. *Construction and Building Materials*, 55, pp.257–273.
- Chen, Q. & Andrawes, B., 2017a. Cyclic Stress-Strain Behavior of Concrete Confined with NiTiNb-Shape Memory Alloy Spirals. *Journal of Structural Engineering (United States)*, 143(5).
- Chen, Q. & Andrawes, B., 2017b. Plasticity Modeling of Concrete Confined With NiTiNb Shape Memory Alloy Spirals. *Structures*, 11(April), pp.1–10.
- Chen, Q., Shin, M. & Andrawes, B., 2014. Experimental study of non-circular concrete elements actively confined with shape memory alloy wires. *Construction and Building Materials*, 61, pp.303–311.
- Choi, E., Nam, T., et al., 2012. Behavior of NiTiNb SMA wires under recovery stress or prestressing. *Nanoscale Research Letters*, 7(1), p.66.
- Choi, E., Choi, D.-H., et al., 2012. Seismic protection of lap-spliced RC columns using SMA wire jackets. *Magazine of Concrete Research*, 64(3), pp.239–252.
- Choi, E. et al., 2008. The behavior of concrete cylinders confined by shape memory alloy wires. *Smart Materials and Structures*, 17(6), p.10.
- Choi, K.-K. & Park, H.-G., 2007. Unified shear strength model for reinforced concrete

-
- beams - Part II: Verification and simplified method. *ACI Structural Journal*, 104(2), pp.153–161.
- Cladera, A., Weber, B., et al., 2014. Iron-based shape memory alloys for civil engineering structures : An overview. *Construction & Building Materials*, 63(MAY), pp.281–293.
- Cladera, A., Ribas, C., et al., 2016. Método de refuerzo activo frente a esfuerzo cortante o punzonamiento en elementos portantes estructurales y sistema de refuerzo activo. , p.Patent ES2592554 (B1), 19p.
- Cladera, A. et al., 2017. One-way Shear Design Method Based on a Multi-Action Model. *Concrete International*, 39(9), pp.40–46.
- Cladera, A. et al., 2015. Predicting the shear-flexural strength of slender reinforced concrete T and I shaped beams. *Engineering Structures*, 101, pp.386–398.
- Cladera, A., Marí, A., et al., 2016. The compression chord capacity model for the shear design and assessment of reinforced and prestressed concrete beams. *Structural Concrete*, 17(6), pp.1017–1032.
- Cladera, A., Oller, E. & Ribas, C., 2014. Pilot Experiences in the Application of Shape Memory Alloys in Structural Concrete. *Journal of Materials in Civil Engineering*, 26(11), p.10.
- Colajanni, P., Recupero, A. & Spinella, N., 2012. Generalization of shear truss model to the case of SFRC beams with stirrups. *Computers and Concrete*, 9(3), pp.227–244.
- Colajanni, P., Recupero, A. & Spinella, N., 2017. Increasing shear capacity of RC beams using steel angles and pre-tensioned stainless steel ribbons. *Structural Concrete*, 17(5), pp.848–857.
- Colajanni, P., Recupero, A. & Spinella, N., 2016. Increasing the flexural capacity of RC beams using steel angles and pre-tensioned stainless steel ribbons. *Structural Concrete*, 17(5), pp.848–857.
- Collins, M.P. et al., 2008. An adequate theory for the shear strength of reinforced concrete structures. *Magazine of Concrete Research*, 60(9), pp.635–650.
- Colotti, V. et al., 2005. Analytical model to evaluate failure behavior of plated reinforced

- concrete beams strengthened for shear. *ACI Structural Journal*, 102(5), pp.784–785.
- Comisión Permanente del Hormigón, 2008. *EHE-2008. Instrucción de Hormigón Estructural* M. M. de Fomento, ed., Madrid: Ministerio de Fomento.
- De Corte, W. & Boel, V., 2013. Effectiveness of spirally shaped stirrups in reinforced concrete beams. *Engineering Structures*, 52, pp.667–675.
- Cui, D., Zhang, Y. & Guan, P., 2012. Research Progress of Smart Concrete Structures reinforced by Shape Memory Alloy. In A. M. and Materials, ed. *Vibration, Structural Engineering and Measurement II*. Switzerland: Trans Tech Publications, pp. 1157–1160.
- Czaderski, C. et al., 2014. Feasibility of iron-based shape memory alloy strips for prestressed strengthening of concrete structures. *Construction and Building Materials*, 56, pp.94–105.
- Czaderski, C., Hahnebach, B. & Motavalli, M., 2006. RC beam with variable stiffness and strength. *Construction and Building Materials*, 20(9), pp.824–833.
- Debbarma, S.R. & Saha, S., 2012a. An experimental study on growth of time-dependent strain in shape memory alloy reinforced concrete beams and slabs. *International Journal of Civil Engineering and Technology*, 3(2), pp.108–122.
- Debbarma, S.R. & Saha, S., 2012b. Review of Shape Memory Alloys applications in civil structures, and analysis for its potential as reinforcement in concrete flexural members. *International Journal of Civil and Structural Engineering*, 2(3), pp.924–942.
- Deng, J. et al., 2017. Fibre Reinforced Polymer Composites for Structural Applications in Construction. *Hindawi International Journal of Polymer Science*, 2017(ID 9218529), p.1.
- Deng, Z., Li, Q. & Sun, H., 2006. Behavior of concrete beam with embedded shape memory alloy wires. *Engineering Structures*, 28(12), pp.1691–1697.
- Derkowski, W., 2015. Opportunities and risks arising from the properties of FRP materials used for structural strengthening. *Procedia Engineering*, 108, pp.371–379.
- Desroches, R. & Delemont, M., 2002. Seismic retrofit of simply supported bridges using

-
- shape memory alloys. , 24, pp.325–332.
- Desroches, R., McCormick, J. & Delemont, M., 2004. Cyclic Properties of Superelastic Shape Memory Alloy Wires and Bars. *J Struct Eng*, 130(1), pp.38–46.
- Dolce, M. & Cardone, D., 2001a. Mechanical behaviour of shape memory alloys for seismic applications. *International Journal of Mechanical Sciences*, 43, p.2631.
- Dolce, M. & Cardone, D., 2001b. Mechanical behaviour of shape memory alloys for seismic applications. *International Journal of Mechanical Sciences*, 43, p.2631.
- Dolce, M., Cardone, D. & Ponzo, F.C., 2007. Shaking-table tests on reinforced concrete frames with different isolation systems. , (September 2006), pp.573–596.
- Dommer, K. & Andrawes, B., 2012. Thermomechanical Characterization of NiTiNb Shape Memory Alloy for Concrete Active Confinement Applications. *Journal of Materials in Civil Engineering*, 24(10), pp.1274–1282.
- Druker, A., Perotti, A. & Baruj, A., 2013. Heat Treatments of Fe-Mn-Si Based Alloys : Mechanical. *Journal of ASTM International*, 8(4), pp.1–9.
- Duerig, T.W., Melton, K.N. & Proft, J.L., 1990. Wide Hysteresis Shape Memory Alloys. In *In Engineering Aspects of Shape Memory Alloys*. pp. 130–136.
- Van Den Einde, L., Zhao, L. & Seible, F., 2003. Use of FRP composites in civil structural applications. *Construction and Building Materials*, 17, pp.507–516.
- El-hacha, R. & Abdelrahman, K., 2015. Confining RC columns subjected to concentric axial loading using Shape Memory Alloy wires. In *SMAR15*. p. 8.
- El-Hacha, R. & Soudki, K., 2013. Prestressed near-surface mounted fibre reinforced polymer reinforcement for concrete structures - a review¹. *Canadian Journal of Civil Engineering*, 2013(September), pp.1127–1139.
- El-Tawil, S. & Ortega-Rosales, J., 2004. Prestressing concrete using shape memory alloy tendons. *ACI Structural Journal*, 101(6), pp.846–851.
- Ferreira, D., 2013. *A model for the nonlinear, time-dependent and strengthening analysis of shear critical frame concrete structures (Doctoral Thesis)*. Universitat Politècnica de Catalunya, Barcelona Tech.

- Ferreira, D., Bairán, J. & Marí, A., 2013. Numerical simulation of shear-strengthened RC beams. *Engineering Structures*, 46, pp.359–374.
- Ferreira, D., Bairán, J.M. & Marí, A., 2016. Shear strengthening of reinforced concrete beams by means of vertical prestressed reinforcement. *Structure and Infrastructure Engineering*, 12(3), pp.394–410.
- FIB - bulletin 24, 2003. Seismic assessment and retrofit of reinforced concrete buildings. , p.312.
- FIB - bulletin 35, 2006. Retrofitting of concrete structures by externally bonded FRPs. , p.221.
- Foster, R.M., Morley, C.T. & Lees, J.M., 2013. Shear transfer across a diagonal crack in reinforced concrete strengthened with externally bonded FRP fabric. In *Advanced Composites in Construction 2013, ACIC 2013 - Conference Proceedings*. Department of Engineering, University of Cambridge, pp. 166–177.
- Herbrand, M. & Classen, M., 2015. Shear tests on continuous prestressed concrete beams with external prestressing. *Structural Concrete*, 16(3), pp.428–437.
- Hollaway, L.C., 2010. A review of the present and future utilisation of FRP composites in the civil infrastructure with reference to their important in-service properties. *Construction and Building Materials*, 24(12), pp.2419–2445.
- Hosseini, E. et al., 2018. Stress recovery and cyclic behaviour of an Fe-Mn-Si shape memory alloy after multiple thermal activation. *Smart Materials and Structures*, 27(2), p.10.
- Hui Shi, M., 2014. *From functional properties to micro / nano-structures : a TEM study of NiTiNb shape memory alloys (Doctoral Thesis)*. Universiteit Antwerpen.
- Isalgue, A. et al., 2015. Behavior of NiTi Wires for Dampers and Actuators in Extreme Conditions. *Journal of Materials Engineering and Performance*, 24(9), pp.3323–3327.
- Jani, J.M. et al., 2014. A review of shape memory alloy research, applications and opportunities. *Materials and Design*, 56, pp.1078–1113.
- Janke, L. et al., 2005. Applications of shape memory alloys in civil engineering structures - Overview, limits and new ideas. *Materials and Structures*, 38(June), pp.578–592.

-
- Johnson, R. et al., 2008. Large scale testing of nitinol shape memory alloy devices for retrofitting of bridges. *Smart Materials and Structures*, 17(3).
- Kajiwara, S., 1999. Characteristic features of shape memory effect and related transformation behavior in Fe-based alloys. *Materials Science and Engineering A*, 273–275(1999), pp.67–88.
- Kajiwara, S. et al., 2001. Remarkable Improvement of Shape Memory effect in Fe-Mn-Si Based Shape Memory Alloys by Producing NbC Precipitates. *SCRIPTA MATERIALIA*, 44(5), pp.2809–2814.
- Karayannis, C.G. & Chalioris, C.E., 2013. Shear tests of reinforced concrete beams with continuous rectangular spiral reinforcement. *Construction and Building Materials*, 46, pp.86–97.
- Kotynia, R., Lasek, K. & Staskiewicz, M., 2014. Flexural Behavior of Preloaded RC Slabs Strengthened with Prestressed CFRP Laminates. *Journal of Composites for Construction*, 18(3), p.11.
- Krstulovic-Opara, N. & Thiedeman, P.D., 2000. Active Confinement of Concrete Members with Self-Stressing Composites. *ACI Materials Journal*, 97(97), pp.297–308.
- Kuang, Y. & Ou, J., 2008. Self-repairing performance of concrete beams strengthened using superelastic SMA wires in combination with adhesives released from hollow fibers. *Smart Materials and Structures*, 17, p.7.
- Kurdjumov, G. V. & Khandros, L.G., 1949. First reports of the thermoelastic behaviour of the martensitic phase of Au-Cd alloys. *Doklady Akademii Nauk SSSR* 66, pp.211–213.
- Kustov, S. et al., 2012. Isothermal and athermal martensitic transformations in Ni-Ti shape memory alloys. *Acta Materialia*, 60, pp.2578–2592.
- Lagoudas, D., 2008. *Shape Memory Alloys* D. Lagoudas, ed., Springer New York LLC.
- Lee, W.J. et al., 2013. Phase transformation behavior under uniaxial deformation of an Fe-Mn-Si-Cr-Ni-VC shape memory alloy. *Materials Science and Engineering A*, 581, pp.1–7.
- Lee, W.J., Weber, B. & Leinenbach, C., 2015. Recovery stress formation in a restrained Fe-

- Mn-Si-based shape memory alloy used for prestressing or mechanical joining. *Construction and Building Materials*, 95, pp.600–610.
- Leinenbach, C. et al., 2016. Creep and stress relaxation of a FeMnSi-based shape memory alloy at low temperatures. *Materials Science and Engineering A*, 677, pp.106–115.
- Leinenbach, C. et al., 2012. Thermo-mechanical properties of an Fe-Mn-Si-Cr-Ni-VC shape memory alloy with low transformation temperature. *Advanced Engineering Materials*, 14(1–2), pp.62–67.
- Lexcellent, C., 2013. *Shape-memory alloys handbook*, London : Iste Ltd and John Wiley.
- Li, H., Liu, Z. & Ou, J., 2008. Experimental study of a simple reinforced concrete beam temporarily strengthened by SMA wires followed by permanent strengthening with CFRP plates. , 30, pp.716–723.
- Li, H., Mao, C. & Ou, J., 2005. Strain Self-Sensing Property and Strain Rate Dependent Constitutive Model of Austenitic Shape Memory Alloy : , (December), pp.676–685.
- Li, L., Li, Q. & Zhang, F., 2007. Behavior of Smart Concrete Beams with Embedded Shape Memory Alloy Bundles. *Journal of Intelligent Material Systems & Structures*, 18(10), pp.1003–1014.
- Lin, F., Hua, J. & Dong, Y., 2017. Shear Transfer Mechanism of Concrete Strengthened with External CFRP Strips. *Journal of Composites for Construction*, 21(2), p.8.
- De Lorenzis, L. & Teng, J.G., 2007. Near-surface mounted FRP reinforcement: An emerging technique for strengthening structures. *Composites Part B: Engineering*, 38(2), pp.119–143.
- Maji, A.K. & Negret, I., 1998. Smart Prestressing with Shape-Memory Alloy. *Journal of Engineering Mechanics*, 124(10), pp.1121–1128.
- Marí, A. et al., 2015. Shear-flexural strength mechanical model for the design and assessment of reinforced concrete beams. *Structure and Infrastructure Engineering*, 11, pp.1399–1419.
- Marí, A. et al., 2016. Shear Design and Assessment of Reinforced and Prestressed Concrete Beams Based on a Mechanical Model. *Journal of Structural Engineering*, 04016064,

p.17.

- Mari, A. et al., 2014. Shear design of FRP reinforced concrete beams without transverse reinforcement. *Composites Part B: Engineering*, 57, pp.228–241.
- Maruyama, T. & Kubo, H., 2011. Ferrous (Fe-based) shape memory alloys (SMAs): Properties, processing and applications. In *Shape Memory and Superelastic Alloys: Technologies and Applications*. Awaji Materia Co. Ltd, 2-3-13 Kanda-Ogawamachi, Chiyoda-ku, Tokyo 101-0052, Japan: Elsevier Ltd, pp. 141–159.
- Mas, B. et al., 2017. Superelastic shape memory alloy cables for reinforced concrete applications. *Construction and Building Materials*, 148, pp.307–320.
- Mas, B., Cladera, A. & Ribas, C., 2016a. Experimental study on concrete beams reinforced with pseudoelastic Ni-Ti continuous rectangular spiral reinforcement failing in shear. *Engineering Structures*, 127(1), pp.759–768.
- Mas, B., Cladera, A. & Ribas, C., 2016b. Fundamentals and pilot experiences of the application of shape memory alloys in structural engineering. *Hormigón y Acero*, 67(280), pp.309–323.
- Mazzolani, F.M. & Mandara, A., 2002. Modern trends in the use of special metals for the improvement of historical and monumental structures. *Engineering Structures*, 24(7), pp.843–856.
- Melton, K., Proft, J. & TW., D., 1986. A new wide hysteresis NiTi based shape memory alloy and its applications. *Proc. Int. Conf. Martensitic Transform. ICOMAT-86*, p.1053–8.
- Melton, K.N., Proft, J.L. & Duerig, T.W., 1989. Wide hysteresis shape memory alloys based on the Ni-Ti-Nb system. In *The Martensitic Transformation in Science and Technology*, ed. *Shape Memory Materials*. pp. 165–170.
- Menna, C., Auricchio, F. & Asprone, D., 2015. Applications of Shape Memory Alloys in Structural Engineering. In *Shape Memory Alloy engineering: for Aerospace, Structural and Biomedical Applications*. pp. 369–403.
- Miyazaki, S. et al., 1986. Effect of cyclic deformation on the pseudoelasticity characteristics

- of Ti-Ni alloys. *Metallurgical Transactions A*, 17(1), pp.115–120.
- Moser, K., 2005. Feasibility of concrete prestressed by shape memory alloy short fibers. *Materials and Structures*, 38(279), pp.593–600.
- Motavalli, M. et al., 2009. Shape memory alloys for civil engineering structures-On the way from vision to reality. *Architecture-Civil Engineering-Environment*, 4, pp.81–94.
- Muntasir Billah, A.H. & Alam, M.S., 2012. Seismic performance of concrete columns reinforced with hybrid shape memory alloy (SMA) and fiber reinforced polymer (FRP) bars. *Construction and Building Materials*, 28(1), pp.730–742.
- Muttoni, A. & Fernandez-Ruiz, M., 2008. Shear Strength of Members without Transverse Reinforcement as Function of Critical Shear Crack Width. *ACI Structural Journal*, 105(2), pp.163–172.
- Navarro Gregori, J. et al., 2007. A 3D numerical model for reinforced and prestressed concrete elements subjected to combined axial, bending, shear and torsion loading. *Engineering Structures*, 29(12), pp.3404–3419.
- Nielsen, M.P., Braestrup, M.W. & Bach, F., 1978. Rational analysis of shear in reinforced concrete beams. In *In: IABSE proceedings, 1978*. pp. 1–16.
- Ocel, J. et al., 2004. Steel beam-column connections using shape memory alloys. *Journal of Structural Engineering*, 130(5), pp.732–740.
- Oller, E. et al., 2015. Shear design of reinforced concrete beams with FRP longitudinal and transverse reinforcement. *Composites Part B: Engineering*, 74, pp.104–122.
- Otsuka, K. & Wayman, C., 1998. *Shape Memory Materials* K. Otsuka & C. M. Wayman, eds., . United Kingdom: Cambridge University Press.
- Ozawa, M., Suzuki, A. & Inaba, T., 2011. The use of shape memory alloys (SMAs) in construction and housing. In *Shape Memory and Superelastic Alloys: Technologies and Applications*. pp. 110–119.
- Ozbulut, O.E., Hurlbauss, S. & Desroches, R., 2011. Seismic Response Control Using Shape Memory Alloys: A Review. *Journal of Intelligent Material Systems and Structures*, 22(14), pp.1531–1549.

-
- Padgett, J.E., Desroches, R. & Ehlinger, R., 2010. Experimental response modification of a four-span bridge retrofit with shape memory alloys Jamie. *Structural Control and Health Monitoring*, 17(1), pp.694–708.
- Park, J. et al., 2011. Comparing the cyclic behavior of concrete cylinders confined by shape memory alloy wire or steel jackets. *Smart Materials and Structures*, 20(9).
- Park, S., Kim, T. & Hong, S.N., 2010. Flexural behavior of continuous steel girder with external post-tensioning and section enhancement. *Journal of Constructional Steel Research*, 66(2), pp.248–255.
- Penar, B.W., 2005. *Recentering Beam-Column Connections Using Shape Memory Alloys (MSc Thesis)*. Georgia Institute of Technology.
- Pereiro-Barceló, J. & Bonet, J.L., 2017. Ni-Ti SMA bars behaviour under compression. *Construction and Building Materials*, 155, pp.348–362.
- Pereiro-Barceló, J., Bonet, J.L. & Albiol-Ibáñez, J.R., 2018. Buckling of steel and Ni-Ti reinforcements in very high performance concrete (VHPC) elements. *Construction and Building Materials*, 160, pp.551–563.
- Petrangeli, M., Pinto, P.E. & Ciampi, V., 1999. Fiber Element for Cyclic Bending and Shear of RC Structures. i: Theory. *Journal of Engineering Mechanics*, 125(September), pp.994–1001.
- Reedlunn, B., Daly, S. & Shaw, J., 2013a. Superelastic shape memory alloy cables: Part i - Isothermal tension experiments. *International Journal of Solids and Structures*, 50(20–21), pp.3009–3026.
- Reedlunn, B., Daly, S. & Shaw, J., 2013b. Superelastic shape memory alloy cables: Part II - Subcomponent isothermal responses. *International Journal of Solids and Structures*, 50(20–21), pp.3027–3044.
- Regan, P.E., 1993. Research on shear: a benefit to humanity or a waste of time? *Structural engineer London*, 71(19), pp.337–347.
- Reineck, K.-H., 1991. Ultimate shear force of structural concrete members without transverse reinforcement derived from a mechanical model. *ACI Structural Journal*,

- 88(5), pp.592–602.
- Ribas González, C.R. & Fernández Ruiz, M., 2017. Influence of flanges on the shear-carrying capacity of reinforced concrete beams without web reinforcement. *Structural Concrete*, 18(5), pp.720–732.
- Rius, J.M. et al., 2017a. Active shear strengthening of RC beams using shape memory alloys. In *Fourth Conference on Smart Monitoring, Assessment and Rehabilitation of Civil Structures - SMAR17*. p. 8.
- Rius, J.M. et al., 2017b. Refuerzo externo activo a cortante mediante aleaciones con memoria de forma. In *VII Congreso de ACHE 2017*. p. 10.
- Rius, J.M. et al., 2018. Shear Strengthening of Reinforced Concrete Beams Using Shape Memory Alloys. *Construction & Building Materials*, (In press), p.25.
- Roh, H. & Reinhorn, A.M., 2010. Hysteretic behavior of precast segmental bridge piers with superelastic shape memory alloy bars. *Engineering Structures*, 32(10), pp.3394–3403.
- Rojob, H. & El-hacha, R., 2017. New anchorage mechanism for smooth Fe-SMA bar used for flexural strengthening of RC beams using NSM technique. In *Fourth Conference on Smart Monitoring, Assessment and Rehabilitation of Civil Structures - SMAR17*. p. 8.
- Rojob, H. & El-Hacha, R., 2017. Self-Prestressing Using Iron-Based Shape Memory Alloy for Flexural Strengthening of Reinforced Concrete Beams. *ACI Materials Journal*, 114-S44, pp.523–532.
- Ruano, G. et al., 2014. Shear retrofitting of reinforced concrete beams with steel fiber reinforced concrete. *Construction and Building Materials*, 54, pp.646–658.
- Saiidi, M.S. et al., 2007. Pilot Study of Behavior of Concrete Beams Reinforced with Shape Memory Alloys. *Journal of Materials in Civil Engineering*, (June 2007), pp.454–461.
- Saiidi, M.S., Brien, M.Q. & Sadrossadat-zadeh, M., 2009. Cyclic Response of Concrete Bridge Columns Using. *ACI Structural Journal*, 106-S08, pp.69–77.
- Sakai, Y. et al., 2003. Experimental study on enhancement of self-restoration of concrete beams using SMA wire. *Smart Structures and Materials 2003: Smart Systems and*

Nondestructive Evaluation for Civil Infrastructures, 5057, pp.178–186.

- Santamarta, R., Pons, J. & Cesari Alberich, E., 2005. Aliatges amb memòria de forma i les seves aplicacions: ortodòncies, detectors d'incendis i anticonceptius. *Revista de la Societat Catalana de Química*, pp.26–38.
- Saritas, A. & Filippou, F.C., 2009. Inelastic axial-flexure-shear coupling in a mixed formulation beam finite element. *International Journal of Non-Linear Mechanics*, 44(8), pp.913–922.
- Sato, A. et al., 1984. Orientation and composition dependencies of shape memory effect IN Fe-Mn-Si alloys. *Acta Metallurgica*, 32(4), pp.539–547.
- Sato, A., Kubo, H. & Maruyama, T., 2006. Mechanical Properties of Fe – Mn – Si Based SMA and the Application. *Materials Transactions*, 47(3), pp.571–579.
- Sawaguchi, T. et al., 2006. Development of Prestressed Concrete Using Fe–Mn–Si-Based Shape Memory Alloys Containing NbC. *Materials Transactions*, 47(3), pp.580–583.
- Shahverdi, M., Czaderski, C. & Motavalli, M., 2016. Iron-based shape memory alloys for prestressed near-surface mounted strengthening of reinforced concrete beams. *Construction and Building Materials*, 112, pp.28–38.
- Shajil, S.M., Srinivasan, M. & Santhanam, N., 2012. Self-centering of shape memory alloy fiber reinforced cement mortar members subjected to strong cyclic loading. *Materials and Structures*, (On-line 2012), p.11.
- Shin, M. & Andrawes, B., 2010. Experimental investigation of actively confined concrete using shape memory alloys. *Engineering Structures*, 32(3), pp.656–664.
- Shin, M. & Andrawes, B., 2012. Modeling and Validation of RC Columns Seismically Retrofitted using Shape Memory Spiral. *Structures Congress 2012 © ASCE 2012 438*, pp.571–580.
- Shin, M. & Andrawes, B., 2014. Parametric study of RC bridge columns actively confined with shape memory alloy spirals under lateral cyclic loading. *Journal of Bridge Engineering*, 19(10).
- Shin, M. & Andrawes, B., 2013. Testing of RC Bridge Columns Confined with Shape

- Memory Alloys. In *SMAR13*. p. 8.
- Song, G., Mo, Y.L., et al., 2006. Health monitoring and rehabilitation of a concrete structure using intelligent materials. *Smart Materials and Structures*, 15(2), p.309.
- Song, G., Ma, N. & Li, H.N., 2006. Applications of shape memory alloys in civil structures. *Engineering Structures*, 28(9), pp.1266–1274.
- Soroushian, P. et al., 2001. Repair and strengthening of concrete structures through application of corrective posttensioning forces with shape memory alloys. *Transportation Research Record: Journal of the Transportation Research Board*, (1770), pp.20–26.
- Souza, R.H.F. & Appleton, J., 1997. Behaviour of shear-strengthened reinforced concrete beams. *Materials and Structures/Materiaux et Constructions*, 30(196), pp.81–86.
- Speicher, M.S., Desroches, R. & Leon, R.T., 2011. Experimental results of a NiTi shape memory alloy (SMA) -based recentering beam-column connection. *Engineering Structures*, 33(9), pp.2448–2457.
- Stanford, N. & Dunne, D.P., 2006. Thermo-mechanical processing and the shape memory effect in an Fe-Mn-Si-based shape memory alloy. *Materials Science and Engineering A*, 422(1–2), pp.352–359.
- Stanford, N., Dunne, D.P. & Li, H., 2008. Re-examination of the effect of NbC precipitation on shape memory in Fe-Mn-Si-based alloys. *Scripta Materialia*, 58(7), pp.583–586.
- Tavousi Tehrani, B., Shameli-Derakhshan, S. & Jarrahi Feriz, H., 2017. An overview on Active Confinement of Concrete column and piers Using SMAs. In *2nd International Conference on researches in Science*. Idtambul, p. 10.
- Tazarv, M. & Saiidi, M.S., 2017. Analysis , Design , and Construction of SMA-Reinforced FRP- Confined Concrete Columns. In *SMAR17*. p. 8.
- Torra, V. et al., 2007. Built in dampers for family homes via SMA : An ANSYS computation scheme based on mesoscopic and microscopic experimental analyses. *Engineering Geology*, 29, pp.1889–1902.
- Torra, V. et al., 2011. SMA in Mitigation of Extreme Loads in Civil Engineering: Study of

-
- their Application in a Realistic Steel Portico. *Applied Mechanics and Materials*, 82, pp.278–283.
- Tran, H., Balandraud, X. & Destrebecq, J.F., 2015. Improvement of the mechanical performances of concrete cylinders confined actively or passively by means of SMA wires. *Archives of Civil and Mechanical Engineering*, 15(1), pp.292–299.
- Tyber, J. et al., 2007. Structural engineering with NiTi. 1: Basic materials characterization. *Journal of Engineering Mechanics*, 133(9), pp.1009–1018.
- Uchida, K. et al., 2011. Effects of pre-strain and heat treatment temperature on phase transformation temperature and shape recovery stress of Ti-Ni-Nb shape memory alloys for pipe joint applications. *Materials Transactions*, 49(7), pp.1650–1655.
- Varela, F. et al., 2017. Relajación tensional en cables de aleaciones con memoria de forma Ni-Ti-Nb. In *VII Congreso de ACHE 2017*. p. 10.
- Varela, S. & Saiidi, M., 2017. Resilient deconstructible columns for accelerated bridge construction in seismically active areas. *Journal of Intelligent Material Systems and Structures*, 28(13), pp.1751–1774.
- Vecchio, F.J. & Collins, M.P., 1986. Modified Compression-Field Theory for Reinforced Concrete Elements Subjected to Shear. *Journal of the American Concrete Institute*, 83(2), pp.219–231.
- Walraven, J., Narayanan, R.S. & Chana, P., 2008. *Eurocode 2 Commentary* J.-P. Jacobs, ed., Brussels: European Concrete Platform ASBL.
- Wang, D.F. et al., 1995. The Effect of Thermochemical Training on the Microstructures of Fe-Mn-Si Shape Memory Alloy. *Journal de Physique IV*, 5, pp.10–13.
- Wang, X. et al., 2014. Evaluation of prestressed basalt fiber and hybrid fiber reinforced polymer tendons under marine environment. *Materials and Design*, 64, pp.721–728.
- Watanabe, Y., Miyazaki, E. & Okada, H., 2002. Enhanced Mechanical Properties of Fe-Mn-Si-Cr Shape Memory Fiber/Plaster Smart Composite. *Materials Transactions*, 43(5), pp.974–983.
- Wierschem, N. & Andrawes, B., 2010. Superelastic SMA – FRP composite reinforcement

- for concrete structures. *Smart Materials and Structures*, 19(025011), p.13.
- Wolf, T.S. & Frosch, R.J., 2007. Shear Design of Prestressed Concrete: A Unified Approach. *Journal of Structural Engineering*, 133(11), pp.1512–1519.
- WSDOT, 2018. Alaskan Way Viaduct. *Washington State Department of Transportation*. Available at: <http://www.wsdot.wa.gov/Projects/Viaduct/>.
- Wu, Z., He, X. & Zhang, Y., 2011. Steel Beam-to-Column Connections Using Martensite Shape Memory Alloys. *Advanced Materials Research*, 243–249(2011), pp.662–665.
- Yang, K.H., Kim, G.H. & Yang, H.S., 2011. Shear behavior of continuous reinforced concrete T-beams using wire rope as internal shear reinforcement. *Construction and Building Materials*, 25(2), pp.911–918.
- Yu, T., Ma, Q. & Tian, L., 2011. Test study on the resisting shear strengthening effect with external pre-stressed wire rope. *1st International Conference on Civil Engineering, Architecture and Building Materials, CEABM 2011*, 243–249, pp.5571–5575.
- Zafar, A. & Andrawes, B., 2013. Fabrication and Cyclic Behavior of Highly Ductile Superelastic Shape Memory Composites. *Journal of Materials in Civil Engineering*, p.43.
- Zafar, A. & Andrawes, B., 2012. Incremental dynamic analysis of concrete moment resisting frames reinforced with shape memory composite bars. *Smart Materials and Structures*, 21, p.14.
- Zararis, I.P., 2006. Shear Strength of Reinforced Concrete T-Beams. *ACI structural journal*, (103-S71), pp.693–700.
- Zararis, P.D. & Papadakis, G.C., 2001. Diagonal shear failure and size effect in RC beams without web reinforcement. *Journal of Structural Engineering*, 127(July), pp.733–742.
- Zsutty, T.C., 1968. Beam Shear Strength Prediction by Analysis of Existing Data. *ACI journal*, Title no.(Nov 1968), pp.943–951.



**APPENDIX. EXPERIMENTAL CAMPAIGN OF
STRENGTHENED RC BEAMS AND MODEL
CALCULATIONS**

Table A1.1. Characteristics of beam specimens of the phases carried out

Phase 1 beams	Age at testing (days)	f_{cm} (MPa)	f_{sp} (MPa)	Shear strengthening				Comments
				ϕ /spacing (mm)	<i>Ni-Ti-Nb state</i>	ϕ_{front} (°)	ϕ_{back} (°)	
1.1 – Reference	49	41.4	3.2	-	-	-	-	-
1.2 – Reference	56	41.7	3.2	-	-	-	-	-
2.1 - S ϕ 3/100/UCR/A	63	41.9	3.2	ϕ 3/100	Activated	90	56	Un-cracked
2.2 - S ϕ 3/100/UCR/A	68	42.1	3.2	ϕ 3/100	Activated	90	56	Un-cracked
3.1a - S ϕ 3/100/UCR/NA	102	42.6	3.3	ϕ 3/100	Non-Activated	90	56	Un-cracked
3.1b - S ϕ 3/100/COL/A	130	42.8	3.3	ϕ 3/100	Activated	90	56	Tested after collapse 3.1a
3.2a - S ϕ 3/100/UCR/NA	102	42.6	3.3	ϕ 3/100	Non-Activated	90	56	Un-cracked
3.2b - S ϕ 3/100/COL/A	116	42.7	3.3	ϕ 3/100	Activated	90	56	Tested after collapse 3.2a
4.1 - S ϕ 3/100/PCR/A	175	43.0	3.3	ϕ 3/100	Activated	90	56	Pre-cracked V_{cr} =17.79 kN
4.2 - S ϕ 3/100/PCR/A	182	43.0	3.3	ϕ 3/100	Activated	90	56	Pre-cracked V_{cr} =18.08 kN
5.1 - S ϕ 3/075/UCR/A	263	43.2	3.4	ϕ 3/75	Activated	90	63	Un-cracked
5.2 - S ϕ 3/075/UCR/A	272	43.2	3.4	ϕ 3/75	Activated	90	63	Un-cracked

Phase 2 beams	Age at testing (days)	f_{cm} (MPa)	f_{sp} (MPa)	Shear strengthening				Comments
				ϕ /spacing (mm)	<i>Ni-Ti-Nb state</i>	ϕ_{front} (°)	ϕ_{back} (°)	
6.1 – Reference	202	39.7	3.4	-	-	-	-	-
6.2 – Reference	202	39.7	3.4	-	-	-	-	-
7.1 - S ϕ 3/100/UCR/A/G	279	39.8	3.5	ϕ 3/100	Activated	90	56	Un-cracked / Grooved
7.2 - S ϕ 3/100/UCR/A/G	279	39.8	3.5	ϕ 3/100	Activated	90	56	Un-cracked / Grooved
8.1 - U ϕ 3/100/UCR/A	224	39.7	3.4	ϕ 3/100	Activated	90	90	Un-cracked / U-shape
8.2 - U ϕ 3/100/UCR/A	244	39.7	3.4	ϕ 3/100	Activated	90	90	Un-cracked / U-shape
9.1 - S ϕ 3/100/UCR/A/S	272	39.8	3.5	ϕ 3/100	Activated	90	37	Un-cracked / Mid shear reinforced
9.2 - S ϕ 3/100/UCR/A/S	279	39.8	3.5	ϕ 3/100	Activated	90	37	Un-cracked / Mid shear reinforced
10.1 - U ϕ 3/075/UCR/A	321	39.8	3.5	ϕ 3/075	Activated	90	90	Un-cracked / U-shape
10.2 - U ϕ 3/075/UCR/A	325	39.8	3.5	ϕ 3/075	Activated	90	90	Un-cracked / U-shape

Table A1.2. Results of compressive and splitting strength tests performed

Phase 1 beams	Age at testing (days)	f_{cm} (MPa)	Compressive average (MPa)	Samples tested	f_{sp} (MPa)	Splitting average (MPa)	Samples tested
1.1 – Reference	49	41.4	40.9	2	3.2	3.1	2
1.2 – Reference	56	41.7	42.5	2	3.2	3.0	2
2.1 - S ϕ 3/100/UCR/A	63	41.9	42.3	2	3.2	3.4	2
2.2 - S ϕ 3/100/UCR/A	68	42.1	41.6	2	3.2	3.1	2
3.1a - S ϕ 3/100/UCR/NA	102	42.6	43.3	2	3.3	3.3	2
3.1b - S ϕ 3/100/COL/A	130	42.8	-	-	3.3	-	-
3.2a - S ϕ 3/100/UCR/NA	102	42.6	43.3	2	3.3	3.3	2
3.2b - S ϕ 3/100/COL/A	116	42.7	-	-	3.3	-	-
4.1 - S ϕ 3/100/PCR/A	175	43.0	45.6	2	3.3	3.0	2
4.2 - S ϕ 3/100/PCR/A	182	43.0	44.7	2	3.3	3.3	2
5.1 - S ϕ 3/075/UCR/A	263	43.2	44.1	2	3.4	3.6	3
5.2 - S ϕ 3/075/UCR/A	272	43.2	46.5	2	3.4	3.4	3
Phase 2 beams	Age at testing (days)	f_{cm} (MPa)	Compressive average (MPa)	Samples tested	f_{sp} (MPa)	Splitting average (MPa)	Samples tested
6.1 – Reference	202	39.7	40.0	3	3.4	3.5	3
6.2 – Reference	202	39.7	40.0	3	3.4	3.5	3
7.1 - S ϕ 3/100/UCR/A/G	279	39.8	39.4	2	3.5	3.5	3
7.2 - S ϕ 3/100/UCR/A/G	279	39.8	39.4	2	3.5	3.5	3
8.1 - U ϕ 3/100/UCR/A	224	39.7	39.0	2	3.4	3.0	3
8.2 - U ϕ 3/100/UCR/A	244	39.7	38.4	2	3.4	3.3	2
9.1 - S ϕ 3/100/UCR/A/S	272	39.8	39.4	3	3.5	3.4	3
9.2 - S ϕ 3/100/UCR/A/S	279	39.8	39.4	2	3.5	3.5	3
10.1 - U ϕ 3/075/UCR/A	321	39.8	37.4	2	3.5	3.8	2
10.2 - U ϕ 3/075/UCR/A	325	39.8	37.4	2	3.5	3.7	2

Table A1.3. Summary of beam test results

Phase 1 beams	V_{test} (kN)	E_{ff}	δ at V_{test} (mm)	δ/l (1/l)	$V_{u,80}$ (kN)	δ at $V_{u,80}$ (mm)	D_{uc}
1.1 – Reference	18.30	1.00	1.59	1/479	14.64	3.45	2.17
1.2 – Reference	18.41	1.00	1.64	1/462	14.73	1.94	1.18
2.1 - S ϕ 3/100/UCR/A	35.41	1.93	4.26	1/178	28.33	5.30	1.24
2.2 - S ϕ 3/100/UCR/A	35.95	1.96	4.94	1/154	28.76	8.32	1.68
3.1a - S ϕ 3/100/UCR/NA	18.23	0.99	1.67	1/456	14.58	2.98	1.79
3.1b - S ϕ 3/100/COL/A	27.14	1.48	3.46	1/220	21.71	5.06	1.46
3.2a - S ϕ 3/100/UCR/NA	21.47	1.17	1.69	1/450	17.18	2.15	1.28
3.2b - S ϕ 3/100/COL/A	35.21	1.92	3.83	1/198	28.17	6.26	1.63
4.1 - S ϕ 3/100/PCR/A	34.35	1.87	3.82	1/199	27.48	6.00	1.57
4.2 - S ϕ 3/100/PCR/A	35.60	1.94	4.10	1/185	28.48	11.33	2.76
5.1 - S ϕ 3/075/UCR/A	37.04	2.02	3.82	1/199	29.63	12.11	3.17
5.2 - S ϕ 3/075/UCR/A	41.82	2.28	6.95	1/109	33.46	8.96	1.29
Phase 2 Beams	V_{test} (kN)	E_{ff}	δ at V_{test} (mm)	δ/l (1/l)	$V_{u,80}$ (kN)	δ at $V_{u,80}$ (mm)	D_{uc}
z							
6.1 – Reference	19.71	1.07	2.505	1/303	15.77	3.03	1.21
6.2 – Reference	18.50	1.01	1.692	1/449	14.80	1.97	1.17
7.1 - S ϕ 3/100/UCR/A/G	25.36	1.38	2.560	1/297	20.29	4.55	1.78
7.2 - S ϕ 3/100/UCR/A/G	35.51	1.93	6.039	1/126	28.41	8.20	1.36
8.1 - U ϕ 3/100/UCR/A	37.74	2.06	5.347	1/142	30.19	17.44	3.26
8.2 - U ϕ 3/100/UCR/A	34.75	1.89	5.148	1/148	27.80	10.11	1.96
9.1 - S ϕ 3/100/UCR/A/S	20.54	1.12	3.007	1/253	16.43	11.94	3.97
9.2 - S ϕ 3/100/UCR/A/S	22.03	1.20	3.695	1/206	17.62	5.72	1.55
10.1 - U ϕ 3/075/UCR/A	36.79	2.00	5.310	1/143	29.43	18.00	3.39
10.2 - U ϕ 3/075/UCR/A	33.65	1.83	4.736	1/160	26.92	6.67	1.41

Table A1.4. Longitudinal reinforcement strain gauges measurements at peak load

Phase 1 Beams	V_{test} (kN)	GLONG. 01 ($\mu\epsilon$)	GLONG. 02 ($\mu\epsilon$)	GLONG. 03 ($\mu\epsilon$)
1.1 – Reference	18.30	454	1174	199
1.2 – Reference	18.41	306	1276	221
2.1 - S ϕ 3/100/UCR/A	35.41	2354	2325	2603
2.2 - S ϕ 3/100/UCR/A	35.95	1821	2053	3013
3.1a - S ϕ 3/100/UCR/NA	18.23	343	1305	806
3.1b - S ϕ 3/100/COL/A	27.14	2081	1634	2462
3.2a - S ϕ 3/100/UCR/NA	21.47	188	1417	211
3.2b - S ϕ 3/100/COL/A	35.21	1963	2042	1090
4.1 - S ϕ 3/100/PCR/A	34.35	1650	2014	2773
4.2 - S ϕ 3/100/PCR/A	35.60	1853	2386	1862
5.1 - S ϕ 3/075/UCR/A	37.04	1559	2441	1396
5.2 - S ϕ 3/075/UCR/A	41.82	2812	25348	2066
Phase 2 Beams	V_{test} (kN)	GLONG. 01 ($\mu\epsilon$)	GLONG. 02 ($\mu\epsilon$)	GLONG. 03 ($\mu\epsilon$)
6.1 – Reference	19.71	376	1311	1854
6.2 – Reference	18.50	393	1332	-
7.1 - S ϕ 3/100/UCR/A/G	25.36	477	1884	1185
7.2 - S ϕ 3/100/UCR/A/G	35.51	2357	1991	2757
8.1 - U ϕ 3/100/UCR/A	37.74	2279	2495	2714
8.2 - U ϕ 3/100/UCR/A	34.75	980	2526	2350
9.1 - S ϕ 3/100/UCR/A/S	20.54	2595	-	826
9.2 - S ϕ 3/100/UCR/A/S	22.03	2504	1559	2888
10.1 - U ϕ 3/075/UCR/A	36.79	3342	2359	2324
10.2 - U ϕ 3/075/UCR/A	33.65	2536	2218	1351

- Gauges did not provide proper data due to an error in test set-up

Table A1.5. Transverse reinforcement strain gauges measurements at peak load

Phase 1 Beams	V_u (kN)	GTR. 01 ($\mu\epsilon$)	GTR. 02 ($\mu\epsilon$)	GTR. 03 ($\mu\epsilon$)	GTR. 04 ($\mu\epsilon$)	GTR. 05 ($\mu\epsilon$)	GTR. 06 ($\mu\epsilon$)	GTR. 07 ($\mu\epsilon$)	GTR. 08 ($\mu\epsilon$)
2.1 - S ϕ 3/100/UCR/A	35.41	-50	1137	3148	-1168	378	1271	4148	-8
2.2 - S ϕ 3/100/UCR/A	35.95	-11	1799	430	137	5	4645	4675	-83
3.1a - S ϕ 3/100/UCR/NA	18.23	*	-48	-89	-38	-4	-389	-139	*
3.1b - S ϕ 3/100/COL/A	27.14	*	-	-42	-5	-	4	-	*
3.2a - S ϕ 3/100/UCR/NA	21.47	*	-9	70	61	-94	-49	-43	*
3.2b - S ϕ 3/100/COL/A	35.21	*	32	2016	5	2	-87	27	*
4.1 - S ϕ 3/100/PCR/A	34.35	*	759	131	-230	-20	60	1968	*
4.2 - S ϕ 3/100/PCR/A	35.60	*	3982	2568	-103	305	2686	1214	*
5.1 - S ϕ 3/075/UCR/A	37.04	26	2371	784	84	-23	32	-490	-661
5.2 - S ϕ 3/075/UCR/A	40.21	2070	83	67	13	31	-72	18	667
Phase 2 Beams	V_u (kN)	GTR. 01 ($\mu\epsilon$)	GTR. 02 ($\mu\epsilon$)	GTR. 03 ($\mu\epsilon$)	GTR. 04 ($\mu\epsilon$)	GTR. 05 ($\mu\epsilon$)	GTR. 06 ($\mu\epsilon$)	GTR. 07 ($\mu\epsilon$)	GTR. 08 ($\mu\epsilon$)
7.1 - S ϕ 3/100/UCR/A/G	25.36	*	-226	-244	-386	-353	1167	1711	*
7.2 - S ϕ 3/100/UCR/A/G	35.51	*	-308	-2842	2159	909	3870	2311	*
8.1 - U ϕ 3/100/UCR/A	37.74	-1	2207	3031	1041	410	3417	3491	-47
8.2 - U ϕ 3/100/UCR/A	34.75	-48	112	2519	-340	1083	5575	3191	-35
9.1 - S ϕ 3/100/UCR/A/S	20.54	*	-34	-2354	-661	-410	77	-18	*
9.2 - S ϕ 3/100/UCR/A/S	22.03	*	-	15	-	-127	-	-101	*
10.1 - U ϕ 3/075/UCR/A	36.79	-33	1829	1332	-124	532	2	2794	1944
10.2 - U ϕ 3/075/UCR/A	33.65	2913	5091	1610	1452	1000	2143	1321	443

* No strain gauge used in position GTR.01 and GTR.08

- Gauges did not provide proper data due to an error in test set-up



TEST: 1.1 – Reference

Date: 2015/12/04 Age: 49 days

Concrete: $f_{cm28d} = 37.5$ MPa $f_{cm} = 41.4$ MPa $f_{sp} = 3.2$ MPa

Longitudinal reinforcement: Steel 1 ϕ 16 $f_y = 513$ MPa $f_u = 642$ MPa

Transverse reinforcement: -

Geometry: 80x150x900 mm

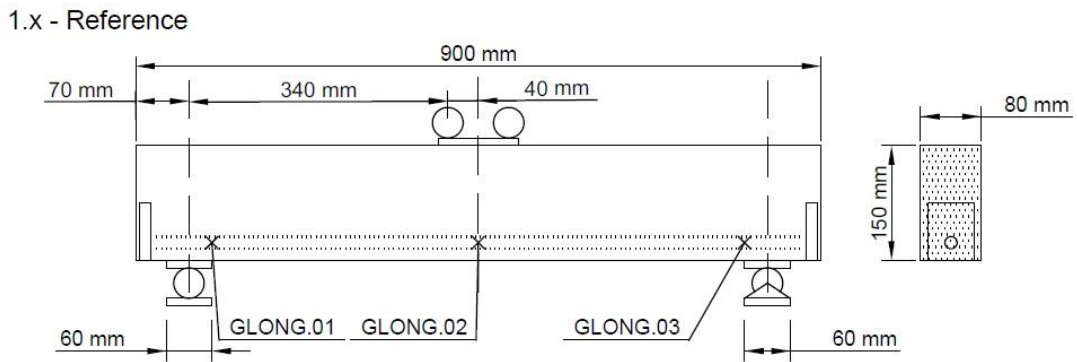


Figure A1.01.1. Beam 1.1 geometry and strain-gauge locations



Figure A1.01.2. Beam 1.1 test after peak load

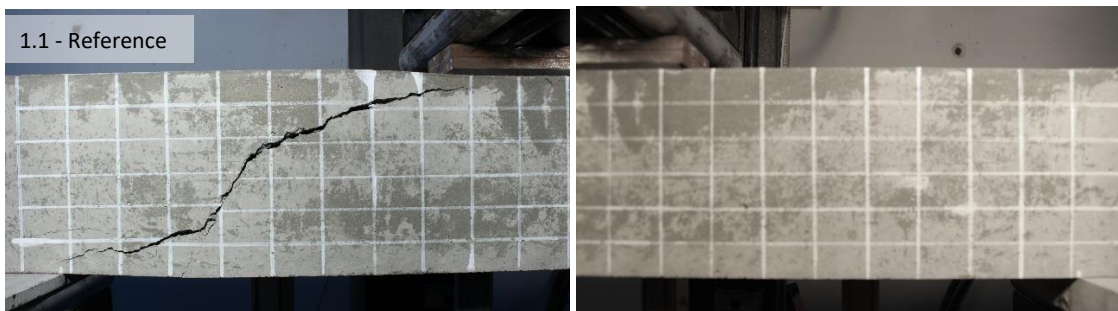


Figure A1.01.3. Beam 1.1 test at test end

Table A1.7. Beam 1.1 test results

Beam	V_{test} (kN)	E_{ff}	δ at V_{test} (mm)	δ/l (1/l)
1.1 – Reference	18.30	-	1.59	1/479

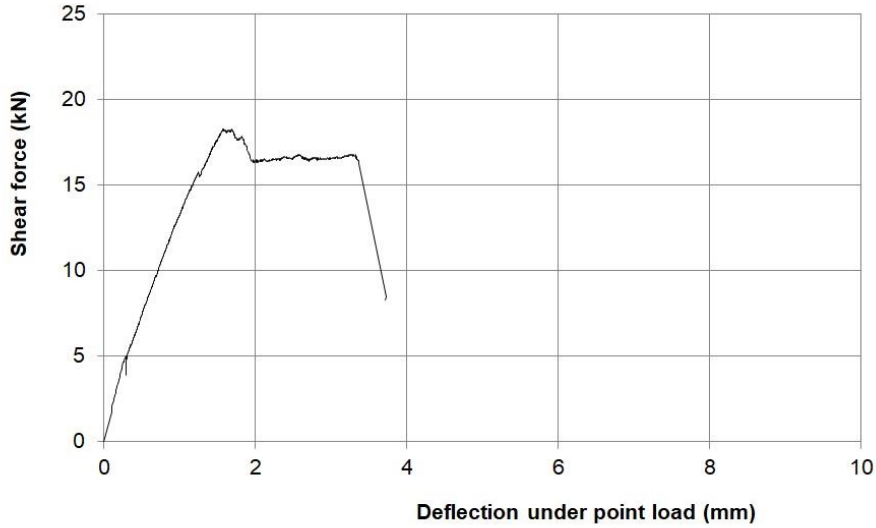


Figure A1.01.4. Shear force-deflection, beam 1.1 test

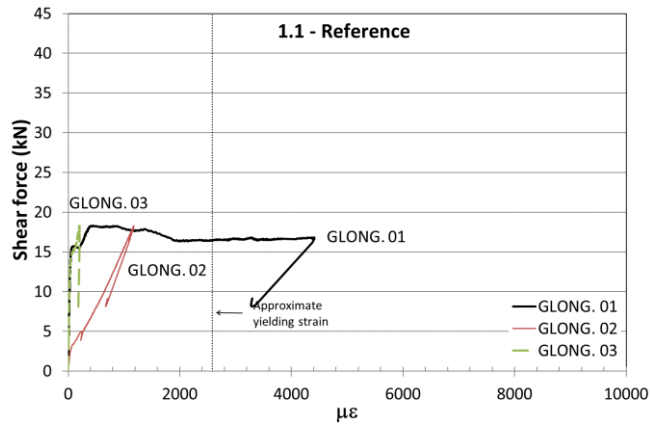


Figure A1.01.5. Shear force-longitudinal strain, beam 1.1 test

TEST: 1.2 – Reference

Date: 2015/12/11 Age: 56 days

Concrete: $f_{cm28d} = 37.5$ MPa $f_{cm} = 41.7$ MPa $f_{sp} = 3.2$ MPa

Longitudinal reinforcement: Steel 1 ϕ 16 $f_y = 513$ MPa $f_u = 642$ MPa

Transverse reinforcement: -

Geometry: 80x150x900 mm

1.x - Reference

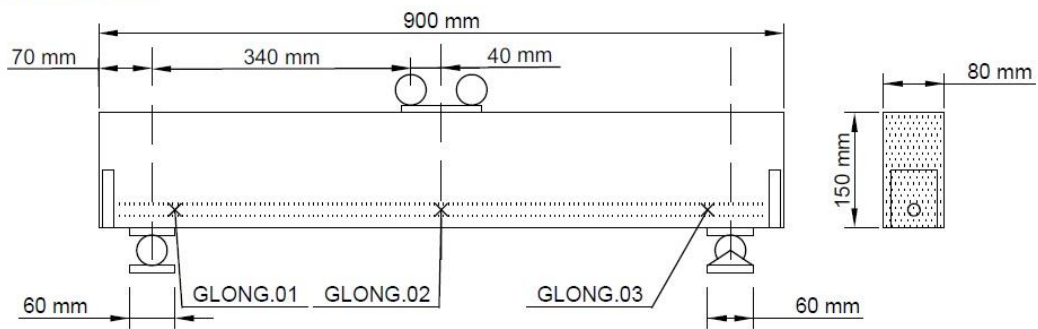


Figure A1.02.1. Beam 1.2 geometry and strain-gauge locations

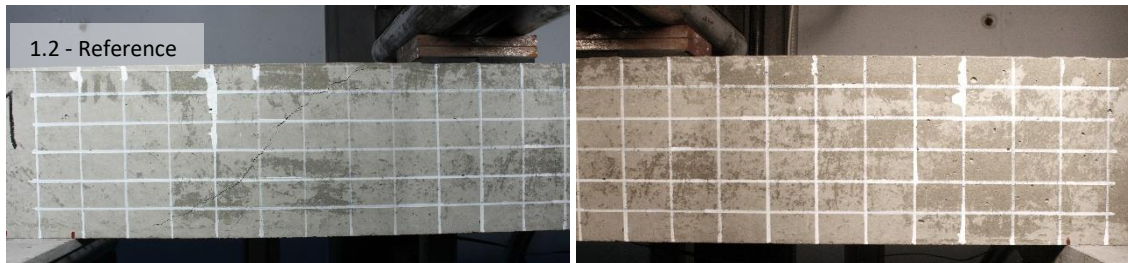


Figure A1.02.2. Beam 1.2 test after peak load

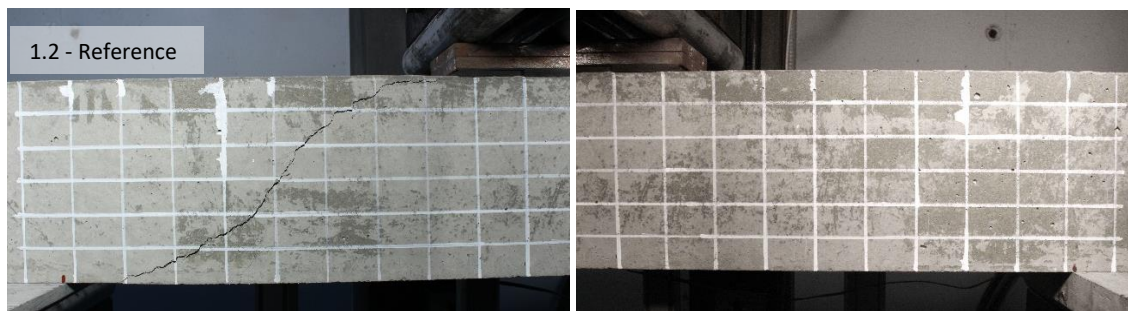


Figure A1.02.3. Beam 1.2 test at test end

Table A1.8. Beam 1.2 test results

Beam	V_{test} (kN)	E_{ff}	δ at V_{test} (mm)	δ/l (1/l)
1.2 – Reference	18.41	-	1.64	1/462

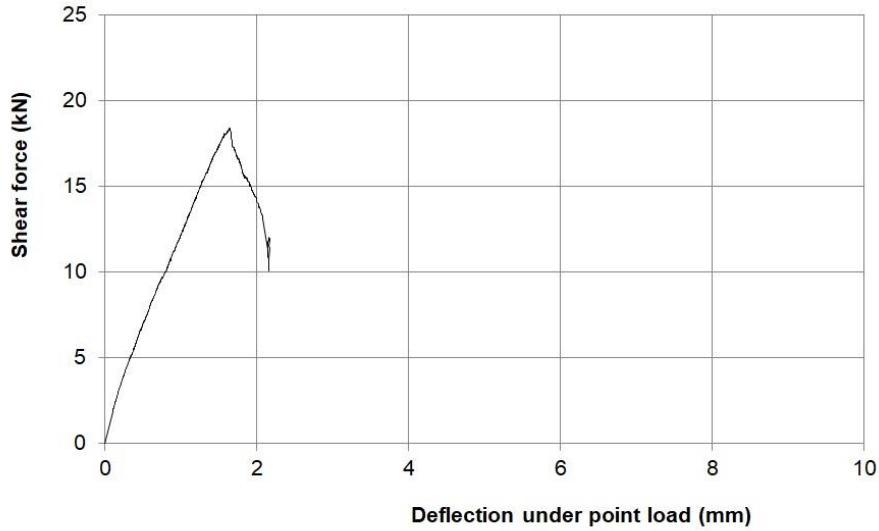


Figure A1.02.4. Shear force-deflection, beam 1.2 test

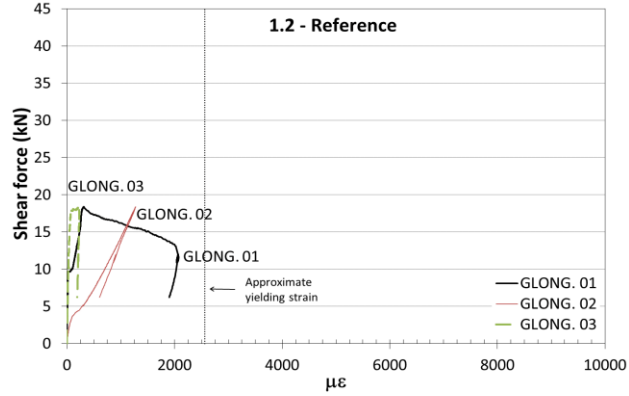


Figure A1.02.5. Shear force-longitudinal strain, beam 1.2 test

TEST 2.1 – S ϕ 3/100/UCR/A

Date: 2015/12/18 Age: 63 days

Concrete: $f_{cm28d} = 37.5$ MPa $f_{cm} = 41.9$ MPa $f_{sp} = 3.2$ MPa

Longitudinal reinforcement: Steel 1 ϕ 16 mm $f_y = 513$ MPa $f_u = 642$ MPa

Transverse reinforcement: Ni-Ti-Nb spiral ϕ 3 mm s = 100 mm $\sigma_r = 417$ MPa

Geometry: 80x150x900 mm

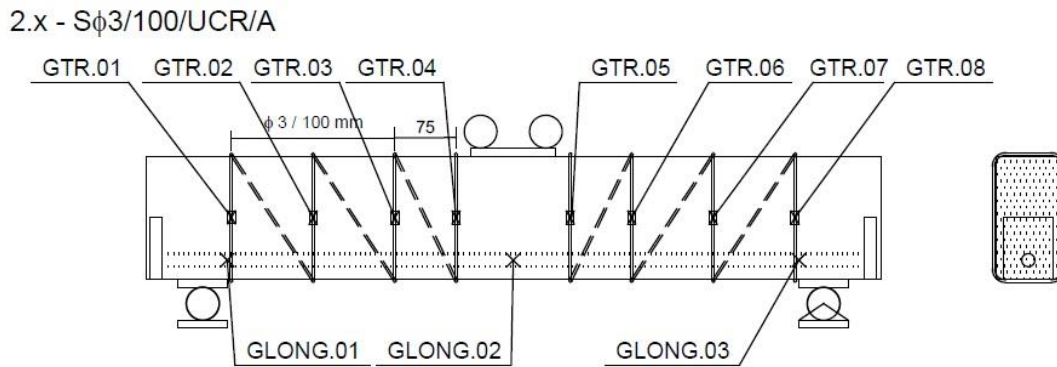


Figure A1.03.1. Beam 2.1 geometry and strain-gauge locations

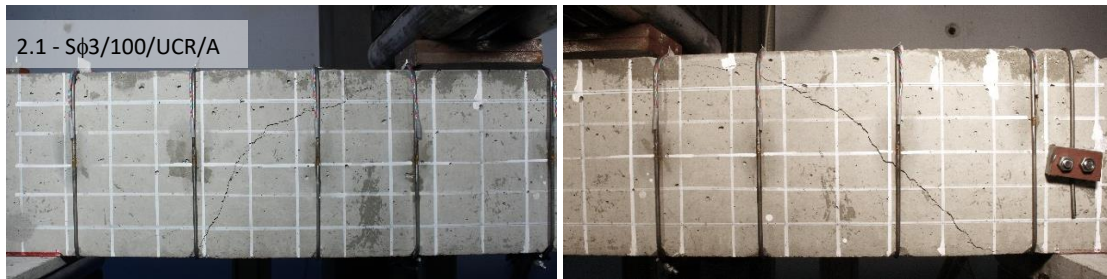


Figure A1.03.2. Beam 2.1 test after peak load



Figure A1.03.3. Beam 2.1 test at test end

Table A1.9. Beam 2.1 test results

Beam	V_{test} (kN)	E_{ff}	δ at V_{test} (mm)	δ/l (1/l)
2.1 - S ϕ 3/100/UCR/A	35.41	1.93	4.26	1/178

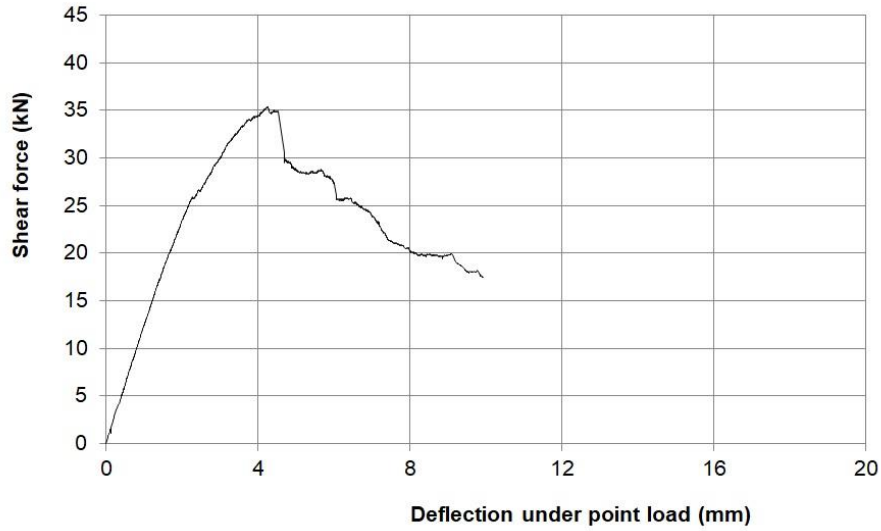


Figure A1.03.4. Shear force-deflection, beam 2.1 test

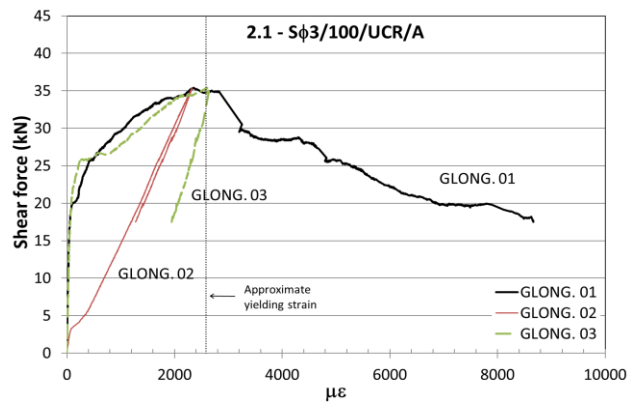


Figure A1.03.5. Shear force-longitudinal strain, beam 2.1 test

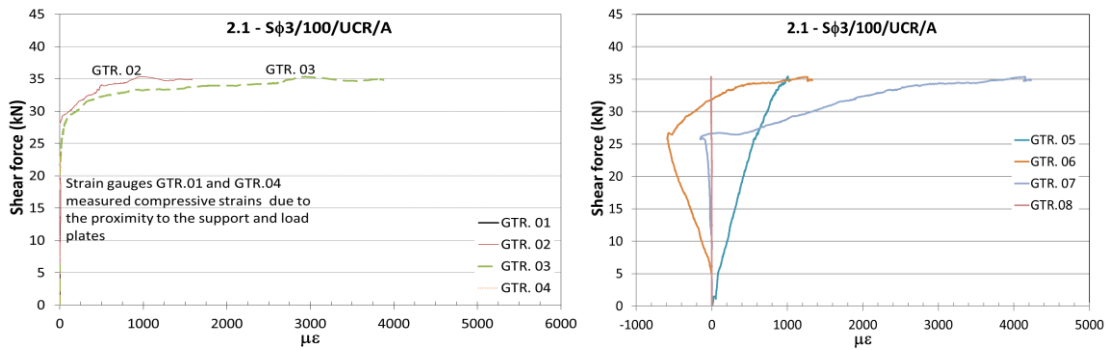


Figure A1.03.6. Shear force-vertical strain, beam 2.1 test

Table A1.10. Beam 2.2 test results

Beam	V_{test} (kN)	E_{ff}	δ at V_{test} (mm)	δ/l (1/l)
2.2 - S ϕ 3/100/UCR/A	35.95	1.96	4.94	1/154

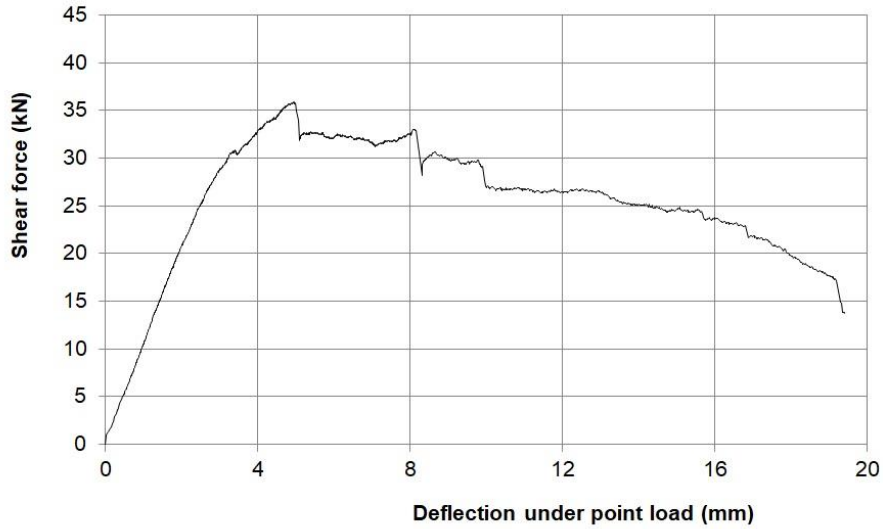


Figure A1.04.4. Shear force-deflection, beam 2.2 test

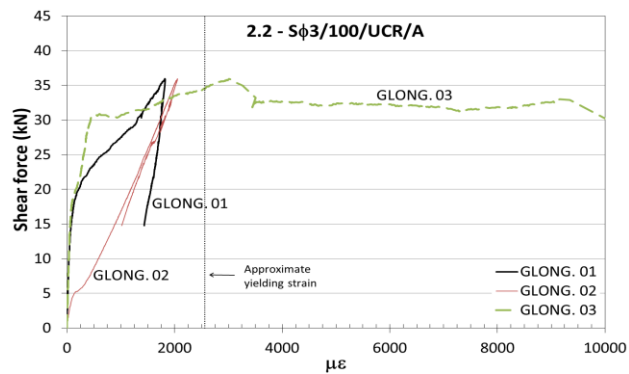


Figure A1.04.5. Shear force-longitudinal strain, beam 2.2 test

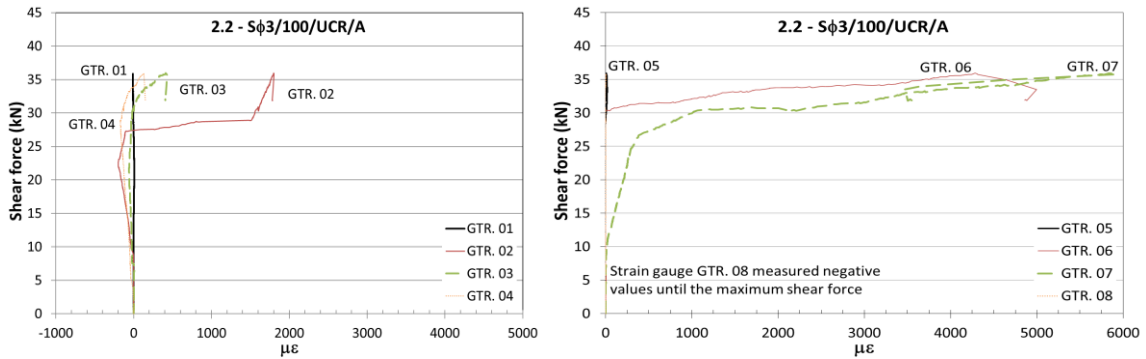


Figure A1.04.6. Shear force-vertical strain, beam 2.2 test

TEST 3.1a – S ϕ 3/100/UCR/NA

Date: 2016/01/26 Age: 102 days

Concrete: $f_{cm28d} = 37.5$ MPa $f_{cm} = 42.6$ MPa $f_{sp} = 3.3$ MPa

Longitudinal reinforcement: Steel 1 ϕ 16 mm $f_y = 513$ MPa $f_u = 642$ MPa

Transverse reinforcement: Ni-Ti-Nb spiral ϕ 3 mm s = 100 mm Not activated

Geometry: 80x150x900 mm

3.xa - S ϕ 3/100/UCR/NA

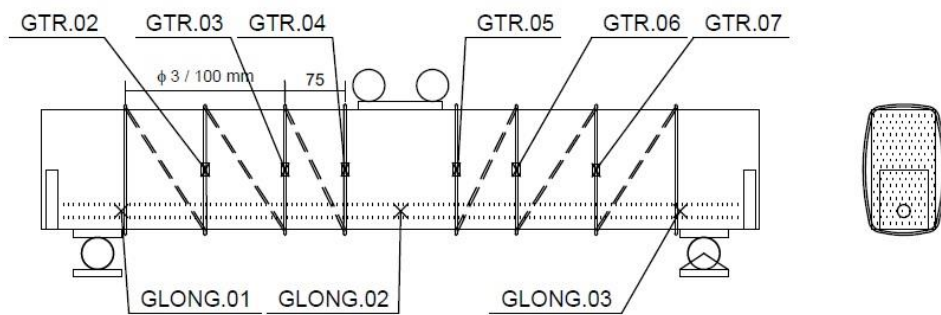


Figure A1.05.1. Beam 3.1a geometry and strain-gauge locations



Figure A1.05.2. Beam 3.1a test after peak load



Figure A1.05.3. Beam 3.1a test at test end

Table A1.11. Beam 3.1a test results

Beam	V_{test} (kN)	E_{ff}	δ at V_{test} (mm)	δ/l (1/l)
3.1a - S ϕ 3/100/UCR/NA	18.23	-	1.67	1/456

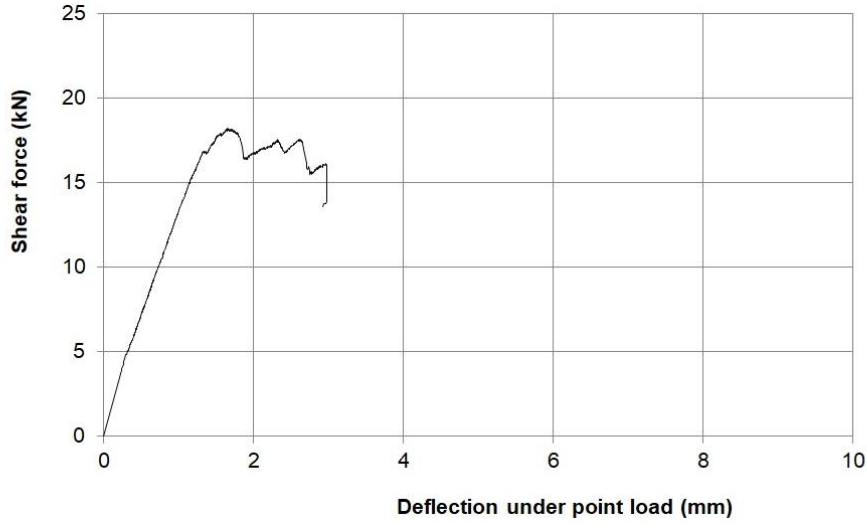


Figure A1.05.4. Shear force-deflection, beam 3.1a test

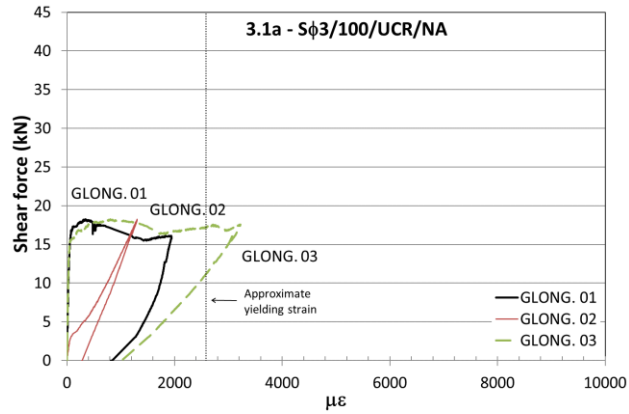


Figure A1.05.5. Shear force-longitudinal strain, beam 3.1a test

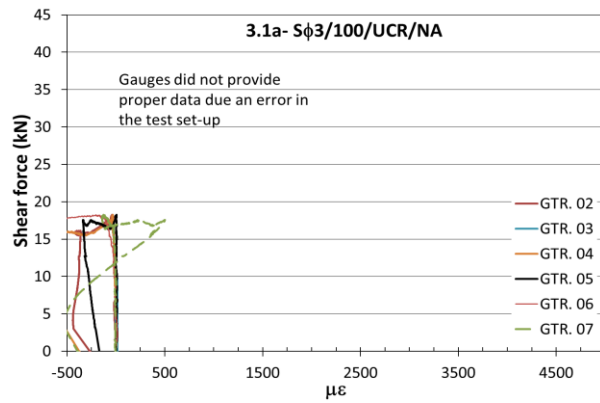


Figure A1.05.6. Shear force-vertical strain, beam 3.1a test

TEST 3.1b – S ϕ 3/100/COL/A

Date: 2016/02/23 Age: 130 days

Concrete: $f_{cm28d} = 37.5$ MPa $f_{cm} = 42.8$ MPa $f_{sp} = 3.3$ MPa

Longitudinal reinforcement: Steel 1 ϕ 16 mm $f_y = 513$ MPa $f_u = 642$ MPa

Transverse reinforcement: Ni-Ti-Nb spiral ϕ 3 mm s = 100 mm $\sigma_r = 435$ MPa

Geometry: 80x150x900 mm

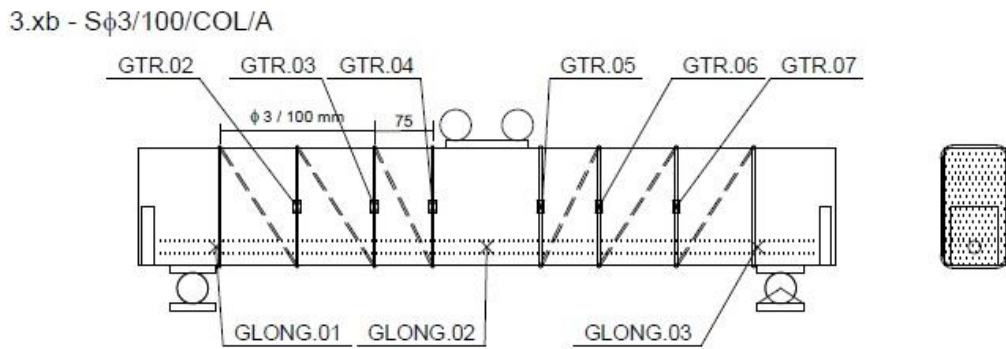


Figure A1.06.1. Beam 3.1b geometry and strain-gauge locations

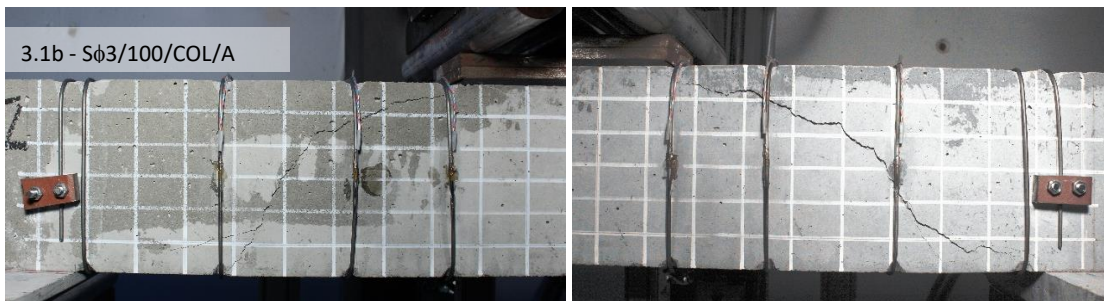


Figure A1.06.2. Beam 3.1b test after peak load

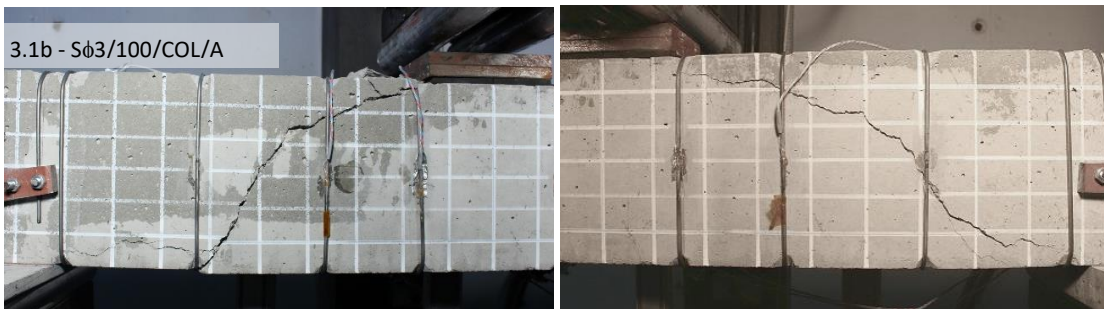


Figure A1.06.3. Beam 3.1b test at test end

Table A1.12. Beam 3.1b test results

Beam	V_{test} (kN)	E_{ff}	δ at V_{test} (mm)	δ/l (1/l)
3.1b - S ϕ 3/100/COL/A	27.14	1.48	3.46	1/220

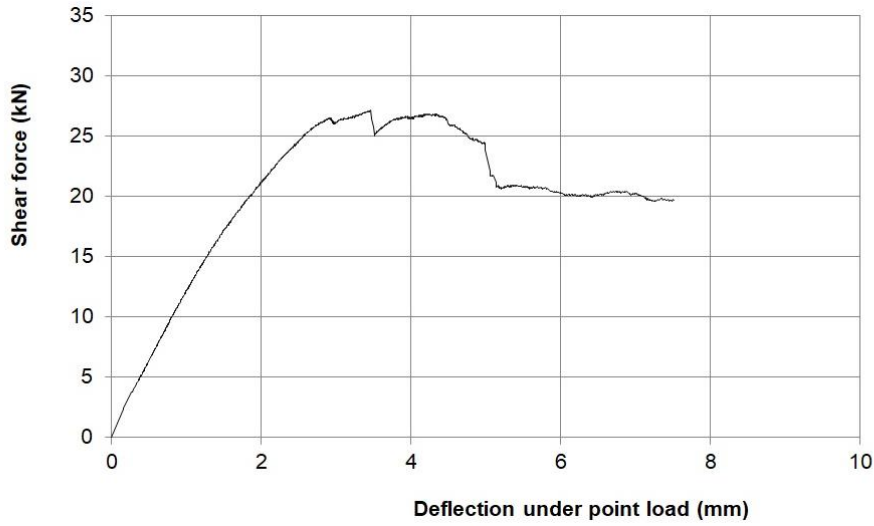


Figure A1.06.4. Shear force-deflection, beam 3.1b test

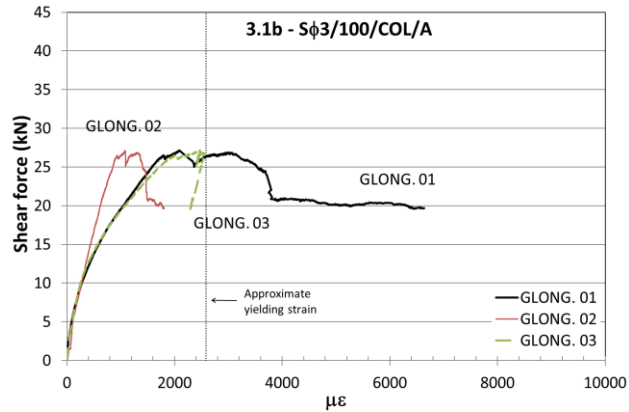


Figure A1.06.5. Shear force-longitudinal strain, beam 3.1b test

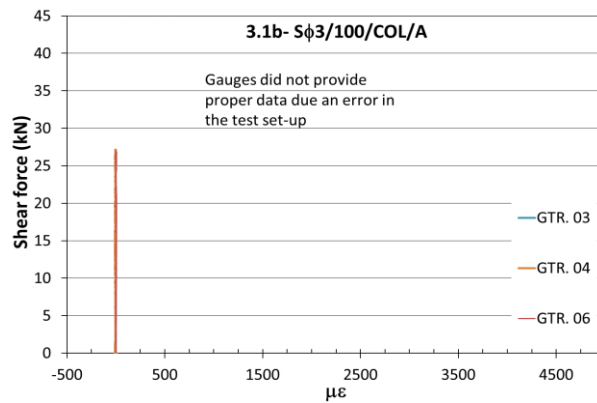


Figure A1.06.6. Shear force-vertical strain, beam 3.1b test

TEST 3.2a – S ϕ 3/100/UCR/NA

Date: 2016/01/26 Age: 102 days

Concrete: $f_{cm28d} = 37.5$ MPa $f_{cm} = 42.6$ MPa $f_{sp} = 3.3$ MPa

Longitudinal reinforcement: Steel 1 ϕ 16 mm $f_y = 513$ MPa $f_u = 642$ MPa

Transverse reinforcement: Ni-Ti-Nb spiral ϕ 3 mm s = 100 mm Not activated

Geometry: 80x150x900 mm

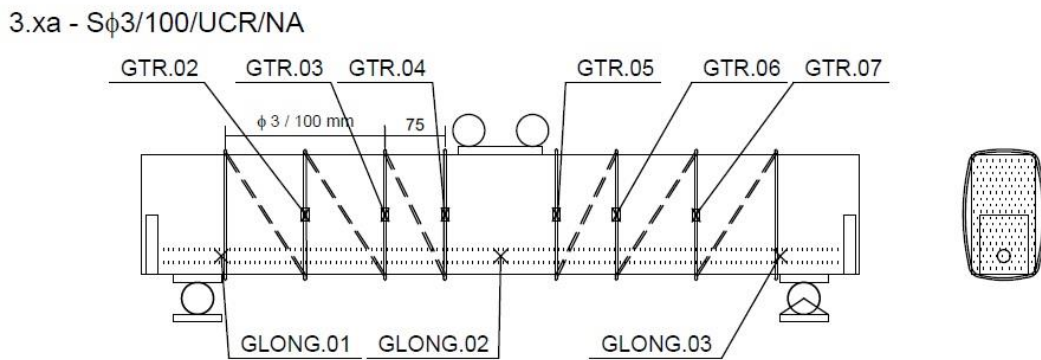


Figure A1.07.1. Beam 3.2a geometry and strain-gauge locations



Figure A1.07.2. Beam 3.2a test after peak load



Figure A1.07.3. Beam 3.2a test at test end

Table A1.13. Beam 3.2a test results

Beam	V_{test} (kN)	E_{ff}	δ at V_{test} (mm)	δ/l (1/l)
3.2a - S ϕ 3/100/UCR/NA	21.47	-	1.69	1/450

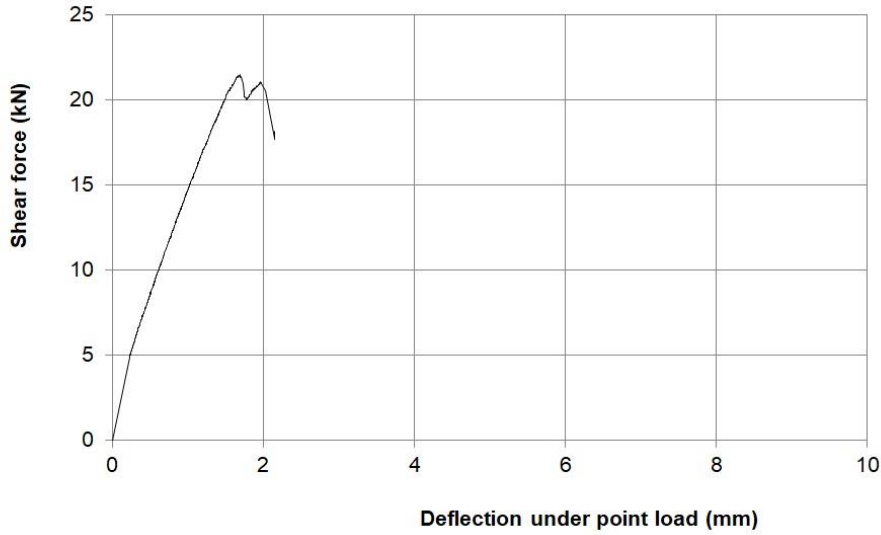


Figure A1.07.4. Shear force-deflection, beam 3.2a test

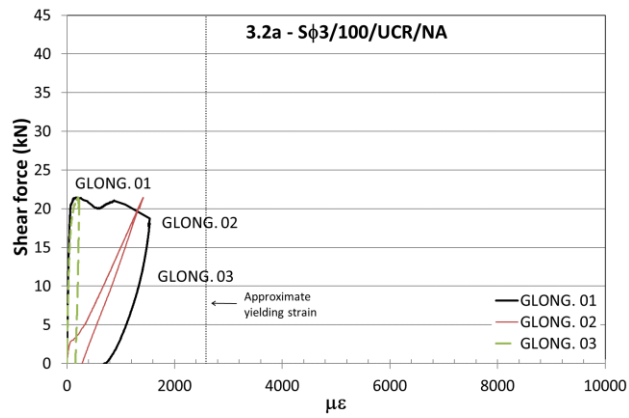


Figure A1.07.5. Shear force-longitudinal strain, beam 3.2a test

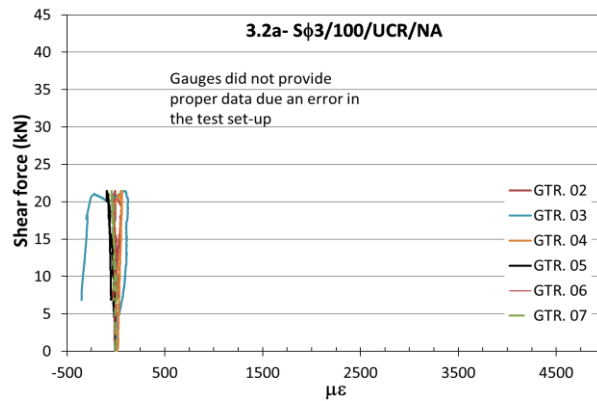


Figure A1.07.6. Shear force-vertical strain, beam 3.2a test

TEST 3.2b – S ϕ 3/100/COL/A

Date: 2016/02/09 Age: 116 days

Concrete: $f_{cm28d} = 37.5$ MPa $f_{cm} = 42.7$ MPa $f_{sp} = 3.3$ MPa

Longitudinal reinforcement: Steel 1 ϕ 16 mm $f_y = 513$ MPa $f_u = 642$ MPa

Transverse reinforcement: Ni-Ti-Nb spiral ϕ 3 mm s = 100 mm $\sigma_r = 428$ MPa

Geometry: 80x150x900 mm

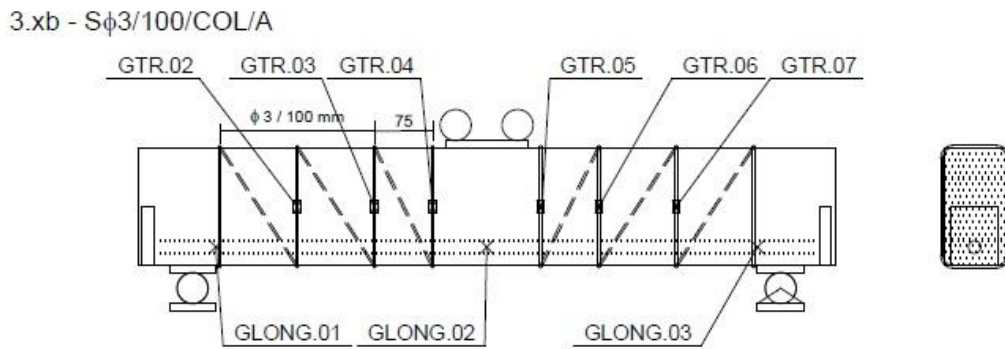


Figure A1.08.1. Beam 3.2b geometry and strain-gauge locations



Figure A1.08.2. Beam 3.2b test after peak load



Figure A1.08.3. Beam 3.2b test at test end

Table A1.14. Beam 3.2b test results

Beam	V_{test} (kN)	E_{ff}	δ at V_{test} (mm)	δ/l (1/l)
3.2b - S ϕ 3/100/COL/A	35.21	1.92	3.83	1/198

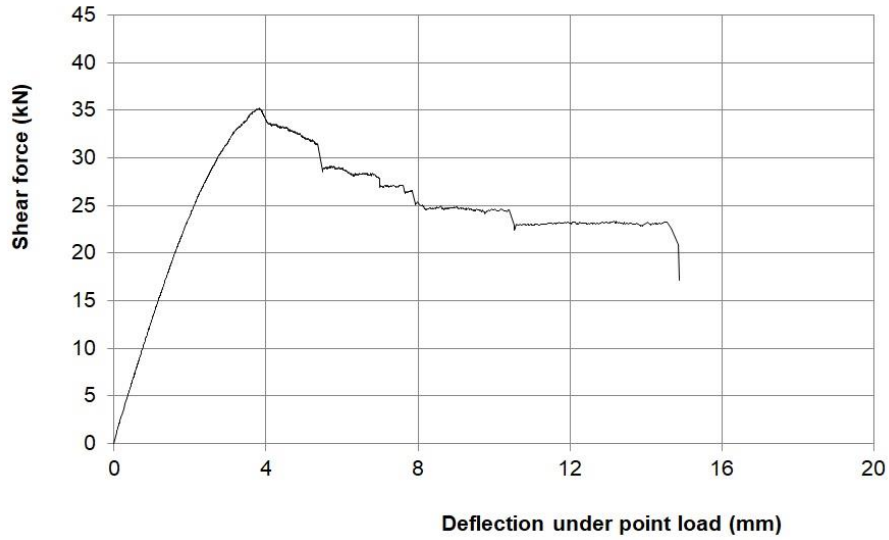


Figure A1.08.4. Shear force-deflection, beam 3.2b test

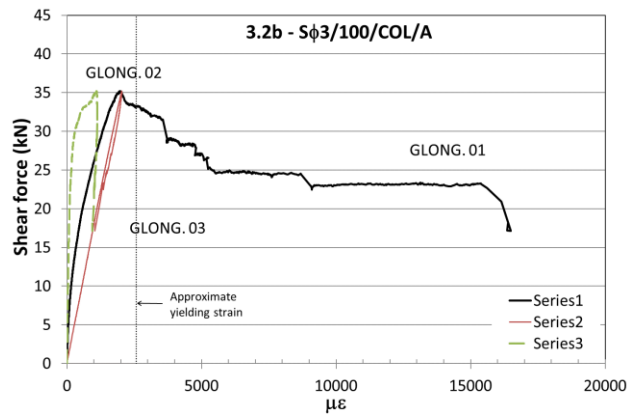


Figure A1.08.5. Shear force-longitudinal strain, beam 3.2b test

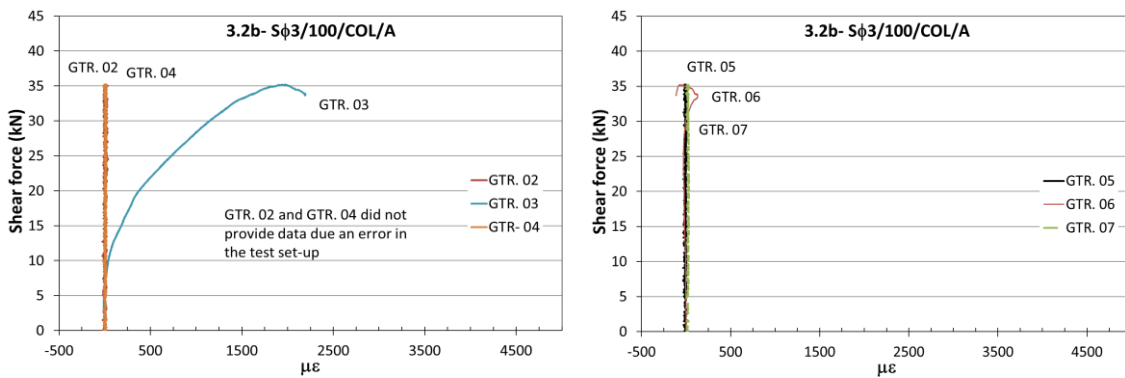


Figure A1.08.6. Shear force-vertical strain, beam 3.2b test

TEST 4.1 – S ϕ 3/100/PCR/A

Date: 2016/04/08 Age: 175 days

Concrete: $f_{cm28d} = 37.5$ MPa $f_{cm} = 43.0$ MPa $f_{sp} = 3.3$ MPa

Longitudinal reinforcement: Steel 1 ϕ 16 mm $f_y = 513$ MPa $f_u = 642$ MPa

Transverse reinforcement: Ni-Ti-Nb spiral ϕ 3 mm s = 100 mm $\sigma_r = 436$ MPa

Geometry: 80x150x900 mm

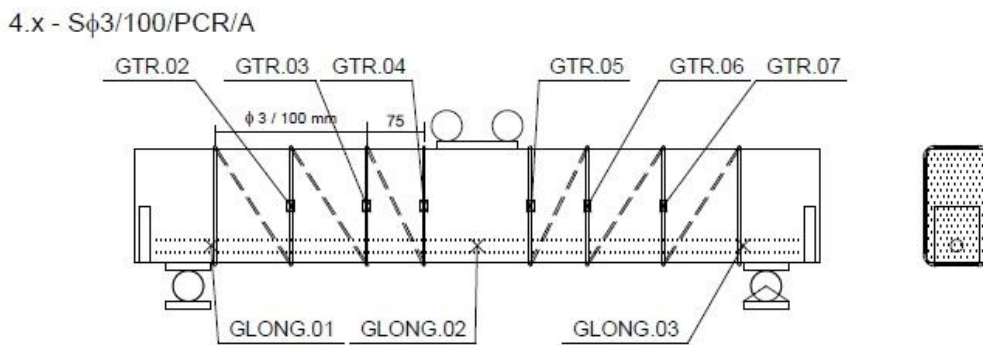


Figure A1.9.1. Beam 4.1 geometry and strain-gauge locations

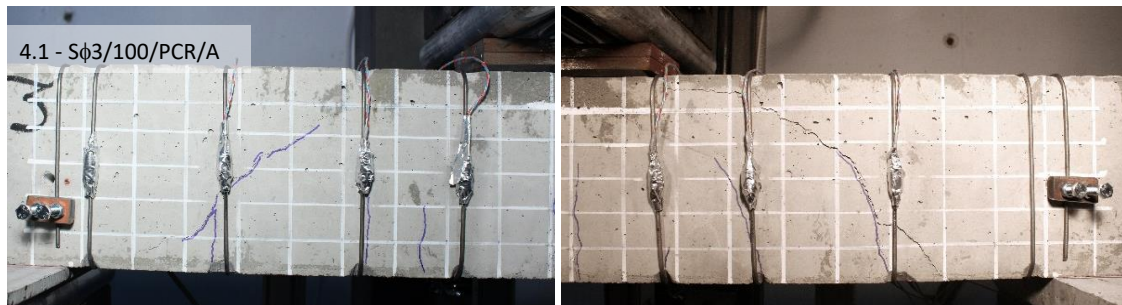


Figure A1.9.2. Beam 4.1 test after peak load

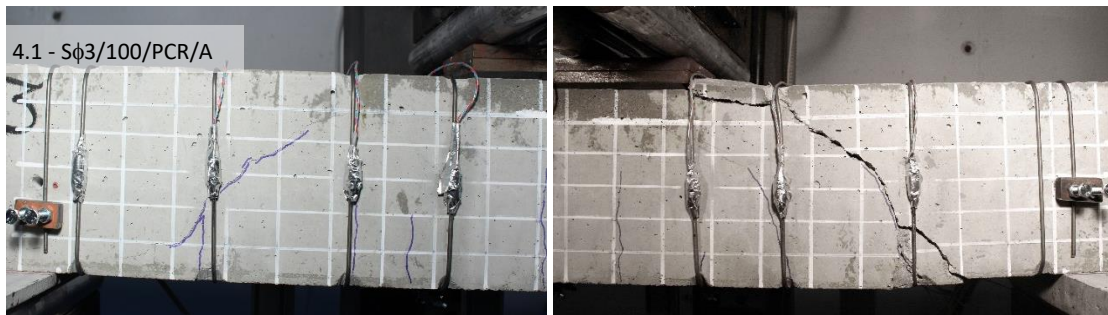


Figure A1.9.3. Beam 4.1 test at test end

Table A1.15. Beam 4.1 test results

Beam	V_{test} (kN)	E_{ff}	δ at V_{test} (mm)	δ/l (1/l)
4.1 - S ϕ 3/100/PCR/A	34.35	1.87	3.82	1/199

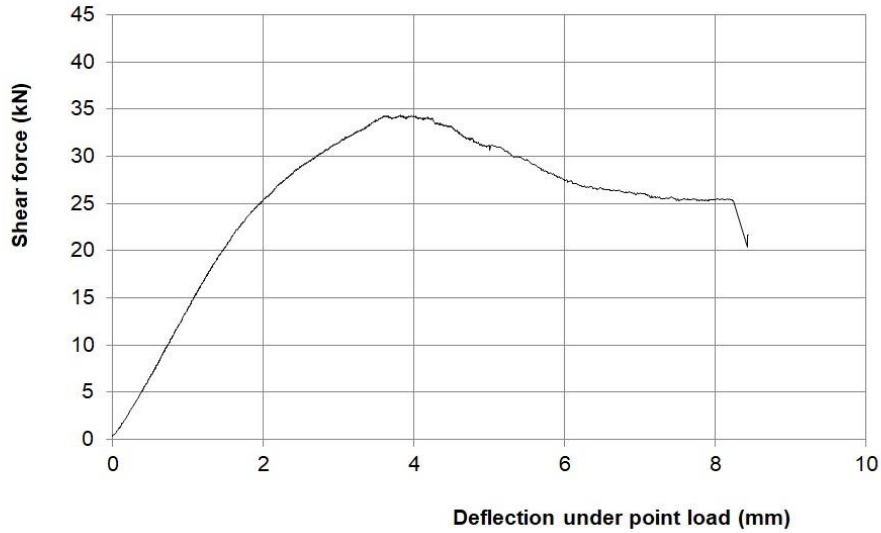


Figure A1.9.4. Shear force-deflection, beam 4.1 test

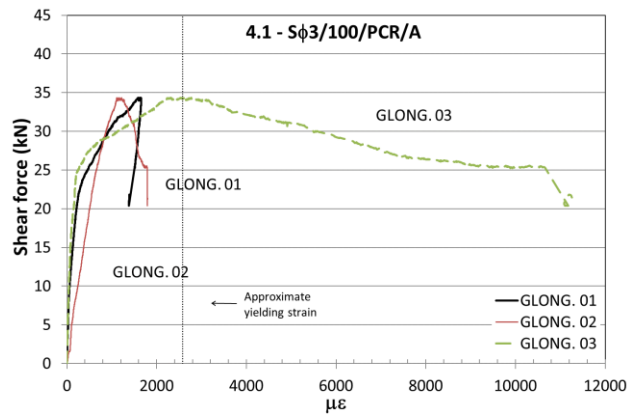


Figure A1.9.5. Shear force-longitudinal strain, beam 4.1 test

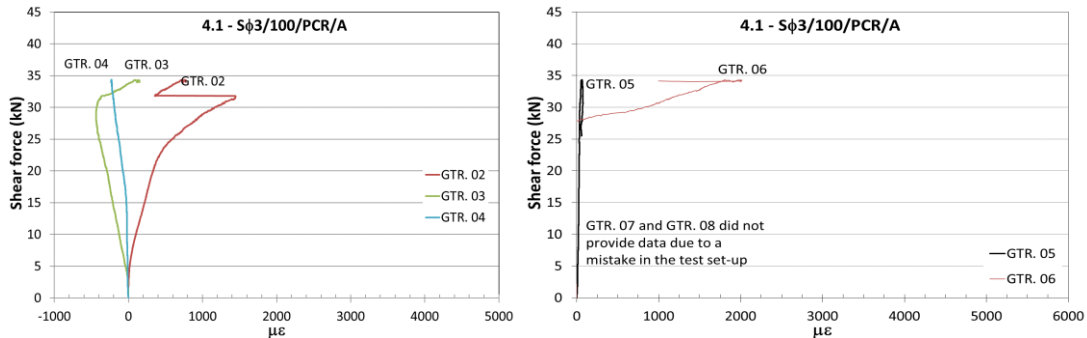


Figure A1.9.6. Shear force-vertical strain, beam 4.1 test

TEST 4.2 – S ϕ 3/100/PCR/A

Date: 2016/04/15 Age: 182 days

Concrete: $f_{cm28d} = 37.5$ MPa $f_{cm} = 43.0$ MPa $f_{sp} = 3.3$ MPa

Longitudinal reinforcement: Steel 1 ϕ 16 mm $f_y = 513$ MPa $f_u = 642$ MPa

Transverse reinforcement: Ni-Ti-Nb spiral ϕ 3 mm s = 100 mm $\sigma_r = 415$ MPa

Geometry: 80x150x900 mm

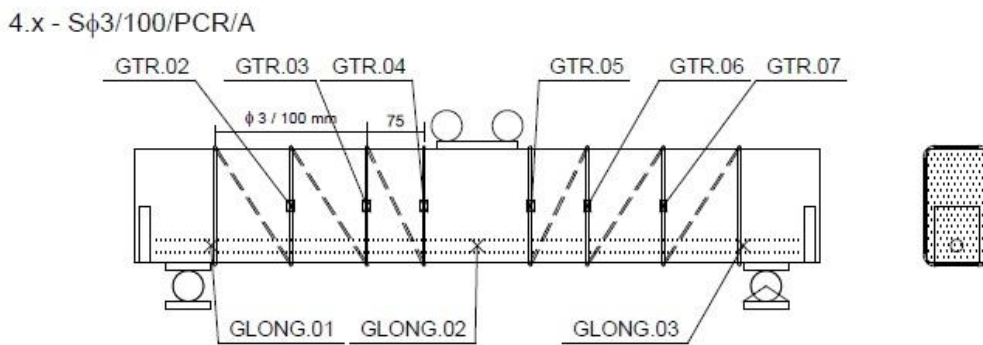


Figure A1.10.1. Beam 4.2 geometry and strain-gauge locations



Figure A1.10.2. Beam 4.2 test after peak load

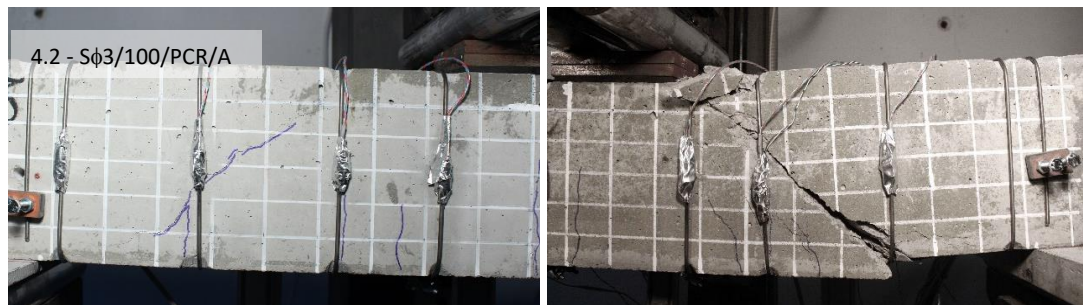


Figure A1.10.3. Beam 4.2 test at test end

Table A1.16. Beam 4.2 test results

Beam	V_{test} (kN)	E_{ff}	δ at V_{test} (mm)	δ/l (1/l)
4.2 - S ϕ 3/100/PCR/A	35.60	1.94	4.10	1/185

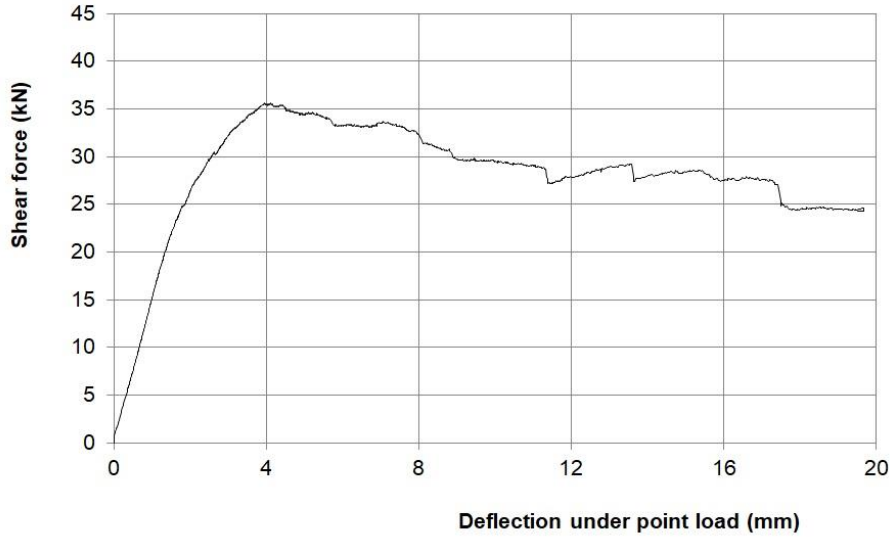


Figure A1.10.4. Shear force-deflection, beam 4.2 test

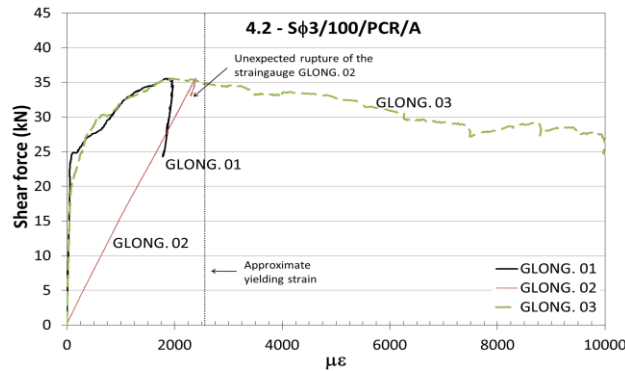


Figure A1.10.5. Shear force-longitudinal strain, beam 4.2 test

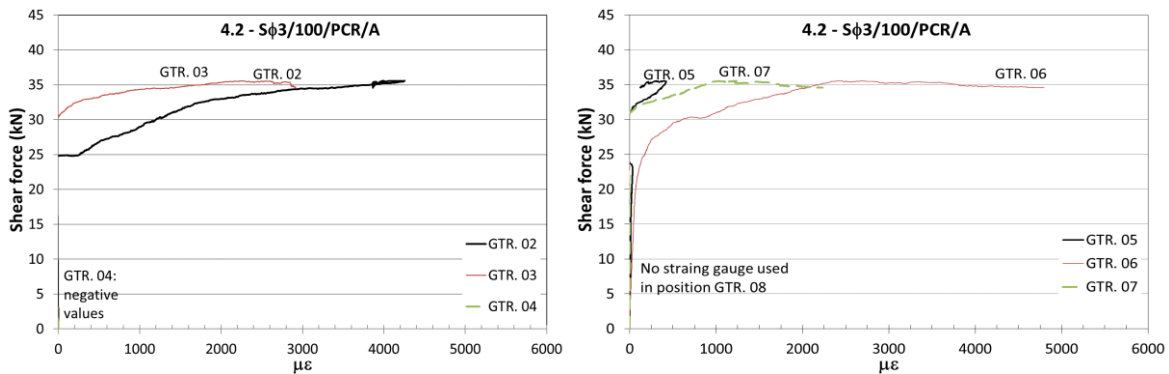


Figure A1.10.6. Shear force-vertical strain, beam 4.2 test

TEST 5.1 – S ϕ 3/075/UCR/A

Date: 2016/07/16 Age: 263 days

Concrete: $f_{cm28d} = 37.5$ MPa $f_{cm} = 43.2$ MPa $f_{sp} = 3.4$ MPa

Longitudinal reinforcement: Steel 1 ϕ 16 mm $f_y = 513$ MPa $f_u = 642$ MPa

Transverse reinforcement: Ni-Ti-Nb spiral ϕ 3 mm s = 75 mm $\sigma_r = 433$ MPa

Geometry: 80x150x900 mm

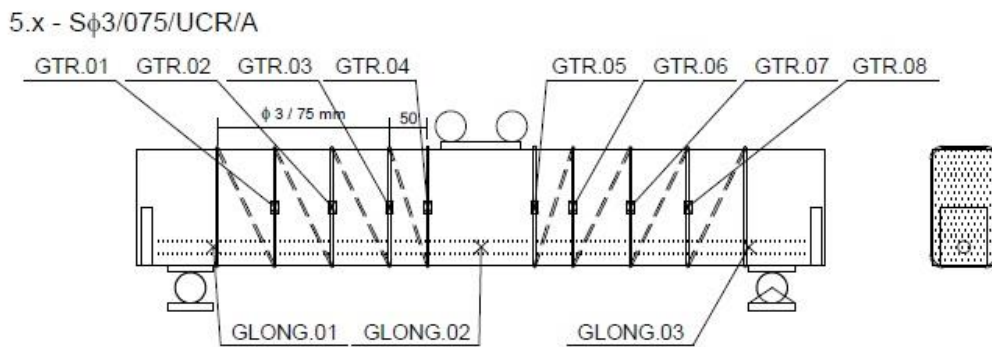


Figure A1.11.1. Beam 5.1 geometry and strain-gauge locations



Figure A1.11.2. Beam 5.1 test after peak load

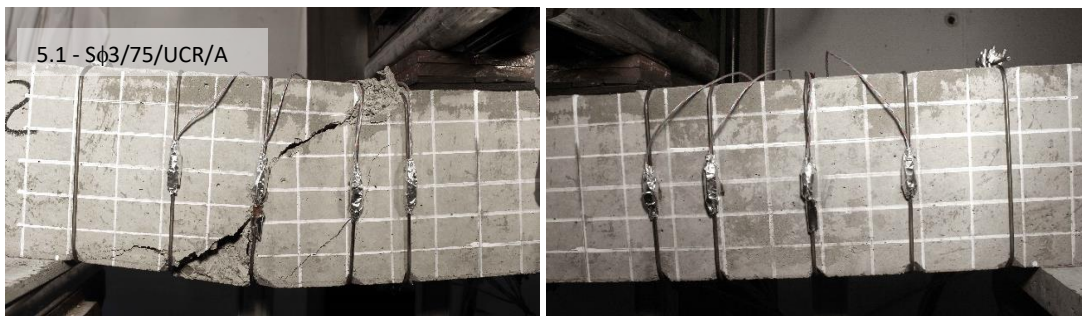


Figure A1.11.3. Beam 5.1 test at test end

Table A1.17. Beam 5.1 test results

Beam	V_{test} (kN)	E_{ff}	δ at V_{test} (mm)	δ/l (1/l)
5.1 - S ϕ 3/075/UCR/A	37.04	2.02	3.82	1/199

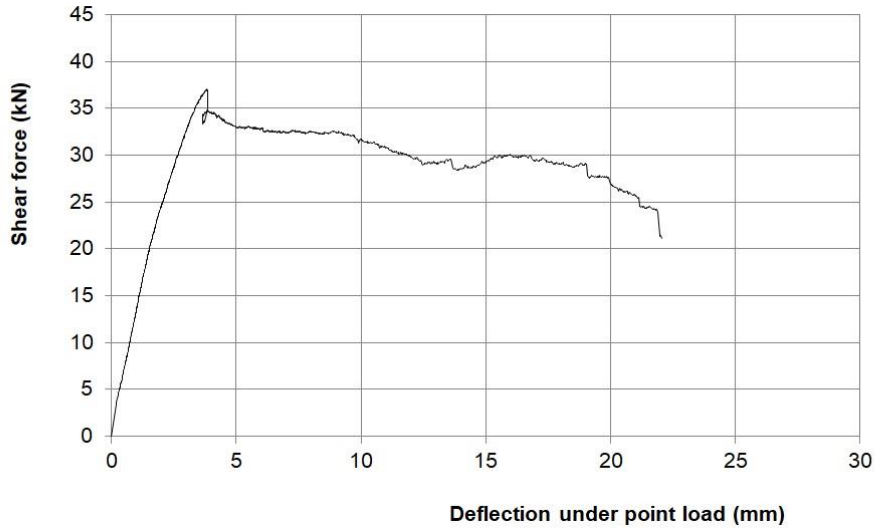


Figure A1.11.4. Shear force-deflection, beam 5.1 test

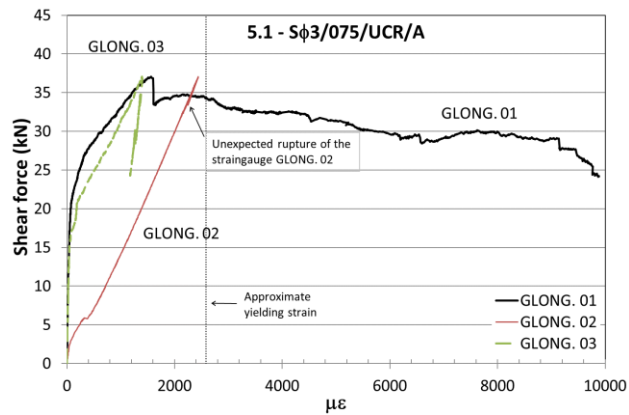


Figure A1.11.5. Shear force-longitudinal strain, beam 5.1 test

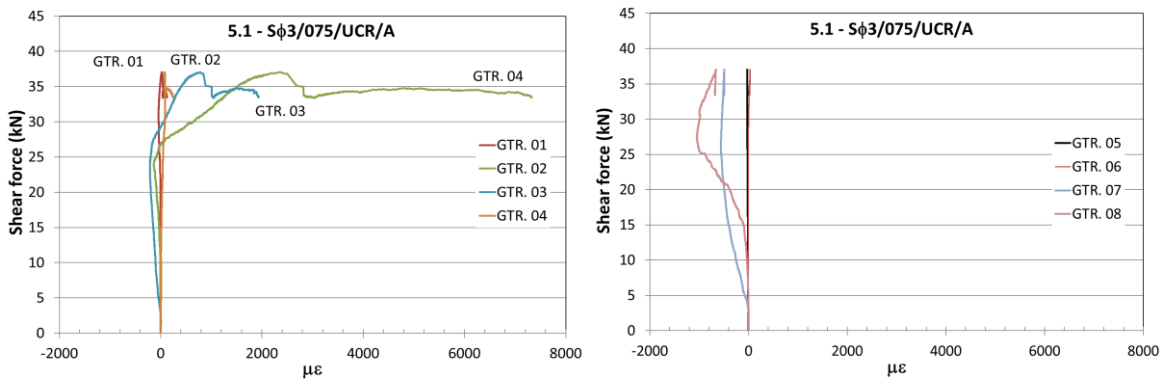


Figure A1.11.6. Shear force-vertical strain, beam 5.1 test

TEST 5.2 – S ϕ 3/075/UCR/A

Date: 2016/07/14 Age: 272 days

Concrete: $f_{cm28d} = 37.5$ MPa $f_{cm} = 43.2$ MPa $f_{sp} = 3.4$ MPa

Longitudinal reinforcement: Steel 1 ϕ 16 mm $f_y = 513$ MPa $f_u = 642$ MPa

Transverse reinforcement: Ni-Ti-Nb spiral ϕ 3 mm s = 75 mm $\sigma_r = 435$ MPa

Geometry: 80x150x900 mm

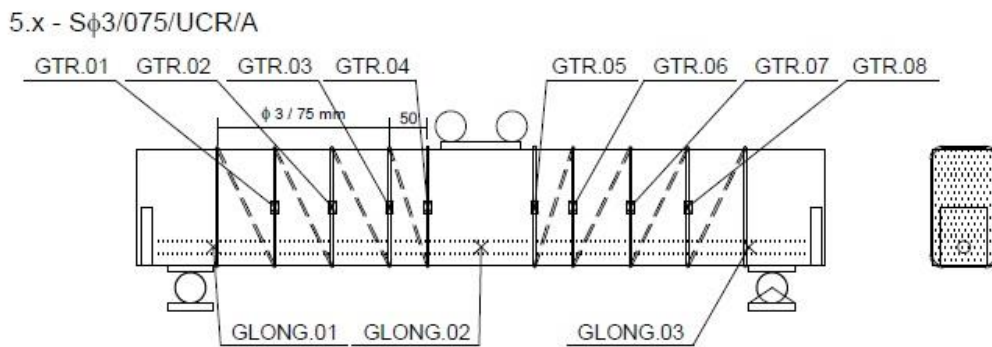


Figure A1.12.1. Beam 5.2 geometry and strain-gauge locations



Figure A1.12.2. Beam 5.2 test after peak load



Figure A1.12.3. Beam 5.2 test at test end

Table A1.18. Beam 5.2 test results

Beam	V_{test} (kN)	E_{ff}	δ at V_{test} (mm)	δ/l (1/l)
5.2 - S ϕ 3/075/UCR/A	41.82	2.28	6.95	1/109

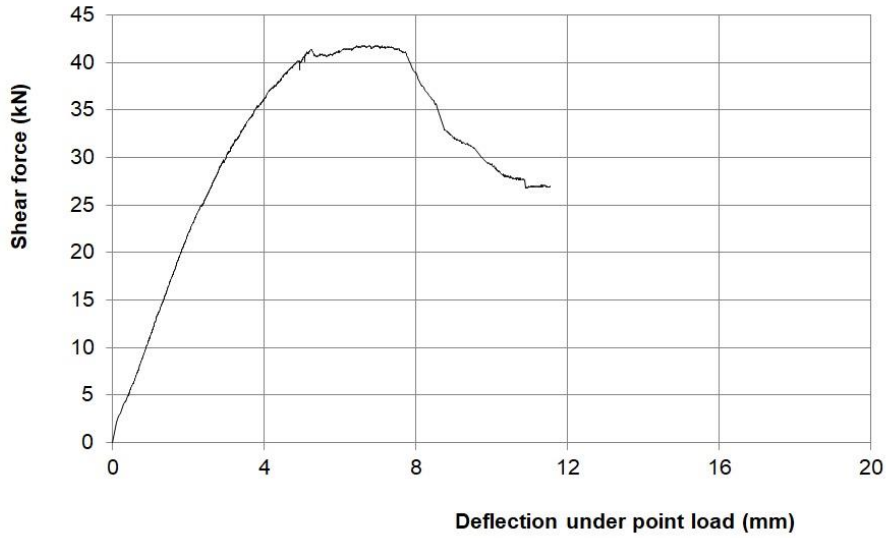


Figure A1.12.4. Shear force-deflection, beam 5.2 test

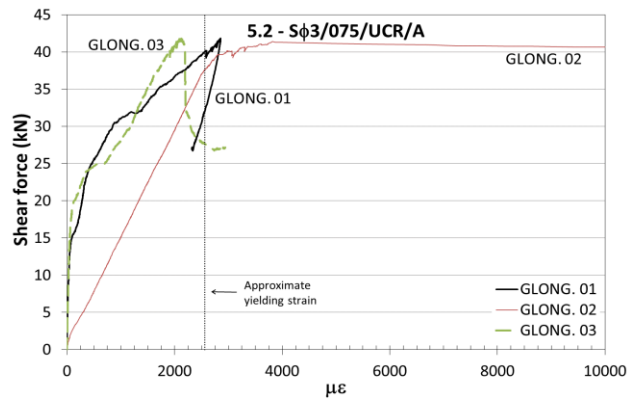


Figure A1.12.5. Shear force-longitudinal strain, beam 5.2 test

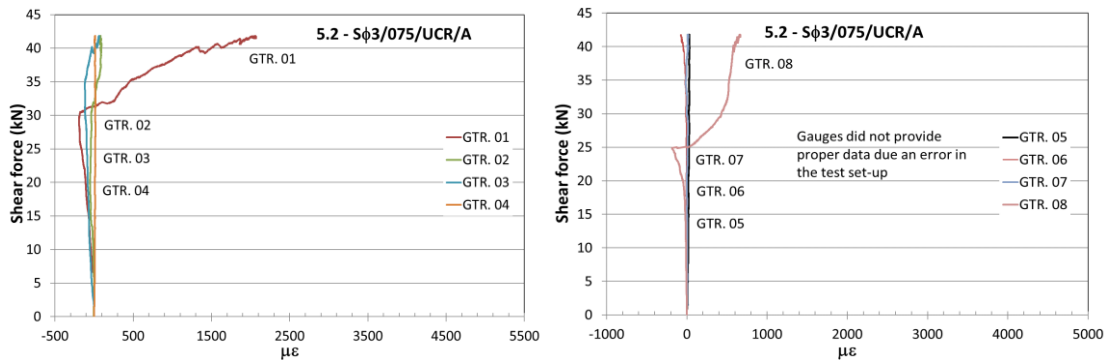


Figure A1.12.6. Shear force-vertical strain, beam 5.2 test

TEST 6.1 – Reference

Date: 2016/05/12 Age: 202 days

Concrete: $f_{cm28d} = 34.5 \text{ MPa}$ $f_{cm} = 39.7 \text{ MPa}$ $f_{sp} = 3.4 \text{ MPa}$

Longitudinal reinforcement: Steel 1 ϕ 16 $f_y = 513 \text{ MPa}$ $f_u = 642 \text{ MPa}$

Transverse reinforcement: -

Geometry: 80x150x900 mm

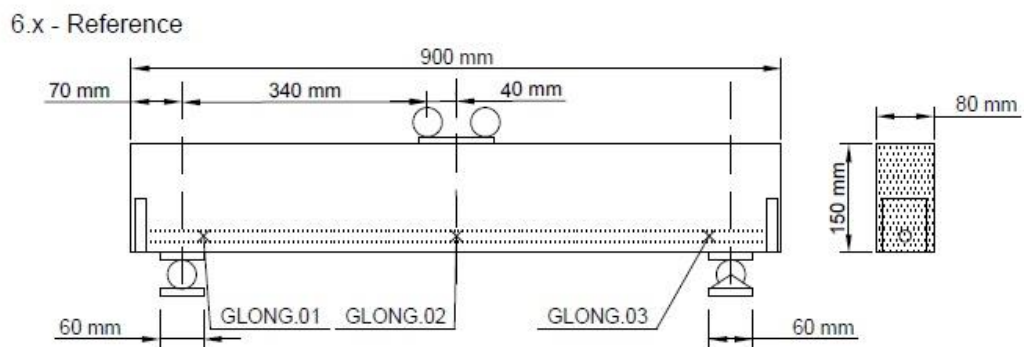


Figure A1.13.1. Beam 6.1 geometry and strain-gauge locations



Figure A1.13.2. Beam 6.1 test after peak load

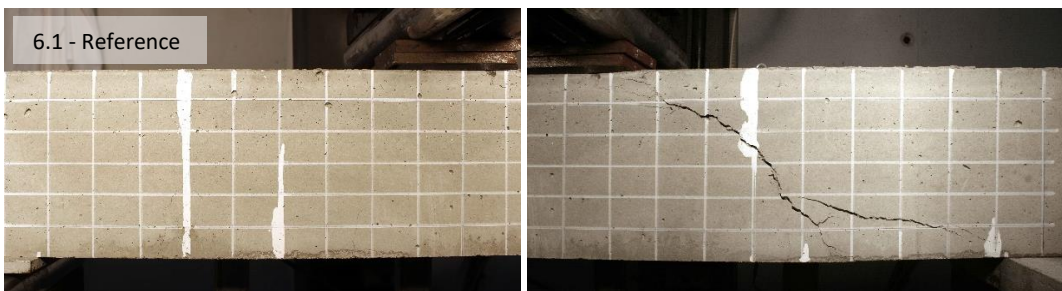


Figure A1.13.3. Beam 6.1 test at test end

Table A1.19. Beam 6.1 test results

Beam	V_{test} (kN)	E_{ff}	δ at V_{test} (mm)	δ/l (1/l)
6.1 – Reference	19.71	-	2.505	1/303

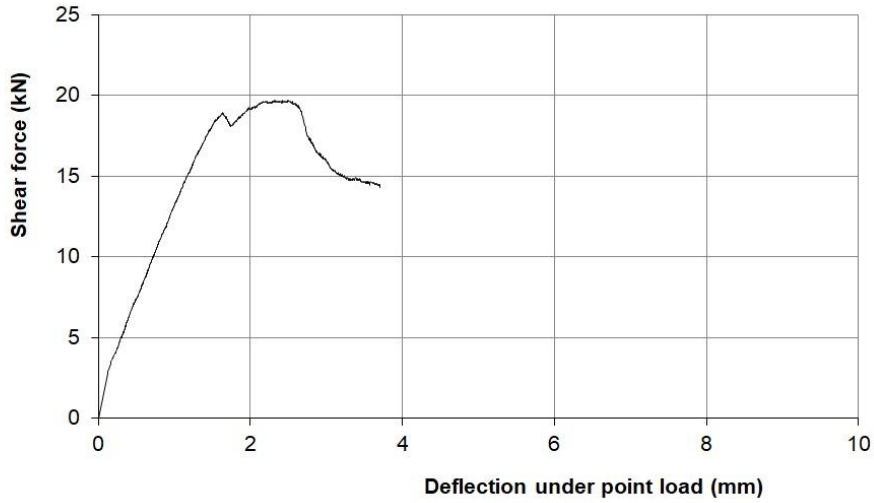


Figure A1.13.4. Shear force-deflection, beam 6.1 test

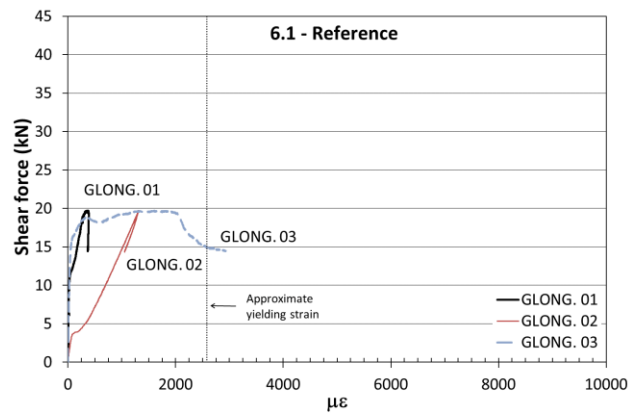


Figure A1.13.5. Shear force-longitudinal strain, beam 6.1 test

TEST 6.2 – Reference

Date: 2016/05/12 Age: 202 days

Concrete: $f_{cm28d} = 34.5 \text{ MPa}$ $f_{cm} = 39.7 \text{ MPa}$ $f_{sp} = 3.4 \text{ MPa}$

Longitudinal reinforcement: Steel 1 ϕ 16 $f_y = 513 \text{ MPa}$ $f_u = 642 \text{ MPa}$

Transverse reinforcement: -

Geometry: 80x150x900 mm

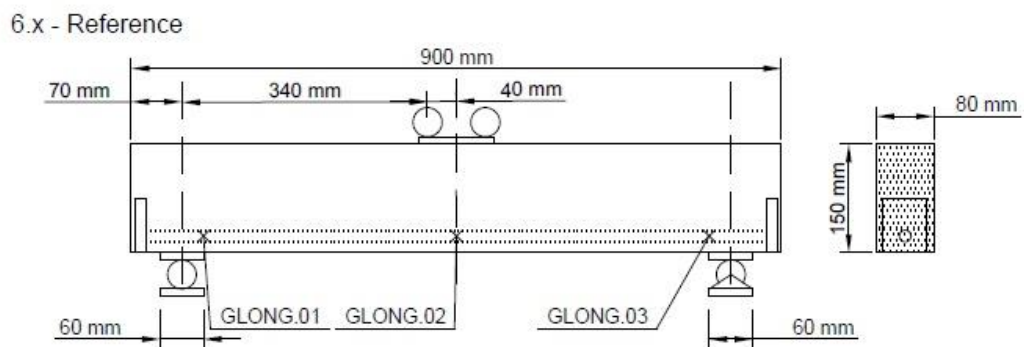


Figure A1.14.1. Beam 6.2 geometry and strain-gauge locations

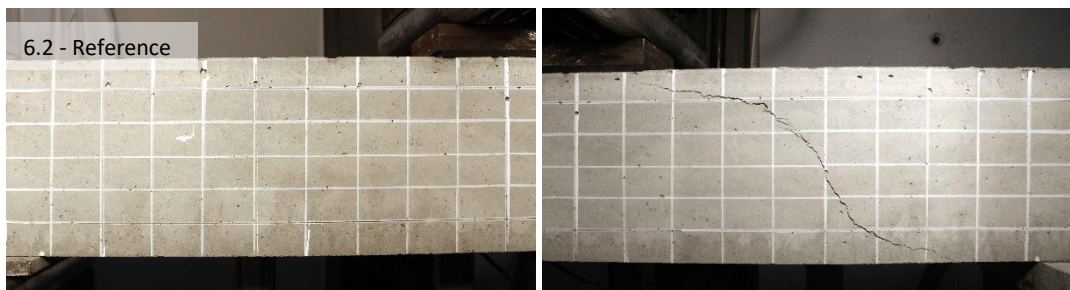


Figure A1.14.2. Beam 6.2 test after peak load

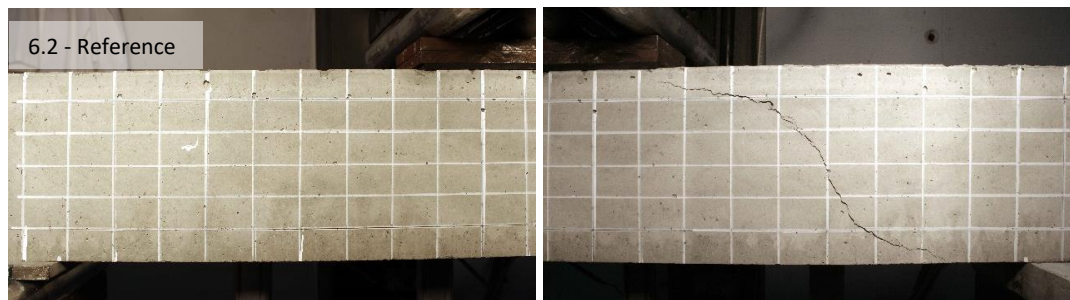


Figure A1.14.3. Beam 6.2 test at test end

Table A1.20. Beam 6.2 test results

Beam	V_{test} (kN)	E_{ff}	δ at V_{test} (mm)	δ/l (1/l)
6.2 – Reference	18.50	-	1.692	1/449

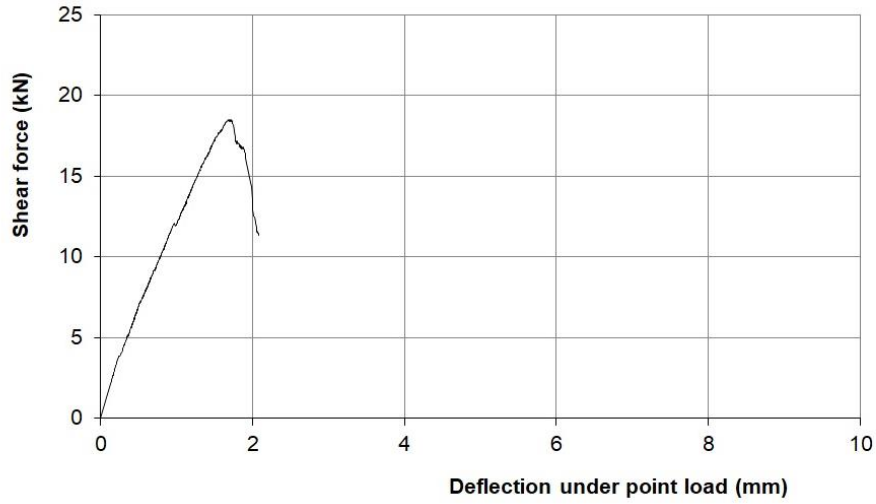


Figure A1.14.4. Shear force-deflection, beam 6.2 test

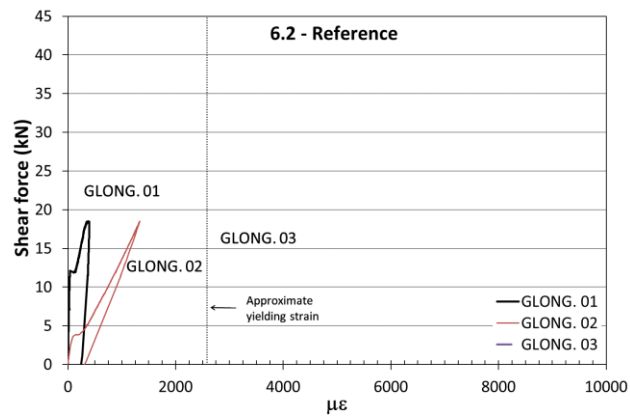


Figure A1.14.5. Shear force-longitudinal strain, beam 6.2 test

TEST 7.1 – S ϕ 3/100/UCR/A/G

Date: 2016/07/26 Age: 279 days

Concrete: $f_{cm28d} = 34.5$ MPa $f_{cm} = 39.8$ MPa $f_{sp} = 3.5$ MPa

Longitudinal reinforcement: Steel 1 ϕ 16 mm $f_y = 513$ MPa $f_u = 642$ MPa

Transverse reinforcement: Ni-Ti-Nb spiral in groove ϕ 3 mm s = 100 mm $\sigma_r = 389$ MPa

Geometry: 80x150x900 mm

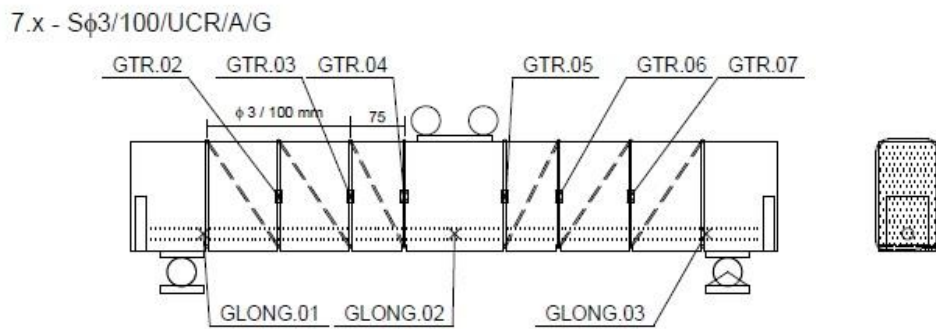


Figure A1.15.1. Beam 7.1 geometry and strain-gauge locations

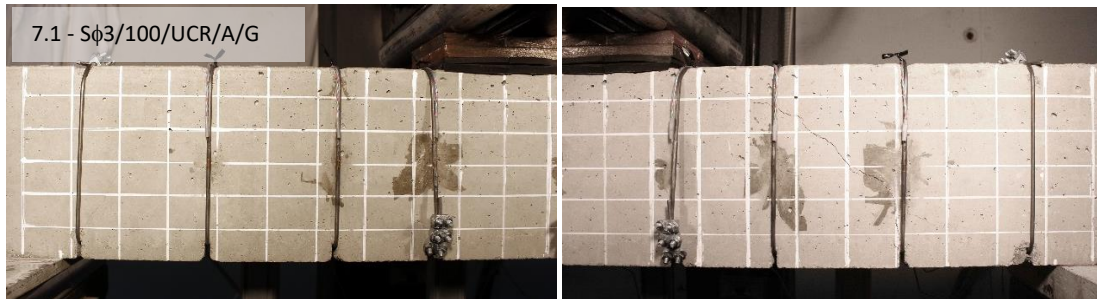


Figure A1.15.2. Beam 7.1 test after peak load



Figure A1.15.3. Beam 7.1 test at test end

Table A1.21. Beam 7.1 test results

Beam	V_{test} (kN)	E_{ff}	δ at V_{test} (mm)	δ/l (1/l)
7.1 - S ϕ 3/100/UCR/A/G	25.36	1.33	2.560	1/297

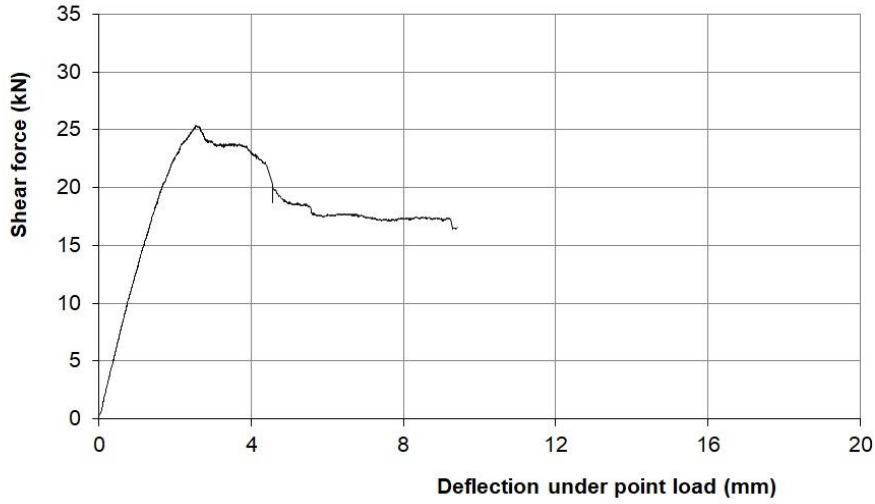


Figure A1.15.4. Shear force-deflection, beam 7.1 test

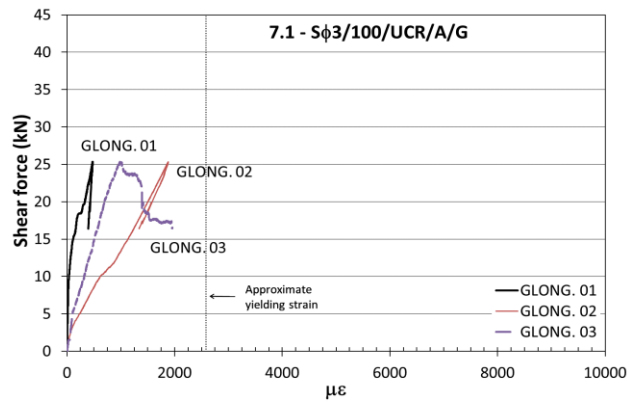


Figure A1.15.5. Shear force-longitudinal strain, beam 7.1 test

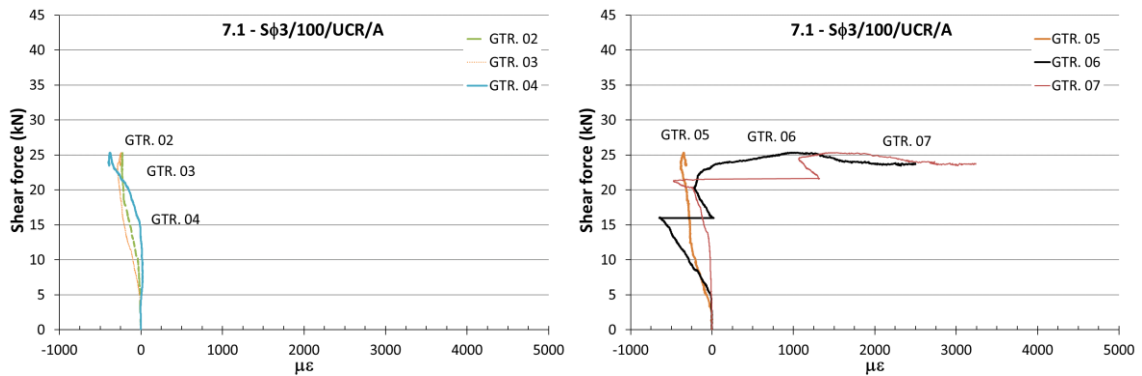


Figure A1.15.6. Shear force-vertical strain, beam 7.1 test

TEST 7.2 – S ϕ 3/100/UCR/A/G

Date: 2016/07/26 Age: 279 days

Concrete: $f_{cm28d} = 34.5$ MPa $f_{cm} = 39.8$ MPa $f_{sp} = 3.5$ MPa

Longitudinal reinforcement: Steel 1 ϕ 16 mm $f_y = 513$ MPa $f_u = 642$ MPa

Transverse reinforcement: Ni-Ti-Nb spiral in groove ϕ 3 mm s = 100 mm $\sigma_r = 409$ MPa

Geometry: 80x150x900 mm

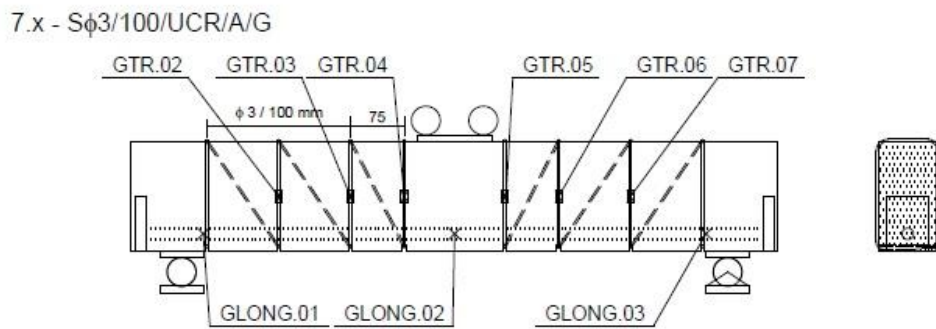


Figure A1.16.1. Beam 7.2 geometry and strain-gauge locations

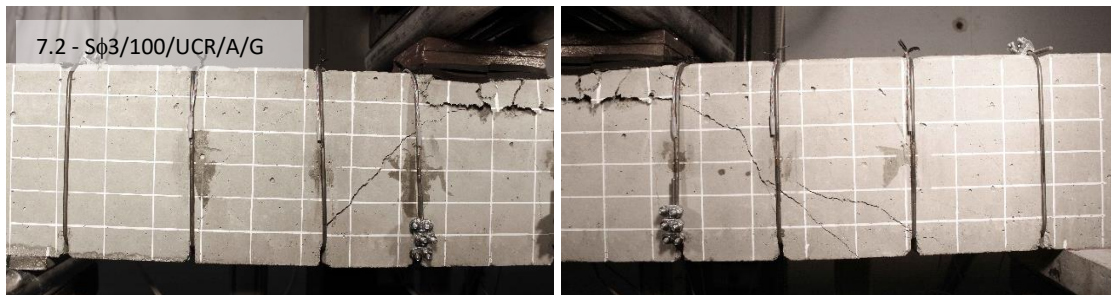


Figure A1.16.2. Beam 7.2 test after peak load



Figure A1.16.3. Beam 7.2 test at test end

Table A1.22. Beam 7.2 test results

Beam	V_{test} (kN)	E_{ff}	δ at V_{test} (mm)	δ/l (1/l)
7.2 - S ϕ 3/100/UCR/A/G	35.51	1.86	6.039	1/126

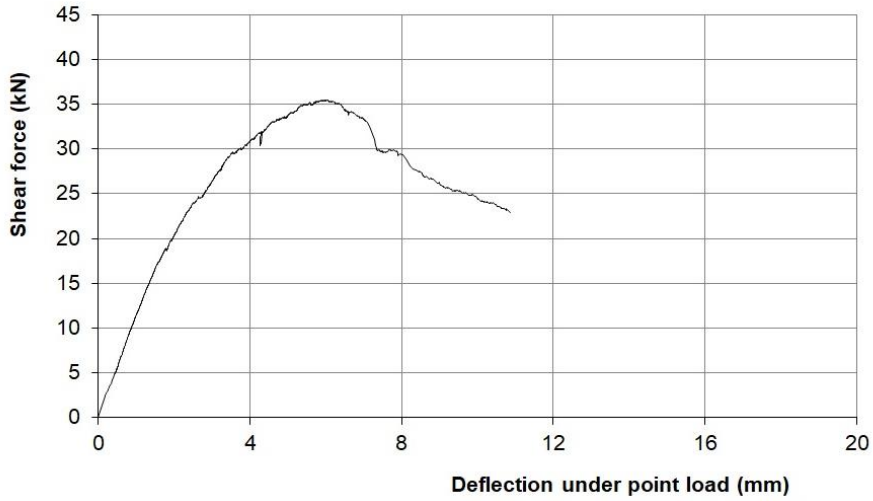


Figure A1.16.4. Shear force-deflection, beam 7.2 test

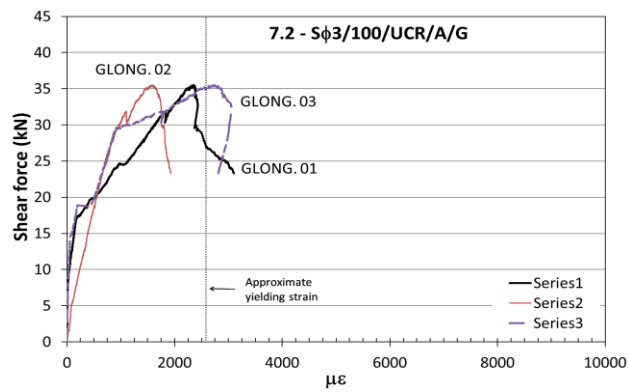


Figure A1.16.5. Shear force-longitudinal strain, beam 7.2 test

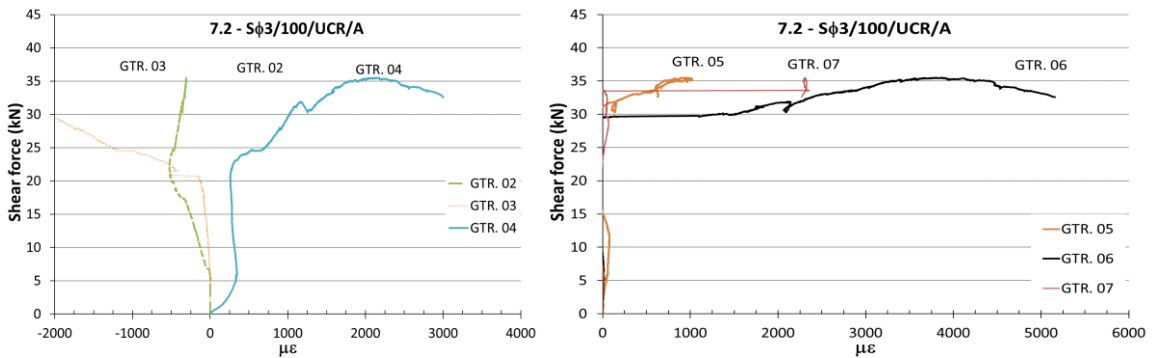


Figure A1.16.6. Shear force-vertical strain, beam 7.2 test

TEST 8.1 – U ϕ 3/100/UCR/A

Date: 2016/06/03 Age: 224 days

Concrete: $f_{cm28d} = 34.5$ MPa $f_{cm} = 39.7$ MPa $f_{sp} = 3.4$ MPa

Longitudinal reinforcement: Steel 1 ϕ 16 mm $f_y = 513$ MPa $f_u = 642$ MPa

Transverse reinforcement: Ni-Ti-Nb U-shape stirrup ϕ 3 mm s = 100 mm $\sigma_r = 440$ MPa

Geometry: 80x150x900 mm

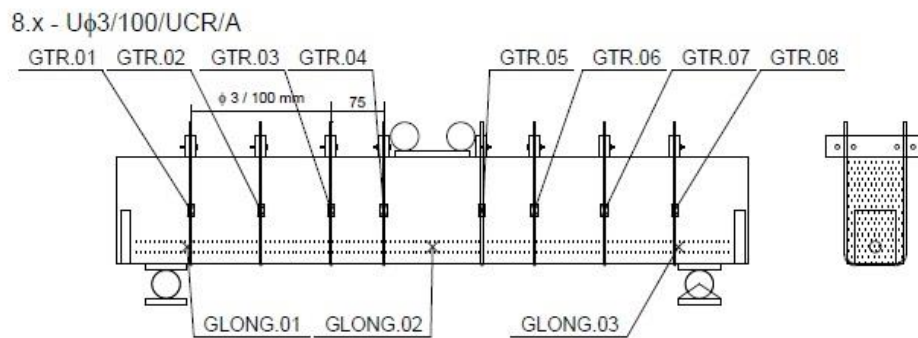


Figure A1.17.1. Beam 8.1 geometry and strain-gauge locations

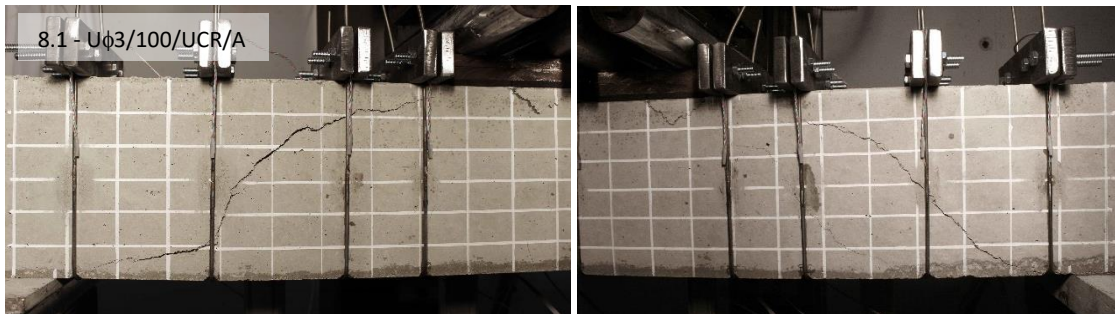


Figure A1.17.2. Beam 8.1 test after peak load

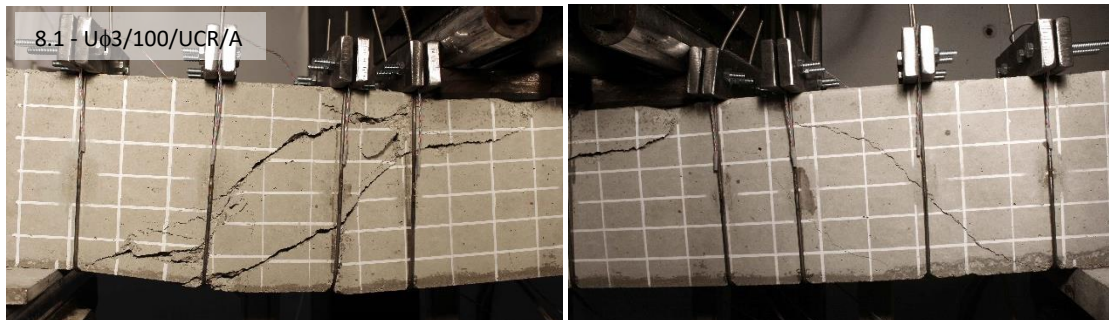


Figure A1.17.3. Beam 8.1 test at test end

Table A1.23. Beam 8.1 test results

Beam	V_{test} (kN)	E_{ff}	δ at V_{test} (mm)	δ/l (1/l)
8.1 - U ϕ 3/100/UCR/A	37.74	1.98	5.347	1/142

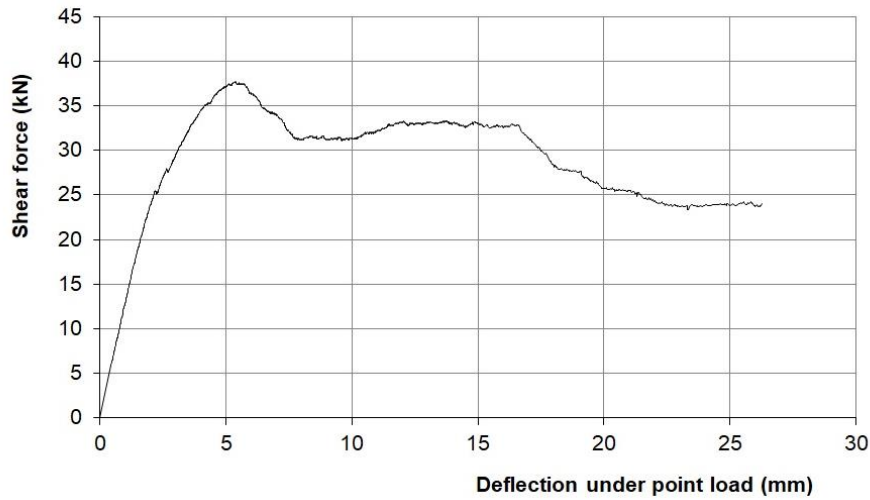


Figure A1.17.4. Shear force-deflection, beam 8.1 test

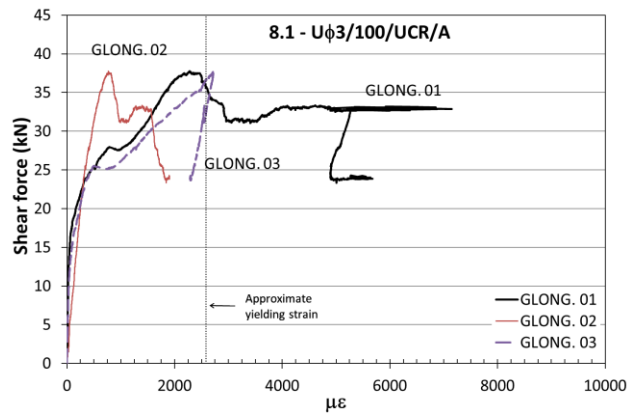


Figure A1.17.5. Shear force-longitudinal strain, beam 8.1 test

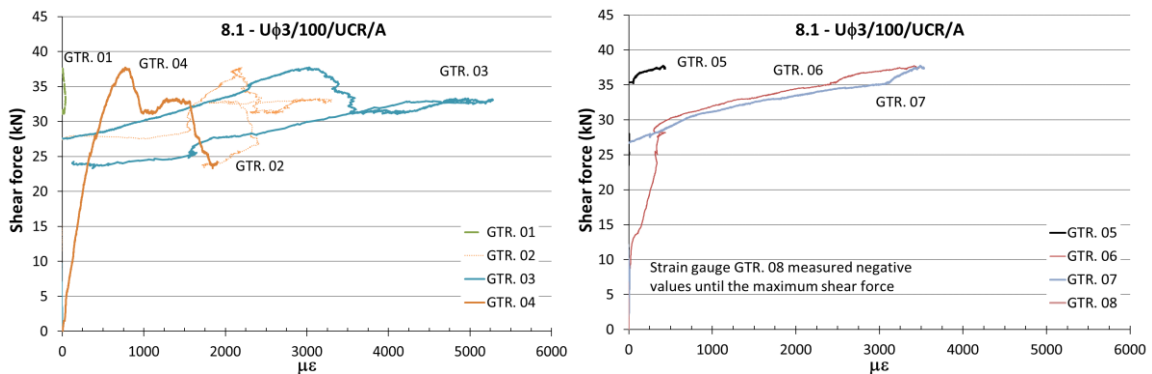


Figure A1.17.6. Shear force-vertical strain, beam 8.1 test

TEST 8.2 – U ϕ 3/100/UCR/A

Date: 2016/06/23 Age: 244 days

Concrete: $f_{cm28d} = 34.5$ MPa $f_{cm} = 39.7$ MPa $f_{sp} = 3.4$ MPa

Longitudinal reinforcement: Steel 1 ϕ 16 mm $f_y = 513$ MPa $f_u = 642$ MPa

Transverse reinforcement: Ni-Ti-Nb U-shape stirrup $\phi 3$ mm s = 100 mm $\sigma_r = 441$ MPa

Geometry: 80x150x900 mm

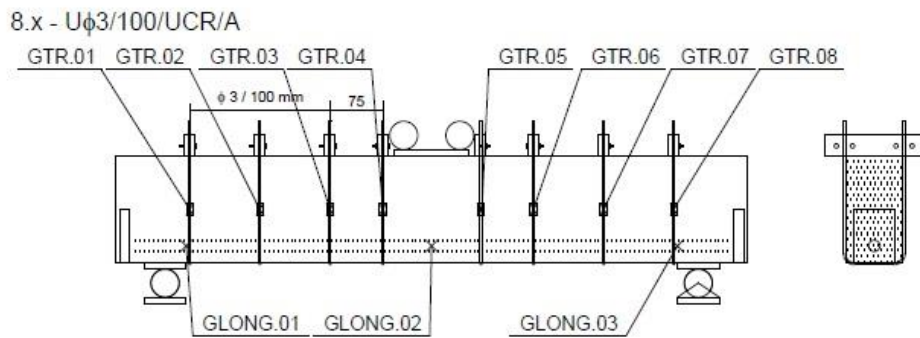


Figure A1.18.1. Beam 8.2 geometry and strain-gauge locations

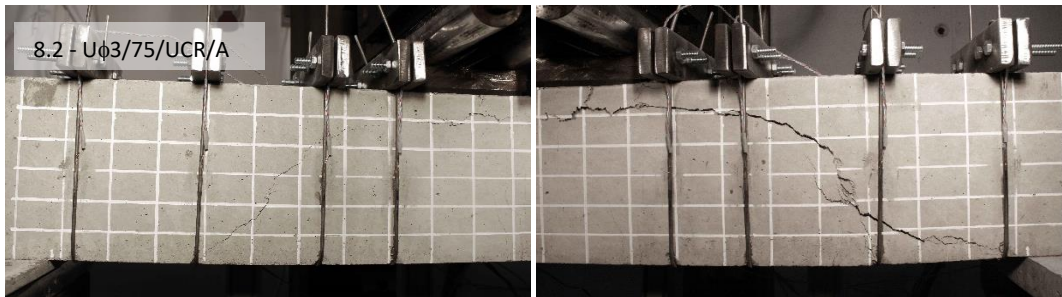


Figure A1.18.2. Beam 8.2 test after peak load

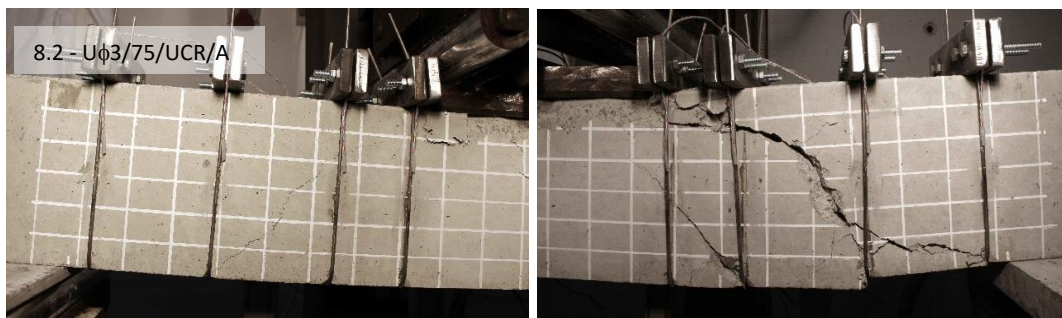


Figure A1.18.3. Beam 8.2 test at test end

Table A1.24. Beam 8.2 test results

Beam	V_{test} (kN)	E_{ff}	δ at V_{test} (mm)	δ/l (1/l)
8.2 - U ϕ 3/100/UCR/A	34.75	1.82	5.148	1/148

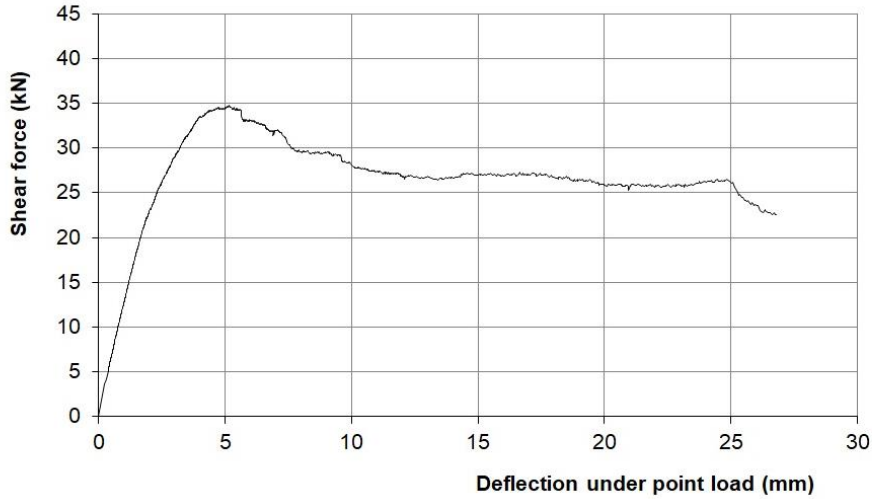


Figure A1.18.4. Shear force-deflection, beam 8.2 test

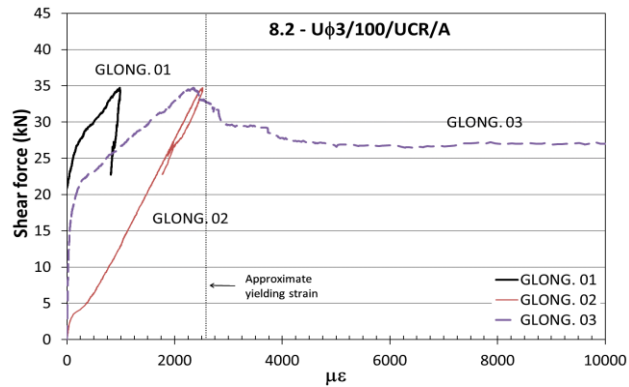


Figure A1.18.5. Shear force-longitudinal strain, beam 8.2 test

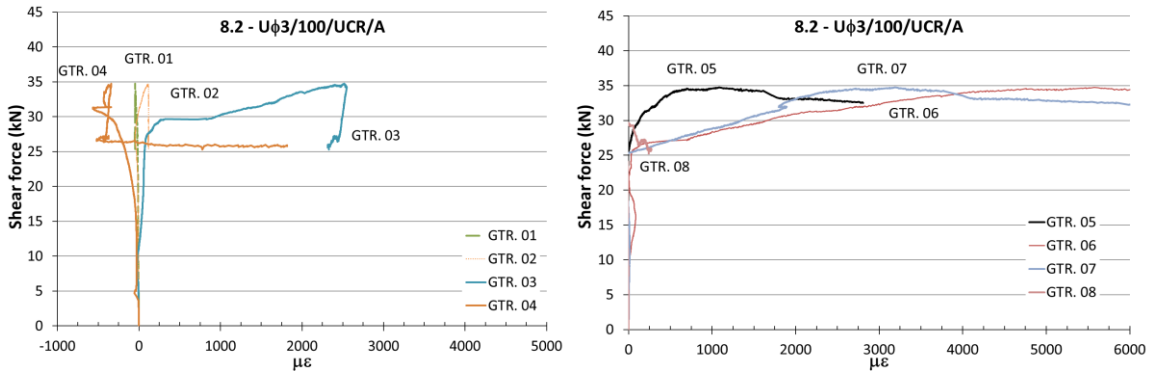


Figure A1.18.6. Shear force-vertical strain, beam 8.2 test

TEST 9.1 – S ϕ 3/100/UCR/A/S

Date: 2016/07/21 Age: 272 days

Concrete: $f_{cm28d} = 34.5$ MPa $f_{cm} = 39.8$ MPa $f_{sp} = 3.5$ MPa

Longitudinal reinforcement: Steel 1 ϕ 16 mm $f_y = 513$ MPa $f_u = 642$ MPa

Transverse reinforcement: Ni-Ti-Nb mid-span spiral ϕ 3 mm s = 100 mm $\sigma_r = 316$ MPa

Geometry: 80x150x900 mm

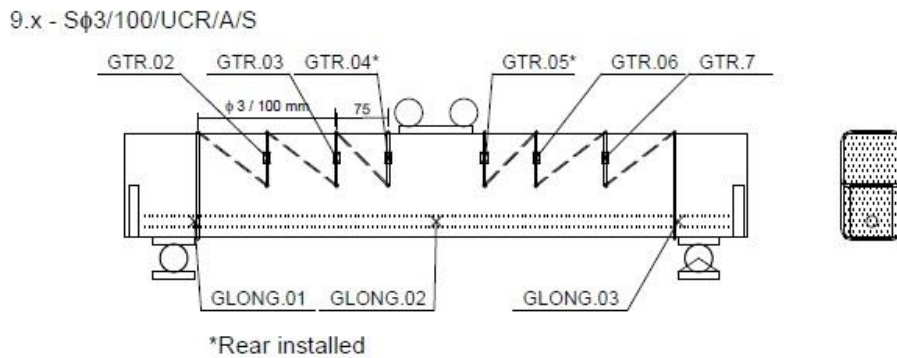


Figure A1.19.1. Beam 9.1 geometry and strain-gauge locations

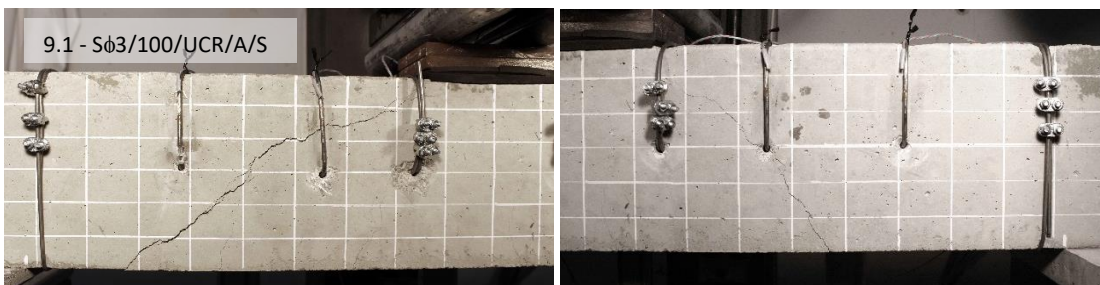


Figure A1.19.2. Beam 9.1 test after peak load

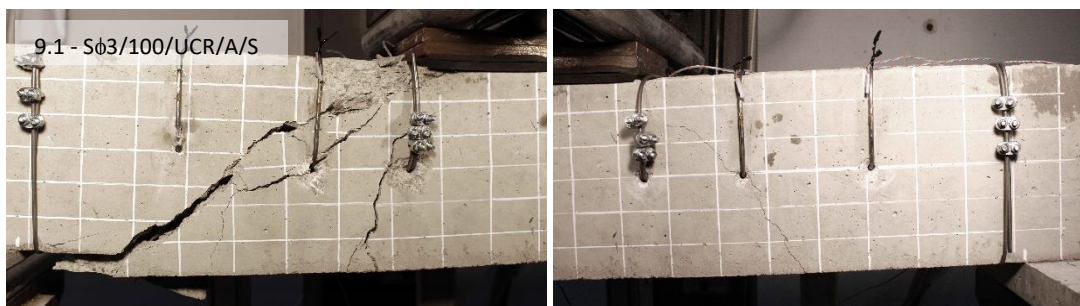


Figure A1.19.3. Beam 9.1 test at test end

Table A1.25. Beam 9.1 test results

Beam	V_{test} (kN)	E_{ff}	δ at V_{test} (mm)	δ/l (1/l)
9.1 - S ϕ 3/100/UCR/A/S	20.54	1.08	3.007	1/253

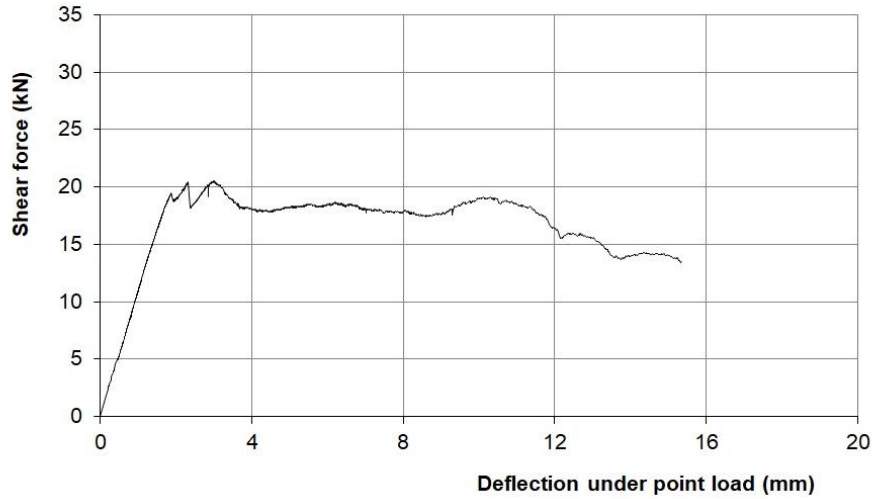


Figure A1.19.4. Shear force-deflection, beam 9.1 test

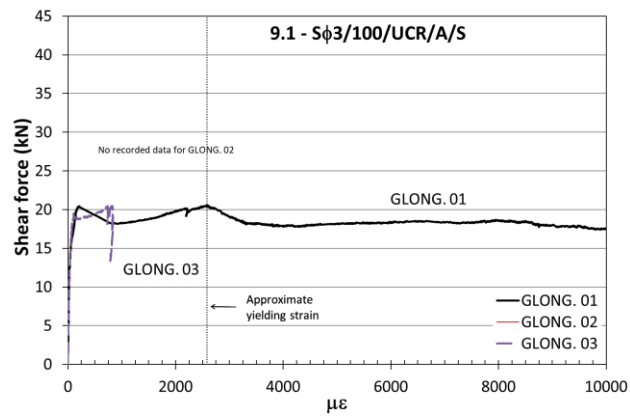


Figure A1.19.5. Shear force-longitudinal strain, beam 9.1 test

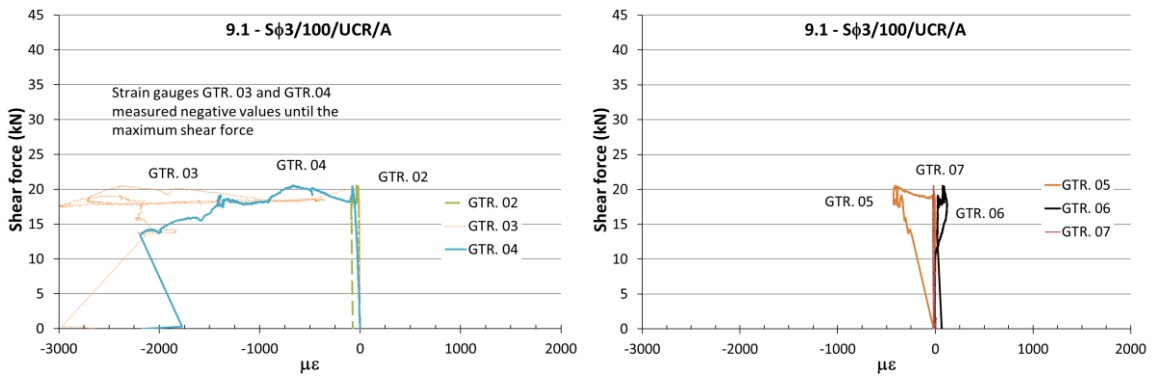


Figure A1.19.6. Shear force-vertical strain, beam 9.1 test

9.2 – S ϕ 3/100/UCR/A/S

Date: 2016/07/25 Age: 272 days

Concrete: $f_{cm28d} = 34.5$ MPa $f_{cm} = 39.8$ MPa $f_{sp} = 3.5$ MPa

Longitudinal reinforcement: Steel 1 ϕ 16 mm $f_y = 513$ MPa $f_u = 642$ MPa

Transverse reinforcement: Ni-Ti-Nb mid-span spiral ϕ 3 mm s = 100 mm $\sigma_r = 338$ MPa

Geometry: 80x150x900 mm

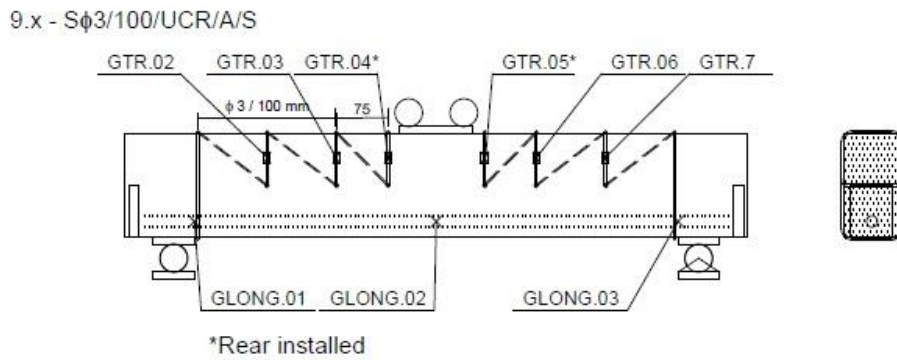


Figure A1.20.1. Beam 9.2 geometry and strain-gauge locations

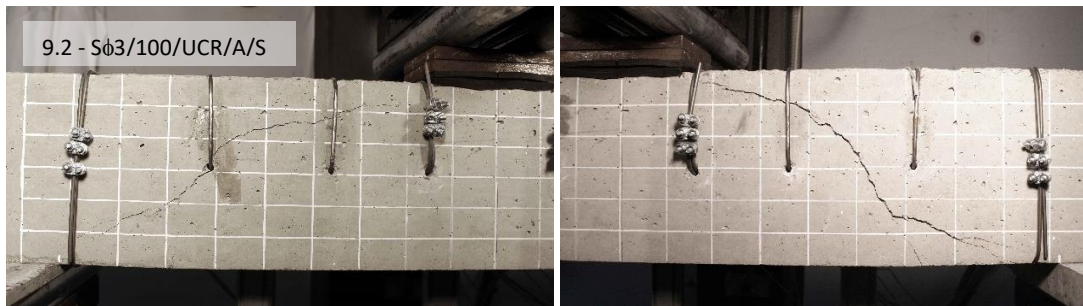


Figure A1.20.2. Beam 9.2 test after peak load

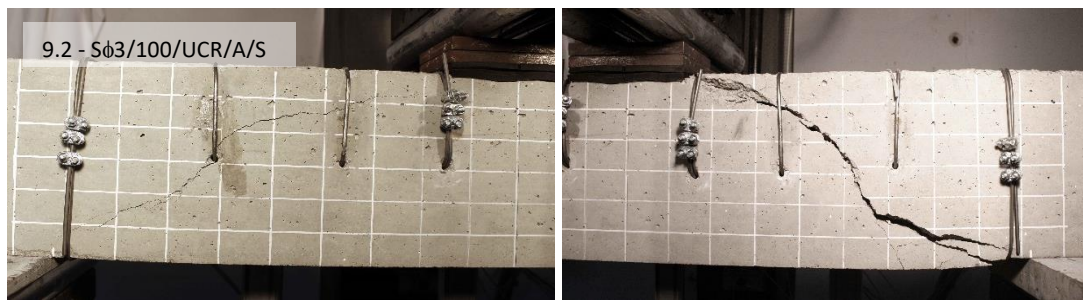


Figure A1.20.3. Beam 9.2 test at test end

Table A1.26. Beam 9.2 test results

Beam	V_{test} (kN)	E_{ff}	δ at V_{test} (mm)	δ/l (1/l)
9.2 - S ϕ 3/100/UCR/A/S	22.03	1.15	3.695	1/206

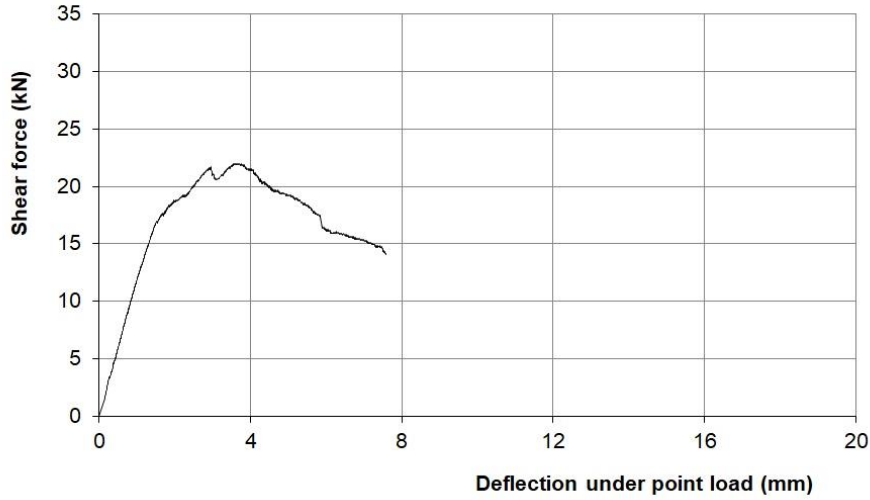


Figure A1.20.4. Shear force-deflection, beam 9.2 test

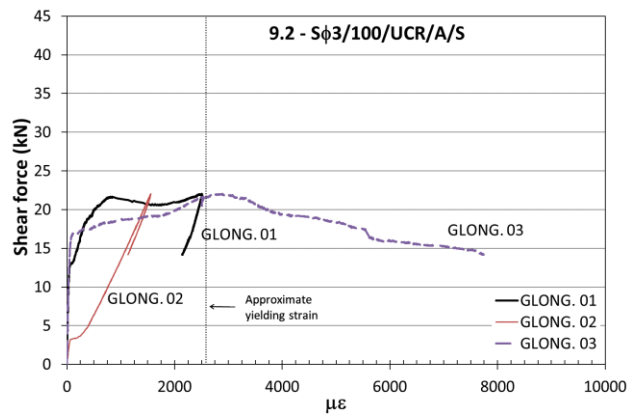


Figure A1.20.5. Shear force-longitudinal strain, beam 9.2 test

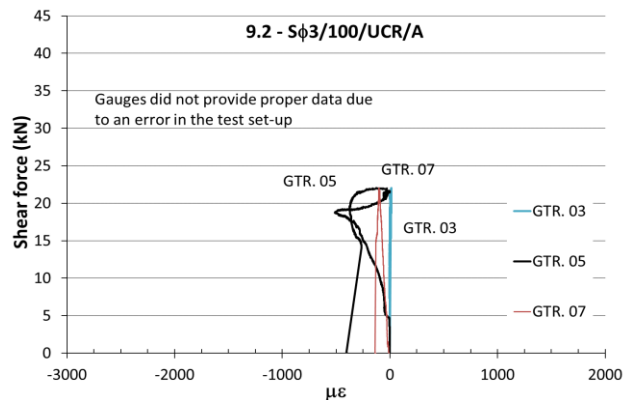


Figure A1.20.6. Shear force-vertical strain, beam 9.2 test

TEST 10.1 – U ϕ 3/075/UCR/A

Date: 2016/09/08 Age: 321 days

Concrete: $f_{cm28d} = 34.5$ MPa $f_{cm} = 39.8$ MPa $f_{sp} = 3.5$ MPa

Longitudinal reinforcement: Steel 1 ϕ 16 mm $f_y = 513$ MPa $f_u = 642$ MPa

Transverse reinforcement: Ni-Ti-Nb U-shape stirrup ϕ 3 mm s = 75 mm $\sigma_r = 441$ MPa

Geometry: 80x150x900 mm

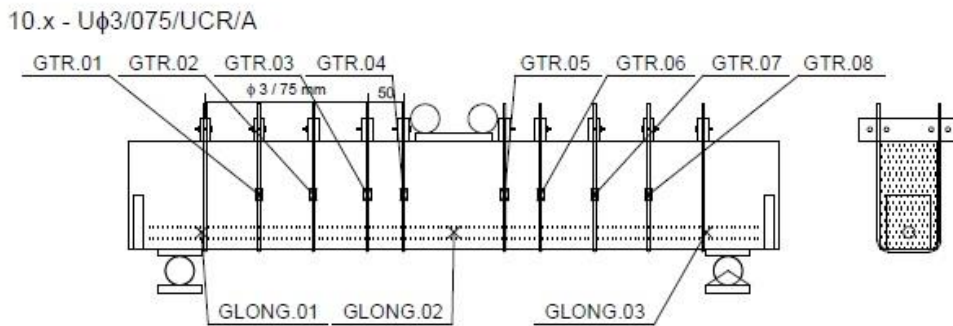


Figure A1.21.1. Beam 10.1 geometry and strain-gauge locations

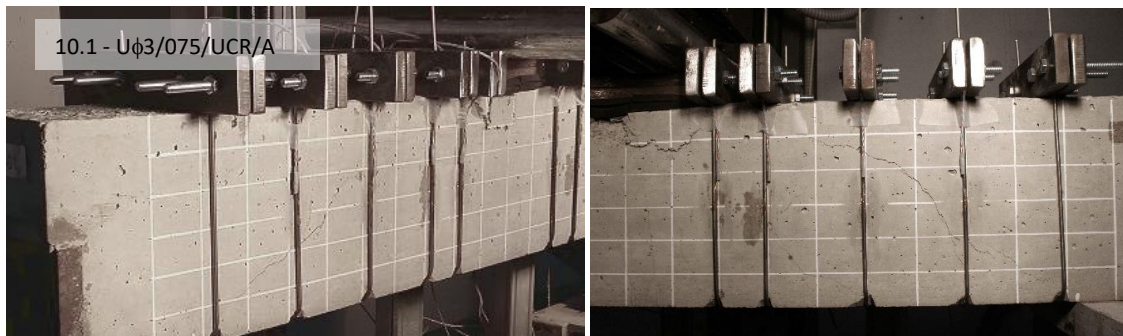


Figure A1.21.2. Beam 10.1 test after peak load



Figure A1.21.3. Beam 10.1 test at test end

Table A1.27. Beam 10.1 test results

Beam	V_{test} (kN)	E_{ff}	δ at V_{test} (mm)	δ/l (1/l)
10.1 - U ϕ 3/075/UCR/A	36.79	1.93	5.310	1/143

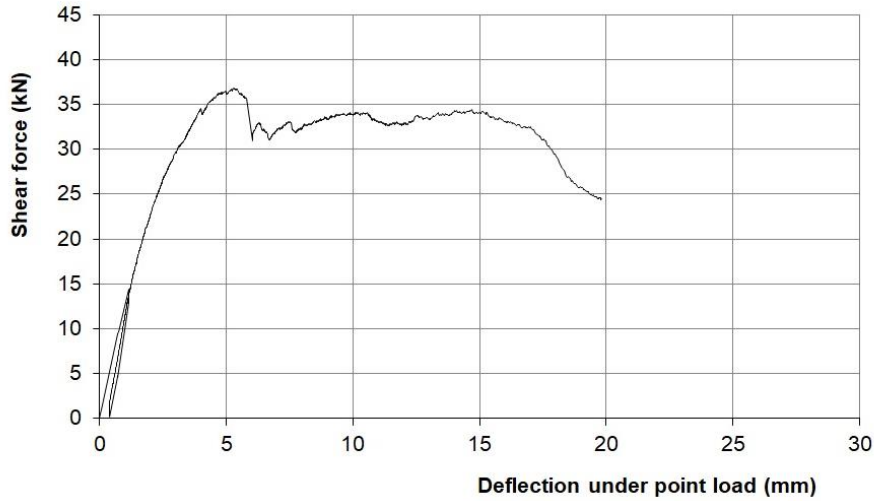


Figure A1.21.4. Shear force-deflection, beam 10.1 test

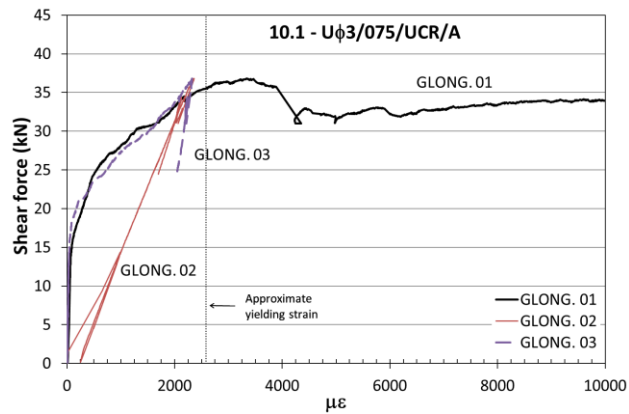


Figure A1.21.5. Shear force-longitudinal strain, beam 10.1 test

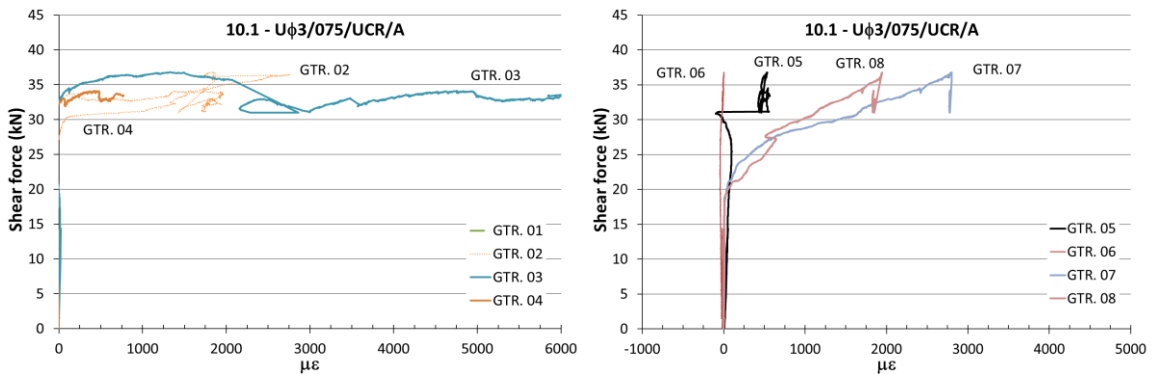


Figure A1.21.6. Shear force-vertical strain, beam 10.1 test

TEST 10.2 – U ϕ 3/075/UCR/A

Date: 2016/09/12 Age: 325 days

Concrete: $f_{cm28d} = 34.5$ MPa $f_{cm} = 39.8$ MPa $f_{sp} = 3.5$ MPa

Longitudinal reinforcement: Steel 1 ϕ 16 mm $f_y = 513$ MPa $f_u = 642$ MPa

Transverse reinforcement: Ni-Ti-Nb U-shape stirrup ϕ 3 mm s = 75 mm $\sigma_r = 441$ MPa

Geometry: 80x150x900 mm

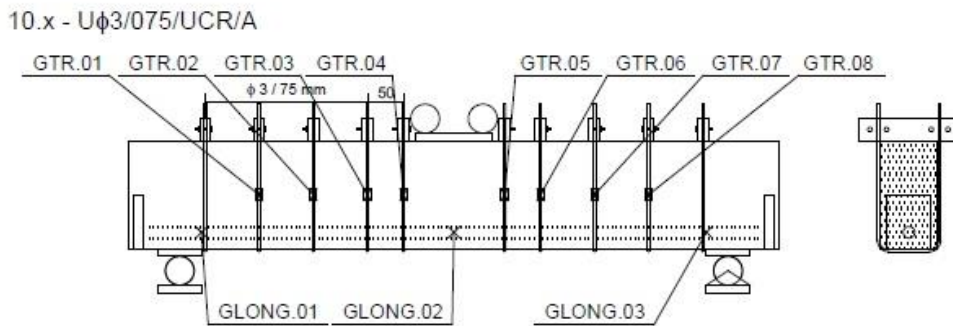


Figure A1.22.1. Beam 10.2 geometry and strain-gauge locations

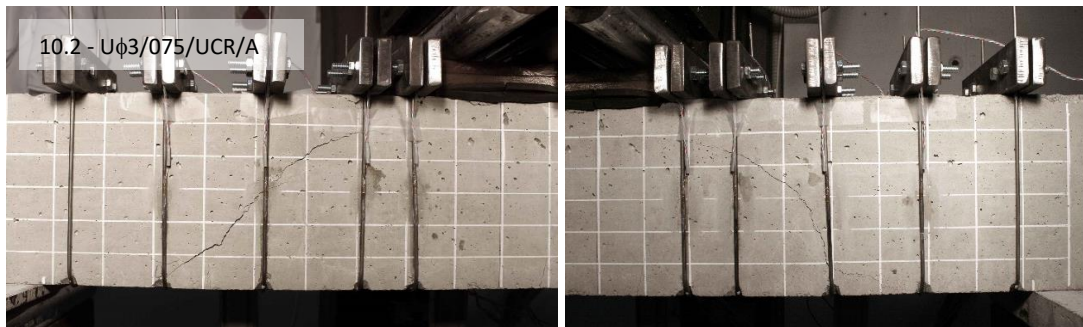


Figure A1.22.2. Beam 10.2 test after peak load



Figure A1.22.3. Beam 10.2 test at test end

Table A1.28. Beam 10.2 test results

Beam	V_{test} (kN)	E_{ff}	δ at V_{test} (mm)	δ/l (1/l)
10.2 - U ϕ 3/075/UCR/A	33.65	1.76	4.736	1/160

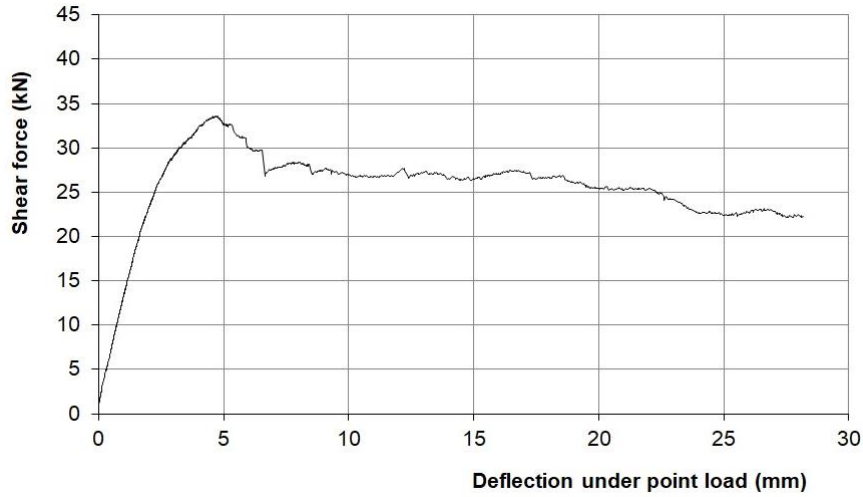


Figure A1.22.4. Shear force-deflection, beam 10.2 test

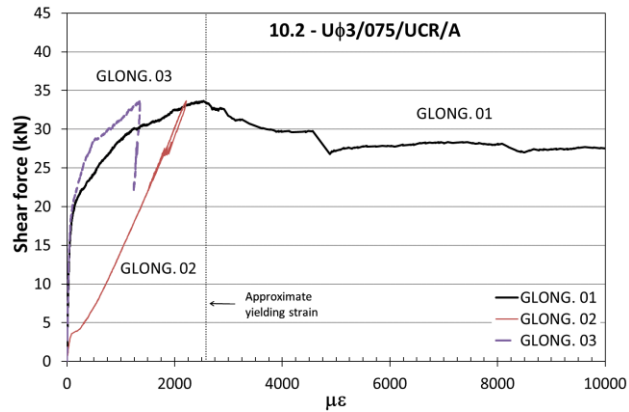


Figure A1.22.5. Shear force-longitudinal strain, beam 10.2 test

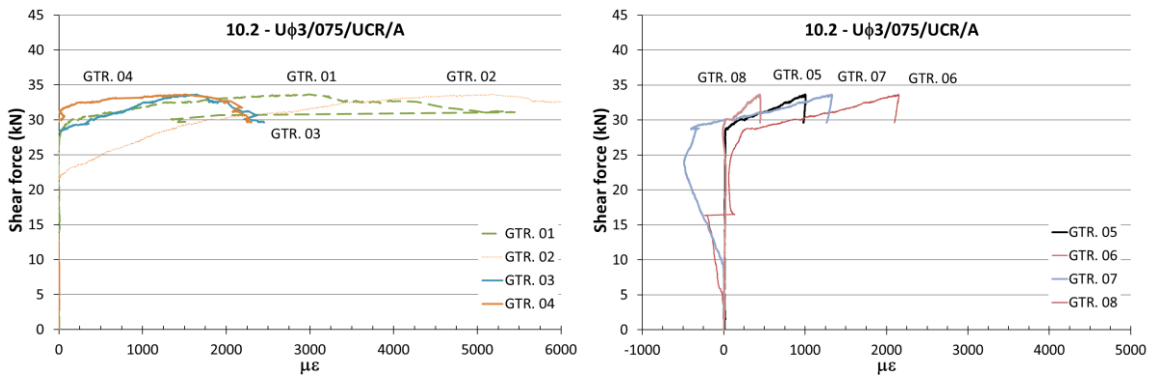


Figure A1.22.6. Shear force-vertical strain, beam 10.2 test

Table A2.1. Geometry and material property parameters of phase 1 beam tests

Beam tests	Geometry			Concrete	Longitudinal reinforcement: Steel					Transverse strengthening: Ni-Ti-Nb						
Phase 1	V_{test} (kN)	d (mm)	b (mm)	a (mm)	$f_{cm,cyl}$ (MPa)	E_c (MPa)	ϕ (mm)	A_t (mm ²)	α	ρ	ϕ (mm)	A_t (mm ²)	s (mm)	f_s (MPa)	Φ_{front} (°)	Φ_{back} (°)
1.1 - Reference	18.3	127	80	340	37.3	32643	16	201	6.13	0.0197835	-	-	-	-	-	-
1.2 - Reference	18.41	127	80	340	37.5	32714	16	201	6.11	0.0197835	-	-	-	-	-	-
2.1 - Sf3/100/UCR/A	35.41	127	80	340	37.7	32761	16	201	6.10	0.0197835	3	7	100	496	90	56
2.2 - Sf3/100/UCR/A	35.95	127	80	340	37.9	32808	16	201	6.10	0.0197835	3	7	100	548	90	56
3.1a - Sf3/100/UCR/NA	18.23	127	80	340	38.3	32924	16	201	6.07	0.0197835	-	-	-	-	90	56
3.1b - Sf3/100/COL/A	27.14	127	80	340	38.5	32971	16	201	6.07	0.0197835	3	7	100	505	90	56
3.2a - Sf3/100/UCR/NA	21.47	127	80	340	38.3	32924	16	201	6.07	0.0197835	-	-	-	-	90	56
3.2b - Sf3/100/COL/A	35.21	127	80	340	38.4	32948	16	201	6.07	0.0197835	3	7	100	479	90	56
4.1 - Sf3/100/PCR/A	34.35	127	80	340	38.7	33017	16	201	6.06	0.0197835	3	7	100	485	90	56
4.2 - Sf3/100/PCR/A	35.6	127	80	340	38.7	33017	16	201	6.06	0.0197835	3	7	100	482	90	56
5.1 - Sf3/075/UCR/A	37.04	127	80	340	38.9	33063	16	201	6.05	0.0197835	3	7	75	492	90	63
5.2 - Sf3/075/UCR/A	41.82	127	80	340	38.9	33063	16	201	6.05	0.0197835	3	7	75	505	90	63

Table A2.2. Geometry and material property parameters of phase 2 beam tests

Beam tests	Geometry				Concrete	Longitudinal reinforcement: Steel					Transverse strengthening: Ni-Ti-Nb					
Phase 2	V_{test} (kN)	d (mm)	b (mm)	a (mm)	$f_{cm.cyl}$ (MPa)	E_c (MPa)	ϕ (mm)	A_t (mm ²)	α	ρ	ϕ (mm)	A_t (mm ²)	s (mm)	f_s (MPa)	ϕ_{front} (°)	ϕ_{back} (°)
6.1 - Reference	19.71	127	80	340	35.7	32235	16	201	6.20	0.0197835	-	-	-	-	-	-
6.2 - Reference	18.5	127	80	340	35.7	32235	16	201	6.20	0.0197835	-	-	-	-	-	-
7.1 - Sf3/100/UCR/A/G	25.36	127	80	340	35.8	32260	16	201	6.20	0.0197835	3	7	100	418	90	53
7.2 - Sf3/100/UCR/A/G	35.51	127	80	340	35.8	32260	16	201	6.20	0.0197835	3	7	100	506	90	53
8.1 - Uf3/100/UCR/A	37.74	127	80	340	35.7	32235	16	201	6.20	0.0197835	3	7	100	495	90	90
8.2 - Uf3/100/UCR/A	34.75	127	80	340	35.7	32235	16	201	6.20	0.0197835	3	7	100	480	90	90
9.1 - Sf3/100/UCR/A/S	20.54	127	80	340	35.8	32260	16	201	6.20	0.0197835	3	7	100	316	90	37
9.2 - Sf3/100/UCR/A/S	22.03	127	80	340	35.8	32260	16	201	6.20	0.0197835	3	7	100	338	90	37
10.1 - Uf3/075/UCR/A	36.79	127	80	340	35.8	32260	16	201	6.20	0.0197835	3	7	75	511	90	90
10.2 - Uf3/075/UCRA	33.65	127	80	340	35.8	32260	16	201	6.20	0.0197835	3	7	75	568	90	90

Table A2.3. CCCM and EC-2 models partial calculations and results of all beams of phase 1 beam tests

Beam tests	CCCM Calculations											EC2 Calculations				
Phase 1	V_{test} (kN)	x/d	x (mm)	ξ	$cot\theta$	V_{cu} (kN)	ΔV_{cu}	$V_{cu}^{confinement}$ (kN)	V_{su} (kN)	V_u (kN)	V_{test}/V_u	k	$V_{Rd,c}$ (kN)	$V_{Rd,s}$ (kN)	V_{Rd} (kN)	V_{test}/V_{Rd}
1.1 - Reference	18.30	0.386	49.003	1.285	-	16.85	-	-	-	16.85	1.09	2	15.34	0	15.34	1.19
1.2 - Reference	18.41	0.386	48.963	1.285	-	16.92	-	-	-	16.92	1.09	2	15.37	0	15.37	1.20
2.1 - S ϕ 3/100/UCR/A	35.41	0.385	48.936	1.285	1.38	16.96	0.495	4.18	8.45	29.60	1.20	2	15.40	20.57	20.57	1.72
2.2 - S ϕ 3/100/UCR/A	35.95	0.385	48.909	1.285	1.38	17.01	0.495	4.62	9.34	30.97	1.16	2	15.42	22.73	22.73	1.58
3.1a - S ϕ 3/100/UCR/NA	18.23	0.385	48.843	1.285	-	17.12	-	-	-	17.12	1.06	2	15.48	0	15.48	1.18
3.1b - S ϕ 3/100/COL/A	27.14	0.384	48.817	1.285	1.38	17.17	0.494	4.25	8.61	30.03	0.90	2	15.51	20.94	20.94	1.30
3.2a - S ϕ 3/100/UCR/NA	21.47	0.385	48.843	1.285	-	17.12	-	-	-	17.12	1.25	2	15.48	0	15.48	1.39
3.2b - S ϕ 3/100/COL/A	35.21	0.384	48.830	1.285	1.38	17.14	0.494	4.03	8.15	29.32	1.20	2	15.49	19.82	19.82	1.77
4.1 - S ϕ 3/100/PCR/A	34.35	0.384	48.791	1.285	1.38	17.21	0.493	4.08	8.27	29.56	1.16	2	15.53	20.11	20.11	1.71
4.2 - S ϕ 3/100/PCR/A	35.60	0.384	48.791	1.285	1.38	17.21	0.493	4.06	8.22	29.49	1.21	2	15.53	19.99	19.99	1.78
5.1 - S ϕ 3/075/UCR/A	37.04	0.384	48.765	1.285	1.38	17.25	0.493	5.49	11.11	33.85	1.09	2	15.56	27.47	27.47	1.35
5.2 - S ϕ 3/075/UCR/A	41.82	0.384	48.765	1.285	1.38	17.25	0.493	5.63	11.41	34.29	1.22	2	15.56	28.19	28.19	1.48
Phase 1 total											Average	1.16		Average		1.47
											Standard deviation	0.07		Standard deviation		0.24
											Coefficient of Variation (%)	5.6		Coefficient of Variation (%)		16.0

Table A2.4. CCCM and EC-2 models partial calculations and results of all beams of phase 2 beam tests

Beam tests	CCCM Calculations											EC2 Calculations				
Phase 2	V_{test} (kN)	x/d	x (mm)	ξ	$cot\theta$	V_{cu} (kN)	ΔV_{cu}	$V_{cu}^{confinement}$ (kN)	V_{su} (kN)	V_u (kN)	V_{test}/V_u	k	$V_{Rd,c}$ (kN)	$V_{Rd,s}$ (kN)	V_{Rd} (kN)	V_{test}/V_{Rd}
6.1 - Reference	19.71	0.388	49.238	1.285	-	16.47	-	-	-	16.47	1.20	2	15.12	-	15.12	1.30
6.2 - Reference	18.50	0.388	49.238	1.285	-	16.47	-	-	-	16.47	1.12	2	15.12	-	15.12	1.22
7.1 - S ϕ 3/100/UCR/A/G	25.36	0.388	49.224	1.285	1.39	16.49	0.498	3.55	7.12	27.16	0.90	2	15.14	17.22	17.22	1.47
7.2 - S ϕ 3/100/UCR/A/G	35.51	0.388	49.224	1.285	1.39	16.49	0.498	4.29	8.62	29.40	1.21	2	15.14	20.85	20.85	1.70
8.1 - U ϕ 3/100/UCR/A	37.74	0.388	49.238	1.285	1.39	16.47	0.498	3.76	7.56	27.79	1.36	2	15.12	20.00	20.00	1.89
8.2 - U ϕ 3/100/UCR/A	34.75	0.388	49.238	1.285	1.39	16.47	0.498	4.41	8.85	29.73	1.17	2	15.12	23.43	23.43	1.48
9.1 - S ϕ 3/100/UCR/A/S	20.54	0.388	49.224	1.285	1.39	16.49	0.498	2.61	-	19.10	1.08	2	15.14	0	15.14	1.36
9.2 - S ϕ 3/100/UCR/A/S	22.03	0.388	49.224	1.285	1.39	16.49	0.498	2.80	-	19.29	1.14	2	15.14	0	15.14	1.46
10.1 - U ϕ 3/075/UCR/A	36.79	0.388	49.224	1.285	1.39	16.49	0.498	5.19	10.40	32.08	1.15	2	15.14	27.53	27.53	1.34
10.2 - U ϕ 3/075/UCRA	33.65	0.388	49.224	1.285	1.39	16.49	0.498	5.76	11.56	33.81	1.00	2	15.14	30.60	30.60	1.10
Phase 2 total											Average	1.16	Average			1.43
											Standard deviation	0.10	Standard deviation			0.23
											Coefficient of Variation (%)	8.6	Coefficient of Variation (%)			16.0
Phase 1 & 2 beams											Average	1.16	Average			1.45
											Standard deviation	0.08	Standard deviation			0.23
											Coefficient of Variation (%)	6.9	Coefficient of Variation (%)			15.7